Non-modal instability mechanisms in stratified and homogeneous shear flow

Cristobal Arratia

École Polytechnique
Laboratoire d'Hydrodynamique

Thèse présentée pour obtenir le grade de
DOCTEUR DE L'ÉCOLE POLYTECHNIQUE

Domaine : Physique
Specialité : Mécanique

par

Cristóbal ARRATIA

Mécanismes d'instabilité non-modaux dans les écoulements cisaillés avec et sans stratification en densité

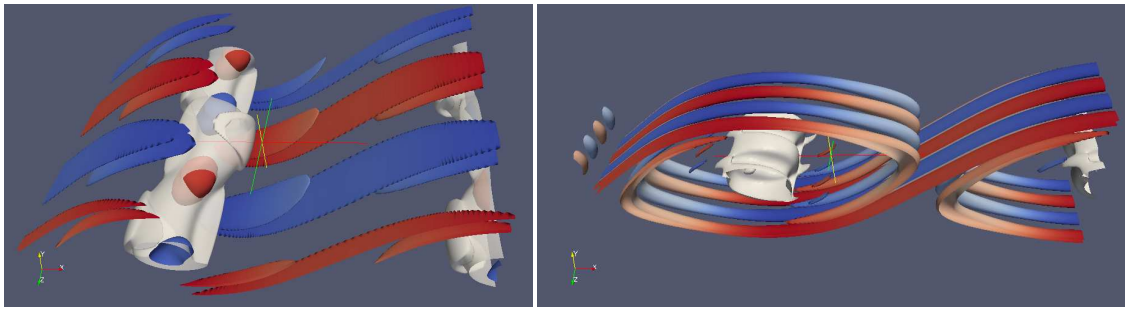

Soutenue le 3 novembre 2011 devant le jury composé de:

Dwight BARKLEY	examinateur	University of Warwick, UK
Claude CAMBON	examinateur	LMFA, Lyon
Jean-Marc CHOMAZ	directeur de thèse	LadHyX, Palaiseau
Richard KERSWELL	rapporteur	University of Bristol, UK
Sabine ORTIZ	directrice de thèse	LadHyX, Palaiseau
Riwal PLOUGONVEN	examinateur	LMD, Paris
Chantal STAQUET	rapporteuse	LEGI, Grenoble

Résumé

Cette thèse est dediée à l'étude des mécanismes d'instabilité non-modaux dans les écoulements cisaillés, principalement des couches de mélange. On se concentre sur les perturbations linéarisées qui ont la plus grande croissance d'énergie à un temps donné, les 'perturbations optimales', différentes du mode propre le plus instable pour les systèmes non-normaux. Une description originale de la non-normalité et ses conséquences est donnée dans le chapitre 2. Le chapitre 3 traite du mécanisme de 'lift-up' dans le cas des perturbations longitudinales non-visqueuses sur un écoulement de base parallèle et arbitraire. On trouve une nouvelle équation 1D qui détermine l'ensemble des perturbations orthogonales, dont l'optimale, et permet de trouver des nouveaux résultats exacts et asymptotiques. Dans le chapitre 4 on s'intéresse aux instabilités secondaires d'une couche de mélange en utilisant comme état de base l'écoulement 2D instationnaire et non-linéaire pour calculer les perturbations optimales 3D. Selon le nombre d'onde et les temps d'optimisation (initial et final), on retrouve comme réponses optimales les perturbations de types 'elliptique' et 'hyperbolique'. Dans les chapitres 5 et 6 on considère une stratification en densité dans la direction orthogonale au plan de l'état de base, et on utilise une décomposition de 'Craya-Herring' pour analyser les perturbations en termes de leur contenu en ondes internes et vorticité verticale. Les équations d'évolution des perturbations linéarisées autour d'un état de base 2D général sont obtenues et analysées au niveau de l'énergie onde/tourbillon. Ces résultats sont appliqués dans le chapitre 6 pour analyser la génération et l'émission d'ondes dans les perturbations optimales sur une couche de cisaillement horizontale.

Abstract

This thesis reports a study of nonmodal instability mechanisms in shear flows, mainly mixing layers. We focus on the linearized perturbations that maximize the energy amplification at finite time, the 'optimal perturbations', which in non-normal systems are different from the most unstable eigenmode. An original description of non-normality and its consequences is provided in chapter 2. Chapter 3 deals with the well known lift-up mechanism, for the case of longitudinal inviscid perturbations to any parallel flow. A new one-dimensional equation determining the orthogonal set of optimal and sub-optimal perturbations is found in that case, allowing to obtain new exact and asymptotic results. In chapter 4 we address the secondary instability of mixing layers, for which we use the naturally evolving 2D flow as a base state to compute the 3D optimal perturbations. Among the optimal responses we recover the usual 'elliptic' and 'hyperbolic' types of perturbation structure, the largest growth depending on the spanwise wavenumber and optimization times (initial and final). In chapters 5 and 6 we consider density stratification in the direction orthogonal to the plane of the base flow, and we use a 'Craya-Herring' decomposition to analyse the flow in terms of its internal wave and vertical vorticity content. The perturbation equations for a general 2D base flow are first derived and interpreted in terms of wave/vortex energetics in chapter 5. These results are used in chapter 6 to analise the strong generation and emission of internal waves produced by the optimal perturbations to a horizontal shear layer.

Resumen

Esta tesis describe un estudio de los mecanismos de inestabilidad no-modal en flujos de corte o con cizalle, especialmente capas de mezcla, que corresponden a la interfaz de contacto entre dos masas de fluido con velocidad relativa. El enfoque esta centrado en las perturbaciones lineales cuya evolución maximiza el crecimiento energético (de la perturbación) a tiempo finito, las 'perturbaciones óptimas', distintas del modo propio mas inestable cuando el sistema es no-normal. En el capítulo 2 se entrega una descripción original de la no-normalidad, sus orígenes y consecuencias. El capítulo 3 está dedicado al ya bien conocido mecanismo de 'lift-up', mecanismo no-modal que amplifica fuertemente las perturbaciones elongadas en la dirección del flujo base, y que ha permitido explicar la aparición de este tipo de perturbaciones en varios contextos experimentales y aplicaciones. Para el caso de un flujo sin viscosidad, hemos encontrado una nueva ecuación que determina el conjunto de perturbaciones ortogonales, entre las cuales se encuentra la perturbación óptima; las soluciones de esta ecuación se pueden entender en analogía con los estados propios (ligados) de una partícula cuántica en un pozo o una caja, la perturbación óptima correspondiendo al estado fundamental. Esta ecuación permite obtener nuevos resultados exactos y aproximaciones asintóticas. En el capítulo 4 consideramos la inestabilidad secundaria de una capa se mezcla. Para ello usamos como estado base la solución no lineal y no estacionaria correspondiente a la evolucion 2D de una capa de mezcla, y calculamos sobre ese flujo las perturbaciones óptimas 3D por medio de un algoritmo iterativo de resolución alternada de los problemas directo y adjunto. De esa forma podemos integrar y describir el crecimiento de las perturbaciones durante las distintas etapas sucesivas de la evolución de la inestabilidad. Como estado final o respuesta, entre las perturbaciones optimales recuperamos los tipos 'elípticos' e 'hiperbólicos', donde el más amplificado depende del numéro de onda de la perturbación y los tiempos (inicial y final) de optimización con respecto a la evolución del flujo base. En los capítulos 5 y 6 consideramos el efecto de una estratificación en densidad en la dirección perpendicular al plano del flujo base, y usamos una descomposición de 'Craya-Herring' para analizar el flujo en terminos de su contenido de ondas internas y vorticidad vertical. Primero, en el capítulo 5, derivamos la descomposición en 'Craya-Herring' de las ecuaciones para las perturbaciones linealizadas sobre un estado base horizontal arbitrario; esas ecuaciones son luego analizadas e interpretadas en términos de las transferencias energéticas estado base/perturbación y onda/vorticidad. Esos resultados son luego aplicados en el capítulo 6 para analizar la intensa generación de ondas internas que se observa en las perturbaciones óptimas a una capa de mezcla horizontal con estratificación vertical.

Remerciements

C'est difficile de trouver les mots justes pour remercier Jean-Marc Chomaz, mon directeur de thèse. Je te remercie d'abord pour me donner cette opportunité de venir faire une thèse avec toi et Sabine au LadHyX, je sens vraiment que c'est une chance et un privilège énorme. J'ai eu la chance de connaître ta qualité humaine dont je remercie la joie et tout ton soutien et ouverture, qualités qui s'expriment aussi dans ton encadrement et font un plaisir de travailler avec toi; c'est une bonne dose de liberté bien guidée. Et bien sûr, bien motivée par ces longues discussions plaines d'ides et du bon sens physique. Merci Jean-Marc pour ces bons moments.

Je remercie aussi ma co-directrice Sabine Ortiz, a qui je dois aussi remercier la confiance, non seulement pour la opportunité de venir faire une thèse mais aussi pour l'enseignement. Merci beaucoup pour ta generosité et ta sympathie, c'été un grand plaisir de partager ses années avec toi. Merci aussi pour tes remarques qui m'ont beaucoup aidé à guider mon travail.

Je remercie les rapporteurs Richard Kerswell et Chantal Staquet pour avoir accepté de lire mon manuscrit. Thank you very much for your interest, conscious reading and comments. I also acknowledge Dwight Barkley, Claude Cambon and Riwal Plougonven for accepting to be part of the jury. Thank you also for your interest, questions and suggestions.

I deeply thank Colm Caulfield for his collaboration and support. Thank you for kindly receiving me and giving me the opportunity to have a splendid experience in Cambridge.

Je remercie tous les permanents du labo qui sont une partie essentiel de la bonne ambiance q'il y a au LadHyX, ce qui a permis la bonne qualité du temps que j'ai passé ces 4 dernières années. Je remercie Patrick Huerre pour le bon esprit q'il a facilité au labo. Je remercie Peter Schmid pour la bonne disposition qu'il a eu plusiers fois que je lui ai posé des questions. Je remercie particulièrement Daniel Guy, non seulement pour ta bonne disposition a aider pour les besoins techniques, mais aussi pour ton ouverture à l'écoute et à la discussion des sujets les plus variées, je garde beaucoup des bons souvenirs. Je remercie aussi Thérèse Lescuyer et Sandrine Laguerre pour tout leur aide et cordialité. Merci aussi Judith et Delphine pour votre joie, Caroline, Alexandre, Charles et Abdul pour votre sympathie.

Je dois bien sûr remercier aussi mes collègues non permanents, les stagières, postdocs et surtout les autres thèsards du labo. On est devenu très nombreux et je ne peux pas rêver de faire justice a tous ceux que pendant ces 4 ans m'ont laissé des bon souvenirs, mais je ne peux pas me permettre de ne pas remercier les plus proches comme ceux qui ont été mes collégues de bureau Elena, Gianluca, Xavier et Miguel, ou Jon et Franz... Merci pour votre amitié et pour beaucoup des discussions interessantes. Merci aussi Nicolas, Pierre, Junho, Christell, Fulvio, Eletta, Yongyun, Alexandre, Marine, Joran, Fabien, Diego, Caro, Baptiste, Eti-

enne, Clement, Remi, Adrien, Dimitry, Madiha, Emmanuel, Kiran, Benoit, Sheryar, Shyam, Herbert, Mathieu, Christoph, Remi, Fred et tout les autres que j'oublie en ce moment, avec qui j'ai passé des bons moments de foot, d'escalade, discusions scientifiques et d'autres, soirées, conversations au labo... ce le moment de vous dire combien j'apprecie les moments partagés avec vous.

Je voudrais remercier aussi François Gallaire pour me faire confiance et bien m'acueillir dans son labo comme post-doc. Merci and thank you all in LFMI for your kind welcome.

Le doy las gracias a mi familia, mis amigos, y a todas aquellas personas que me dieron su apoyo pese a la distancia; gracias, no sería lo que soy sin ustedes. Y muchísimas gracias a los que se transformaron en mi familia y me apoyaron durante estos 4 años: Gustavo, Mario con Caro (¡y la Nini!), Lucho, Miguel, Giorgio, Claudio... y tant@s con l@s que compartí tantos buenos momentos como Jaime, Jorge, Claudia, Blanca, Gaby, Pancha, Khamila, Juan con Barbara, Diane, Caro, Draltan, Ceci, María Luisa, Pablo con Claudia y Simón, Mauricio, Anna, los Tamarillos, Sonia, Enric, David, Juampi, Amari, Fanny, Maël, Gaby, Loïc, Cony, Nestor, Dani, Nelson, Paulina, Julien, Lorena, Antonieta, Claudia, Matías, Ulises... en fin, no l@s puedo mencionar a tod@s, pero no puedo dejar de mancionar a mis 'herederos de departamento' Victor y Belén, gracias por el apoyo y la ayuda durante mis últimas semanas parisinas.

And last but definately not least, I want to thank Marie with whom I had the luck to share a large part of this process. Thank you sweetie for your caring love and encouraging support.

Contents

Chapter 1

Introduction

The great problem of contemporary science is the explanation of observed phenomena which can not be directly explained from basic principles. This is a problem of the most fundamental, even philosophical importance [18]. It concerns all scientific disciplines and spans a huge variety of scales and phenomena, from molecular organization to the formation of galaxies, passing through climate and the origin and dynamics of the living. While there can be similarities, each discipline concerned with the study of these and other phenomena has its own intrinsic interest. In particular Fluid Mechanics, having well established basic principles and presenting an enormous variety of non trivial phenomena, is a field that gives the opportunity to apply and develop techniques and concepts for understanding various types of complex phenomena. During the last few decades, there have been important advances concerning instability in Fluid Mechanics For example, during the last few decades, there have been important advances in Fluid Mechanics concerning instability, that is, the During the last few decades, for example, there have been important advances in the theory of instabilities in Fluid Mechanics, theory that deals with the study of the propensity or likeliness of a given flow, typically in an idealised situation, to remain or change in a way that should be determined.

The main focus of this dissertation is on instability mechanisms on shear flows. Mostly linear mechanisms, and more specifically, *non-modal* instability mechanisms. The relevance of non-modal instability mechanisms went for long time unnoticed, linear instability mechanisms being searched for within *classical stability theory* [42]. But very large transient growth (produced by non-modal instability mechanisms) in systems that were stable according to classical stability theory, demonstrated the shortcomings of the classical stability theory. This brought about major developments in the study of linear stability [46, 47, 90]. More generally, the developments concern linear dynamics.

I consider it important to remark that methodological developments can have a further reach than that concerning the theories in which they are developed. Prob-

ably the most robust backbone for parallels between subjects seemingly completely different, is provided by similarities of the mathematical models pertinent on each case. It is a personal conviction that there is much to learn from establishing connections between different subjects; it is a personal choice to remain open in the search of those connections. I consider thus of primary importance the possibility that the developments used and performed in this work be applicable for other domains. To achieve that, it is useful to understand as deeply as possible.

An essential mathematical ingredient related to the occurrence of non-modal instability mechanisms is *non-normality*. In chapter 2 we define what non-normality is, explore what produces it and what are its consequences. (The reader interested in the rigorous mathematical theory concerning non-self-adjoint linear operators is referred to [36].) Also explained in chapter 2 is the methodology and aspects of linear dynamics that are relevant in this manuscript. It also provides some (seemingly) original results that are unfinished, and introduces the basic non-modal instability mechanisms of shear flow.

In chapter 3 we show a simple new result concerning the lift-up mechanism, one of the key pieces of shear flow stability that was missing for decades. The lift up mechanism is arguably the most important non-modal instability mechanism in plane shear flow. An important limitation in classical stability theory concerns dealing with time dependent systems. In chapter 4, using the tools of the non-modal stability theory, we study the stability of an unstationary flow. That flow is a full solution of the two-dimensional Navier-Stokes equations corresponding to a mixing layer. We include the effect of density stratification on chapter 5. There we derive the expression of the perturbative Navier-Stokes equations under the Boussinesq approximation in the *Craya-Herring* frame. The results from chapter 5 are used in chapter 6, where we study the stability of a horizontal shear layer with vertical stratification. The Craya-Herring decomposition there allows tracing the generation and emission of internal waves. We finish in chapter 7 with the conclusions and perspectives.

Chapter 2

Some ideas on non-normality

2.1 Mathematical framework

2.1.1 Eigenmode decomposition of linear dynamics

Consider a linear dynamical system of the form

$$\frac{\mathrm{d}\mathbf{u}}{\mathrm{d}t} = L\mathbf{u}, \tag{2.1}$$

where L is an autonomous (no time dependence) linear operator acting on the state vector $\mathbf{u}$ and determining its evolution. The solution of (2.1) at time t can be written as

$$\mathbf{u}(t) = e^{Lt}\mathbf{u}_0, \tag{2.2}$$

where $\mathbf{u}_0$ is the initial condition. For generality, we will not specify the vector space $\mathcal{U}$ to which the state vector $\mathbf{u}$ belongs. We will assume, however, that the operator L has a complete set of eigenvectors and a discrete spectrum, implying that any initial condition $\mathbf{u}_0$ can be written as a linear combination of the eigenvectors of L, that is

$$\mathbf{u}_0 = \sum_i u_i \mathbf{l}_i, \tag{2.3}$$

where $\mathbf{l}_i$ are the eigenvectors of L satisfying

$$L\mathbf{l}_i = \lambda_i \mathbf{l}_i, \tag{2.4}$$

and the sub index $i \in \mathbb{N}$ runs from 1 to the dimension of the vector space $\mathcal{U}$. The complex numbers λ_i are the eigenvalues and the spectrum is the set of eigenvalues $\{\lambda_i\}$. The spectrum $\{\lambda_i\}$ and the set of eigenvectors $\{\mathbf{l}_i\}$ are a property of the linear

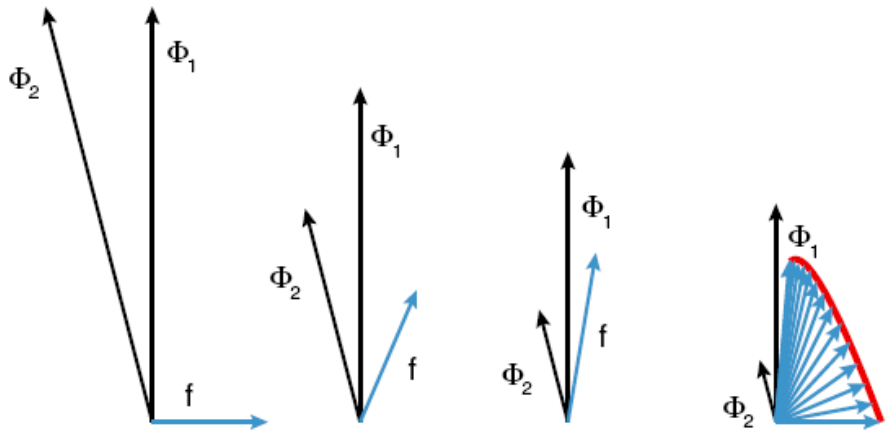

Figure 2.1: Consider the evolution of an initial condition $\mathbf{f}$ composed of the difference between two decaying eigenmodes $\mathbf{\Phi}_1$ and $\mathbf{\Phi}_2$. The eigenmodes $\mathbf{\Phi}_1$ and $\mathbf{\Phi}_2$ decay in time from left to right, at different rates. As a result, $\mathbf{f}$ increases during a transient before eventually decaying while becoming parallel to the mode with slowest decay. Image from Schmid, 2007 [90].

operator L acting on $\mathcal{U}$. Under these assumptions, the solution of equation (2.1) given in (2.2) becomes

$$\mathbf{u}(t) = \sum_i u_i \mathbf{l}_i e^{\lambda_i t}. \tag{2.5}$$

2.1.2 Normality

Equation (2.5) is key for discussing the evolution of most linear systems. The real part of the eigenvalue λ_i determines whether the contribution to $\mathbf{u}(t)$ of the eigenmode $\mathbf{l}_i$ grows or decays in time. Classical stability theory concentrates on the spectrum λ_i, following the intuition that if every term of the sum in (2.5) decays, then $\mathbf{u}(t)$ should also decay. As graphically described on figure 2.1, this intuition can be misleading if the eigenmodes can partially cancel each other in the right hand side of (2.5). In the left of figure 2.1 taken from [90], two eigenmodes $\mathbf{\Phi}_1$ and $\mathbf{\Phi}_2$ *similar to each other*, yield an initial condition $\mathbf{f}$ in which much of their contributions cancel. As time increases (moving to the right in figure 2.1), one can see how $\mathbf{f}$ evolves and the cancellation between the two eigenmodes is partially destroyed; this produces a *growth* of $\mathbf{f}$ despite the decrease in the contribution from each of the eigenmodes. If $\mathbf{\Phi}_1$ and $\mathbf{\Phi}_2$ in figure 2.1 were *orthogonal* (*normal*) to each other, the decay of the $\mathbf{\Phi}_1$ and $\mathbf{\Phi}_2$ contributions to $\mathbf{f}$ would necessarily lead to a decay of $\mathbf{f}$.

The geometric notion of whether two eigenmodes belonging to a vector space $\mathcal{U}$ are *orthogonal* or '*similar to each other*' needs to be made precise. This can be

done by introducing an inner product, $\langle \cdot, \cdot \rangle$ say, which associates a scalar $\langle \mathbf{v}, \mathbf{w} \rangle$ to any pair of vectors $\mathbf{v}$ and $\mathbf{w}$ in $\mathcal{U}$. Any pair of vectors $\mathbf{v}$ and $\mathbf{w}$ are said to be orthogonal (normal) if $\langle \mathbf{v}, \mathbf{w} \rangle = 0$. It is after the definition of an inner product that one can assess normality (orthogonality) between eigenmodes; that the eigenmodes are normal to each other means that

$$\langle \mathbf{l}_i, \mathbf{l}_j \rangle \propto \delta_{ij}, \tag{2.6}$$

where δ_{ij} is the Kronecker's delta function. Normality between eigenmodes is thus not a property of the linear operator L only, it also depends on the inner product. Similarly, making precise the *growth* of $\mathbf{u}$ (or $\mathbf{f}$ in figure 2.1) requires a measure of $\mathbf{u}$ (or $\mathbf{f}$). An inner product $\langle \cdot, \cdot \rangle$ generates a norm $\| \cdot \|$ directly as[1]

$$\|\mathbf{u}\| := \langle \mathbf{u}, \mathbf{u} \rangle, \tag{2.7}$$

providing a measure for assessing the growth or decay of $\mathbf{u}$. As it is natural, the growth in time of $\mathbf{u}(t) = e^{Lt}\mathbf{u}_0$ (2.2) does not depend on $\mathbf{u}_0$ and L only, it also depends on the way of measuring $\mathbf{u}(t)$.

In a way similar as an inner product is required to determine orthogonality between eigenmodes, *normality* of the linear operator L is not a property of the linear operator L alone, it also depends on the inner product. The linear operator L acting on $\mathcal{U}$ with inner product $\langle \cdot, \cdot \rangle$ is defined to be *normal* if and only if L and its adjoint L^+ satisfy

$$L^+ L = L L^+, \tag{2.8}$$

where the defining property of the adjoint L^+ under the inner product $\langle \cdot, \cdot \rangle$ is that

$$\langle \mathbf{v}, L\mathbf{w} \rangle = \langle L^+\mathbf{v}, \mathbf{w} \rangle \tag{2.9}$$

for all $\mathbf{v}$ and $\mathbf{w}$ in $\mathcal{U}$. The eigenmodes $\mathbf{l}_i$ are normal to each other under the inner product $\langle \cdot, \cdot \rangle$ if and only if L is normal under that inner product. According to this definition, non-normality of L occurs when it does not commute with its adjoint.

We can also remark that normality of the operator L implies that it has a complete set of eigenvectors $\{\mathbf{l}_i\}$. As a consequence, non completeness of $\{\mathbf{l}_i\}$ implies that L is non-normal. Moreover, as $\{\mathbf{l}_i\}$ does not depend on the choice of inner product, an incomplete set $\{\mathbf{l}_i\}$ implies that L is non-normal for any inner product.

As the eigenvalues and eigenmodes do not depend on a choice of inner product, they are more fundamental properties of L. One could thus be tempted to disregard (non-)normality as superfluous and focus only on the "more essential" eigenvalues and their eigenmodes. We will see why this is simplistic in the following, when describing an aspect that plays a very important role in this thesis.

[1] A norm from an inner product is usually defined as $\|\mathbf{u}\| := \sqrt{\langle \mathbf{u}, \mathbf{u} \rangle}$. We define (2.7) because we will concentrate more on quadratic measures such as energy. It does not make an important difference.

2.1.3 Optimal perturbations

The computation of optimal perturbations constitutes a central part of the results of this dissertation. The need for characterizing the linear dynamics of non-normal systems has led to major developments on linear stability theory (see [90] for a review). In classical stability theory, much importance is ascribed to the most unstable (or least stable) eigenmode. Implicit in this stance is the idea that the characteristics of the most unstable eigenmode are what one expects to *observe*. What one observes, however, necessarily implies a selection of a particular feature of the system under study. This "selection of a particular feature" implies a measure, and a measure which is sensitive to all possible features is a norm. One step in the way to precise the notion of "what one expects to observe" can be given by the computation of the *optimal perturbations*.

The optimal perturbation for optimization time T is given by the solution to

$$G_{max}(T) = \max_{\mathbf{u}_0} \left(\frac{\|\mathbf{u}(T)\|}{\|\mathbf{u}_0\|} \right), \tag{2.10}$$

where $\mathbf{u}(T)$ corresponds to the vector state $\mathbf{u}$ at time T that evolved from the initial condition $\mathbf{u}_0$. The optimization problem (2.10) can be solved with a variational formulation [90], which has the flexibility that it allows including extra costs and constraints. We shall take here a different approach that puts forward the solution procedure while highlighting a very important aspect of the dynamics. In (2.10) we have

$$\|\mathbf{u}(T)\| = \langle \mathbf{u}(T), \mathbf{u}(T) \rangle, \tag{2.11a}$$

$$= \langle e^{LT}\mathbf{u}_0, e^{LT}\mathbf{u}_0 \rangle, \tag{2.11b}$$

$$= \langle e^{L^+T} e^{LT}\mathbf{u}_0, \mathbf{u}_0 \rangle, \tag{2.11c}$$

where in (2.11c) we have used that $(e^{LT})^+ = e^{L^+T}$. On the other hand, the adjoint equation to (2.1) is[2]

$$-\frac{\mathrm{d}\mathbf{v}}{\mathrm{d}t} = L^+\mathbf{v}, \tag{2.12}$$

so that e^{L^+T} corresponds to the evolution of (2.12) up to time T after the change $t \to -t$. Thus, the operator $e^{L^+T}e^{LT}$ corresponds to the successive evolution of the direct system (2.1) followed by the evolution of (2.12) with $t \to -t$. This can be efficiently performed in large systems by numerically simulating the evolution of the direct and adjoint systems.

Equation (2.11) indicates that maximizing $\|\mathbf{u}(T)\|$ amounts to finding the $\mathbf{u}_0$ which grows the most under the effect of $e^{L^+T}e^{LT}$. When applying the operator $e^{L^+T}e^{LT}$ on $\mathbf{u}_0$, the outcome $e^{L^+T}e^{LT}\mathbf{u}_0$ approaches the leading eigenvector of

[2]The adjoint equation comes from writing (2.1) as $A\mathbf{u} = 0$ with $A = \frac{\mathrm{d}}{\mathrm{d}t} - L$.

$e^{L^+T}e^{LT}$, say $\mathbf{l}_{T1}$ corresponding to the largest eigenvalue λ_{T1} ($\mathbf{u}_0$ approaches $\mathbf{l}_{T1}$ unless they are perfectly orthogonal). When applying the operator $e^{L^+T}e^{LT}$ successively, say n times on $\mathbf{u}_0$, the outcome $(e^{L^+T}e^{LT})^n\mathbf{u}_0$ approaches $\mathbf{l}_{T1}$ as $n \to \infty$. This procedure for finding the leading eigenvector of an operator is known as the power iteration method (or just 'power method'). Applied to the direct-adjoint evolution operator $e^{L^+T}e^{LT}$, it constitutes a simple algorithm for computing the optimal perturbations. The first time it was reported in relation to fluid dynamical systems was probably by Farrell & Moore in 1992 [51], altough it did not receive much attention until Luchini & Bottaro in 1998 [73].

It is important to remark that the operator $e^{L^+T}e^{LT}$ is normal. As we have seen, that normality implies that it has an orthogonal set of eigenvectors $\{\mathbf{l}_{Ti}\}$, of which the leading one $\mathbf{l}_{T1}$ is the optimal initial perturbation. Note that computing the optimal perturbation corresponds to computing the leading 'input mode' of the singular value decomposition of e^{LT}, the linear operator propagating the initial conditions to time T. The singular value decomposition (SVD) defines an orthogonal base of inputs (initial conditions) and the corresponding orthogonal base of responses, outcomes at time T of the initial conditions. The rest of the inputs of the SVD are given by the set of eigenvectors $\{\mathbf{l}_{Ti}\}$. In a way completely symmetric between direct and the adjoint (the adjoint of the adjoint is the direct), the corresponding set of responses is given by the eigenvectors of the operator $e^{LT}e^{L^+T}$. The amplification factors or singular values are correspondingly given by the set $\{\sqrt{\lambda_{Ti}}\}$.

Consistently with the exponential time dependence of the eigenmodes, the optimal response approaches the most unstable eigenmode as $T \to \infty$. The optimal initial condition in the $T \to \infty$ limit is given by the most unstable eigenmode of the adjoint L^+. For a normal system, the optimal initial condition and the optimal response for any time T, are given by the most unstable eigenmode.

A full precise answer to the notion of "what one expects to observe" would require the knowledge of the full singular value decomposition. While there is no reason to expect that the initial condition of the optimal perturbation will be preferentially excited by a random initial condition, the outcome at time T of the optimal perturbation, the *optimal response*, will be the one with the largest energy if all initial conditions are equally excited. Concerning stability, the optimal perturbation provides a rigorous bound (within linear dynamics) on the growth of the perturbations while providing the particular case that best exploits the instability mechanisms available.

2.2 A simple case study

The relevance of non-normality for linear dynamics has gone unnoticed for long and is still fairly unknown in some fields. In order to have an idea about the situations

in which non-normality can be relevant, it is key to understand the reasons that make a physical system non-normal. For that we shall study a prototypical case.

Consider the partial differential equation (PDE)

$$\frac{\partial^2 u}{\partial t^2} = c^2 \frac{\partial^2 u}{\partial x^2} + \alpha \frac{\partial u}{\partial t}. \tag{2.13}$$

Equation (2.13) is a damped wave equation for $u(x,t) \in \mathbb{R}$. The sign of α determines the stability of the $u = 0$ solution; negative α corresponds to damping and exponential decay, positive α implies exponential instability and $\alpha = 0$ gives purely oscillatory motion. We will consider a space dependent wave speed $c(x)$ and a 1-dimensional domain from x_a to x_b; we shall not yet specify boundary conditions. For writing equation (2.13) in the form (2.1) we define

$$\mathbf{u} := \begin{pmatrix} u_1 \\ u_2 \end{pmatrix}, \tag{2.14}$$

where $u_1 = \partial_x u$ and $u_2 = \partial_t u$. Now we can write (2.13) in the form (2.1) which is

$$\partial_t \begin{pmatrix} u_1 \\ u_2 \end{pmatrix} = \underbrace{\begin{pmatrix} 0 & \partial_x \\ c^2 \partial_x & \alpha \end{pmatrix}}_{L} \begin{pmatrix} u_1 \\ u_2 \end{pmatrix}. \tag{2.15}$$

We will denote, in this formulation, the set of boundary conditions of the direct wave equation (2.15) as $BC^L(\mathbf{u}, x_a, x_b) = 0$.

To assess the normality (or non-normality) of L lets consider the inner product

$$\langle \mathbf{v}, \mathbf{u} \rangle_r := \int_{x_a}^{x_b} \mathbf{v}^T M \mathbf{u} \, \mathrm{d}x = \int_{x_a}^{x_b} (r v_1 u_1 + v_2 u_2) \, \mathrm{d}x, \tag{2.16}$$

in which $M = \mathrm{diag}(r, 1)$ is a diagonal matrix with a positive relative weight parameter r. Note that $r > 0$ is required to satisfy the positive definiteness of $\langle \cdot, \cdot \rangle$, which is one of the standard defining properties of an inner product, and needed for the inner product to generate a norm. We use (2.16) as a simple but sensible choice for addressing some simple aspects of the choice of norm when assessing non-normality. It is almost always possible[3] to find a suitable inner product or change of coordinates that will make an operator normal; we will consider here that there is an intrinsic interest on the coordinates u_1 and u_2 of $\mathbf{u}$.

Having defined the inner product (2.16) we can compute L^+, the adjoint of L. Integrating by parts and rewriting inside the integral the matrix product on the form $(L^+\mathbf{v})^T M \mathbf{u}$, we obtain the Lagrange identity

$$\langle \mathbf{v}, L\mathbf{u} \rangle_r - \langle L^+ \mathbf{v}, \mathbf{u} \rangle_r = BT(\mathbf{v}, \mathbf{u}) \Big|_{x_a}^{x_b}, \tag{2.17a}$$

[3] it is possible when the set of eigenmodes is complete (almost always the case in physically motivated problems).

wherein the adjoint operator L^+ is given by

$$L^+ = \begin{pmatrix} 0 & -r^{-1}(2cc' + c^2\partial_x) \\ -r\partial_x & \alpha \end{pmatrix}, \tag{2.17b}$$

and the sum of boundary terms by

$$BT(\mathbf{v}, \mathbf{u})\Big|_{x_a}^{x_b} = \Big[r v_1 u_2 + c^2 v_2 u_1 \Big]_{x_a}^{x_b}. \tag{2.17c}$$

We remark that, in general, (2.17a) is valid for any $\mathbf{u}$ and $\mathbf{v}$, whether or not they are solutions of the direct and adjoint equations (2.1) and (2.12). The adjoint equation must imply, however, that the sum of boundary terms is zero when $\mathbf{u}$ and $\mathbf{v}$ are solutions of the direct and adjoint equations (2.1) and (2.12), respectively. The requirement $BT(\mathbf{v}, \mathbf{u})\big|_{x_a}^{x_b} = 0$ is thus what defines the adjoint boundary conditions $BC^{L^+}(\mathbf{v}, x_a, x_b) = 0$. We will assume that the direct boundary conditions $BC^{L}(\mathbf{u}, x_a, x_b) = 0$ are such that $BT(\mathbf{v}, \mathbf{u})\big|_{x_a}^{x_b} = 0$ holds if the adjoint boundary conditions $BC^{L^+}(\mathbf{v}, x_a, x_b) = 0$ are the same. That is, we will assume that the adjoint boundary conditions are the same as the direct or $BC^{L^+}(\,\cdot\,, x_a, x_b) = BC^{L}(\,\cdot\,, x_a, x_b)$. This assumption holds for combinations of Dirichlet ($u_2 = \partial_t u = 0$), Neumann ($u_1 = \partial_x u = 0$) and periodic boundary conditions. If the assumption is not verified, adjoint boundary conditions $BC^{L^+}(\,\cdot\,, x_a, x_b) \neq BC^{L^+}(\,\cdot\,, x_a, x_b)$ will have to apply on $\mathbf{v}$ such that $BT(\mathbf{v}, \mathbf{u})\big|_{x_a}^{x_b} = 0$.

We assess the normality of L by computing the commutator $[L^+, L] := L^+L - LL^+$; we get

$$[L^+, L] = \begin{pmatrix} r\left(1 - \frac{c^4}{r^2}\right)\partial_x^2 & -2\alpha\frac{cc'}{r} - \alpha\left(1 + \frac{c^2}{r}\right)\partial_x \\ r\alpha\left(1 + \frac{c^2}{r}\right)\partial_x & \frac{2c^2}{r}\left[(cc')' + 2cc'\partial_x\right] - r\left(1 - \frac{c^4}{r^2}\right)\partial_x^2 \end{pmatrix}, \tag{2.18}$$

which being in general different from zero implies that L is in general non-normal under the inner product (2.16). It is apparent from the different terms in (2.18) that there are multiple sources of non-normality. This is indeed the case and in the following we will start from (2.18) to comment on non-normality and some related aspects.

2.2.1 Some possible origins of non-normality

Space dependent coefficients

An important source of non-normality is the space dependence of c. This effect is well known. The presence of non constant coefficients implies that the linear PDE can not be separated in independent Fourier modes. In (2.18) we can distinguish

the effect of the non-homogeneity of c on the terms of the right column of $[L^+, L]$, in which c' is present. The effects of spatial dependence can be eliminated in some cases by choosing an appropiate weight function in the integral. In this case, choosing $M = \mathrm{diag}(1, c^{-2})$ in the inner product definition (2.16) would result in a matrix product ML with constant coefficients; thus, the integration by parts would not produce the terms with c' in (2.18).

Homogeneous conservative case

We consider now the conservative, time reversible wave equation with constant wave velocity such that $\alpha = c' = 0$. In that case we have

$$[L^+, L]\Big|_{c',\alpha=0} = \begin{pmatrix} r\left(1 - \frac{c^4}{r^2}\right)\partial_x^2 & 0 \\ 0 & -r\left(1 - \frac{c^4}{r^2}\right)\partial_x^2 \end{pmatrix}, \tag{2.19}$$

which is zero only if $r^2 = c^4$. This shows the possibility of non-normality simply because of the relative weight of the components in the inner product. If one chooses $r = c^2$, then the norm of $\mathbf{u}$ becomes

$$\|\mathbf{u}\|_{c^2} = \langle \mathbf{u}, \mathbf{u} \rangle_{c^2} = \int_{x_1}^{x_2} (c^2 u_1^2 + u_2^2)\, \mathrm{d}x, \tag{2.20}$$

which is the (conserved) energy of the system. We then see that, in the energy conservative case, L is normal in the inner product that generates the energy norm or, as it is commonly phrased for short, L is normal in the energy norm. If $r \neq c^2$, the norm $\|\mathbf{u}\|_r$ will not be constant during the evolution of $\mathbf{u}$ but will oscillate according to the mismatch between potential and kinetic energy as measured by $\|\mathbf{u}\|_r$.

That eigenmodes are orthogonal in the inner product generating a quadratic conserved quantity of a linear system has been established by Held [60]. Held showed it explicitly for the *pseudomomentum* and *pseudoenergy* of perturbations to some atmospheric shear flow models[4]. As we shall see, there are some subtleties regarding the orthogonality of eigenmodes when associated to conserved quantities.

[4]Pseudomomentum and pseudoenergy are conserved quantities which, analogous to momentum and energy, are related to space and time continuous symmetries [93][98, §7][21, §4.5]. They are related to symmetries of the basic flow and they are, in general, different from the actual perturbation energy and momentum [75].

Damped oscillatory case

If we include dissipation by making $\alpha \neq 0$, the system is no longer conservative and we have for the commutator

$$[L^+, L]\Big|_{c'=0} = \begin{pmatrix} r\left(1-\frac{c^4}{r^2}\right)\partial_x^2 & -\alpha\left(1+\frac{c^2}{r}\right)\partial_x \\ r\alpha\left(1+\frac{c^2}{r}\right)\partial_x & -r\left(1-\frac{c^4}{r^2}\right)\partial_x^2 \end{pmatrix}. \tag{2.21}$$

We see that taking $r = c^2$ does no longer make $[L^+, L] = 0$, or L normal, because the off diagonal terms are non-zero. The only way (with the inner product 2.16)[5] to make $[L^+, L] = 0$ so as to have mutually orthogonal eigenmodes is to choose $r = -c^2$. This orthogonality yields, as in the previous case, that $\|\mathbf{u}\|_{-c^2}$ is a constant of motion. However, choosing $r = -c^2$ implies that $\langle \cdot\,, \cdot \rangle_r$ is no longer positive definite so it does not generate a norm. In this case, it can be verified that $\|\mathbf{u}\|_{-c^2} = 0$ for any $\mathbf{u}$ solution of (2.13). It is then obvious that $\|\cdot\|_{-c^2}$ can not be a useful measure of $\mathbf{u}$ in this particular case.

What is generic of this particular case is what was shown by Held [60], namely that if there is a quadratic form yielding a conserved quantity (pseudomomentum, pseudoenergy, or $\|\mathbf{u}\|_{-c^2} = 0$ in this case), the amount of conserved quantity associated to any growing or decaying eigenmode is zero. This implies that if there is an unstable eigenmode, $\mathbf{u}_u$ say, on a conservative system, then the quadratic form yielding the conserved quantity does not generate a norm[6] because the would-be-norm of $\mathbf{u}_u$ is zero. Conversely, if the quadratic conserved quantity is positive (or negative) definite, then (minus) the conserved quantity generates a norm in which the operator is normal and instability is forbidden [60][98, §7.6; §7.7]. The positive (or negative) definiteness of a conserved quantity (and indirectly the normality of the operator in the corresponding inner product) is in this way useful for finding necessary conditions for instability. Fjørtoft's condition [42], for example, can be derived in this way [98, §7.7.1].

Boundary conditions

Consider once again $\alpha, c' = 0$ but now boundary conditions on (2.15) given by

$$u_2(x_a) = 0, \tag{2.22a}$$
$$u_1(x_b) + \eta u_2(x_b) = 0, \tag{2.22b}$$

[5]Recalling that the eigenvectors are complex, we remark that the present discussion remains valid if we change $\mathbf{v}^T$ by its complex conjugate $\mathbf{v}^{T*}$ in the definition of $\langle \cdot\,, \cdot \rangle_r$ (2.16).

[6]Considering the spread use of the word *norm*, I consider that this has not been properly acknowledged, in particular in [60] and [98, §7.2.3; §7.6].

where $\eta > 0$. The boundary condition (2.22b) corresponds to an absorbing boundary such that $\partial_t u(x_b) = -\eta \partial_x u(x_b)$ on the wave equation (2.13). Imposing the adjoint boundary conditions such that $BT(\mathbf{u}, \mathbf{v}) = 0$ in (2.17) yields

$$v_2(x_a) = 0, \tag{2.23a}$$
$$v_1(x_b) - \eta v_2(x_b) = 0, \tag{2.23b}$$

which is different from the direct boundary conditions; boundary conditions (2.22) thus fall off the initial assumption because $BC^{L^+}(\,\cdot\,, x_a, x_b) \neq BC^{L}(\,\cdot\,, x_a, x_b)$. The boundary condition (2.23b) implies that there is energy injection at the boundary x_b, as opposed to the energy absortion of the direct boundary condition (2.22b). The wave equation with the absorbing boundary conditions (2.22) has been studied by Driscoll and Trefethen [43]. Among other things, they quantify the degree of non-normality and find that it is maximum for $\eta = 1$, perfectly absorbing case in which the spectrum is empty and all initial conditions go to zero in a finite time.

The case considered here is an example of non-normality produced by boundary conditions. As in the previous case, normality in the energy norm of the conservative system is broken as energy conservation is violated. This gives an example in which violating the equality $BC^{L^+}(\,\cdot\,, x_a, x_b) = BC^{L}(\,\cdot\,, x_a, x_b)$ between boundary conditions of the direct and adjoint equations produces non-normality.

Structural non-normality

We have restricted so far to a linear dynamical system which was derived from a differential equation (2.13) on a single function u. This is a strong restriction concerning the type of non-normality that can be present. In a system with more independent components, non-normality will greatly depend on the particular way in which the different components affect each other. Those mutual effects between different components of a system are reflected in the non-zero elements of the matrix representation of the operator L. The non-normality brought about by these inter-component interactions is of a different type than the previously described non-normalities; it might be called *structural non-normality*, where the structure referred to is the way in which different components couple to each other. As an example we can consider the addition of a coupled variable into system (2.15) as

$$\begin{aligned} \frac{\partial^2 u}{\partial t^2} &= c^2 \frac{\partial^2 u}{\partial x^2} + \alpha \frac{\partial u}{\partial t} + \beta g, \\ \frac{\partial g}{\partial t} &= \gamma g. \end{aligned} \tag{2.24a}$$

which in the form (2.1) becomes

$$\partial_t \begin{pmatrix} u_1 \\ u_2 \\ u_3 \end{pmatrix} = \underbrace{\begin{pmatrix} 0 & \partial_x & 0 \\ c^2\partial_x & \alpha & \beta \\ 0 & 0 & \gamma \end{pmatrix}}_{L_3} \begin{pmatrix} u_1 \\ u_2 \\ u_3 \end{pmatrix}, \tag{2.24b}$$

where $u_3 = g$. The role of g in (2.24a) (or u_3 in 2.24b) is clear, it excites the equation for u while evolving independently. It can be easily verified that system (2.24) is indeed non-normal.

2.2.2 Non-normality is normal

It might seem surprising that the simple addition of dissipation brakes the normality of L in the energy norm. The surprise may arise because the dissipative term appears in the diagonal of L and in the same position in the adjoint L^+, so one could say that the α term is self-adjoint (compare α in (2.15) and in (2.17b)). In this particular case the destroyed non-normality makes sense if one thinks that damped eigenmodes on a finite domain are not purely sinusoidal, so they do not satisfy simple orthogonality relations. More in general, the destroyed non-normality makes sense if we consider that the addition of two normal operators L_1 and L_2 (as can be conceptualized the addition of dissipation to the pure wave operator) is not necessarily normal since

$$[L_1^+ + L_2^+, L_1 + L_2] = [L_1^+, L_2] + [L_2^+, L_1]. \tag{2.25}$$

That is, for $L_1 + L_2$ to be normal is also needed that L_1 and L_2 commute with each other's adjoints. If we think on the damped wave equation, however, it does not seem that the non-normality of L plays an important dynamical role, nor is it clear how non-normality could help understanding the dynamics. This indicates that non-normality is ubiquituous and that it should be explained and characterized when it manifests itself relevant for the dynamics, as it could be in the case of structural non-normality. But non-normality does not need explanation in the general case. On the contrary, the particular situation needing a good reason to happen is *normality* rather than non-normality.

We have seen that for conservative systems, normality occurs for the norm yielding the conserved quantities. But the relation between normality and conserved quantities can not be kept when there are exponentially growing or decaying modes. Farrell & Ioannou [50] have shown that the general norm in which a system is normal corresponds to a weighted sum of the amplitude of each mode in the eigenmode expansion. That is, the evolution of $\|\mathbf{u}\|$ in the (quadratic) general normal norm (existing for an L with a complete set of eigenvectors) is given by

$$\|\mathbf{u}\| = m_i |u_i|^2 |\exp 2\lambda_i t|^2 \tag{2.26}$$

where $m_i > 0$ and the u_i are as in (2.5). This means that, for a normal system, all change in $\|u(t)\|$ is due to exponentially damping or unstable eigenmodes. In a subspace of purely oscillatory eigenmodes, the energy norm does not explicitly correspond to the sum of amplitudes (2.26), but it attributes the same weight to each pair of conjugate modes.

To conclude, non-normality in the energy norm is given by the possibility of $\mathbf{u}$ to change its energy during its evolution in the absence of unstable or decaying eigenmodes. This extends directly to other norms.

2.3 Probing non-normality without eigenmodes Some new ideas

In this section I sketch some open reflections developed during the course of my thesis.

2.3.1 A conserved quantity for normal systems

Consider $\mathbf{u} \in \mathbb{R}^n$ evolving according to the autonomous linear dynamical system

$$\frac{\mathrm{d}\mathbf{u}}{\mathrm{d}t} = L\mathbf{u}. \tag{2.27a}$$

Consider also $\mathbf{v} \in \mathbb{R}^n$ evolving back in time on the same dynamical system, that is, following

$$-\frac{\mathrm{d}\mathbf{v}}{\mathrm{d}t} = L\mathbf{v}, \tag{2.27b}$$

corresponding to (2.27a) under the transformation $t \to -t$. As before, we will assume that L has a complete set of eigenvectors $\mathbf{l}_i$ and a discrete spectrum $\{\lambda_i\}$ satisfying

$$L\mathbf{l}_i = \lambda_i \mathbf{l}_i. \tag{2.28}$$

Now let's consider an inner product $\langle \mathbf{a}, \mathbf{b} \rangle$ for $\mathbf{a}, \mathbf{b} \in \mathbb{R}^n$. The inner product $\langle \cdot\,, \cdot \rangle$, being defined over $\mathbb{R}^n$, is also a bilinear form, meaning that it satisfies

$$\langle \alpha_1 \mathbf{a}_1 + \alpha_2 \mathbf{a}_2, \mathbf{b} \rangle = \alpha_1 \langle \mathbf{a}_1, \mathbf{b} \rangle + \alpha_2 \langle \mathbf{a}_2, \mathbf{b} \rangle, \tag{2.29a}$$
$$\langle \mathbf{a}, \beta_1 \mathbf{b}_1 + \beta_2 \mathbf{b}_2 \rangle = \beta_1 \langle \mathbf{a}, \mathbf{b}_1 \rangle + \beta_2 \langle \mathbf{a}, \mathbf{b}_2 \rangle. \tag{2.29b}$$

If we use the inner product $\langle \cdot\,, \cdot \rangle$ to characterize the combined evolution of the

linear systems (2.27a) and (2.27b), we have that

$$\frac{\mathrm{d}\langle \mathbf{u}, \mathbf{v}\rangle}{\mathrm{d}t} = \left\langle \frac{\mathrm{d}\mathbf{u}}{\mathrm{d}t}, \mathbf{v} \right\rangle + \left\langle \mathbf{u}, \frac{\mathrm{d}\mathbf{v}}{\mathrm{d}t} \right\rangle, \tag{2.30a}$$

$$= \langle L\mathbf{u}, \mathbf{v}\rangle - \langle \mathbf{u}, L\mathbf{v}\rangle \tag{2.30b}$$

$$= \langle u_i L\mathbf{l}_i, v_j \mathbf{l}_j\rangle - \langle u_i \mathbf{l}_i, v_j L\mathbf{l}_j\rangle \tag{2.30c}$$

$$= u_i v_j \langle \lambda_i \mathbf{l}_i, \mathbf{l}_j\rangle - u_i v_j \langle \mathbf{l}_i, \lambda_j \mathbf{l}_j\rangle \tag{2.30d}$$

$$= u_i v_j \langle \mathbf{l}_i, \mathbf{l}_j\rangle (\lambda_j - \lambda_i), \tag{2.30e}$$

where sum over repeated indices is implied. In (2.30c), $\mathbf{u}$ and $\mathbf{v}$ have been expanded in the basis of eigenvectors of L as in (2.3). Then, in (2.30d,e) we have used (2.29) and the eigenmode defining property (2.28) in (2.30d).

In (2.30e), it is straightforward to see that $\langle \mathbf{u}, \mathbf{v}\rangle$ is a conserved quantity of the composed system if $\langle \mathbf{l}_i, \mathbf{l}_j\rangle = \delta_{ij}$, independently of the initial conditions for $\mathbf{u}$ and $\mathbf{v}$. That is, if L is normal (the $\mathbf{l}_i$ mutually orthogonal) under the scalar product $\langle \cdot, \cdot\rangle$, then the value of the quantity $\langle \mathbf{u}, \mathbf{v}\rangle$ is conserved under the evolution of systems (2.27a) and (2.27b). The converse, namely $(\mathbf{u}, \mathbf{v})$ being conserved for a non-normal system, may be valid only for properly chosen initial conditions (setting appropriately the set of u_i and v_i coefficients). Thus, $\langle \mathbf{u}, \mathbf{v}\rangle$ is conserved under the evolution of (2.27) for any pair of initial conditions $(\mathbf{u}_0, \mathbf{v}_0)$, if and only if L is normal.

It should be noted that the computation $\frac{\mathrm{d}}{\mathrm{d}t}\langle \mathbf{u}, \mathbf{v}\rangle$ does not require knowledge of the eigenmodes $\{\mathbf{l}_i\}$, which in some applications can be very expensive to obtain. Note also that the variation rate of $\langle \mathbf{u}, \mathbf{v}\rangle$ is given by the sum of the eigenmodes superposition (given by the value of $\langle \mathbf{l}_i, \mathbf{l}_j\rangle$) weighted by the coefficients u_i and v_j of the expansion in eigenmodes, and the difference between eigenvalues. Taking a look at figure 2.1 showing the graphic description of transient growth, one can see that these are the aspects involved in transient growth, namely the superposition of the eigenmodes composing the evolving solution and the difference of growth rate between eigenvalues. This suggests that the conservation property shown in (2.30) could be helpful to assess non-modal transient growth.

2.3.2 Manifestation of the conservation on trajectories

We would like to assess the possible effects of the conservation shown in (2.30) for the evolution of the time forward system (2.27a) alone. Lets then consider $\mathbf{u}(t)$ for $t \in [0, \tau]$ given by the evolution of (2.27a). We can define then a function $M(t_1, t_2)$ of two time variables as

$$M(t_1, t_2) = \langle \mathbf{u}(t_1), \mathbf{u}(t_2)\rangle, \tag{2.31}$$

such that $M\big|_{t_1=t_2=t} = \|u(t)\|$ is the norm of $\mathbf{u}(t)$. Figure 2.2 shows the (t_1, t_2)-plane.

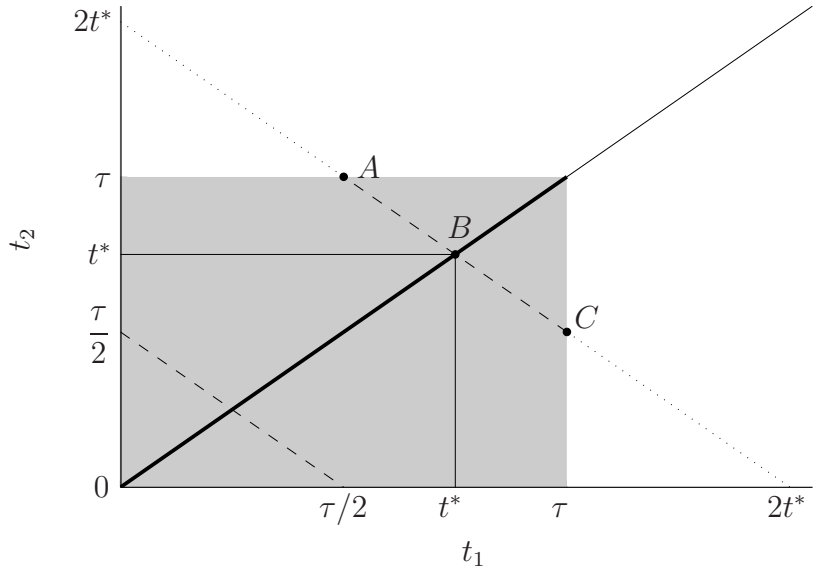

Figure 2.2: The grey area corresponds to $t_1, t_2 < \tau$. When going from A to C we have constant $t_1 + t_2 = 2t^*$ and M varying as $M(t^* + t, t^* - t)$ with t going from $t^* - \tau$ to $\tau - t^*$. The curvature of M when passing through B (along the dashed path) vanishes for normal systems.

Knowledge of $\mathbf{u}(t)$ in $[0, T]$ implies knowledge of $M(t_1, t_2)$ over the grey area in figure 2.2. Along the diagonal $t_1 = t_2$ we have $M\big|_{t_1=t_2=t} = \|u(t)\|$, corresponding to the evolution of the norm of $\mathbf{u}(t)$. The dashed lines inside the shaded area correspond to lines of constant $t_1 + t_2$. When moving down and to the right along the constant $t_1 + t_2$ lines, $M(t_1, t_2)$ varies according to (2.30). Thus, if L is normal, M will remain constant along constant $t_1 + t_2$ lines, for any trajectory $\mathbf{u}(t)$. Equivalently, M can vary along constant $t_1 + t_2$ lines only if L is non-normal.

It would be interesting to assess the effects of non-normality in the variation of $\|\mathbf{u}(t)\|$, instantaneously at any given time $t = t^*$ say, by computing the variation of M along constant $t_1 + t_2$ lines. However, the first derivative of M along constant $t_1 + t_2$ is zero when evaluated at $t_1 = t_2$, by symmetry. A possibility is given by the second derivative, or the curvature of M along constant $t_1 + t_2$ lines, which can be easily computed as

$$\frac{\mathrm{d}^2}{\mathrm{d}\bar{t}^2}\langle \mathbf{u}(t^* + \bar{t}), \mathbf{u}(t^* - \bar{t})\rangle = 2\left[\left\langle \frac{\mathrm{d}^2\mathbf{u}}{\mathrm{d}t^2}, \mathbf{u}\right\rangle - \left\langle \frac{\mathrm{d}\mathbf{u}}{\mathrm{d}t}, \frac{\mathrm{d}\mathbf{u}}{\mathrm{d}t}\right\rangle\right]_{t=t^*}, \tag{2.32a}$$

$$= \sum_{i,j} u_i(t^*)u_j(t^*)\langle \mathbf{l}_i, \mathbf{l}_j\rangle(\lambda_j - \lambda_i)^2, \tag{2.32b}$$

where (2.32b) is obtained from the eigenmode decomposition and some simple manipulations. While the right hand side of (2.32a) shows that there is no need of the modal decomposition to compute (2.32), the expression (2.32b) shows that there is indeed no contribution from each eigenmode alone; only superpositions between different eigenmodes contribute. The idea is to relate 2.32 to the non-normal effects in $\|\mathbf{u}(t)\|$ and understand its meaning and significance. For example, on dimensional grounds and because 2.32 is a second derivative in time, the quantity (2.32) can be compared to the acceleration of $\|\mathbf{u}(t)\|$ due to non normality, which is given by

$$\frac{\mathrm{d}^2}{\mathrm{d}t^2}\langle \mathbf{u}(t), \mathbf{u}(t)\rangle = \underbrace{\sum_i (2u_i\lambda_i)^2}_{\text{modal}} + \underbrace{\sum_{i\neq j} u_i u_j \langle \mathbf{l}_i, \mathbf{l}_j\rangle (\lambda_j + \lambda_i)^2}_{\text{non modal}}. \tag{2.33}$$

Clearly, for normal systems only the first term in the right hand side of (2.33) will be present. It could be interesting to explore the possibility that 2.32 (or, perhaps, some comparison/combination between 2.33, (2.32) and each of the terms in the right hand sides of (2.32a)) could give some information about the non modal terms in (2.33). However, the quantitative relevance of this connection is for the moment speculative.

As already mentioned, computing (2.32) does not require knowledge of the eigenmodes. It should be noted that an explicit expression of the linear operator L is not required either. Those characteristics are shared by other popular algorithms, for example the one used during this thesis for the computation of the optimal perturbations (section 2.1.3). In contrast, different to other characterisations of non-normality (like pseudospectra and others in [90], or the Henrici index used in [53]), the proposed characterisation is not necessarily relevant to the linear operator but, being applicable to any particular trajectory, it could serve as a tool for understanding some particular behaviour of interest. This is a matter of further study.

2.4 Some methodological essentials

2.4.1 Perturbative Navier-Stokes equations

We will focus on the stability of a given solution of the Navier-Stokes equations which we will call the base flow and generally denote as $\mathbf{U}$. The full flow field $\mathbf{u}_f$ is split as $\mathbf{u}_f = \mathbf{U} + \mathbf{u}$ and only the terms that are linear in $\mathbf{u}$ are kept. This describes the evolution of infinitesimal perturbations of the base flow.

The Navier-Stokes equations linearized around a base flow $\mathbf{U} = (U, V, W)^T$ can

be written as

$$L_{\mathbf{U}}\mathbf{u} = -\nabla p - (\mathbf{u}\cdot\nabla)\mathbf{U}, \tag{2.34a}$$
$$\nabla\cdot\mathbf{u} = 0. \tag{2.34b}$$

where the operator $L_{\mathbf{U}}$ is given by

$$L_{\mathbf{U}} = \frac{\partial}{\partial t} + (\mathbf{U}\cdot\nabla) - \nu\nabla^2 \tag{2.35}$$

describes viscous diffusion and advection by the base flow. A very important reason for concentrating on the linear dynamics is that the nonlinear terms are conservative, that is, they do not contribute to the energy of the perturbation [62, 91].

We will often consider a parallel shear flow of the form $\mathbf{U} = U(y)\mathbf{e}_x$, corresponding to a vorticity $\mathbf{\Omega} = \Omega = -U'(y)\mathbf{e}_z$. The linear evolution of perturbations $\mathbf{u} = (u, v, w)$ over this parallel flow is given by

$$L_U u = -\partial_x p - U'v, \tag{2.36a}$$
$$L_U v = -\partial_y p, \tag{2.36b}$$
$$L_U w = -\partial_z p, \tag{2.36c}$$
$$\nabla\cdot\mathbf{u} = 0, \tag{2.36d}$$

with the operator $L_U = \partial_t + U\partial_x - \nu\nabla^2$ that represents advection by the base flow and diffusion. As all the coefficients in (2.36) are independent of x and z, we can make a plane wave decomposition by rewriting

$$[u; v; w; p](\mathbf{x}, t) \longrightarrow [u; v; w; p](y, t)e^{i(k_x x + k_z z)}, \tag{2.37}$$

so that we can consider the wavenumbers as parameters, the evolution of $\mathbf{u}$ and p for a given pair (k_x, k_z) being independent of the existence of a contribution with different wavenumbers. We also have $\nabla^2 = \partial_y^2 - k_x^2 - k_z^2$.

2.4.2 Adjoint equations

As shown in section 2.1.3, the adjoint equations can be used to compute the optimal perturbations. The perturbative Navier-Stokes equations (2.34) can be written in operator form as

$$L_{NS}\mathbf{q} = 0 \tag{2.38}$$

where $\mathbf{q} = (u, v, w, p)^T$ and

$$L_{NS} = \begin{pmatrix} L_{\mathbf{U}} + \frac{\partial U}{\partial x} & \frac{\partial U}{\partial y} & \frac{\partial U}{\partial z} & \frac{\partial}{\partial x} \\ \frac{\partial V}{\partial x} & L_{\mathbf{U}} + \frac{\partial V}{\partial y} & \frac{\partial V}{\partial z} & \frac{\partial}{\partial y} \\ \frac{\partial W}{\partial x} & \frac{\partial W}{\partial y} & L_{\mathbf{U}} + \frac{\partial W}{\partial z} & \frac{\partial}{\partial z} \\ \frac{\partial}{\partial x} & \frac{\partial}{\partial y} & \frac{\partial}{\partial z} & 0 \end{pmatrix}. \tag{2.39}$$

Using the inner product $\{\mathbf{q}_d, \mathbf{q}\} = \int (\mathbf{u}_d \cdot \mathbf{u} + p_d p)\, \mathrm{d}x\mathrm{d}y\mathrm{d}z$, the adjoint equations can be obtained after arranging terms and integrating by parts such that $\{\mathbf{q}_d, L_{NS}\mathbf{q}\} - \{L_{NS}^+ \mathbf{q}_d, \mathbf{q}\} = BT(\mathbf{q}_d, \mathbf{q})$, where $BT(\mathbf{q}_d, \mathbf{q})$ are the boundary terms [64]. After some manipulations and changing $\tau = -t$, the adjoint equations satisfying $L_{NS}^+ \mathbf{q}_d = 0$, can be written, in vector form as

$$\frac{\partial \mathbf{u}_d}{\partial \tau} = \mathbf{\Omega} \times \mathbf{u}_d - \nabla \times (\mathbf{U} \times \mathbf{u}_d) - \nabla p_d + \nu \nabla^2 \mathbf{u}_d, \tag{2.40a}$$

$$\nabla \cdot \mathbf{u}_d = 0, \tag{2.40b}$$

where $\mathbf{\Omega} = \nabla \times \mathbf{U}$. In the case of parallel flow considered before, (2.40) become

$$L_U^+ u_d = -\partial_x p_d, \tag{2.41a}$$

$$L_U^+ v_d = -\partial_y p_d - U' u_d, \tag{2.41b}$$

$$L_U^+ w_d = -\partial_z p_d, \tag{2.41c}$$

$$\nabla \cdot \mathbf{u}_\mathbf{d}^+ = 0, \tag{2.41d}$$

where $L_U^+ = \partial_\tau - U\partial_x - \nu\nabla^2$ is the adjoint of the advection diffusion operator. All the previous arguments about the plane wave decomposition (2.37) are obviously valid for (2.41), same as for (2.36).

2.4.3 Numerical methods

An essential tool was already available at the beginning of my thesis. That tool is an efficient direct numerical simulation (DNS) code for solving the Navier-Stokes equations, either perturbative (on a two-dimensional base flow) or not, either linear or fully nonlinear, linearly stratified or not. The DNS code is pseudospectral, computing derivatives in Fourier space and products in physical space, efficiently changing between spaces by means of fast Fourier transforms (FFT). The code was originally written by Vincent & Meneguzzi for studying turbulence [100]. It was subsequently developed in LadHyX by several people (Pierre Brancher [19], Ivan Delbende [37], Paul Billant[16], François Gallaire [52], Jean-Marc Chomaz [31]...). At my arrival, the DNS code had been upgraded and parallelized (as an option) by Axel Deloncle [38], who also developed different time schemes in addition to the original Adams-Bashforth scheme. The boundary conditions are periodic.

My work then involved first the implementation of the adjoint NSE and the iterative optimization routine described in 2.1.3. As I dealt with stability analyses considering independently the evolution of spatial plane waves in one or two directions, the optimization routine involved the normalization of the initial condition for each of the corresponding wavenumbers. Also, as the base flow corresponding to a mixing layer is not periodic, a special case was added for computing the contribution of a parallel non-periodic shear flow avoiding the computation of base flow

derivatives in the adjoint equations, that is, explicitly computing (2.41) instead of (2.40) for the parallel flow component.

Another important development on the code concerns the time evolving base flow used for chapter 4. This involves the storage in hard disk of several base flow 'snapshots'. At execution time, two base flow fields are stored in the RAM at every moment, the base flow at the current time and the next snapshot. The base flow at the current time is updated every time step by the addition of the corresponding fraction of the next snapshot. When the time of the next snapshot is reached, the snapshot becomes the current base flow and the following snapshot is read from disk. During the adjoint phase of the optimization routines, the time corresponding to the next snapshot is lower than the current time, in accordance with the backwards in time resolution of the adjoint equation.

A set of post-processing routines was also developed in MATLAB®. This set of post-processing routines was composed of different level functions adapted to visualize the gain and flow fields for the different wavenumbers. The Craya-Herring decomposition involved in chapters 5 and 6 was also performed in MATLAB.

2.5 Non-modal instability mechanisms in plane shear flow

Here we briefly describe the Orr and lift up mechanisms, two well known mechanisms of non-modal energy growth of perturbations to parallel shear flow. These mechanisms occur in two limiting cases, the Orr mechanism for purely 2D flow ($k_z = 0$) and the lift up for perturbations infinitely elongated in the streamwise direction ($k_x = 0$). These introductory descriptions of the Orr and lift up mechanisms are placed here for consistency, most of their content can be also found later in the manuscript. After describing these well known mechanism, we end up by mentioning some insights on the more general oblique wave perturbations taking place for $k_x, k_z \neq 0$. These mechanisms are essentially inviscid so we set $\nu = 0$ in this section.

2.5.1 Orr mechanism

The Orr mechanism (Orr [82], for more recent discussions see for example [92, 45]) is responsible for the possibility of transient growth of perturbation energy in the 2D case ($k_z = 0$). This mechanism originates in the kinematic deformation of perturbation vorticity $\omega_z = \partial_x v - \partial_y u$ by base flow advection, as exemplified in the figure 2.3 (same as figure 6.3). Figure 2.3 shows the evolution of the vorticity ω_z of the optimal perturbation for $\mathbf{U} = \tanh(y)\mathbf{e}_x$, streamwise wavenumber $k_x = 3.77$ and optimization time $T = 7$. Shown are the optimal initial perturbation (at time $t = 0$), the optimal response (at $t = T = 7$) and the optimal perturbation at the

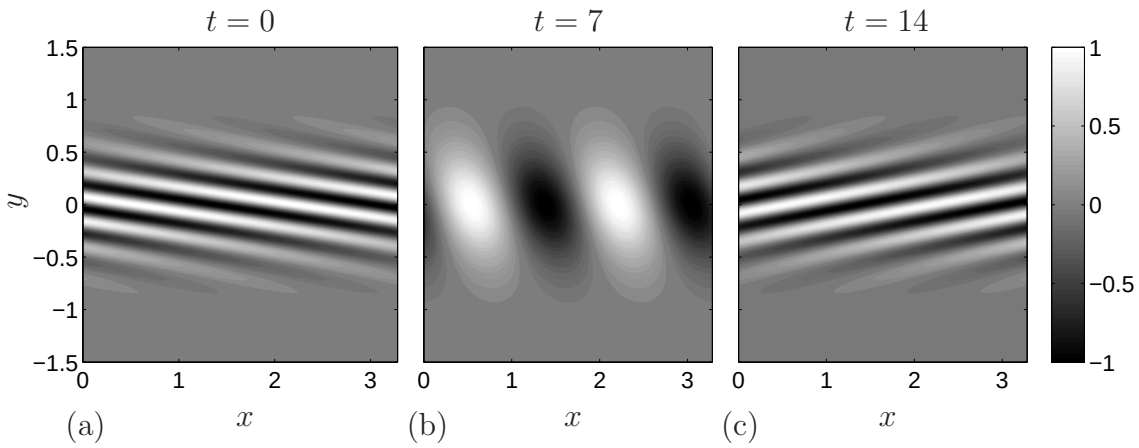

Figure 2.3: Optimal perturbations for the 2D case ($k_z = 0$). (a) ω_z distribution of the optimal perturbation for $k_x = 3.77$ and $T = 7$ at the initial time $t = 0$(a), the optimization time $t = T = 7$(b) and the later time $t = 14$(c). The horizontal axes show 2 wavelengths.

later time $t = 14$. The contours of the optimal perturbation are initially oriented against the base flow shear (figure 6.3a). As time evolves to $t = 7$ (figure 6.3b), the corresponding ω_z is sheared to an almost cross-stream orientation, leading at this time to the maximum of energy amplification. As the optimal perturbation evolves in time until $t = 14$ (figure 6.3c), ω_z is sheared further and the perturbation energy decreases back to a lower value.

The energy amplification results from the kinematic deformation of ω_z by the base flow. This kinematic deformation reduces the length of the ω_z contours while leaving unchanged the integral of the ω_z enclosed by the contours[7]. Stokes theorem implies that the velocity magnitude along the (reduced in length) contours must increase to keep the circulation along the contours equal to the (constant) integral of ω_z. This mechanism produces a large increase in cross-stream velocity v. When time evolves further and ω_z is sheared as in figure 6.3(c), the kinematic process just described is reversed and the energy goes to zero as $t \to \infty$.

2.5.2 Lift-up mechanism

The lift-up mechanism was first reported as an algebraic instability by Ellingsen & Palm [44] in the simple case of streamwise independent perturbations to inviscid linear flow. It can be understood as the flow induced by streamwise vorticity that, superposed on positive shear, lifts up fluid at low velocity while pushing down high-

[7] ω_z is strictly advected as a scalar by the base flow only when the shear is constant. Otherwise, the base flow can act as a source of vorticity, which is indeed what happens for the shear instability.

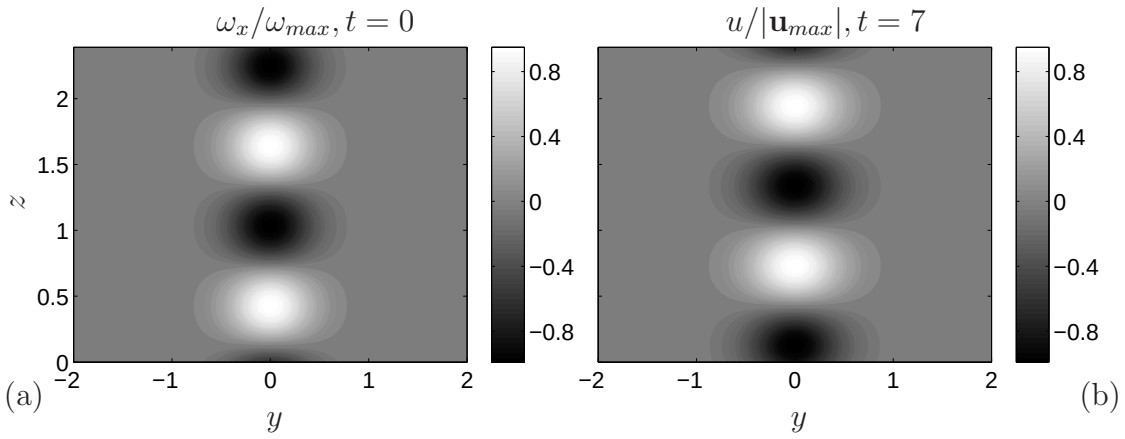

Figure 2.4: Optimal perturbations for $(k_x, k_z) = (0, 5.174)$ and $T = 7$. (a) ω_x of the optimal perturbation at $t = 0$. (b) u of the optimal perturbation at $t = T = 7$. The vorticity ω and velocity u fields are respectively normalized so that the maximum value of enstrophy $(\omega_x^2 + \omega_y^2 + \omega_z^2)$ and twice the energy is 1.

velocity fluid. Here we show again results for the tanh profile. Figure 2.4 (same as 6.4) shows the streamwise vorticity ω_x of the optimal initial perturbation (figure 6.4a) and the streamwise velocity u (figure 6.4b) of the optimal response, leading to the optimal gain at $T = 7$ for $k_z = 5.174$ and $k_x = 0$. The ω_x and u fields in figure 2.4 are respectively normalized by the maximum total enstrophy at $t = 0$ and twice the maximum total energy at $t = T = 7$. Both fields are localized around $y = 0$, in the region with strong shear. The colorbar on figure 6.4(a) reflects the fact that at the initial time, 97.6% of the total enstrophy is given by ω_x. As time evolves, ω_x remains constant and induces a constant cross-stream velocity v. That v excites u through transport of base flow momentum, generating streamwise streaks. The colorbar on figure 6.4(b) reflects the fact that, after the perturbation evolves to $t = 7$, most of the perturbation velocity corresponds to u. As time evolves further, the forcing of u by v remains constant, implying that the energy of the perturbation grows unbounded as $t \to \infty$.

2.5.3 A look at the energy evolution of perturbations of unbounded constant shear flow

We are now familiar with the development of linear perturbations in two different cases, $k_z = 0$ with Orr and $k_x = 0$ in which there is lift-up. In a general case of oblique waves, the two mechanisms can be present in a non-trivial way. These are the types of perturbations that show the largest instantaneous growth rate, and so they are likely of importance for transition or turbulent structures.

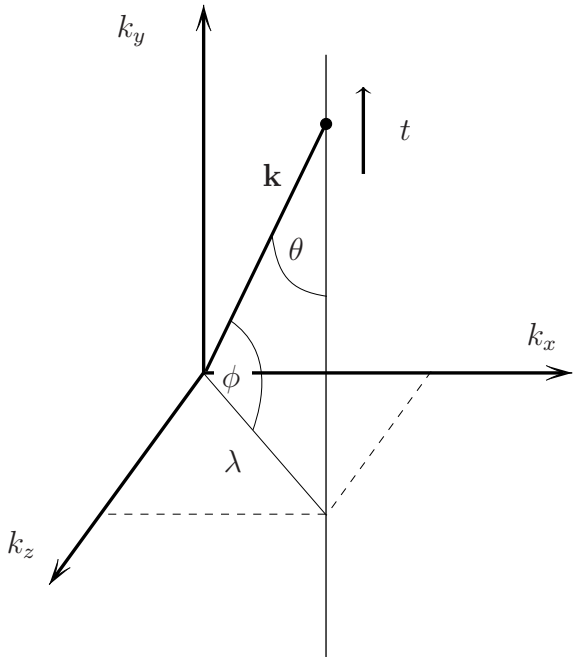

Figure 2.5: Schematic of the evolution of the time dependent wavenumber $\mathbf{k}(t)$ and the different parameters of its evolution.

To address the dynamics of oblique wave perturbations, we consider the case of unbounded constant shear flow with constant vorticity $\Omega = -U'(y)$, in which case analytical solutions for plane waves with time dependent wavenumber are known. We start from the expressions given by Farrell & Ioannou [48] for the energy evolution, namely

$$\frac{E(t)}{E_0} = \frac{|\omega_y|^2 + (K_0^4/K^2(t))|v_0|^2}{|\omega_{y0}|^2 + K_0^2|v_0|^2}, \tag{2.42}$$

where the cross-stream vorticity is given by

$$|\omega_y|^2 = |\omega_{y0}|^2 + |v_0|^2 \left(\frac{k_z K_0^2}{k_x \lambda}\right)^2 (\theta(t) - \theta_0)^2 \tag{2.43}$$

and the parameters of the time dependent wavenumbers are

$$K^2(t) = \lambda^2 + k_y^2(t), \tag{2.44}$$

$$k_y = k_{y0} + \Omega k_x t, \tag{2.45}$$

$$\theta(t) = \arctan\left(\frac{\lambda}{k_y(t)}\right), \tag{2.46}$$

where $\lambda^2 = k_x^2 + k_z^2$ and k_y is the (time dependent) cross-stream wavenumber. The zero subscript $(\cdot)_0$ indicates the $(\cdot)$ quantity at time $t = 0$. A geometric description

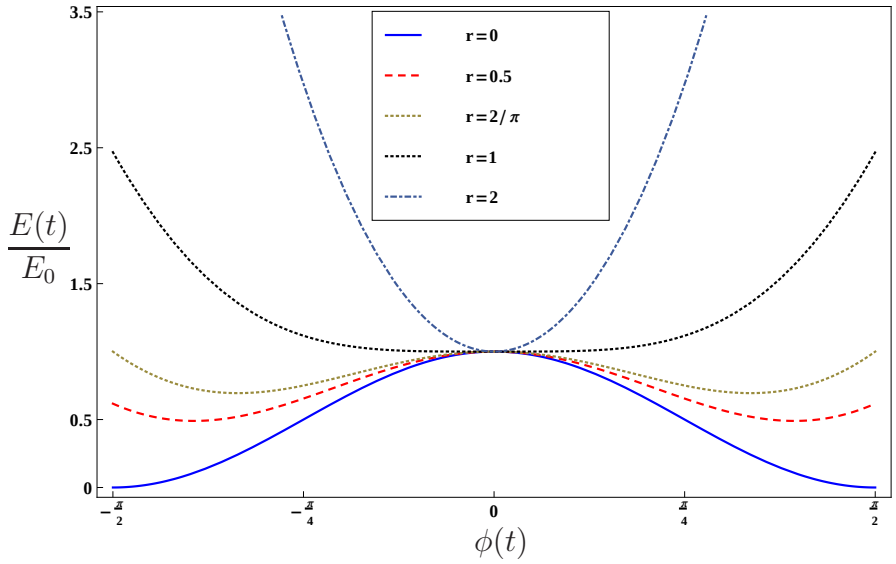

Figure 2.6: Energy evolution history of oblique wave perturbations for $\rho = 0$. The horizontal axis corresponds to the $\phi(t)$, which varies from $-\pi/2$ to $\pi/2$ when t varies from $-\infty$ to ∞.

of the evolution of the wavenumber $\mathbf{k}$ can be seen in figure 2.5. (k_x, k_z) remains constant while, for positive base flow vorticity Ω, k_y goes from $-\infty$ to $+\infty$ when t goes from $-\infty$ to $+\infty$. Accordingly, θ goes from π to 0.

Let's now describe ω_y in terms of the angle $\phi = \pi/2 - \theta$ which, for $\Omega > 0$, varies between $-\pi/2$ and $+\pi/2$ when t goes from $-\infty$ to $+\infty$. Also, without loss of generality, we can choose the time origin $t = 0$ such that $k_{y0} = 0$, which implies $K_0 = \lambda$ and $\phi_0 = 0$. With these choices, the energy evolution (2.42) becomes

$$\frac{E(t)}{E_0} = \frac{|\omega_{y0}|^2 + \lambda^2 r^2 \phi^2 |v_0|^2 + \lambda^2 \cos^2(\phi(t)) |v_0|^2}{|\omega_{y0}|^2 + \lambda^2 |v_0|^2}$$

where we have introduced the ratio $r = k_z/k_x$. The ratio r controls the orientation of the oblique waves, for $r = 0$ the perturbations are purely 2D and they can grow due to the Orr mechanism. As r increases the perturbations become oblique, becoming streamwise independent as $r \to \infty$ when the lift-up mechanism is present. Introducing further $\rho^2 = |\omega_{y0}|^2/\lambda^2|v_0|^2$ we obtain

$$\frac{E(t)}{E_0} = \frac{\rho^2 + r^2\phi^2(t) + \cos^2\{\phi(t)\}}{\rho^2 + 1}, \tag{2.47}$$

which is in a simple form that shows the $\phi \to -\phi$ reflectional symmetry of the

energy evolution. The energy as $t \to \infty$ is simply

$$\frac{E(\phi = \pm\pi/2)}{E_0} = \frac{\rho^2 + r^2\pi^2/4}{\rho^2 + 1}. \tag{2.48}$$

Figure 2.6 shows the energy evolution of the perturbations for $\rho = 0$ and different r. For $r = 0$ the energy goes to zero as $t \to \pm\infty$, and reaches its maximum at $t = 0$. In that case, energy growth occurs for negative times, and the optimal perturbations (for any optimization time T) evolve in the left part with $\phi < 0$. As r increases, the energy at $\phi = \pm\pi/2$ (or $t \to \pm\infty$) increases. For $r = 2/\pi$, the energy at $t = \pm\infty$ ($\phi = \pm\pi/2$) is the same as the energy at $t = 0$, that is, $E(\pm\pi/2)/E_0 = 1$. Thus, for $r > 2/\pi$, the perturbation with the largest possible energy amplification (for any time interval) goes from the global minimum to $t \to \infty$. The energy at $t = 0$ is a maximum (local or global according to r) for $r < 1$ and becomes the global minimum for $r \geq 1$. As $r \to \infty$, the energy at $\phi = \pi/2$ diverges. That is the case for the lift up mechanism. Surprisingly enough, the optimal energy gain for any fixed time T is equal for the Orr and the lift-up cases [48].

Chapter 3

A note on the inviscid algebraic growth for parallel shear flow: a novel formal solution and asymptotic approximation

Cristóbal Arratia, Jean-Marc Chomaz
Article in preparation

3.1 Introduction

Many studies have demonstrated that linear perturbations to parallel shear flow can exhibit very large energy growth in the absence of unstable eigenmodes [57, 25, 48, 86, 91]. The mechanism responsible for the largest energy growth is essentially the same for all inviscid or viscous shear flows at sufficiently large Reynolds number Re: the forcing of cross-stream vorticity by cross-stream velocity varying in the span. This so-called lift-up mechanism is more efficient for streamwise elongated perturbations. It can also be understood as the flow induced by streamwise vorticity that, superposed on positive shear, lifts up fluid at low speed while pushing down high-velocity fluid.

The lift-up mechanism was first reported as an algebraic instability by Ellingsen & Palm [44] in the simple case of streamwise indepedent perturbations to inviscid constant shear flow. Still in the inviscid case, Landahl [70] showed that the integrals along the streamwise direction of localized perturbations satisfy the same equations as the streamwise independent perturbations (infinitely elongated). He then showed that the constant growth of the perturbation integral corresponds to a streamwise spreading of the disturbance, and that the integrated energy grows

faster than linearly in time.

Most subsequent work deals with viscous flows. In wall bounded flows, it has been shown that for large Re the largest possible amplification due to lift-up scales as Re^2, and is attained after a time scaling as $\sim Re$ [57, 86, 91]. The dynamics of these perturbations consists of an initial phase of energy growth due to the inviscid lift-up mechanism and a later decay due to viscous diffusion. The spanwise wavenumber k_z corresponding to this largest possible amplification is of order one [86], The situation changes if instead of focusing on the largest transient growth for all times, one takes into account the growth rate intensity of the perturbations. Such is the case, for example, when looking for the most amplified perturbation up to a prescribed time T. In such case the most amplified k_z results from the competition between the inviscid lift up mechanism tending to select small scale strucures efficiently localized around the maximum shear, and viscous effects damping small scale structure.

The case of inviscid longitudinal perturbations to an arbitrary parallel shear flow admits very simple solutions in closed form [91]. Concerning the optimal perturbation problem, the analytical expression for the optimal energy growth at any optimization time T has been given by Farrell & Ioannou [48] in the case of infinite constant shear flow. Their formula has no dependence on the spanwise wavenumber because there is no length scale associated to an infinite constant shear flow. Other works dealing with the inviscid limit of optimal perturbations of the lift-up type in compressible flow have relied on numerical computations even for their inviscid reference cases, as done for example by Hanifi & Henningson [58] for boundary layers and by Malik, Dey & Alam [74] for non-isothermal plane Couette flow. Still, to the authors best knowledge, the problem of the optimal perturbations in the simpler case of inviscid incompressible flow has not been treated in detail in the literature.

Here we solve the problem of the optimal streamwise independent perturbations for an arbitrary shear flow. In section 3.2, we give first the solution for inviscid longitudinal perturbations to plane parallel flow. We highligth the connection by time translation among the different elements belonging to a same trajectory in phase space. We use this connection to reformulate the optimization problem in the whole phase space to the optimization in a time variable and in a codimension-1 subspace. Solving those optimization problems leads to a differential eigenvalue problem in one dimension, whose solutions allow constructing the orthogonal ensemble of the optimal and sub-optimal perturbations. In section 3.3 we consider plane Couette and Poiseuille flow as examples, and we provide the exact solutions allowing to construct the optimal perturbations. In section 3.4 we consider the two main classes of parallel shear flows: an inflectional profile with a region with maximum shear in the flow domain, and a wall bounded flow with maximum shear at the wall. In those two broad classes we provide, for large k_z, asymptotic estimates of the optimal amplification and of the localisation width of the optimal perturbation around the maximum shear.

3.2 Formulation

We consider infinitesimal perturbations $\mathbf{u} = \mathrm{Re}\{[u, v, w] \exp(ik_x x + ik_z z)\}$ to parallel inviscid flow $\mathbf{U} = U(y)\mathbf{e}_x$ with shear $S(y) = U'$. In the case of longitudinal perturbations $k_x = 0$ the linearised Euler equations reduce to

$$\partial_t u(y,t) = -S(y)v(y,t), \tag{3.1a}$$
$$\partial_t v(y,t) = 0, \tag{3.1b}$$
$$\partial_t w(y,t) = 0, \tag{3.1c}$$
$$v'(y,t) + ik_z w(y,t) = 0, \tag{3.1d}$$

where the domain is $y \in (y_1, y_2)$, the superscript $'$ denotes y-derivative and the boundary conditions are

$$v(y_1,t) = v(y_2,t) = 0. \tag{3.2}$$

The general solution of (3.1) is

$$u(y,t) = u_o(y) - S(y)v_o(y)t, \tag{3.3a}$$
$$v(y,t) = v_o(y), \tag{3.3b}$$
$$w(y,t) = iv_o'(y)/k_z, \tag{3.3c}$$

where $u_o(y)$ and $v_o(y)$ denote, respectively, the streamwise and crosstream velocities at $t = 0$. The energy E of solution (3.3) is

$$E(t) = E_o - \mathrm{Re}(\langle u_o, Sv_o\rangle)\, t + \frac{\|Sv_o\|^2}{2} t^2, \tag{3.4}$$

where

$$2E_o = \|u_o\|^2 + \|v_o\|^2 + \frac{\|v_o'\|^2}{k_z^2}, \tag{3.5}$$

and the inner product $\langle f, g\rangle$ between any two functions f and g is defined as

$$\langle f, g\rangle = \int_{y_1}^{y_2} f(y)^* g(y)\, dy, \tag{3.6}$$

where $(\,\cdot\,)^*$ denotes complex conjugation. The associated norm $\|\cdot\|$ is

$$\|f\|^2 = \langle f, f\rangle. \tag{3.7}$$

We can define a shifted time variable by

$$\bar{t} = t - \frac{\mathrm{Re}(\langle u_o, Sv_o\rangle)}{\|Sv_o\|^2}. \tag{3.8}$$

In terms of this shifted time variable we can write the energy of any initial condition $(u_o, v_o, iv_o'/k_z)$ as

$$E(t) = \bar{E}(\bar{t}) = \bar{E}_o + \frac{\|Sv_o\|^2}{2}\bar{t}^2, \tag{3.9}$$

where

$$2\bar{E}_o = \|\bar{u}_o\|^2 + \|v_o\|^2 + \frac{\|v_o'\|^2}{k_z^2}, \tag{3.10}$$

$$\bar{u}_o = u_o - Sv_o\frac{\mathrm{Re}(\langle u_o, Sv_o\rangle)}{\|Sv_o\|^2} \tag{3.11}$$

are respectively the energy and the streamwise velocity at the new time origin $\bar{t} = 0$ corresponding to $t = \mathrm{Re}(\langle u_o, Sv_o\rangle/\|Sv_o\|^2)$, which may be positive or negative. We stress the different explicit form of the energy in terms of the shifted variable by writing $\bar{E}$. Note that $\bar{E}_o \leq E(t)$ for all t. Accordingly, $\|\bar{u}_o\|^2$ is the minimum of the streamwise kinetic energy during the whole evolution history. It can also be noted that $\langle \bar{u}_o, Sv_o\rangle = 0$, which means that the streamwise velocity at $\bar{t} = 0$, $\bar{u}_o$, is orthogonal to its time varying part $Sv_o t$, given by (3.3a).

3.2.1 Reformulating the optimization problem

Consider the problem of computing the optimal perturbation at a finite time T, that is

$$G_{opt}(T) = \max_{\mathbf{u}_o \in \mathcal{P}} \left(\frac{E(T)}{E(0)} \right), \tag{3.12}$$

where $\mathcal{P}$ represents the set of all perturbation fields $\mathbf{u}_o$ that satisfy the incompressibility condition (3.1d).

Finding the optimal perturbation involves the identification of the particular energy evolution that maximizes the energy growth amongst all attainable possibilities of energy evolution. The optimization problem (3.12) is then equivalent to

$$G_{opt}(T) = \max_{\bar{t}_o \in \mathbb{R}, \bar{\mathbf{u}}_o \in \mathcal{S}_\perp} \left(\frac{\bar{E}(T + \bar{t}_o)}{\bar{E}(\bar{t}_o)} \right), \tag{3.13}$$

meaning that any element of $\mathcal{P}$ can be expressed by a time shift $\bar{t}_o$ and an initial condition at $\bar{t} = 0$, $\bar{\mathbf{u}}_o$, in the codimension-1 subspace $\mathcal{S}_\perp$ such that $\langle \bar{u}_o, Sv_o\rangle = 0$. Any initial condition $\mathbf{u}_o$ in (3.12) is now given by $\bar{\mathbf{u}}(\bar{t} = \bar{t}_o)$ passing through $\bar{\mathbf{u}}_o$ in $\mathcal{S}_\perp$ at time $t = -\bar{t}_o$ (now $\bar{t} = 0$).

We shall now maximize $\bar{E}(T + \bar{t}_o)/\bar{E}(\bar{t}_o)$. Note first that, for $\bar{t}_{opt}$ realizing the maximum (3.13), the variation respect to $\bar{t}_o$ should vanish:

$$\frac{\partial}{\partial \bar{t}_o}\frac{E(T + \bar{t}_o)}{E(\bar{t}_o)} = 0, \tag{3.14}$$

implying that the instantaneous growth rate of the perturbation

$$\sigma(t) = \frac{1}{2E(t)} \frac{\partial E(t)}{\partial t}, \tag{3.15}$$

should be equal at the initial and final times, i.e.[1]

$$\sigma(\bar{t}_{opt}) = \sigma(T + \bar{t}_{opt}). \tag{3.16}$$

Condition (3.16) is only a necessary condition. For any element of $\mathcal{S}_\perp$ such that $\|Sv_o\| \neq 0$ ($\|Sv_o\| = 0$ is a trivial stationary solution that is obviously not optimal), (3.16) is realized for two $\bar{t}_o$:

$$\bar{t}_o = \bar{t}_{op}^{\pm} \equiv -\frac{T}{2} \pm \sqrt{\left(\frac{T}{2}\right)^2 + \tau^2}, \tag{3.17}$$

where $\tau = \sqrt{2\bar{E}_o/\|Sv_o\|^2}$. The optimal initial condition for a given $\bar{\mathbf{u}}_o \in \mathcal{S}_\perp$ is given by the upper + sign, the − sign corresponding to an evolution interval $[\bar{t}_{op}, \bar{t}_{op} + T]$ in the negative $\bar{t}$ domain in which $\bar{E}(\bar{t})$ decays (see (3.9)).

Replacing $\bar{t}_o \to \bar{t}_{op}^{+}$ in the optimization problem (3.13) gives

$$G_{opt}(T) = \max_{\bar{\mathbf{u}}_o \in \mathcal{S}_\perp} \left(\bar{G}_{op}\right) \tag{3.18a}$$

where

$$\bar{G}_{op} = 1 + \frac{T^2}{2\tau^2} + \frac{T}{\tau}\sqrt{1 + \left(\frac{T}{2\tau}\right)^2}. \tag{3.18b}$$

Equations (3.18) show that all the degrees of freedom, i.e. the $\bar{\mathbf{u}}_o \in \mathcal{S}_\perp$, enter the optimization problem through a single parameter τ. For a given time horizon T, $\bar{G}_{op}$ is a decreasing function of τ and the optimization problem therefore reduces to find $\bar{\mathbf{u}}_o \in \mathcal{S}_\perp$ that minimizes τ. In terms of the components of $\bar{\mathbf{u}}_o$ we have

$$\tau^2 = \frac{\|\bar{u}_o\|^2 + \|v_o\|^2 + k_z^{-2}\|v_o'\|^2}{\|Sv_o\|^2}, \tag{3.19}$$

imposing that $\bar{u}_o = 0$ for the optimal perturbations (minimizing τ). The optimal perturbation problem is now reduced to the variational problem of finding v_o that minimizes τ^2. This is a standard variational problem, it can be formulated by writing τ^2 as a function of $v_o = v_{opt} + \delta v$, where v_{opt} is the optimal v_o giving $\tau_{opt} = \min(\tau)$ and δv is an arbitrary variation. The first, δv order in the expansion of τ^2 around

[1] Equation (3.16) can be used as a test for numerical results.

v_{opt} gives the functional derivative $\delta\tau^2/\delta v$ evaluated at v_{opt}. The optimality condition imposes that the functional derivative $\delta\tau^2/\delta v\big|_{v_{opt}} = 0$ for all δv, giving

$$v''_{opt} + k_z^2\left(\tau^2 S^2 - 1\right) v_{opt} = 0. \tag{3.20}$$

To obtain the first term in (3.20) we have integrated by parts and used that δv satisfies the boundary conditions (3.2), which are also satisfied by v_{opt}.

Equation (3.20) is the main result of the paper. It is valid for the streamwise independent optimal perturbations to *any* shear profile $S(y)$ and *any* optimization time T. Equation (3.20) is a generalized eigenvalue problem on the 'optimal parameter' τ and the optimal perturbation $v_{opt}(y)$. When (3.20) is satisfied by v_{opt}, the optimal τ, τ_{opt}, is given by

$$\tau_{opt}^2 = \frac{\|v_{opt}\|^2 + k_z^{-2}\|v'_{opt}\|^2}{\|Sv_{opt}\|^2}. \tag{3.21}$$

From the solution of equation (3.20) we find the other components of the optimal perturbation $\mathbf{u}_{opt}$ as

$$u_{opt}(y,t) = S(y)v_{opt}(y)(t+\bar{t}_{opt}), \tag{3.22a}$$
$$w_{opt}(y,t) = iv'_{opt}(y)/k_z, \tag{3.22b}$$

where $\bar{t}_{opt}$ is given directly by (3.17) and τ_{opt} as

$$\bar{t}_{opt} = -\frac{T}{2} + \sqrt{\left(\frac{T}{2}\right)^2 + \tau_{opt}^2}. \tag{3.23}$$

Similarly, the optimal gain for optimization time T is given by (3.18b) as

$$G_{opt}(T) = 1 + \frac{T^2}{2\tau_{opt}^2} + \frac{T}{\tau_{opt}}\sqrt{1 + \left(\frac{T}{2\tau_{opt}}\right)^2}. \tag{3.24}$$

From (3.20) it can be thought that v_{opt} satisfies a wave equation which is evanescent when $\tau^2 S^2 < 1$ and oscillatory when $\tau^2 S^2 > 1$. Thus, for (3.20) to have a non trivial solution satisfying the boundary conditions (3.2), it is necessary that $\tau^2 > \frac{1}{S(y_m)^2}$ for y_m in some region around the maximum of S^2. This requirement imposes a lower bound on τ such that

$$\tau^2 > \frac{1}{S_{max}^2}, \tag{3.25}$$

where S_{max}^2 is the maximum of S^2. Lower bound (3.25) implies an upper bound on G_{opt} which is equal to the optimal gain given by Farrell & Ioannou [48] for streamwise independent perturbations to unbounded constant shear flow.

Equation (3.20) is analogous to the Schrödinger equation governing the energy eigenstates of a quantum particle of mass m. Indeed, the optimal perturbation v_{opt} corresponds to the ground state wavefunction of a particle with energy -1 on an atractive potential $-\tau_{opt}^2 S^2$. In this analogy, k_z^2 is equal to $2m/\hbar^2$, which indicates that increasing k_z corresponds to decreasing $\hbar$ or increasing the mass. This suggests that increasing k_z allows for a more concentrated v_{opt} (more localized eigenfunction) around the maximum of the shear (minimum of the potential $-\tau_{opt}^2 S^2$). This is in agreement with what is expected from the lift up mechanism, i.e., that the optimal perturbation will be localized in the region of maximum shear.

The quantum analogy does not provide a full parallel because in the present case the eigenvalue multiplies the function of the coordinate $S(y)^2$ instead of the function v_{opt} only, implying that different eigenvalues of a same velocity profile correspond to energy levels (with the same energy) for different quantum potentials. Still, being in both cases eigenvalue problems of the Sturm-Liouville type [97, §5], eq. (3.20) shares several important properties with the Schrödinger equation. It is known, in particular, that for bounded domains[2] there are infinite numerable real eigenvalues τ_i, each associated with an eigenfunction v_i. The eigenvalues can be ordered in ascending order $\tau_0, \tau_1, \tau_2, \ldots$, the index number corresponding to the quantity of nodes of the respective eigenfuction. The parameters of the optimal perturbation are then given by $v_{opt} = v_0$ and $\tau_{opt} = \tau_0$. Finally, the eigenfunctions v_i form an orthogonal set with respect to the weight function S^2 so that, after normalization, we have $\langle v_i S, v_j S \rangle = \delta_{ij}$. This provides an orthonomal basis (in the energy related inner product (3.6)) for the time dependent part of u. This orthonormal base contains the optimal and all the sub-optimal perturbations. The base formed by the set $\mathbf{u}_i = (Sv_i, 0, 0)$ is orthogonal and, altough incomplete, it spans the range of the evolution operator for any initial condition v_o. It thus provides the non trivial part of the singular value decomposition, the rest of the space has no time dependence and can be span by any orthogonal base.

[2]One could expect that in the present case this is also true for infinite domains, at least when the shear is localized in a finite region. In that case, solutions in the quantum analogy correspond to bound states in a potential well (given by the shear region) whose depth increases with τ. Thus, where a quantum well potential provides a finite set of bound states depending on the depth of the well [see for example 71, problem 2 in §22], a similar localised shear problem should provide infinite eigenfunctions because the 'potential well' becomes deeper as the eigenvalue τ_n increases with n.

3.3 Base flow examples: Couette and Poiseuille flow

3.3.1 Couette

We consider plane Couette flow in the region $y \in [0, 1]$. For plane Couette flow the shear rate S is constant and (3.20) has infinite solutions of the form

$$v_{n-1} = \sin(n\pi y) \tag{3.26a}$$

$$\tau_{n-1}^2 = \frac{1}{S^2}\left(1 + \frac{n^2\pi^2}{k_z^2}\right) \tag{3.26b}$$

for $n = 1, 2, \ldots, \infty$. The optimal crosstream velocity $v_{opt} = v_0$ is then obtained by evaluating (3.26a) at $n = 1$. Similarly, the eigenvalue leading to the optimal amplification is given by

$$\tau_{opt} = \tau_0 = \frac{1}{|S|}\sqrt{1 + \left(\frac{\pi}{k_z}\right)^2}, \tag{3.27}$$

which, after replacing in (3.24), yields the optimal gain at time T

$$G_{opt}(T) = 1 + \frac{T^2S^2 + T|S|\sqrt{T^2S^2 + 4(1+\lambda^2)}}{2(1+\lambda^2)}, \tag{3.28}$$

where

$$\lambda = \frac{\pi}{k_z}, \tag{3.29}$$

is half the spanwise wavelength of the perturbation. From (3.22a), the optimal initial streamwise velocity is given by

$$u_{opt}\Big|_{t=0} = Sv_{opt}\left[\frac{T}{2} - \left(\frac{1+\lambda^2}{S^2} + \frac{T^2}{4}\right)^{1/2}\right]. \tag{3.30}$$

Equation (3.30) is similar to the expression given by Farrell & Ioannou [48, see their equation (19)] for the optimal initial condition in the constant shear case. Their expression within square brackets reduces to ours if one sets their crosstream wavenumber to satisfy the boundary conditions for v. However, they do not give explicitly the ratio between the amplitudes of the different components of the flow, so a full comparison with their solution can not be directly made. Still, the correspondence of the two square brackets confirms, up to a multiplicative constant, the dependence of $u_{opt}\big|_{t=0}$ on the different parameters.

3.3.2 Poiseuille

We consider plane Poiseuille flow $U(y) = 1 - y^2$ for $y \in [-1, 1]$. Equation (3.20) can be written as

$$v'' + (\bar{y}^2 - \alpha)v = 0, \tag{3.31a}$$

after change of variables

$$\bar{y} = \sqrt{2\tau k_z}y, \tag{3.31b}$$

$$\alpha = \frac{k_z}{2\tau}, \tag{3.31c}$$

and the boundary conditions are

$$v\big|_{\bar{y}=\pm\sqrt{2\tau k_z}} = 0. \tag{3.31d}$$

The even solutions of (3.31a), such that $v(\bar{y}) = v(-\bar{y})$, are given by

$$v(\bar{y}) = e^{-i\bar{y}^2/2}{}_1F_1(-\frac{i}{4}(i+\alpha); \frac{1}{2}; i\bar{y}^2), \tag{3.32}$$

where ${}_1F_1(a; b; z)$ is the confluent hypergeometric function of the first kind [1]. The τ_{2n} for each k_z are obtained parametrically as

$$\tau_{2(n-1)} = \frac{\iota_n}{2\sqrt{\alpha}} \tag{3.33a}$$

$$k_z = \iota_n\sqrt{\alpha} \tag{3.33b}$$

where ι_n is the n-th zero of ${}_1F_1(-\frac{i}{4}(i+\alpha); \frac{1}{2}; i\bar{y}^2)$. The first zero ι_1 has been computed with MATHEMATICA®, allowing for the computation of the optimal gain.

Figure 3.1 shows the optimal gain for optimization time $T = 0.1$ as a function of k_z for this inviscid case, as presently given using (3.33), and for the viscous case computed directly by numerically solving the singular value decomposition for different Reynolds numbers by Soundar, Chomaz & Huerre ([94], details of the numerical procedure in their paper). As Reynolds number Re increases, the optimal gain increases and the corresponding k_z also increases, approaching the inviscid curve computed presently.

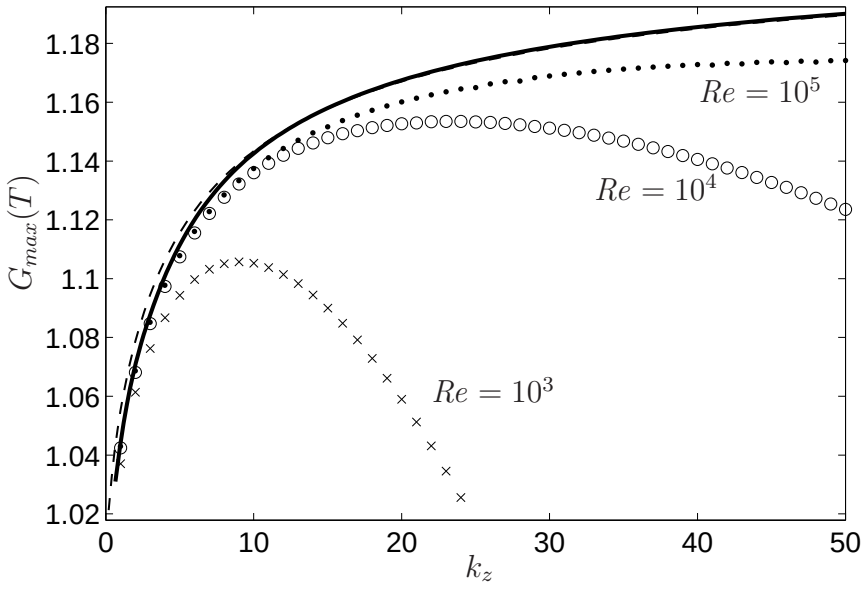

Figure 3.1: Optimal gain for Poiseuille flow and $T = 0.1$. The thick black line shows the present inviscid result obtained from (3.24) and (3.33). The $\times, \circ$ and $\cdot$ symbols correspond to the optimal gain for viscous flow at Reynolds numbers as specified on the figure, courtesy of Jon Soundar [94]. The dashed line distinguishable from the exact solution (thick black line) for $k_z \lesssim 10$, shows the asymptotic estimate of the optimal gain obtained from (3.62) evaluated up to order $\delta^{4/3}$.

3.4 Large k_z estimates

3.4.1 Inflectional shear flow in infinite domain

Consider the case of an infinite domain where the shear is maximum at a y location taken to be $y = 0$. Then S^2 can be approximated around that maximum as

$$S^2(y) \approx S_o^2 + S_o S_o'' y^2 \tag{3.34}$$

where S_o^2 and S_o'' are respectively the value of S^2 and the second derivative of S at $y = 0$, and $S_o S_o'' < 0$ so that S_o^2 is maximum. Replacing the approximation (3.34) into (3.20) yields

$$-v'' + \tau^2 k_z^2 |S_o S_o''| y^2 v = k_z^2 (\tau^2 S_o^2 - 1) v, \tag{3.35}$$

where we have omitted the subscript $(\cdot)_{opt}$. This equation (3.35) can be identified with the Schrödinger equation for a quantum particle with mass m in a harmonic potential $m\omega^2 y^2/2$

$$-\psi'' + \frac{m^2\omega^2}{\hbar^2} y^2 \psi = \frac{2mE}{\hbar^2}\psi, \tag{3.36}$$

where ψ is the wave function and the eigenvalue E is the energy of the corresponding eigenstate. Equation (3.36) is the same as (3.35) after the corresponding identifications

$$\frac{m^2\omega^2}{\hbar^2} \quad \leftrightarrow \quad \tau^2 k_z^2 |S_o S_o''|, \tag{3.37a}$$

$$\frac{2mE}{\hbar^2} \quad \leftrightarrow \quad k_z^2(\tau^2 S_o^2 - 1) \tag{3.37b}$$

and

$$\psi \leftrightarrow v. \tag{3.37c}$$

Equation (3.36) is treated in standard quantum mechanics textbooks [11]. It is known to have solutions satisfying the boundary conditions $\psi(\pm\infty) = 0$ (strictly valid here when the flow is unbounded) when

$$\frac{E}{\hbar\omega} = n + \frac{1}{2}, \tag{3.38}$$

for $n = 0, 1, 2, \ldots$ etc. Using the identification (3.37), equation (3.38) reads

$$\frac{k_z}{\sqrt{|S_o S_o''|}}\left(\tau S_o^2 - \frac{1}{\tau}\right) = 2n + 1. \tag{3.39}$$

Solving the quadratic equation (3.39) for $\tau > 0$ yields

$$\tau_n = \frac{\delta_m}{|S_o|}\left(n + \frac{1}{2}\right) + \frac{1}{|S_o|}\sqrt{\delta_m^2\left(n + \frac{1}{2}\right)^2 + 1} \tag{3.40}$$

where

$$\delta_m = \frac{1}{|k_z|}\sqrt{\frac{|S_o''|}{|S_o|}}. \tag{3.41}$$

For $n = 0$, (3.42) gives an estimate of τ_0 for large k_z (or $\delta_m \ll 1$)

$$\tau_0 = \frac{\delta_m}{2|S_o|} + \frac{1}{|S_o|}\sqrt{\frac{\delta_m^2}{4} + 1}, \tag{3.42}$$

which yields an estimate for G_{opt}.

The circles ($\circ$) in figure (3.2) show the optimal gain for $T = 7$ as a function of k_z for a tanh profile $U(y) = \tanh(y)$, computed numerically as described in chapter 2. The continuous line shows the corresponding estimate given by (3.42) with $\delta_m = \sqrt{2}/|k_z|$ (corresponding to (3.41) for $U(y) = \tanh(y)$) replaced into (3.24). The estimate (3.42) provides the good asymptotic behaviour of the optimal gain as $k_z \to \infty$.

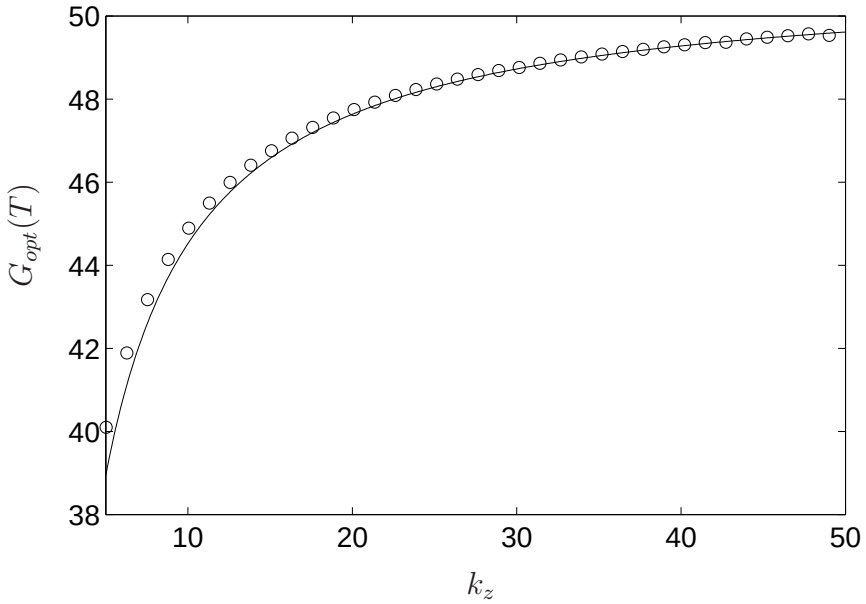

Figure 3.2: Optimal gain for $T = 7$ for an inflectional flow. The circles show the optimal gain for an inviscid tanh profile and the line the estimate from (3.42). Note that the k_z-axis has been cut at low k_z for a better vertical resolution.

The full solution of (3.35) is given by the corresponding set of eigenfunctions

$$v_n = H_n(\gamma_n y) e^{-\frac{\gamma_n^2 y^2}{2}} \tag{3.43a}$$

where

$$\gamma_n = \sqrt{\tau_n |k_z S_o S_o''|} \tag{3.43b}$$

and H_n is the Hermite polynomial of degree n [1]. For $n = 0$ we have that the optimal perturbation v_{opt} reduces to a Gaussian

$$v_{opt} \equiv v_0 = e^{-\frac{\gamma_0^2 y^2}{2}}, \tag{3.44a}$$

where

$$\gamma_0 = \left(\frac{|S_o''|}{2|S_o|} + \sqrt{\frac{S_o''^2}{4S_o^2} + k_z^2 \frac{|S_o''|}{|S_o|}} \right)^{1/2}. \tag{3.44b}$$

Expressions (3.44) provide the asymptotic localisation of the eigenfunction around the inflection point (maximum of S^2) as $k_z \to \infty$. Indeed, for $k_z \to \infty$, (3.44b) goes as $k_z^{1/2}(|S_o''/S_o|)^{1/4}$ and the optimal perturbation in the limit becomes

$$v_{opt} \approx \exp\left(-\frac{1}{2} \sqrt{\frac{|S_o''|}{|S_o|}} k_z y^2 \right), \tag{3.45}$$

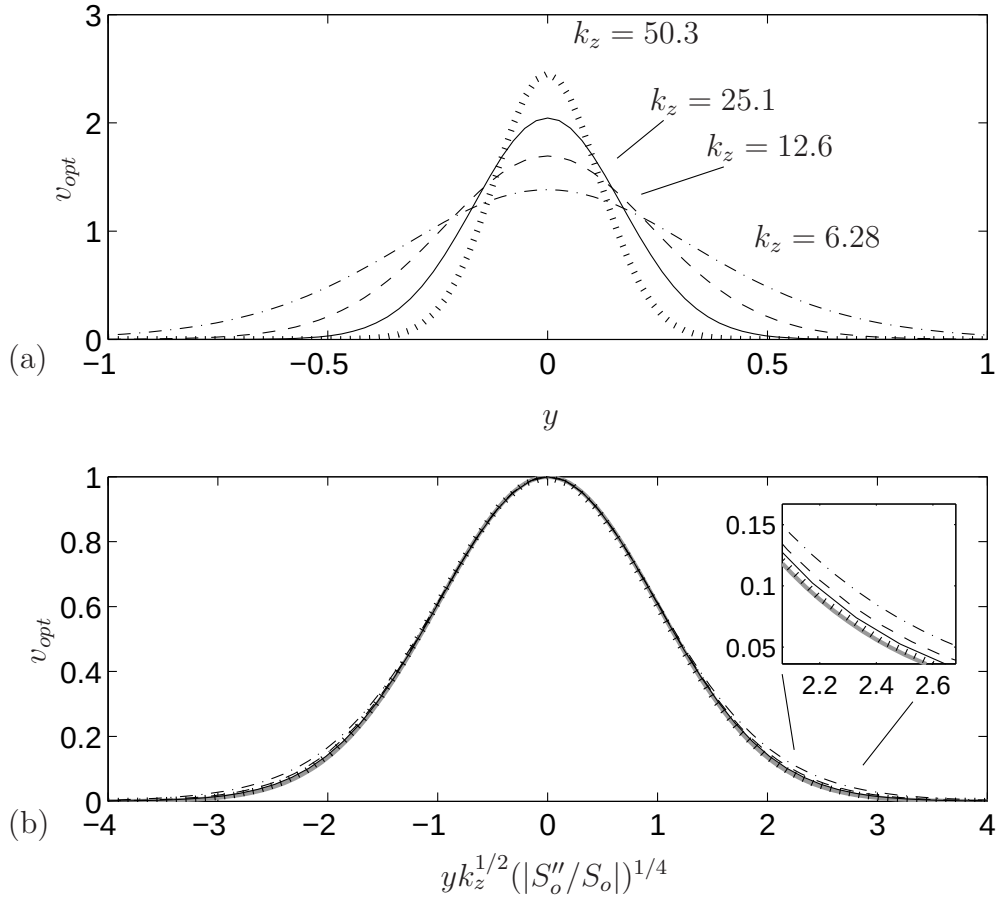

Figure 3.3: v_{opt} for an inflectional ($\tanh(y)$) profile and $k_z = 6.28$ (dash-dotted line), $k_z = 12.6$ (dashed line), $k_z = 25.1$ (continuous black line) and $k_z = 50.3$ (dotted line). (a) $v_{opt}(y)$ showing the localization of the optimal perturbations around the maximum of shear. The different perturbations are normalized so that all optimal initial conditions have the same energy. (b) Same v_{opt} as in (a) but normalized (such that $v_{opt}\big|_{y=0} = 1$) and plotted as a function of $yk_z^{1/2}(|S_o''/S_o|)^{1/4}$. The grey line shows v_{opt} as given by (3.45).

implying that the optimal perturbation becomes increasingly localized in a region whose width scales as $k_z^{-1/2}$.

Figure 3.3(a) shows $v_{opt}(y)$ for the tanh profile (same as in figure 3.2) and for different k_z. It can be observed that the optimal perturbations indeed become increasingly localised around $y = 0$ as k_z increases. Figure 3.3(b) shows the same v_{opt} as in 3.3(a) but normalized and plotted as a function of the rescaled coordinate

$k_z^{1/2}(|S_o''/S_o|)^{1/4}y$, and also the limiting optimal perturbation given by (3.45) (grey line). It can be seen that (3.45) constitutes a remarkably good approximation of the computed v_{opt}, becoming increasingly accurate as k_z increases. These results support the pertinence of the local approximation considered here.

The present estimate may be turned into a full asymptotic solution by introducing an inner layer around the inflection point scaling as $k_z^{-1/2}$ where the solution is given by (3.43), matched with two surrounding outer layers where the solution is evanescent. This solution should become a good approximation around the inflection point even in a confined domain (provided the maximum is not close to a wall).

3.4.2 Bounded flow with maximum shear at a wall

Consider now the domain $y \in [0, \infty)$ and that $S^2(y)$ has its maximum at $y = 0$. Close to the boundary, S^2 can be approximately written as

$$S^2(y) \approx S_o^2 + 2S_o S_o' y, \tag{3.46}$$

where $S_o S_o' < 0$. Replacing (3.46) into (3.20) yields

$$v'' - (ay - b)v = 0 \tag{3.47}$$

where

$$a = 2k_z^2 \tau^2 |S_o S_o'| \tag{3.48}$$

and

$$b = k_z^2(\tau^2 S_o^2 - 1). \tag{3.49}$$

Equation (3.47) is subject to the boundary conditions $v(0) = 0$ and $v(\infty) = 0$. Replacing into (3.47) the rescaled coordinate

$$Y \equiv a^{1/3} y \tag{3.50}$$

yields

$$v'' - \left(Y - \frac{b}{a^{2/3}}\right) v = 0. \tag{3.51}$$

Introducing now the shifted coordinate

$$\bar{Y} = Y - \frac{b}{a^{2/3}} \tag{3.52}$$

allows to write the problem in the standard form

$$v'' - \bar{Y} v = 0, \tag{3.53}$$

and the boundary condition at $y = 0$ reads now

$$v\Big|_{\bar{Y}=\frac{-b}{a^{2/3}}} = 0. \tag{3.54}$$

Equation (3.53) can be solved in terms of Airy functions $\mathrm{Ai}(\bar{Y})$ (Abramowitz, Stegun, page 446). The Airy function $\mathrm{Ai}(\bar{Y})$ decays monotonically to zero when $\bar{Y} > 0$ and is oscillatory for $\bar{Y} < 0$. To satisfy the boundary condition at the wall (3.54), it is needed that $-b/a^{2/3}$ be a zero of $\mathrm{Ai}(\bar{Y})$, i.e.

$$(\tau^2 S_o^2 - 1)^3 = -4\alpha_n^3 \delta^2 \tau^2 S_o^2, \tag{3.55}$$

where

$$\delta^2 \equiv \frac{S_o'^2}{S_o^2 k_z^2} \tag{3.56}$$

and $\alpha_n < 0$ is the n-th zero of the Airy function. Condition (3.55) is a cubic equation for τ^2 whose roots can be found by standard formulas, yielding the discrete set of eigenvalues

$$(\tau_n S_o)^2 = 1 + \frac{\zeta_n}{3} + \frac{\zeta_n(6+\zeta_n)}{3D(\zeta_n)} + \frac{D(\zeta_n)}{3}, \tag{3.57}$$

where

$$\zeta_n = -4\alpha_n^3 \delta^2 \tag{3.58}$$

and

$$D(\zeta) \equiv \left(\frac{27}{2}\zeta + 9\zeta^2 + \zeta^3 + \frac{3}{2}\zeta\sqrt{3(27+4\zeta)} \right)^{1/3}. \tag{3.59}$$

It is however more instructing to consider the perturbations of the limiting solution $\tau^2 S_o^2 = 1$ at the large wavenumber limit $\delta^2 = 0$. The leading order correction can be found by writing $\tau^2 S_o^2 = 1 + \beta\delta^\gamma$ into (3.55) leading to

$$\beta^3 \delta^{3\gamma} = -4\alpha_n^3 \delta^2 (1 + 2\beta\delta^\gamma + \beta^2 \delta^{2\gamma}). \tag{3.60}$$

To balance the equation at leading order in δ we must have $\gamma = 2/3$. We then have an equation for β

$$\beta^3 = -4\alpha_n^3 (1 + 2\beta\delta^{2/3} + \beta^2\delta^{4/3}) \tag{3.61}$$

which can be solved as a series in powers of $\delta^{2/3}$. After solving for the 3 leading order terms of this β expansion we have

$$\tau^2 S_o^2 = 1 + \left(-4\alpha_n^3\delta^2\right)^{1/3} + \frac{2}{3}\left(-4\alpha_n^3\delta^2\right)^{2/3} + \frac{1}{3}(-4\alpha_n^3\delta^2) + \mathcal{O}(\delta^{8/3}), \tag{3.62}$$

where it should be remembered that $\alpha_n < 0$. The dashed line in figure 3.1 shows the estimate of the optimal gain G_{opt} obtained from the first three terms of (3.62). The agreement is strikingly good for $k_z \gtrsim 10$.

Regarding the localization of the perturbation near the wall, one can replace the leading order solution of τ on the coordinate rescaling parameter a given in (3.48) giving

$$a = \frac{|S_o'|}{2|S_o|} k_z^2 + \mathcal{O}(k_z^{2/3}). \tag{3.63}$$

Recall that the rescaling in (3.50) is given by $a^{1/3}$, which at leading order when $k_z \to \infty$ becomes $a^{1/3} \to (2|S_o'|/|S_o|)^{1/3} k_z^{2/3}$. Thus, in this case of maximum shear at a wall, the inviscid optimal perturbations localize in an inner layer scaling like $k_z^{-2/3}$ asymptotically as $k_z \to \infty$.

3.5 Conclusion

We have formally solved the optimal perturbation problem for streamwise independent perturbations to arbitrary inviscid parallel flow. An important aspect in this derivation was the use of time invariance. For every problem invariant under time translation (stationary), the optimisation over all initial conditions can be split in an optimization over an initial time t_o which satisfies (3.16), and an optimisation on a subspace of codimension 1. In this inviscid case, the $\bar{E}(\bar{t}) = \bar{E}(-\bar{t})$ symmetry of the energy evolution further constrains the possibilities for energy evolution, simplifying the resulting expressions.

It turns out that, for a given base flow profile and spanwise wavenumber k_z, the maximum amplification for any optimization time T depends on a single real parameter τ. We have provided the expression of the optimal gain $G_{opt}(T)$ as a function of τ, which appears as the eigenvalue in an eigenvalue problem that also yields the shape of the optimal perturbation and all the sub-optimal perturbations. The eigenvalue problem was solved to provide exact analytical solutions for the inviscid streamwise independent optimal perturbations for plane Couette and Poiseuille flow.

Asymptotic approximations in the limit $k_z \to \infty$ were provided in two generic cases: inflectional shear and wall bounded shear with the maximum at the wall. For inflectional shear (with a maximum within the domain),the thickness of the optimal perturbation scales as $k_z^{-1/2}$, becoming increasingly localized at the inflection point. For maximum shear at a wall,the localization of the optimal perturbation at the maximum of the shear is stronger, the thickness scaling as $k_z^{-2/3}$.

Chapter 4

Transient perturbation growth in time-dependent mixing layers

Cristóbal Arratia, Colm-Cille Caulfield, Jean-Marc Chomaz
Article submitted to Journal of Fluid Mechanics

Abstract

We investigate numerically the transient linear growth of three-dimensional perturbations in an homogeneous time-evolving mixing layer, which perturbations are optimal in terms of their kinetic energy gain over a finite, predetermined time interval. We model the mixing layer with an initial parallel velocity distribution $\mathbf{U}(y) = U_0 \tanh(y/d)\mathbf{e}_x$ with Reynolds number $Re = U_0 d/\nu = 1000$, where ν is the kinematic viscosity of the fluid. We consider a range of time intervals on both a constant 'frozen' background flow and a time-dependent two-dimensional flow associated with the growth and nonlinear saturation of the most-unstable eigenmode of linear theory of the initial parallel velocity distribution, which rolls up into the classical Rayleigh instability commonly referred to as a 'Kelvin-Helmholtz' (KH) billow. For short enough times, the most amplified perturbations on the frozen tanh profile are inherently three-dimensional, and are most appropriately described as 'oblique wave' perturbations which grow through a subtle combination of the Orr and lift-up mechanisms (and hence we refer to these as 'OL' perturbations), while for longer times, the optimal perturbations are two-dimensional, the optimal response being very similar to the KH normal mode, with a slight enhancement of gain due to enhanced energy extraction from the mean shear through the Orr mechanism. For the time-evolving KH base flow, OL perturbations continue to dominate over sufficiently short time intervals. However, for longer time intervals, which involve substantial evolution of the non-parallel primary KH billow into isolated elliptical

vortices, two broad classes of inherently three-dimensional linear optimal perturbation arise, associated at low wavenumbers with the well-known core-centred elliptical translative instability, and at higher wavenumbers with the braid-centred hyperbolic instability. The 'hyperbolic' perturbation is relatively inefficient in exploiting the gain of the OL perturbations, and so only dominates the smaller wavenumber (ultimately) core-centred perturbations when the time evolution of the base flow or the start time of the optimization interval does not allow the OL perturbations much opportunity to grow. When the OL perturbations can grow at relatively small spanwise wavenumber on a time-evolving flow, they initially grow in the braid, and then trigger an elliptical core-centred perturbation by a strong coupling with the primary KH billow.

4.1 Introduction

Gaining an understanding of the mechanisms by which initially laminar flows undergo the transition to disordered turbulent motion is one of the fundamental challenges of fluid dynamics research. A particularly important archetype flow is the so-called mixing layer, where the fluid has initially a vertical, ('cross-stream') inflectional and monotonic variation in streamwise velocity, due for example to viscous diffusion of a step-change in velocity some distance downstream of a splitter plate. Provided the flow's Reynolds number $Re = Ud/\nu$ is sufficiently large (where U is some characteristic scale of the streamwise velocity which varies over a characteristic vertical (or equivalently cross-stream) distance d, and ν is the kinematic viscosity of the fluid) it is very well-known that this flow is susceptible to a strong primary instability, commonly referred to as the Kelvin-Helmholtz (KH) instability, though in an unstratified flow where the mixing layer has a finite depth and an inflectional velocity profile, it is perhaps more appropriate to refer to the instability as a 'Rayleigh' instability (see for example Drazin & Reid [42] for a fuller discussion).

The primary instability manifests itself at finite amplitude as a two-dimensional train of elliptical spanwise vortices, (centred on elliptical stagnation points) which 'roll up' from the initial strip of spanwise vorticity, and are connected by 'braid' regions of high strain and depleted (spanwise) vorticity, in turn centred on hyperbolic fixed points. These primary instabilities have been observed in experiment (e.g. Brown & Roshko [20]) and numerical simulation (Metcalfe et al. [78]) and are known to be strongly subject to subharmonic merging quasi-two-dimensional instabilities which lead to an increase in depth of the mixing layer (Winant & Browand [103]). However, it appears that they are merely an intermediate stage in the approach of a flow to the 'mixing transition' (see Dimotakis [40] for a review) which seems to require the development of some secondary, inherently three-dimensional 'instability', which upon growth to finite amplitude and interaction with the primary

billow train leads to a break down to small scale motions, and a marked increase in dissipation characteristic of turbulent motion. In this paper, we focus on these (experimentally-observed) three-dimensional perturbations, and deliberately filter out the complicating effect of subharmonic merging instabilities by restricting the time-dependent flow to a streamwise extent equivalent to the wavelength of the most unstable KH 'billow'.

There have been two main candidates proposed for this secondary instability which allows the transition to turbulence. Since the primary KH 'billows' are elliptical (and centred on elliptical stagnation points of the flow) and are affected by the strain field associated with their neighbours, it has often been hypothesized that they may be subject to a relatively low-wavenumber, inherently three-dimensional 'elliptical instability' of a strained elliptical vortex (see Pierrehumbert & Widnall [85]; Bayly [14]; Waleffe [101]; and Kerswell [67] for a comprehensive review). Although numerical simulations do show evidence of core-centred perturbations, the most noticeable three-dimensional structures in both experiment and numerical simulations are relatively higher wavenumber 'rib vortices' (see Hussain [65] for an early review) i.e. 'thin' essentially streamwise-aligned braid-centred vortices that wrap around the primary billow cores. This apparent mismatch in the initial growth location and the finite amplitude manifestation for these rib vortices was initially a major point of concern for theoreticians.

Pierrehumbert & Widnall [85] had identified a core-centred instability (which they referred to as the 'translative instability' due to the fact that this instability is characterised by a periodic shift of the vortical core) on a periodic row of Stuart vortices and speculated as to their relevance for the streamwise vortices observed in mixing layers. The fact that the translative instability is localized in the vortex cores led Corcos & Lin [33] to speculate about a different mechanism: "*... it is likely that the strong streamwise vorticity that appears and persists in the central part of the braids, and which is responsible for the streamwise streaks... is caused early on by the original (three-dimensional) shear instability rather than by the translative instability, and thereafter lives a fossil life.*" That the dynamics of the initial stages of the flow could play a role on the later development of the mixing layer is stressed by Corcos & Lin [33]: "*Either nonlinear interactions of waves of neighbouring spanwise wavenumber (particularly difficult to study numerically over a finite domain) or the competitive advantage given by particular initial conditions may lead to a selective mechanism.*" A precise assessment of these conjectures was difficult at that time. Subsequent research for mechanisms causing the observed three-dimensional features of shear layers have focused mainly on secondary instabilities present on the fully-developed KH billows; this program succeeded in finding various unstable modes and instability mechanisms.

Of particular significance was the secondary stability analysis of Klaassen & Peltier [68]. Under the (strong) assumption that the primary billow flow is com-

pletely frozen in time, Klaassen & Peltier [68] showed that the billow was susceptible to another secondary three-dimensional 'hyperbolic' instability, at substantially smaller wavelength than the elliptical instability and centred on the braid region between neighbouring billow cores. Another distinguishing characteristic between the two instabilities is that the elliptical instability, associated as it is with periodic deflections of the primary billow core, is associated with substantial spanwise perturbation vorticity, while the hyperbolic instability is associated with substantial vertical (cross-stream) and streamwise perturbation vorticity between neighbouring primary billow cores.

Numerical simulation (for example Rogers & Moser [88]; Caulfield & Peltier [29], who also confirmed the analysis of Klaassen & Peltier [68] at higher resolution) suggest strongly that both elliptical and hyperbolic instabilities can occur within the evolving flow. Yet at finite amplitude, the 'rib' streamwise-aligned vortices appear to be braid-centred. Therefore, there is a strong suggestion that hyperbolic instabilities play the key role in transition. Nevertheless, since the primary billows are indeed susceptible to 'elliptical' or 'translative' instabilities, there is every chance that the complicated interactions conjectured by Corcos & Lin [33] may well occur. Indeed, numerical simulations show that perturbations in the braid lead to streamwise-aligned rib vortices and substantial perturbation of billow core, and in some way the combination leads to transition, leading Rogers & Moser [88] to argue that: "*While it may be useful, in attempting to understand the translative instability, to distinguish between instability mechanisms that are localized to the roller cores or the braid region, the results discussed above make it clear that perturbations in the core and braid grow together. Therefore, in interpreting results of experiments or simulations, the three-dimensional instability should be considered to be a global instability of the entire flow.*"

However, the central 'frozen-in-time' assumption of the analysis presented by Klaassen & Peltier [68] is not completely supported by evidence from numerical simulations. If seeded with a small-amplitude initial perturbation, the primary billow instability does indeed saturate at finite amplitude, after a period of close to exponential growth. Even in the absence of merger, the primary billow is by no means steady, but undergoes quasi-periodic oscillations, with energetic exchange between the base flow and the perturbation. Therefore, it is important to consider the inherent time-dependence of the underlying flow in the development of three-dimensional perturbations, particularly in considering the growth of perturbations over a finite time interval. Furthermore, from such frozen-in-time analyses it is natural to think of elliptical and hyperbolic instabilities as instabilities of the saturated primary billow, with the billow acting as a 'catalyst' for their onset. But in reality the primary billow takes a certain amount of time to 'roll-up' to its saturated state, and so a natural open question is the extent to which significant perturbations can grow on a time-evolving base state, as it is at least possible that these perturba-

tions might be growing right from when the flow is organised as a simple, essentially parallel inflectional shear flow.

Naturally, considering such problems of the development of perturbations on a time-evolving underlying flow is further complicated by the inherent non-normality of the linearised Navier-Stokes operator. Because of this, it is well-known that the energy of the perturbations can grow transiently (i.e. over a finite time interval) on a stationary background flow even in the absence of a primary 'normal mode' instability, or alternatively at a rate transiently larger than the underlying normal mode growth rate, and the development of non-modal stability theory (see Schmid [90] for a review) allows the investigation of the role of initial conditions over finite time intervals in a time-varying base state in a systematic way. Indeed, there is evidence from simple models of the braid region, as presented by Caulfield & Kerswell [28], that the hyperbolic instability is particularly suited to transient growth, and recently, Ortiz & Chomaz [83] have identitified a new possible growth mechanism for braid-like regions, which they relate to the 'anti-lift-up' mechanism previously described by Antkowiak & Brancher [4].

From a physical viewpoint, there are two natural mechanisms which have been identified as causing (energetic) transient growth of perturbations in shear flows, known as the Orr mechanism (as originally presented by Orr [82]) and the lift-up mechanism (see Ellingsen & Palm [44], Landahl [70]). The Orr mechanism involves counter-rotating vortices which are parallel to the base flow's (and hence spanwise) vorticity being tilted into and against the mean shear and hence amplified by the base shear via the working of the Reynolds stress. This mechanism is efficient at relatively high streamwise wavenumbers (i.e. small scales) on short time scales as demonstrated by Butler & Farrell [25]. On the other hand, in the lift-up mechanism, streamwise vortices interact with the basic shear to generate streamwise perturbation velocity. As shown by Butler & Farrell [25], this mechanism operates at somewhat smaller wavenumbers, and on somewhat larger time scales. Naturally, in an intermediate range of either wavenumber or time interval, combinations or 'mixtures' of these two growth mechanisms can occur, as discussed for example by Guégan, Huerre & Schmid [56].

Much of the focus of research into 'optimal' transient growth (i.e. the identification of perturbations which have the largest relative growth in their perturbation kinetic energy or gain over some finite time interval) has been on flows such as plane Couette flow or pipe flow where there is no linear instability, or channel flow where the linear instability onsets at a much higher Reynolds number than transition is observed to occur in experiment and simulations. In such circumstances, the transiently growing perturbations will clearly dominate the flow evolution. On the other hand, if there are unstable 'normal' modes, it is not immediately obvious what role, if any is played by transient perturbations (utilising the Orr mechanism, the lift-up mechanism, or indeed some mixture of the two) in the flow evolution.

The conventional picture (consistent with experimental and numerical evidence) is that the flow will be ultimately dominated by the most-unstable (eigen) mode of linear theory. However, it is not at all clear how long this process takes, and it is at least conceivable that an appropriately chosen initial perturbation may grow very rapidly, at least over a short time. Such a transient perturbation, allowed to develop to finite amplitude, and thus to modify the base flow in a nontrivial manner, may actually preclude the development of the primary KH billow, leading potentially to a kind of 'bypass' transition with no primary instability development.

In summary, there are therefore three key open questions of interest. Firstly, are the previously-identified elliptical and/or hyperbolic instabilities 'optimal' perturbations of an inflectional shear layer in any sense? Secondly, what is the role of the time-dependence of the evolving billow in the development of optimal growing perturbations? In particular, do elliptical and hyperbolic instabilities rely fundamentally on the primary billow being fully saturated, or can they grow as the primary billow rolls up? And thirdly, how relevant are the simple idealized pictures of modal instability and physical growth mechanisms to the actual development of perturbations within an inflectional shear layer flow?

These questions will be addressed in this paper using the tools of non-modal stability analysis (as discussed in detail in the review of Schmid [90]). In particular a linearized time-stepping Navier-Stokes equation solver and its adjoint will be 'looped' and hence iterated mutiple times to identify the properties of the 'optimal' linear perturbation (in the sense that the relative gain of the kinetic energy of the perturbation is maximised over some time interval). This power iteration looping method is very well suited to the problem at hand, as this method can straightforwardly embed the properties of a time-evolving base state in the equation solvers (both direct and adjoint) which are used. Indeed, with an evolving base flow, there is an interesting mathematical subtlety to do with the fact that not only the length of the time interval over which optimization of gain occurs is important, but also the chosen start time (in the evolution of the base state) is significant to the secondary perturbations.

This paper is organised as follows. After briefly introducing the (largely now conventional) mathematical formulation and algorithm in section 4.2, focussing on the implications of using a time-evolving base flow state, we first consider transient perturbation growth (over a wide range of optimizing time intervals) on an initial hyperbolic tangent frozen in time by the application of a body force. In section 4.3, we focus in particular on identifying the time interval over which the conventional KH instability mode is **not** the optimal response. Having considered transient perturbation growth on the steady hyperbolic tangent base flow, we generate a time-evolving two-dimensional single KH billow at sufficiently high Reynolds number to grow to a non-trivial finite amplitude. In section 4.4 we then consider transient perturbation growth on this time-evolving, non-parallel billow base flow over a range of time

intervals. We classify and characterise the predicted optimal perturbations both in terms of energy within core, and also the relative size of components of enstrophy. This compartmentalization of the enstrophy is very useful to interpret the properties of the (in general) three-dimensional perturbations, and to identify any possible connection to the previously-predicted elliptical and hyperbolic instabilities, as well as the crucial physical growth mechanisms. In section 4.5 we then also consider the importance of the chosen start time of the optimization time interval relative to the time-evolution of the primary KH billow on the 'optimal' perturbation, discussing the possible significance of the of the 'anti-lift-up' mechanism described in Ortiz & Chomaz [83] for initial perturbation growth in the braid. Finally, in section 4.6 we draw our conclusions, and present suggestions for future work, particularly considering the possible use of full nonlinear direct numerical simulations to investigate the finite amplitude evolution of the identified 'optimal' perturbations.

4.2 Mathematical formulation

We consider the linear evolution of perturbations $\mathbf{u}_p$ to a base flow $\mathbf{U}(t)$ under the incompressible Navier-Stokes equations. The base flow $\mathbf{U} = (U(x, y, t), V(x, y, t), 0)^T$ is restricted to (at most) two dimensions, while the perturbation $\mathbf{u}_p$ is allowed to evolve in three dimensions. We choose a coordinate system so that x is in the streamwise direction, y is in the vertical (or equivalently cross-stream) direction, and z is in the spanwise direction. Scaling the flow variables with the characteristic velocity scale U and the shear layer length scale d (mentioned in the introduction) to define the Reynolds number, the nondimensional linearized Navier-Stokes equations are thus

$$\frac{\partial \mathbf{u}_p}{\partial t} + (\mathbf{U}(t)\cdot\nabla)\mathbf{u}_p = -\nabla p_p - (\mathbf{u}_p\cdot\nabla)\mathbf{U}(t) + Re^{-1}\nabla^2\mathbf{u}_p, \tag{4.1a}$$

$$\nabla \cdot \mathbf{u}_p = 0. \tag{4.1b}$$

The boundary conditions are periodic in x and z, with $\mathbf{u}_p$ and ∇p_p tending to zero when $|y| \to \infty$.

Formally, the calculations of solutions to the governing equations (4.1) may be thought of as a propagator of the (perturbation) velocity field from some initial time t_i to some final time t_f, i.e.

$$\mathbf{u}_p(t_f) = \Phi_\lambda(t_f, t_i)\mathbf{u}_p(t_i) \tag{4.2}$$

where the sub-index λ represents the parameters, the Reynolds number and the geometry (and perhaps discretization in practice) of the flow domain under consideration. We are thus interested in the optimization of the gain $\mathcal{G}(\lambda, T, T_0)$ defined

as

$$\mathcal{G}(\lambda, T, T_0) \equiv \frac{E(\lambda, T)}{E(\lambda, T_0)} = \frac{\langle \mathbf{u}_p(T), \mathbf{u}_p(T) \rangle}{\langle \mathbf{u}_p(T_0), \mathbf{u}_p(T_0) \rangle} \tag{4.3a}$$

$$= \frac{\langle \Phi_\lambda(T, T_0)\mathbf{u}_p(T_0), \Phi_\lambda(T, T_0)\mathbf{u}_p(T_0) \rangle}{\langle \mathbf{u}_p(T_0), \mathbf{u}_p(T_0) \rangle} \tag{4.3b}$$

$$= \frac{\langle \mathbf{u}_p(T_0), \Phi_\lambda^\dagger(T, T_0)\Phi_\lambda(T, T_0)\mathbf{u}_p(T_0) \rangle}{\langle \mathbf{u}_p(T_0), \mathbf{u}_p(T_0) \rangle}, \tag{4.3c}$$

where angled brackets denote the conventional inner product yielding the energy E, and the superscript $\dagger$ denotes the **adjoint** such that

$$\langle \mathbf{u}_d, \Phi_\lambda \mathbf{u}_p \rangle = \langle \Phi_\lambda^\dagger \mathbf{u}_d, \mathbf{u}_p \rangle, \tag{4.4}$$

for all $\mathbf{u}_d$ and $\mathbf{u}_p$. Without loss of generality, we normalise the inner product so that $E(\lambda, T_0) = 1$.

It can be easily seen that the adjoint of the propagator $\Phi_\lambda^\dagger(T, T_0)$ corresponds to the propagator of the adjoint equations from T to T_0. (For time dependent equations, this can be directly shown by taking the adjoint of the propagator as given in the equation (4) of Farrell & Ioannou [47].) It is straightforward to establish (see for example Hill [64], Donnadieu *et al.* [41]) that the adjoint equations of (4.1) are

$$\frac{\partial \mathbf{u}_d}{\partial \tau} = \boldsymbol{\Omega}(-\tau) \times \mathbf{u}_d - \nabla \times (\mathbf{U}(-\tau) \times \mathbf{u}_d) - \nabla p_d + Re^{-1} \nabla^2 \mathbf{u}_d, \tag{4.5a}$$

$$\nabla \cdot \mathbf{u}_d = 0. \tag{4.5b}$$

In these equations $\tau = -t$, $\boldsymbol{\Omega} = \nabla \times \mathbf{U}$, $\mathbf{u}_d$ is the adjoint velocity variable, p_d is the equivalent 'pressure' adjoint variable enforcing incompressibility, the boundary conditions are the same as for (4.1), and the initial condition according to (4.3c) is $\mathbf{u}_d(T) = \Phi_\lambda(T, T_0)\mathbf{u}_p(T_0)$. As is commonly understood, due to the integration by parts that is implicit in the definition of the adjoint, the relative signs of the time derivative and the Laplacian are different for the direct and the adjoint Navier-Stokes equations, implying that the adjoint equations are well-posed when integrated backwards in time. It is also clear that even if the propagator Φ_λ is not self-adjoint, the combination $\Phi_\lambda^\dagger \Phi_\lambda$ is self-adjoint. The optimal perturbation is that which attains the maximum gain

$$\mathcal{G}_{max}(\lambda, T, T_0) = \max_{\mathbf{u}_p(T_0)} \{\mathcal{G}(\lambda, T, T_0)\}, \tag{4.6}$$

where the maximisation is over all choices of initial conditions $\mathbf{u}_p(T_0)$. Since the operator $\Phi_\lambda^\dagger \Phi_\lambda$ is self-adjoint this maximum is given by its leading eigenmode. Throughout this paper we will set the central flow parameter $Re = 1000$, which is sufficiently large to ensure that the primary instability rolls up into a finite amplitude, energetic billow.

These adjoint equations can be solved using a straightforward modification of a pseudo-spectral DNS code with an Adams-Bashforth time scheme (as previously described and utilised by Donnadieu *et al.* [41]). In particular, the central point arising from the integration by parts that the Laplacian operator has an opposite sign (and hence that the adjoint propagator is well-posed when integrating **backward** in time) is very simple to implement computationally. The iterative optimization algorithm essentially relies on power iteration (see Schmid [90] for more details). A guess for the initial conditions $\mathbf{u}_0$ is integrated forwards in time from $t = T_0$ to the target time $t = T$ using the (forward) propagator Φ_λ. The final state $\mathbf{u}_T$ is then used as the 'initial' conditions for the adjoint propagator $\Phi_\lambda^\dagger$, which is then integrated 'backward' in time from T to T_0. This 'final' state (after appropriate rescaling, see for example (4.11)) is then used as the initial condition for the next loop of this iteration. Multiple iterations of this entire loop will naturally lead to the solution being dominated by the eigenfunction of the (combined) operator $\Phi_\lambda^\dagger \Phi_\lambda$ associated with the eigenvalue with the largest real part. This leading eigenmode of course corresponds (up to scaling) to the initial perturbation which has the largest gain over the target time interval.

4.3 Transient response of a frozen parallel hyperbolic tangent shear flow

4.3.1 Base flow and decomposition of perturbations

As discussed in the introduction, the first problem we consider is the transient growth of infinitesimally small perturbations on a steady parallel inflectional shear flow. We consider a tanh profile

$$\mathbf{U}(y) = \tanh(y)\mathbf{e}_x, \tag{4.7}$$

as an appropriate choice for this parallel base flow. Due to the fact that the flow we consider has finite diffusion (with $Re = 1000$), over time such a profile will spread vertically (or equivalently cross-stream). Therefore, for the base flow (4.7) to be a solution to the governing equations, we formally add a body force

$$\mathbf{F} = -Re^{-1} \tanh(y)''\mathbf{e}_x, \tag{4.8}$$

to the full Navier-Stokes equations so that $\mathbf{U}(y) = \tanh(y)\mathbf{e}_x$ is actually a solution. This is done in classical stability studies (Drazin & Reid [42]) and yields (4.1a) without a source term from base flow diffusion. Therefore, the perturbations are evolving in a flow with finite Re, but the base (parallel) flow $\mathbf{U}(y)$ defined by (4.7) is 'frozen'.

Because the governing equations (4.1) with the base flow (4.7) have coefficients with no dependence on x and z, we can spectrally decompose the perturbations as

$$[\mathbf{u}_p, p_p](x, y, z, t) = \mathrm{Re}\left([\mathbf{u}, p](y, t)e^{i(k_x x + k_z z)}\right). \tag{4.9}$$

We can then compute the y-dependent eigenfunctions $[\mathbf{u}, p]$ independently for each (k_x, k_z). This computation can be implemented efficiently within a three-dimensional linearized code, as there is no interaction between modes with different (k_x, k_z) combinations. We can thus identify the energy of each of the perturbations as

$$E(k_x, k_z, t) = \int_{y_{\min}}^{y_{\max}} \mathbf{u}^* \cdot \mathbf{u}\, \mathrm{d}y, \tag{4.10}$$

where * denotes the complex conjugate, and $y_{\min} = -12.5$ and $y_{\max} = 12.5$ are the minimum and maximum vertical extents of the flow domain respectively. It is also important to note that the energy is normalized so that the total energy on each of the modes is one initially, i.e.

$$E(k_x, k_z, T_0) = 1, \tag{4.11}$$

so that consecutive iterations converge to the optimal perturbation for all the computed (k_x, k_z), avoiding potential computational problems if the less amplified modes were allowed to have significantly smaller amplitude than the most amplified ones. A convenient way to characterize the various perturbations is by using the mean optimal growth rate

$$\sigma_m(k_x, k_z, T) = \frac{\ln[\mathcal{G}_{max}(k_x, k_z, T)]}{2T}, \tag{4.12}$$

where the optimization is across all possible y-dependent eigenfunctions of the gain from $T_0 = 0$ to the target time T.

As the optimization time increases, unsurprisingly the maximum optimal mean growth rate (further maximised over all choices of k_x and k_z) approaches from above the maximum growth rate of the classic (modal) KH instability, that is, $\max(\sigma_m) \to \max(\sigma_{KH})$ as $T \to \infty$, with the maximising streamwise wavenumber $k_x^{max} \to k_{KH}$ approaching that of the most unstable KH modal instability and $k_z \to 0$. A more detailed quantitative description of this behaviour is shown in figure 4.1.

4.3.2 Optimal perturbations: OL-type and K-type

Figures 4.1a and b show the optimal mean growth rates $\sigma_m(k_x, k_z)$ for $T = 7$ (figure 4.1a) and $T = 20$ (figure 4.1b). For $T = 7$, it is clear that the most amplified optimal perturbation is inherently three-dimensional (3D, i.e. with $k_z \neq 0$). The largest

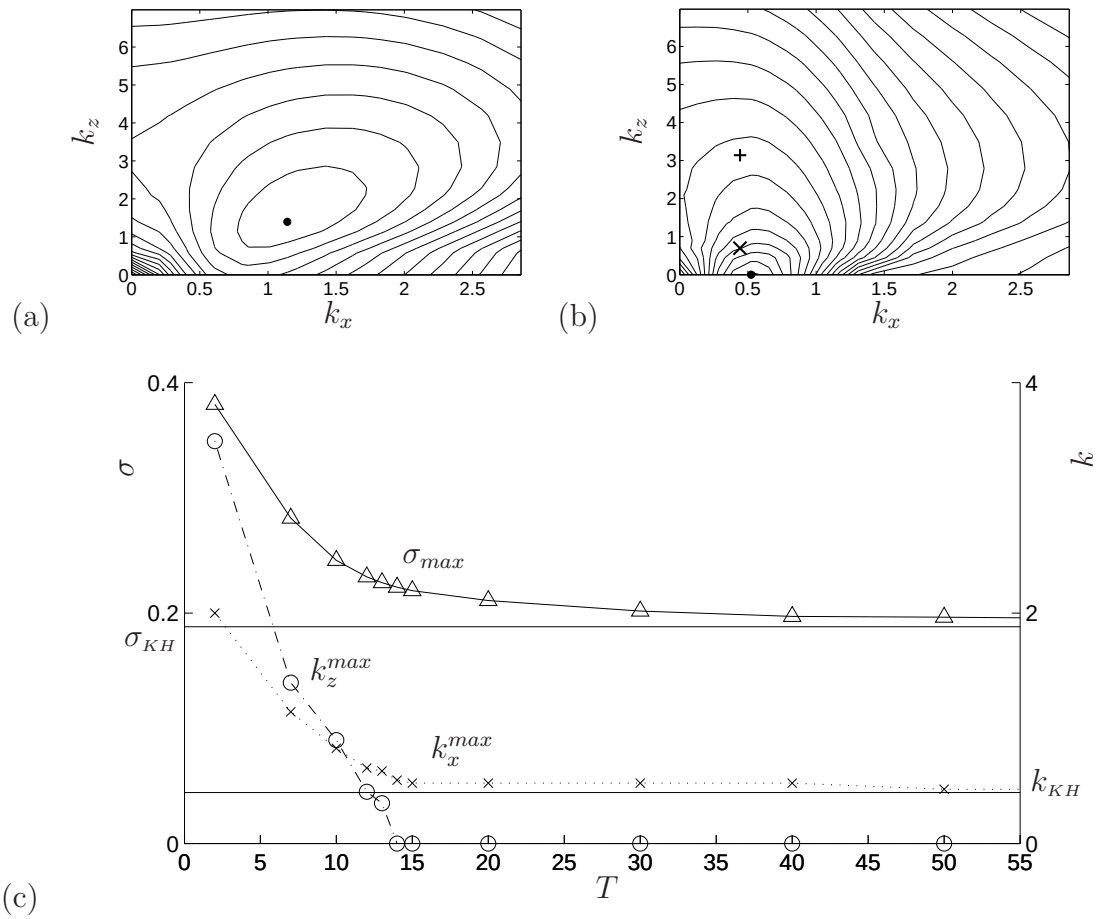

Figure 4.1: (*Top*) Contours of the optimal mean growth rate σ_m as defined in (4.12) for optimization times T=7 (a) and T=20 (b). In both figures the contour levels are set in steps of 0.011, decreasing from 0.275 for $T = 7$ (a) and from 0.209 for $T = 20$ (b). Each global maximum is indicated by a black dot ($\cdot$) and two characteristic 'OL-type' optimal perturbations, 'OLE' and 'OLH' as discussed in the text, are represented in (b) by the $\times$ (OLE) and the + (OLH) symbols. (*Bottom*) σ_{max} ($\triangle$), k_z^{max} ($\circ$) and k_x^{max} ($\times$) i.e. maximum over (k_x, k_z) of $\sigma_m(T)$ and associated k_z and k_x. The upper horizontal line (associated with the left hand vertical axis) indicates the maximum growth rate of the KH instability that occurs for streamwise wavenumber $k_{KH} = 0.4425$ (indicated by the lower horizontal line, associated with the right hand vertical axis) and $k_z = 0$.

σ_m computed is $\sigma_{max} = 0.2824$ at $(k_x^{max}, k_z^{max}) = (1.142, 1.396)$ and is marked with a black dot ($\cdot$) in figure 4.1a. Conversely, for $T = 20$, the most amplified optimal perturbation is two-dimensional (2D, i.e. with $k_z = 0$), and the largest σ_m computed is $\sigma_{max} = 0.2109$ at $(k_x^{max}, k_z^{max}) = (0.5236, 0)$ and marked with a black dot ($\cdot$) in figure 4.1b. This particular combination of wavenumbers is in the region of parameter space that is known to be susceptible to the KH instability. Figure 4.1c shows, for different T, the largest computed optimal mean growth rates σ_{max} (left axis) and their corresponding wavenumbers (k_x^{max}, k_z^{max}) (right axis). The horizontal lines of figure 4.1c correspond to $\sigma_{KH} = 0.1881$, the growth rate of the most unstable mode of the KH instability at this Re (upper horizontal line), and to $k_{KH} = 0.4425$, the streamwise wavenumber corresponding to the most unstable mode. As T increases, σ_{max}, k_x^{max} and k_z^{max} decrease and approach the values corresponding to the most unstable KH mode, σ_{KH}, k_{KH} and 0, respectively. The most amplified perturbations are inherently 3D for $T \leq 13$, but then become 2D for $T \gtrsim 14$. Thus, we can distinguish between two qualitatively different types of strongly amplified optimal perturbations, which dominate depending on the particular target time chosen. We find that 3D perturbations dominate for short T, while 2D perturbations (clearly related to the KH normal mode instability) dominate for larger T.

As already discussed in the introduction, the large amplification of 3D, oblique wave perturbations for $T \sim 10$ is a universal feature of plane shear flow, as discussed in detail by Farrell & Ioannou [49]. Both the Orr (Orr [82]) and the lift-up (Ellingsen & Palm [44]) mechanism have an effect on the evolution of 3D perturbations in plane shear flows. As discussed in detail by Farrell and Ioannou [48], the large amplification for such 3D perturbations is due to a synergy between the two mechanisms; according to their description, the increased vertical (cross-stream) perturbation velocity v produced by the Orr mechanism excites u through the lift-up mechanism. Therefore, we choose to refer to these early-time interval 3D perturbations as being of 'OL-type', as they may be thought of as utilizing both Orr and lift-up mechanisms. In this simplified picture, the relative contribution of the Orr and lift-up mechanisms depends on the orientation of the oblique waves, going from pure Orr for $k_z = 0$ (and perhaps some KH-like behaviour if in the KH unstable region) to pure lift-up as $k_x/k_z \to 0$. In terms of the different components of vorticity, it is important to keep in mind that the Orr mechanism acts on the spanwise vorticity ω_z, and that the lift-up mechanism corresponds to large production of cross-stream (or vertical) vorticity ω_y.

Furthermore, the early-time OL-type perturbation is inherently transient, unlike the perturbations which are identified over longer time intervals. This aspect of the perturbations' character is shown in figure 4.2 where we plot the instantaneous growth rate

$$\sigma(t) = \frac{1}{2E}\frac{dE}{dt} \tag{4.13}$$

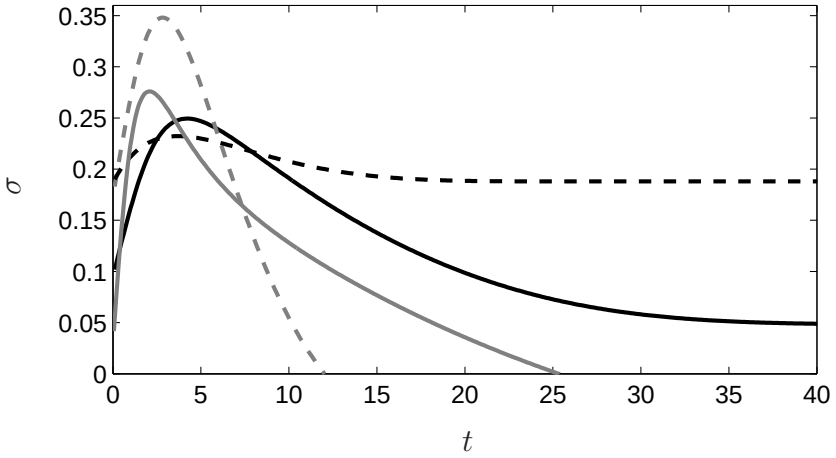

Figure 4.2: The variation of the growth rate σ (as defined in (4.13)) with time of some representative optimal perturbations. The grey-dashed line corresponds to the optimal perturbation for $T = 7$ and $(k_x, k_z) = (1.142, 1.396)$, (marked with a black dot on figure 4.1a); the black-dashed line corresponds to the optimal perturbation for $T = 20$ and $(k_x, k_z) = (k_{KH}, 0)$, (marked with a black dot on figure 4.1b); the black line corresponds to the 'OLE' perturbation for $T = 20$ and $(k_x, k_z) = (k_{KH}, 0.698)$ (marked with a $\times$ on figure 4.1b), and the grey line corresponds to the 'OLH' perturbation for $T = 20$ and $(k_x, k_z) = (k_{KH}, 3.142)$ (marked with a $+$ on figure 4.1b).

of optimal perturbations for $T = 7$ (grey-dashed line, the most amplified OL-type mode marked with $(\cdot)$ in figure 4.1a), $T = 20$ for $(k_x, k_z) = (k_{KH}, 0)$ (black-dashed line, corresponds to the most unstable k_x), which since it corresponds to a KH instability we refer to as a K-type perturbation, and $T = 20$ for $(k_x, k_z) = (k_{KH}, 0.698)$ and $(k_x, k_z) = (k_{KH}, 3.142)$ (marked respectively by $\times$ and $+$ in figure 4.1b, discussed in more detail in section 4.4.2), which are OL-type perturbations labelled as OLE and OLH respectively, in anticipation of the 'elliptical' and 'hyperbolic' instabilities to which these perturbations will be related. The growth rate σ of the $T = 7$ optimal perturbation is very large at the beginning and then decays rapidly, becoming negative at about $t \sim 12$, as is typical for such transient perturbations. Conversely, the growth rate for the K-type perturbation eventually asymptotes to a finite value (the growth rate of the modal KH instability). Initially however, this perturbation also shows a slight non-normal mode enhancement of the (instantaneous) growth rate, associated with the perturbation extracting energy transiently via the Orr mechanism.

Finally, the 3D longer time-interval OL-type perturbations labelled OLE and OLH show both early-time strong transient growth (with an earlier and stronger

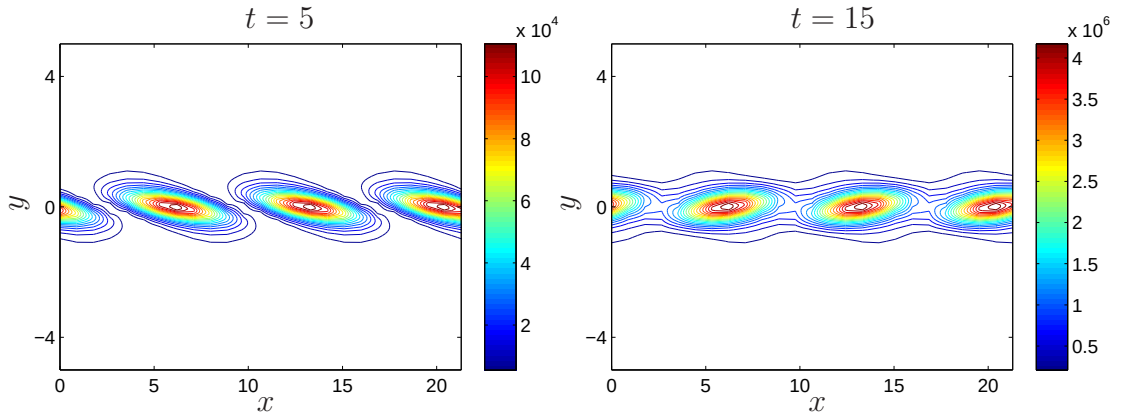

Figure 4.3: Energy density in the (x, y)-plane of the OLE optimal perturbation for $T = 20$ and $(k_x, k_z) = (k_{KH}, 0.698)$ at $t = 5$ and $t = 15$.

peak for OLH but larger growth up to $t = T = 20$ for OLE), and much smaller (but for OLE still positive) growth rate at later times. The positive growth rate of the OLE perturbation at late times is consistent with the sub-dominant mode of the KH instability existing at its corresponding wavenumbers $(k_x, k_z) = (k_{KH}, 0.698)$. Figure 4.3 shows the energy density of the same perturbation labelled OLE at times $t = 5$ and $t = 15$. This quantity is normalised such that its integral over the (x, y) domain containing one wavelength is one at $t = T_0 = 0$. At $t = 5$, the optimal perturbation is oriented slightly against the shear, and for $t = 15$ it has been tilted, as is characteristic of short time optimal perturbations, at least partially subject to the Orr mechanism. The smaller longer-time growth rate for this perturbation is also consistent with the classic Squire transformation (Squire [95]) which demonstrates that oblique 3D disturbances are equivalent to 2D disturbances in a flow with a lower Re (and hence lower growth rate). In light of all these characteristics, we call this perturbation OL-type because most of the growth up to $t = 20$ corresponds to non-modal growth.

These observations are entirely consistent with previous work, and in particular do not show evidence of either 'elliptical' instability or 'hyperbolic' instability (henceforth referred to as E-type and H-type perturbations for consistency with the OL-type and K-type nomenclature introduced above) which numerical simulation and laboratory experiment suggest are essential characteristics of transition in inflectional shear layers. Of course, this is largely unsurprising as a parallel base state has no elliptical or hyperbolic points. Indeed, it seems entirely reasonable that the primary billow, or a developing nonlinear K-type perturbation, will act as a catalyst for transition by encouraging the development of E-type or H-type perturbations. To investigate whether the OL-type perturbations can be related to the appearance

of E-type or H-type perturbations, one should consider the natural, nonlinear evolution of the K-type perturbation giving rise to the primary billow. Therefore, in the next section, we describe the properties of just such a non-parallel, time-dependent yet inherently 2D 'base' flow, whose non-modal 'stability' properties we can then analyse.

4.4 Transient response of K-type time-dependent flow

4.4.1 Base flow

To generate a non-parallel, time-dependent 2D K-type base flow, we performed a sequence of fully nonlinear direct numerical simulations (DNS) of 2D perturbations of the hyperbolic tangent parallel base flow discussed in the previous section 4.3. The size of the computational domain in the streamwise direction is set to $L_x = 14.2$, (i.e. $k_x = 0.4425 = k_{KH}$) which corresponds to one wavelength of the most unstable eigenmode of K-type. In particular, this size of computational domain, along with periodic boundary conditions suppresses the possibility of subharmonic mergings. It also restricts the possible choices of streamwise wavenumber to (integer) multiples of k_{KH}. From the numerical evidence this is unlikely to be too restrictive, although from figure 4.1, the streamwise wavenumber of the most unstable OL-type perturbation is substantially larger than k_{KH}. The number of gridpoints in the x-direction is $N_x = 256$. The number of points in the vertical cross-stream, y-direction is $N_y = 512$ and the corresponding box size is (as already noted) $L_y = 25$, which we believe (see for example Hazel [59]) is sufficiently large for the evolution of the primary KH billow not to be affected significantly by the vertical boundaries.

The DNS was initialized with random perturbations with zero mean and small amplitude. The initial amplitude was chosen small enough so that, after the initial transients, the most unstable mode appears long before nonlinear effects are noticeable. However, the procedure we chose to construct the base flow subsequently used in our stability analysis is a little involved, due to the complicating effect of the diffusion of the inflectional shear layer due to the finite value of the flow's Reynolds number. As a first step in this procedure, we simulated a flow with the body force (4.8) which 'freezes' the inflectional shear layer included in the governing (nonlinear) Navier-Stokes equations. The curve in figure 4.4 shows part of the evolution in time of the perturbation energy E, in this first reference simulation with the body force. In figure 4.4, $\ln(E)$ grows linearly in time first, (at a rate entirely consistent with (twice) the growth rate of a K-type modal instability) then begins to saturate, reaches a maximum and finally oscillates slightly. Those stages correspond to the exponential growth of energy due to the KH instability and the subsequent nonlin-

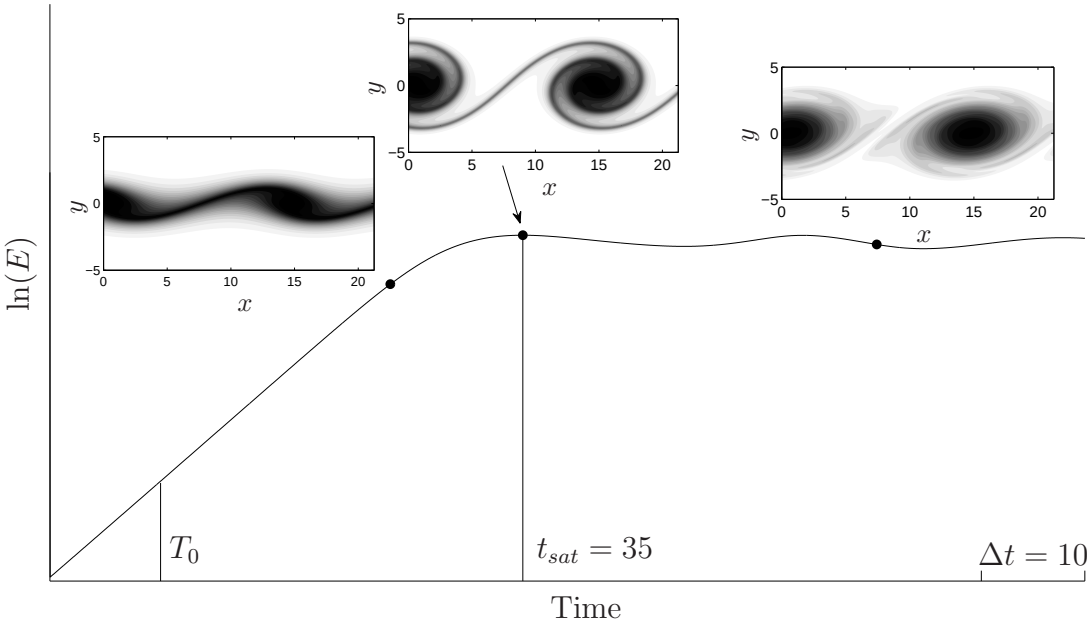

Figure 4.4: The evolution of the base flow state with time. Vertical units are arbitrary. Base flow vorticity is shown from left to right at times $t = 22.2$, $t = t_{sat} = 35$ and $t = 69.2$, corresponding to the $\bullet$ signs on the curve.

ear saturation leading to the roll-up of a non-stationary KH billow (see for example Corcos & Sherman [34]). The saturation time t_{sat} of the primary billow naturally depends on the amplitude of the initial condition and the Reynolds number of the flow, and for this reference simulation we have $t_{sat} = 35 = t_{sat\_\mathrm{bf}}$ (for 'base flow'). We refer to the entire time-dependent 2D flow obtained from this reference simulation with the body force as $\mathbf{U}_{\mathrm{bf}}(t)$.

We then conduct other simulations without the body force (and thus solutions to the actual full nonlinear Navier-Stokes equations). Each simulation is constructed for a specific start time T_0 of the optimization time interval, and is also specifically tailored so that the primary billow still saturates at a time $t_{sat} \simeq t_{sat\_\mathrm{bf}} = 35$. For an optimization interval starting at T_0, a DNS without the body force is initialized with $\mathbf{U}_{\mathrm{bf}}(T_0 - \delta t)$ at time $t = T_0 - \delta t$. In this new DNS, the saturation time t_{sat} would in general occur at a time slightly different from the reference time $t_{sat-\mathrm{bf}} = 35$, say $35 + t_{-\nu}$. We tune the offset time δt used for initializing the DNS until $0 < t_{-\nu} < 1$. We then reset the zero of time so that we obtain a 2D flow $\mathbf{U}(t)$ with no body force from $T_0 - t_{-\nu}$ which thus saturates, similarly to the reference flow (with a

body force) at $t_{sat} = t_{sat-\mathrm{bf}} = 35$. As a specific example, the insets of figure 4.4 show vorticity snapshots of $\mathbf{U}(t)$ for $T_0 = 0$ and $t_{-\nu} = 0.8$. Therefore, the evolving base flow always reaches its maximum amplitude at $t = t_{sat}$. Although formally the algorithm requires $\mathbf{U}(t)$ at every time step, for computational efficiency, we save the full flow field $\mathbf{U}(t)$ and then linearly interpolate it every 2 time units. We then use this linearly interpolated base flow for our optimization calculations. Interpolating the base flow every time unit required shorter time stepping in the optimization calculations but provided similar results.

4.4.2 Optimal perturbations from $T_0 = 0$: E-type and H-type

A natural place to start in our consideration of linear perturbation growth on a time-evolving base flow susceptible to a primary KH instability is to consider optimization time intervals starting at the very beginning of the flow evolution, and thus potentially including (for sufficiently long intervals) the roll-up before saturation of the primary K-type instability. Figure 4.5 shows $\mathcal{G}_{max}$ for $T_0 = 0$ and different T. For all these curves the minimal streamwise wavenumber is constrained to be $k_x = k_{KH}$, but all integer multiples are allowed. Also indicated is the gain of the optimal perturbations for the frozen (by a body force) tanh profile (as discussed in section 4.3) at $k_x = k_{KH}$ for $T = 20$ and at $k_x = 2k_{KH}$ for $T = 10$. (Choosing this increased streamwise wavenumber is consistent with figure 4.1 for the early-time interval OL-type perturbations.) For these short optimization times ($T \lesssim 20$), optimal energy growth resembles that of the parallel, frozen hyperbolic tangent profile considered in the section 4.3 (except for large k_z in which case the optimal perturbations concentrate more around the incipient braid). In particular, the most amplified optimal perturbation is clearly 3D for $T = 10$ and 2D for $T = 20$, entirely consistent with figure 4.1. For $T = 30$, the most amplified optimal perturbation is still 2D, yet for $T \gtrsim 50$, the most amplified optimal perturbation is definitely inherently 3D, and occurs for a particular spanwise wavenumber $k_z \approx 0.6$.

It is apparent that for sufficiently long optimization times, $T \gtrsim 50$, the structure of the gain's dependence on k_z changes qualitatively, and there appears to be a new perturbation type appearing centred around $k_z \simeq 0.6$. It could seem that the abrupt change of slope of $\mathcal{G}_{max}$ at the end of the peaked area around $k_z \simeq 1$ is due to the cross-over of branches corresponding to different modes of the composed direct-adjoint propagator ($\Phi_\lambda^\dagger \Phi_\lambda$ in section 4.2). A Krylov method similar to that described in Donnadieu *et al.* [41] was used to approximate the leading subdominant modes of the direct-adjoint propagator for $T = 60$. (The convergence of the results was checked by using different Krylov subspaces typically of dimension 5 or 6.) The two leading subdominant branches were followed around $k_z \simeq 1$ (where the slope of $\mathcal{G}_{max}$

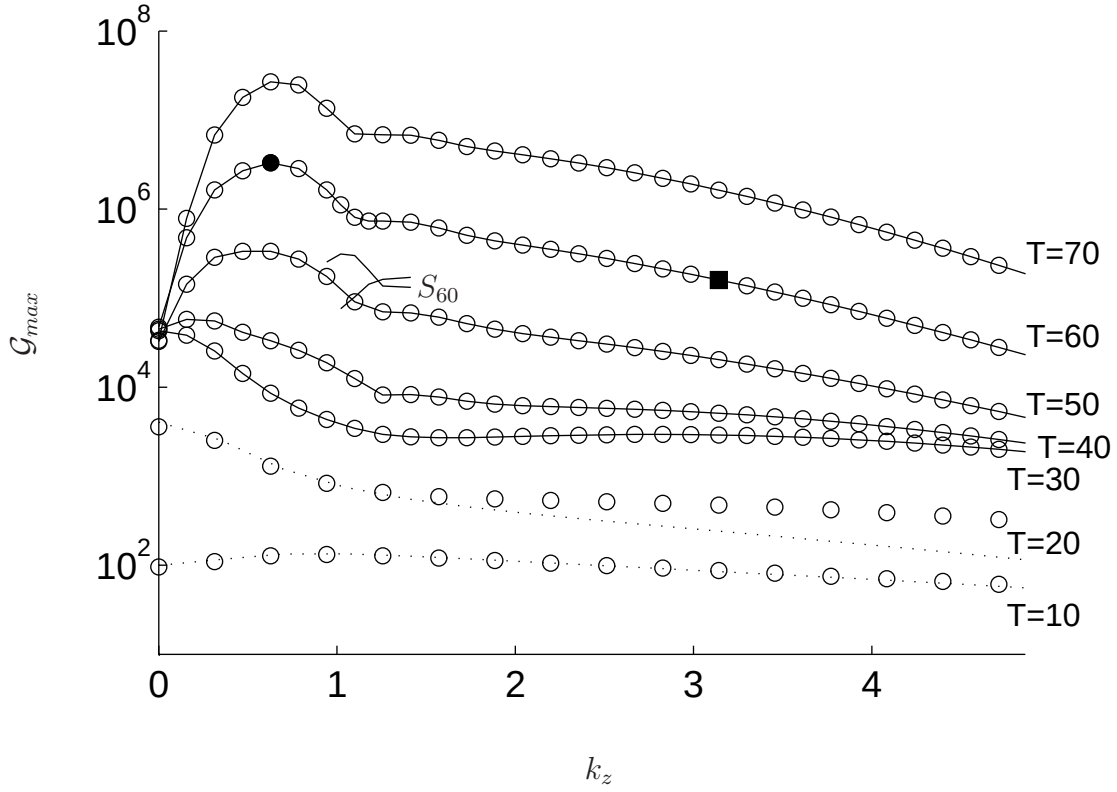

Figure 4.5: Optimal gain versus k_z for different optimization times as indicated on the figure with an optimization interval starting at $T_0 = 0$. For comparison the dotted lines show the results for $T = 10, 20$ of the primary instability presented on section 4.3. The (•) and the (■) signs on the $T = 60$ curve correspond respectively to the E-type and H-type perturbations subsequently described in more detail. For all curves, the $k_x = k_{KH} = 0.4425$, except for the dotted line for $T = 10$, where $k_x = 2k_{KH}$. The lines marked as S_{60} are segments of two subdominant branches for $T = 60$.

changes abruptly) and are indicated as S_{60} in the figure 4.5, showing that there is actually no cross-over involving the branch of the optimal perturbations. It turns out that for $T = 60$ (and plausibly for $T \gtrsim 50$) the leading branch and the corresponding optimal perturbations are strongly dependent on k_z in the region $1 \lesssim k_z \lesssim 1.8$, just after the peak. Since this time interval corresponds to times definitely longer than the saturation time, and so optimization intervals when the primary billow has definitely reached finite amplitude, analysis of perturbation structure both in this peaked area, and in the qualitatively different higher wavenumber tail is clearly of interest.

As already noted, the particular different types of perturbation (elliptical E-type or hyperbolic H-type) can be characterized by their spatial location and the relative vorticity distribution. Although the definition of being core-centred or braid-centred is naturally somewhat arbitrary, we have found it useful to consider how the fraction of spanwise vorticity with respect to total enstrophy i.e. $\int \omega_z^2 dV / \int |\boldsymbol{\omega}(t)|^2 dV$ varies for perturbations with different spanwise wavenumbers k_z, and different optimization intervals starting at $T_0 = 0$. This quantity is shown in figure 4.6 for the different optimization intervals starting at $T_0 = 0$. We expect E-type responses to be associated with relatively large spanwise ω_z components, while H-type perturbations should be associated with relatively large vertical ω_y (and to a lesser extent streamwise ω_x) components, which reflects directly in a lower ω_z fraction. Interpreted in this way, the data shown in the figure suggests that smaller k_z wavenumber perturbations may be E-type, while larger k_z wavenumber perturbations may well be H-type.

This suggestion is reinforced by consideration of the spatial compartmentalization of the perturbation kinetic energy. Once again, this is somewhat arbitrary, but we define the 'core' of the primary K-type billow to be the fluid included within an ellipse which best fits the contour containing the spanwise vorticity equal to or greater than 70% of the instantaneous maximum of the spanwise vorticity in the primary K-type billow. We then identify a particular optimal perturbation as being of core-centred E-type if 25% or more of the perturbation kinetic energy is contained within this 'core contour ellipse'. On the same figure 4.6, we plot with grey circles the fraction of the perturbation kinetic energy contained within this core contour ellipse, and mark with shading those perturbations which we identify as being of E-type (i.e. where this fraction is larger than 0.25). Over all the shown optimizing intervals (all starting at $T_0 = 0$) smaller spanwise wavenumbers k_z are then classified as being of E-type, while higher wavenumbers appear to be more plausibly described as being of H-type (particularly noticeably the higher k_z perturbations have virtually no kinetic energy in the primary K-type billow core).

To investigate in more detail whether these classifications are appropriate, we consider the development of four specific perturbations in detail. We describe the development of the optimal perturbation for $T = 60$ and $k_z = 0.628$, (wavenumber of the most amplified perturbation at $T = 60$) marked with a ($\bullet$) on figure 4.5, which within our classification we expect to be of elliptical E-type. This perturbation has very similar values of streamwise and spanwise wavenumbers ($(k_x, k_z) = (k_{KH}, 0.628)$) to the OL-type perturbation optimized over a short interval with $T = 20$ on the frozen parallel hyperbolic tangent flow ($(k_x, k_z) = (k_{KH}, 0.698)$) labelled as OLE and shown in figure 4.1. As we shall see, the early-time behaviour of the most amplified perturbation for the longer time interval with $T = 60$ actually has many points of similarity with the OLE perturbation. Since the higher wavenumber 'tail' is also of interest, and appears to be (at least potentially) of H-type, we also then consider a perturbation with $k_z = 5 * 0.628 = 3.142$ for the same

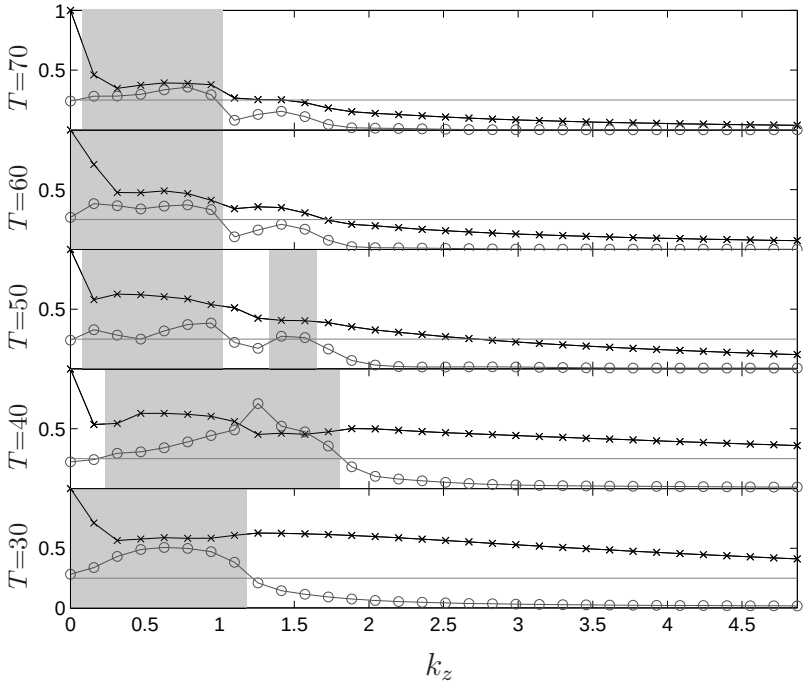

Figure 4.6: The black line with ($\times$) symbols shows the k_z dependence of the fraction of spanwise vorticity ω_z with respect to total enstrophy $\int \omega_z^2 dV / \int |\boldsymbol{\omega}(t)|^2 dV$ for the optimal responses from $T_0 = 0$. The grey line with $\circ$ symbols shows the energy fraction inside the ellipse that best fits the contour corresponding to 0.7 of the instantaneous maximum base flow vorticity. When this fraction is larger than 0.25 (shown with the grey horizontal line) we identify the response as being of E-type, which is shaded on the figure. Indicated on each plot is the final time T of the optimization interval.

optimizing interval i.e. with $T_0 = 0$ and $T = 60$, and compare it with the OLH perturation that has the same wavenumbers.

4.4.3 E-type response with maximum growth rate for $T_0 = 0$, $T = 60$

The optimal perturbation for $T = 60$ with $k_z = 0.628$ has the maximum gain over this time interval of all possible perturbations. However, since we have a complete numerical simulation of its evolution during this optimization interval, we can also identify the instantaneous growth rate of the perturbation at all times. Indeed, by consideration of the perturbation kinetic energy, it is straightforward to derive an

evolution equation for this growth rate. Taking the scalar product of $\mathbf{u}$ with the momentum equation (4.1a), integrating on the (x, y)-plane and arranging terms we have

$$\begin{aligned}\frac{dE}{dt} &= -\overbrace{\int uv\frac{\partial \bar{U}}{\partial y}\,\mathrm{d}x\mathrm{d}y}^{\text{Mean shear}} - \overbrace{\int uv\left(\frac{\partial U_{2D}}{\partial y}+\frac{\partial V_{2D}}{\partial x}\right)\mathrm{d}x\mathrm{d}y}^{\text{Shear 2D}} \\ &\quad \underbrace{-\int (u^2-v^2)\frac{\partial U_{2D}}{\partial x}\,\mathrm{d}x\mathrm{d}y}_{\text{Strain 2D}} \underbrace{- Re^{-1}\int \mathbf{u}\cdot\nabla^2\mathbf{u}\,\mathrm{d}x\mathrm{d}y}_{\text{Dissipation}},\end{aligned} \tag{4.14}$$

where we have introduced

$$\bar{U}(t) = \frac{1}{L_x}\int_0^{L_x} U(t)\,\mathrm{d}x, \tag{4.15a}$$

the streamwise-averaged (parallel but time varying) base flow and

$$(U_{2D}, V_{2D}, 0)^T = \mathbf{U}_{2D}(t) = \mathbf{U}(t) - \bar{U}\cdot\mathbf{e}_x \tag{4.15b}$$

is the inherently non-parallel 2D flow associated with the K-type billow. This decomposition shows that there are four contributions to the growth in the energy of the secondary 3D perturbation: energy extraction from the streamwise-averaged mean (parallel) shear via the Reynolds stress; energy extraction from the non-parallel shear associated with the primary K-type billow; energy extraction from the strain field associated with the primary K-type billow; and dissipation, which of course always acts as a sign-definite sink of perturbation kinetic energy. (See for example Caulfield & Peltier [29] for a more detailed discussion of this decomposition.)

In figure 4.7(a) we plot the instantaneous growth rate $\sigma(t)$ and these various components for the (presumed E-type) optimal perturbation for $T = 60$ with $k_z = 0.628$. Although this perturbation grows across the entire optimization interval, it is clear that the largest growth rate occurs at the beginning of the flow evolution. We also plot (with a dashed line) the instantaneous growth rate for the OLE perturbation until $t = 20$, essentially a replotting of the data shown in figure 4.2. Clearly the optimal perturbation behaves initially very similarly to the OLE perturbation (the corresponding dashed line being barely distinguishable from the thick line), and this strong initial growth is thus associated with a (transient) exploitation of the Orr and lift-up mechanisms before the primary K-type billow has rolled up. Unsurprisingly, in terms of energetics, the dominant driving mechanism is extraction from the streamwise-averaged shear, which though initially strongest, continues to occur throughout the subsequent (base flow) evolution when the primary billow has rolled up.

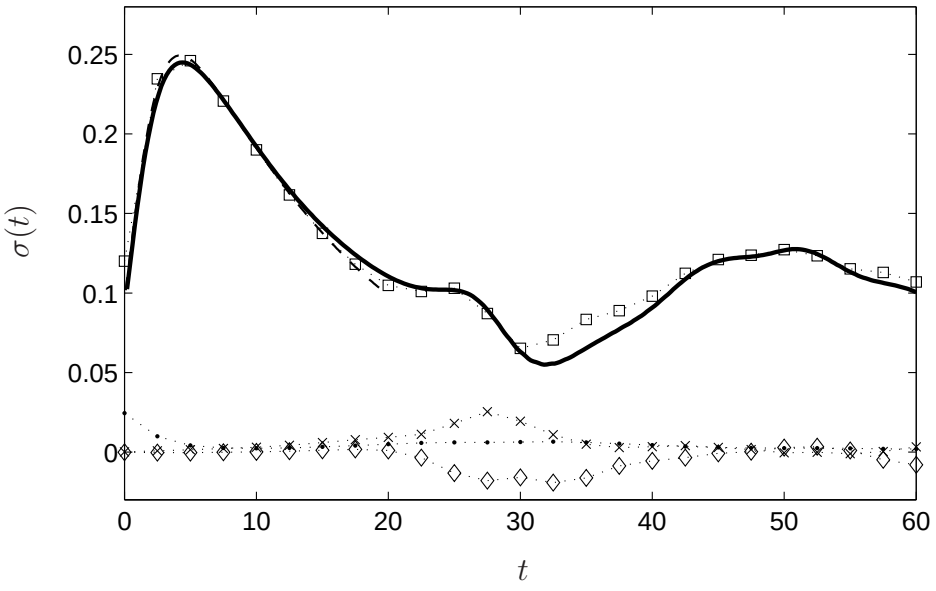

(a)

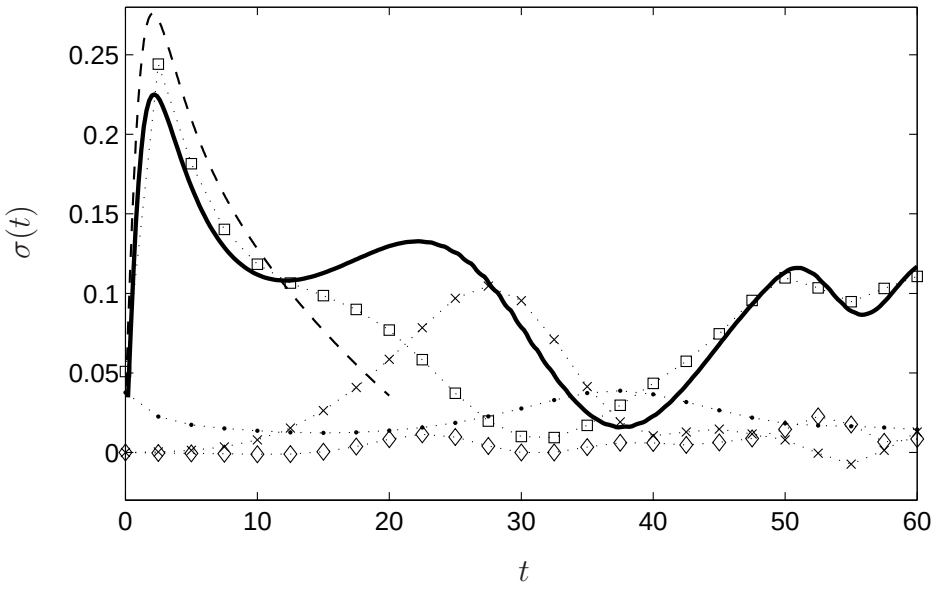

(b)

Figure 4.7: Instantaneous growth rate $\sigma(t)$ (thick continuous line, as defined in (4.13)), for the optimal perturbations from $t = 0$ to $t = 60$, $k_z = 0.628$ of the E-type mode in (a), and $k_z = 3.142$ of the H-type mode in (b). Dashed lines in (a) and (b) show respectively the growth rate of the OLE and OLH optimal perturbations of the frozen tanh profile for $T = 20$. Also shown are the dissipation ($\cdot$) and the growth rate contributions from the mean shear ($\Box$), the shear 2D ($\Diamond$) and the strain 2D ($\times$).

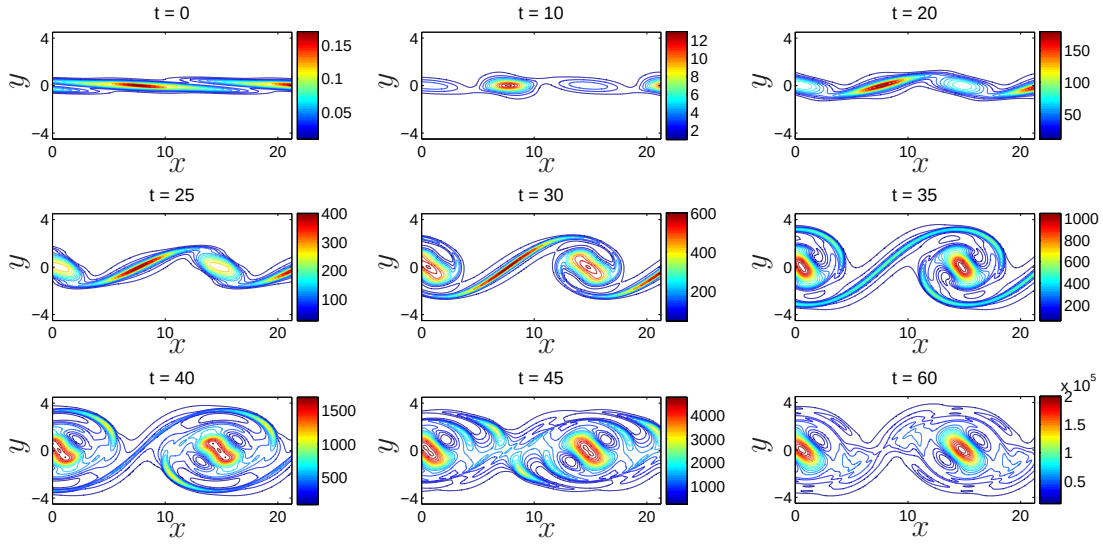

Figure 4.8: Scaled energy density of the optimal perturbation from $t = 0$ to $t = 60$ with $k_x = k_{KH}$ and $k_z = 0.628$ (E-type) at: a) $t = 0$; b) $t = 10$; c) $t = 20$; d) $t = 25$; e) $t = 30$; f) $t = 35$; g) $t = 40$; h) $t = 45$; i) $t = 60$. At $t = T_0 = 0$, the integral over the domain of the energy density is set to one.

Furthermore, the spatial distribution of the perturbation confirms that this perturbation is appropriately described as being of elliptical E-type. In figure 4.8, we plot contours of the energy density for this optimal perturbation at different times. The flow evolution is now clear. At early times, the perturbation is tilted 'into' the shear (as well as being periodically varying in the streamwise direction). Therefore, it is perfectly arranged to exploit the Orr and lift-up mechanisms to extract transient growth at early times from the quasi-parallel shear flow, almost exactly like the OLE perturbation discussed above and shown in figure 4.3, the main difference being that the early E-type perturbation has more energy in the braid. Since the base flow is now no longer streamwise-independent, there is now a preference for such a perturbation to grow within the strong strain field in the vicinity of the braid. As the billow rolls up further, this essentially braid-centred perturbation is then well-placed to perturb the billow core strongly, and trigger behaviour that is closely related to the idealized elliptical instability, and thus appropriately described as an E-type perturbation. The spanwise wavenumber of these perturbations is particularly well-suited to trigger an elliptical 'instability', consistently with the 'frozen-in-time' calculations of Klaassen & Peltier [68] and Caulfield & Peltier [29]. Loosely, the braid-centred perturbations have just the right wavenumber to make the elliptical core 'ring' with a translative/elliptical instability (as is apparent in the $t = 25$ and $t = 30$ panels) which then in turn grows strongly. Interestingly, as is apparent from figure 4.7(a),

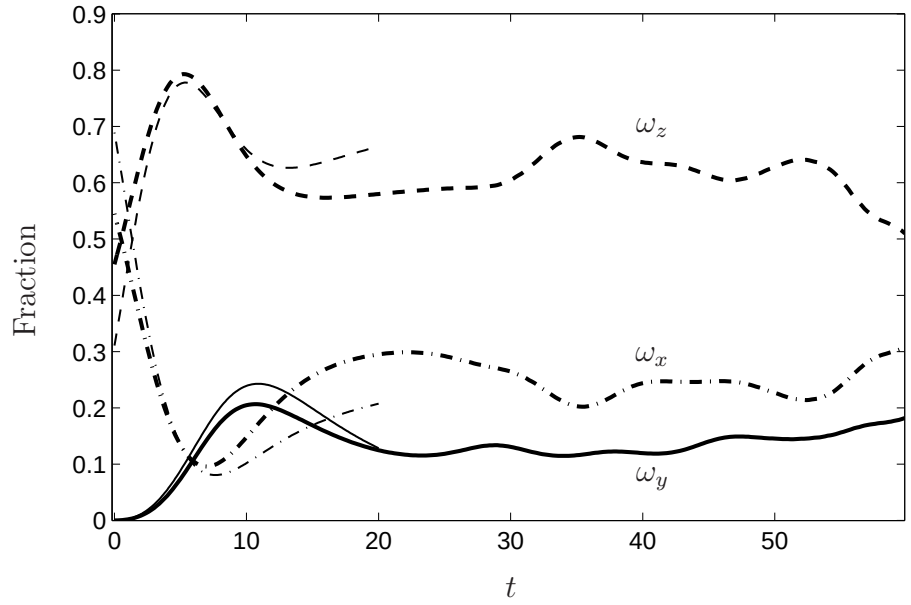

(a)

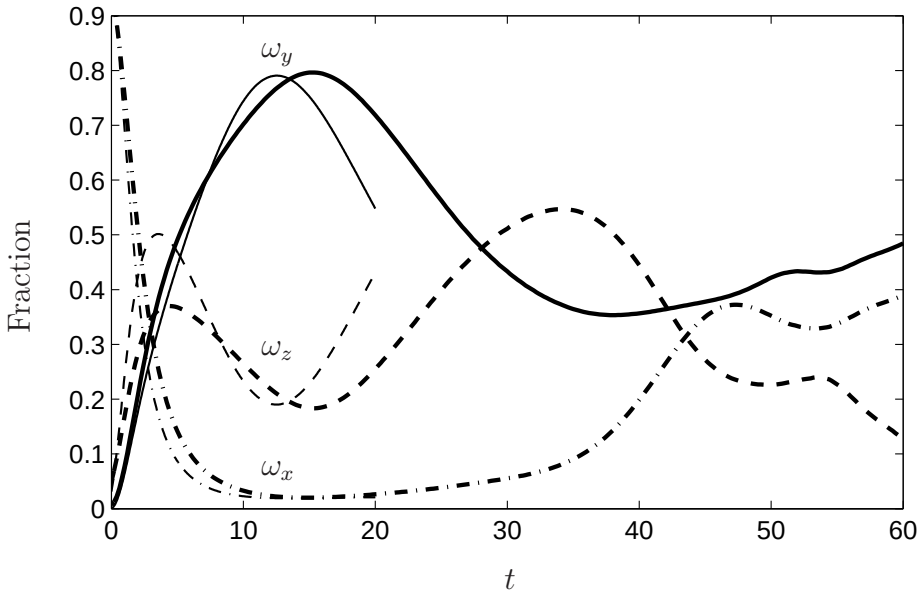

(b)

Figure 4.9: Evolution of the fraction of each vorticity component with respect to total enstrophy $\int \omega_i(t)^2 dV / \int |\boldsymbol{\omega}(t)|^2 dV$ for the optimal perturbation from $t = 0$ to $t = 60$ with $k_x = k_{KH}$, and $k_z = 0.628$ (E-type) in (a) and $k_z = 3.142$ (H-type) in (b). The continuous lines correspond to ω_y, the dashed lines correspond to ω_z and the dash-dotted lines correspond to ω_x. Also shown with thin lines extending up to $t = 20$ are the same quantities for the OLE (a) and OLH (b) optimal perturbations of the frozen tanh profile.

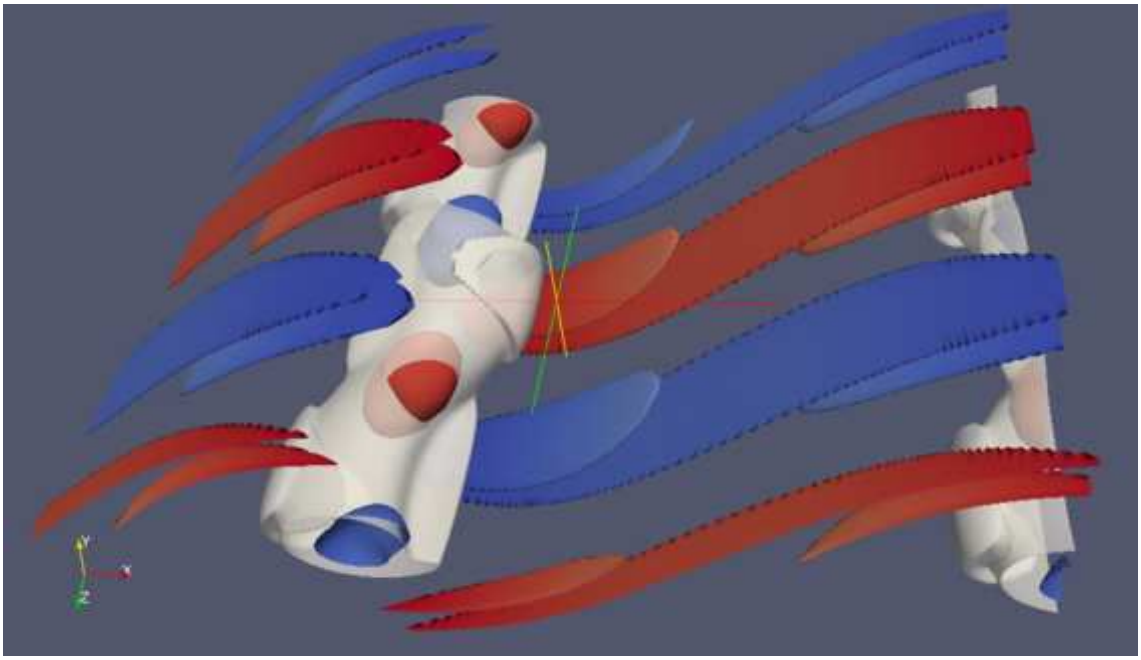

Figure 4.10: E-type optimal perturbation at time $t = 45$ superposed on the base flow. The perturbation amplitude is such that the maximum value of the ω_z vorticity (spanwise) is 0.4. The white semi-transparent contour corresponds to the isocontour $\omega_z = -0.9$. The red/blue contours correspond to $\sqrt{(}\omega_x^2 + \omega_y^2) = 0.2$, the coloring being given according to the magnitude of ω_x, red (resp. blue) color representing positive (negative) values of ω_x.

the time ($t \sim 30$) when the braid-centred perturbation is interacting with the core to trigger the more overtly E-type behaviour is actually associated with a relatively small value of the instantaneous growth rate σ (as defined in (4.13)), presumably due to the flow reorganising itself as it passes from one stage of perturbation growth to another.

This two-stage growth process is also confirmed by considering the time-evolution of the different components of vorticity for both this E-type perturbation, and the early-time OLE perturbation, as shown in figure 4.9(a). The evolution of the perturbation is always strongly dominated by spanwise vorticity, ω_z which is seeded by the early-time transient growth spurt associated with the mixture of the Orr and lift-up mechanisms experienced by the OLE perturbation on the parallel hyperbolic tangent shear flow, and is characteristic of elliptical or translative instabilities. Finally, this concept of an OL-type Orr/lift-up mixed perturbation developing in the braid that then perturbs the billow core is reinforced by considering the 3D rendering of the perturbation at $t = 45$, as shown in figure 4.10. This clearly shows that the

perturbation has a strong signal in the braid, which is wrapping around the core, leading to a 'ringing' of the primary billow core. This coupled structure is consistent with the quote from Rogers & Moser [88] presented in the introduction. However, it is important to appreciate that the spanwise wavenumber of this perturbation is too small to be consistent with the rib vortices numerically observed by Caulfield & Peltier [29] for example, and, of course, the perturbation shown in figure 4.10 has been calculated in a strictly linear regime.

Nevertheless, it appears that using the tools of non-modal stability theory leads to the natural identification of 'optimal' perturbations which have many of the characteristics of core-centred elliptical instabilities, with the added insight that such E-type perturbations are actually very strongly excited by OL-type behaviour at early times. This naturally raises the question as to how sensitive is the development of such E-type perturbations to the chosen start time T_0 for the optimization interval. We return to this question after considering the properties of the higher wavenumber H-type optimal perturbations.

4.4.4 H-type response for large k_z

The behaviour is, in many important aspects, qualitatively different for the perturbation at higher wavenumber, as shown in the figures 4.7(b), 4.11 and 4.9(b), equivalent to their E-type counterparts. Considering the instantaneous growth rate first, this perturbation also experiences an early-time enhanced growth from the Orr and lift-up mechanisms, extracting energy from the mean shear. The characteristic tilting over of the perturbation by the mean shear is clearly apparent in the early-time panels of figure 4.11 showing the energy density distribution of the perturbations. Initially, this growth is (naturally) dominated by energy extraction from the mean shear. However, the physical character of this perturbation is very different, as this early time evolution is dominated by the expected vertical vorticity ω_y as shown in figure 4.9(b). This is entirely consistent with a larger contribution from the lift-up mechanism that can be expected for this larger k_z, as described in section 4.3.

This structural difference ensures that the subsequent evolution (once the primary K-type billow is saturated) is also qualitatively different. There is a substantial and essential contribution to growth at times around $t \sim 30$ from the strain field, as these vertical vortices are stretched and tilted by the strain field at the hyperbolic points in the braid and wrapped around the primary billow cores. As is apparent in the later time energy panels (and through comparison with for example figures 7, 13 and 14 of Caulfield & Peltier [29]) this perturbation is strongly localized in the braid region, has much of the character of both the hyperbolic instability and also the finite amplitude development of rib vortices. Indeed, the spanwise wavenumber for this perturbation is much closer to that typically observed for rib vortices than

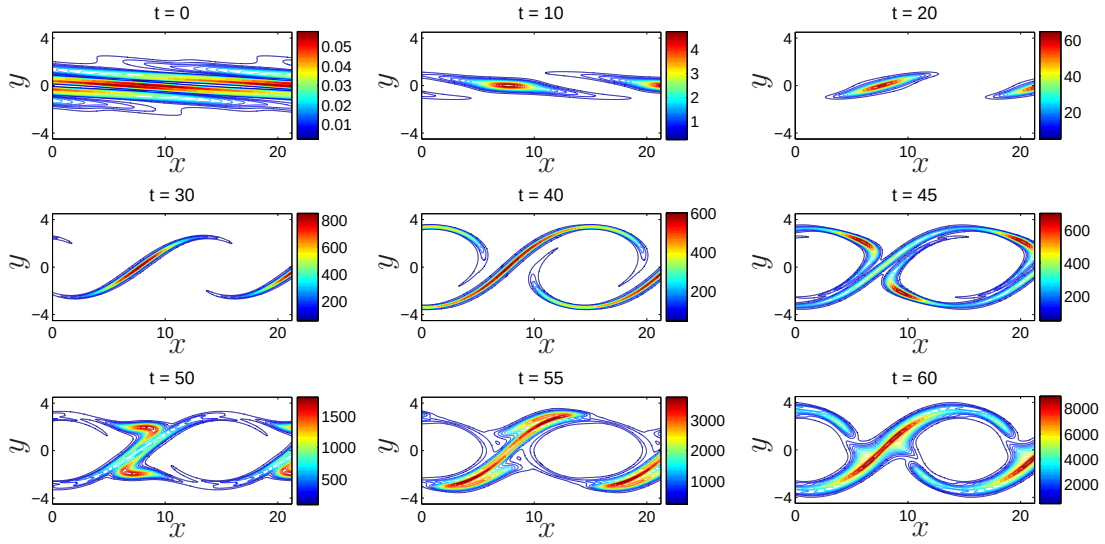

Figure 4.11: Scaled energy density of the optimal perturbation from $t = 0$ to $t = 60$ with $k_x = k_{KH}$ and $k_z = 3.142$ (H-type) at: a) $t = 0$; b) $t = 10$; c) $t = 20$; d) $t = 30$; e) $t = 40$; f) $t = 45$; g) $t = 50$; h) $t = 55$; i) $t = 60$. At $t = T_0 = 0$, the integral over the domain of the energy density is set to one.

for the optimal E-type perturbation discussed above. The wavenumber is also too large for the inevitable disruption of the core to trigger a significant E-type perturbation. The H-type perturbation does wrap around the core, as is shown in panels for $t \simeq 50$ of figure 4.11, when there is reinjection of vorticity associated with enhanced instantaneous perturbation growth rate σ (see figure 4.7(b)), but there is still no significant energy density for the perturbation in the elliptical core. This picture is further reinforced by considering the 3D rendering of this H-type perturbation at $t = 45$ (figure 4.12), which shows the much smaller wavelength of the streamwise vortices compared to those shown in figure 4.10, and the absence of any significant perturbation in the primary billow core.

Therefore, we believe that this perturbation can appropriately be described as being of H-type, although it is important to appreciate that as yet no causal relationship between this (inherently linear) perturbation and the profoundly nonlinear 'rib' vortices has been established. Nevertheless, it has been shown that E-type and H-type perturbations naturally arise from a non-modal optimal calculation, consistently (for the H-type perturbation at least) with previous simplified models (see for example Caulfield & Kerswell [28]). Furthermore, our calculations appear to suggest that the two types of perturbations are distinct classes of perturbations, utilizing qualitatively different growth mechanisms, both in terms of spatial vorticity and energy distribution and source of energy for growth. We now consider a time interval

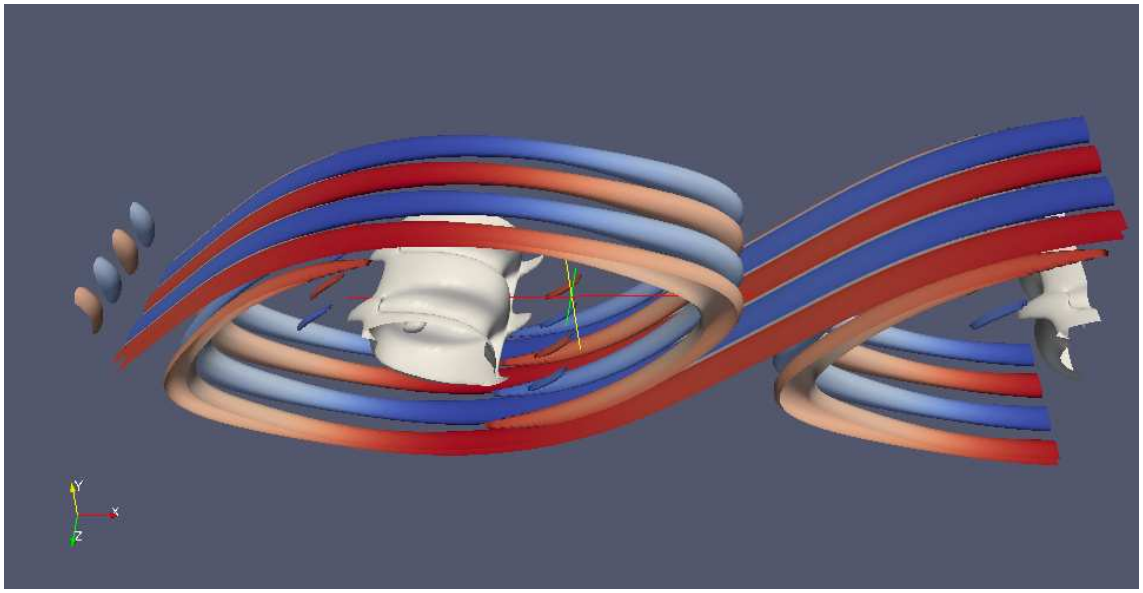

Figure 4.12: H-type optimal perturbation at time $t = 45$ superposed on the base flow. The perturbation amplitude is such that the maximum value of the ω_z vorticity (spanwise) is 0.4. The white contour corresponds to the isocontour $\omega_z = -0.9$. The red/blue contours correspond to $\sqrt{(}\omega_x^2+\omega_y^2) = 0.2$, the coloring being given according to the magnitude of ω_x, red (resp. blue) color representing positive (negative) values of ω_x.

with a later start time, (i.e. $T_0 > 0$) in an attempt to investigate how important the initial OL-type perturbation growth is to the ultimate character of the optimal perturbations.

4.5 Variation in optimization interval start time $T_0 \neq 0$

In this section we choose $T_0 = 20$, in an attempt to remove the influence of any initial period where the evolving base flow is close to parallel. As shown in figure 4.4, by $t \simeq 20$, the base flow is strongly non-parallel and nonlinear, though the primary K-type billow has not saturated at its maximum amplitude. Essentially repeating the analysis of section 4.4.2, in figure 4.13, we plot optimal gain against k_z for different final times T, for optimization intervals with start time $T_0 = 20$. By comparison with the equivalent figure 4.5 for optimizations with $T_0 = 0$, it is apparent that the gain is (unsurprisingly) reduced across all the wavenumbers, but most significantly for the relatively low-wavenumber peak which has now been

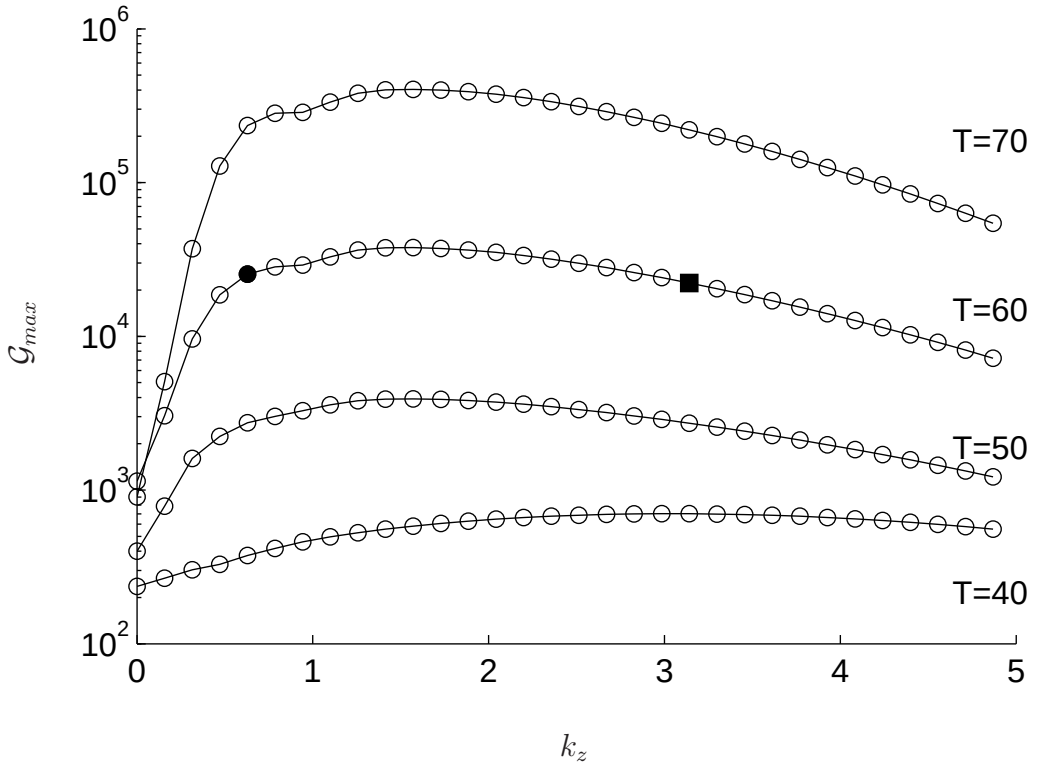

Figure 4.13: Optimal gain versus k_z for different optimization times as indicated on the figure, with an optimization interval starting at $T_0 = 20$. The (•) sign on the $T = 60$ curve corresponds to the E-type perturbation subsequently described in more detail. For all curves, $k_x = k_{KH} = 0.4425$.

identified as being characteristic of E-type perturbations. This is evidence that the strong growth associated with initial OL-type behaviour has been at least partially suppressed by removing the initial time period when the Orr and lift-up mechanisms are most efficient in causing energy gain.

4.5.1 E-type response

This picture of relative suppression of E-type behaviour is reinforced by consideration of the compartmentalization of kinetic energy and vorticity in figure 4.14. By comparison with the equivalent figure for $T_0 = 0$, (i.e. figure 4.6), it is clear that E-type behaviour is significantly rarer, and over much more of the wavenumber range both the vorticity and energy distributions have more of the characteristics of H-type perturbations. In particular, at the specific marked value of $k_z = 0.628$ for a perturbation optimized over the interval $20 \leq t \leq 60$, consideration of the instantaneous

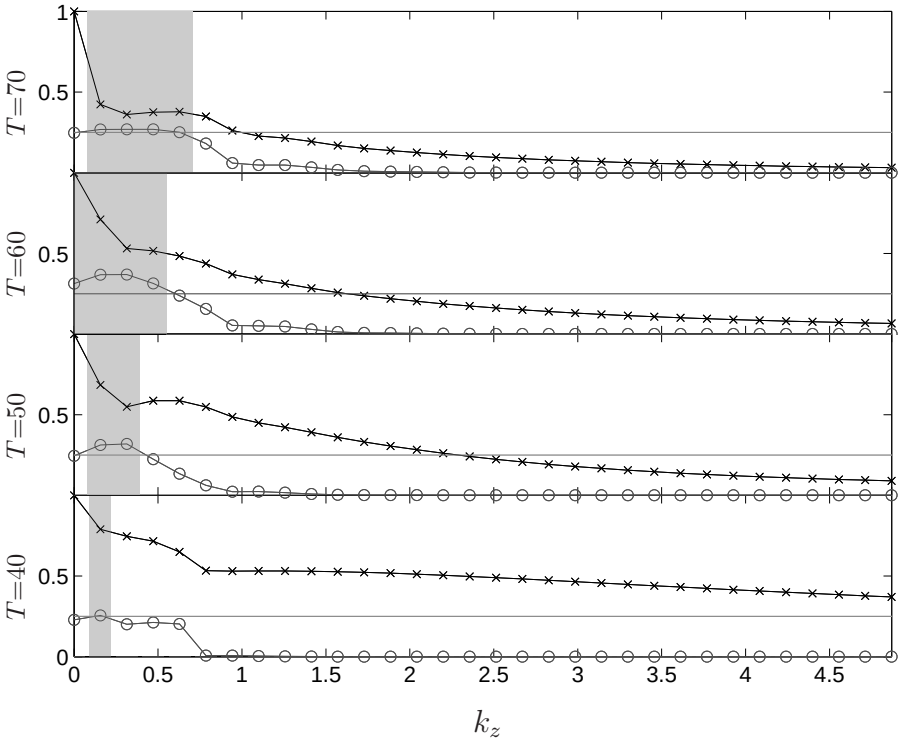

Figure 4.14: The black line with (×) symbols shows the k_z dependence of the fraction of spanwise vorticity ω_z with respect to total enstrophy $\int \omega_z^2 dV / \int |\boldsymbol{\omega}(t)|^2 dV$ for the optimal responses from $T_0 = 20$. The grey line with ∘ symbols shows the energy fraction inside the ellipse that best fits the contour corresponding to 0.7 of the instantaneous maximum base flow vorticity. When this fraction is larger than 0.25 (shown with the grey horizontal line) we identify the response as being of E-type, which is shaded on the figure. Indicated on each plot is the final time T of the optimization interval.

growth rate shown in figure 4.15, and the perturbation kinetic energy shown in 4.17 show that at least initially the perturbation has certain H-type aspects. After a substantially weaker (compared to the perturbation from a flow with $T_0 = 0$) initial Orr mechanism 'tilting', there is an early-time contribution to the growth rate from the strain field (around $t \simeq 20 - 30$). This contribution leads to much stronger energy density in the braids, which only eventually leads to strong perturbation energy in the billow core (by $t \simeq 60$) which is more characteristic of E-type behaviour. (There is once again a drop in instantaneous perturbation energy growth rate σ apparent in figure 4.15 as the perturbation starts to switch from being in the braid to being

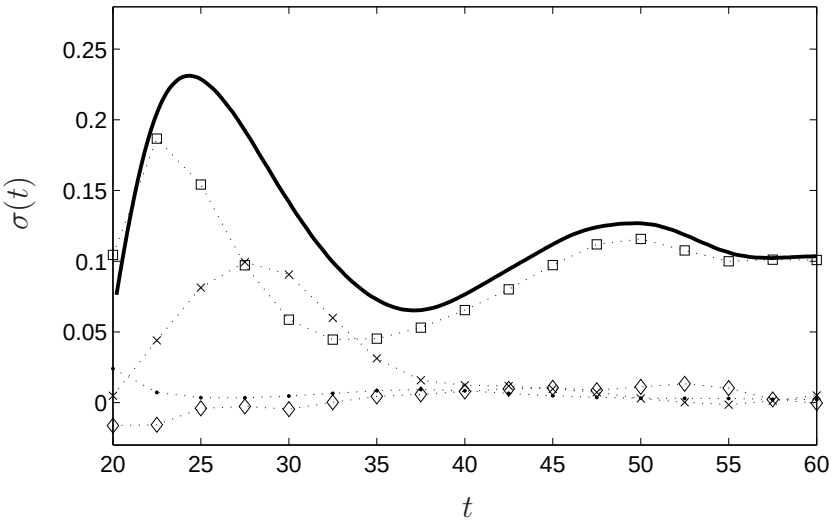

Figure 4.15: Instantaneous growth rate $\sigma(t)$ (thick continuous line, as defined in (4.13)) of the optimal perturbation from $t = 20$ to $t = 60$ and $k_z = 0.628$ of the E-type mode. Also shown are the dissipation ($\bullet$) and the growth rate contributions from the mean shear ($\square$), the shear 2D ($\lozenge$) and the strain 2D ($\times$).

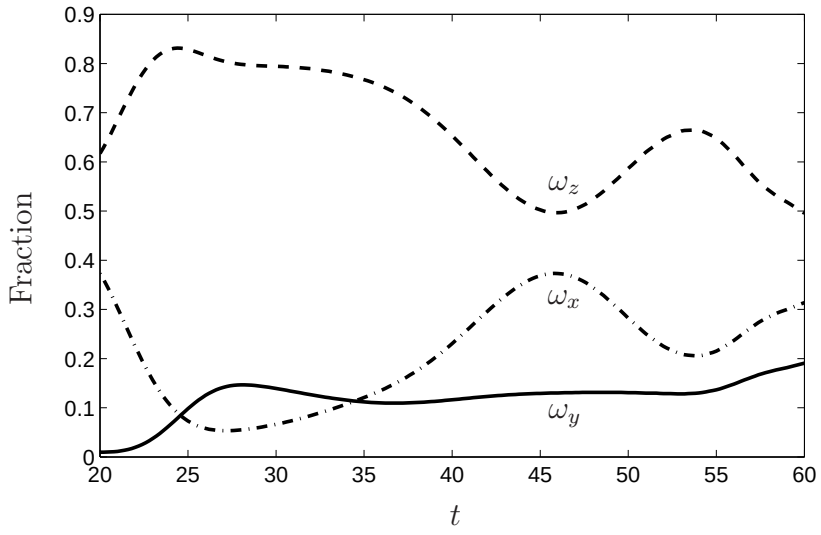

Figure 4.16: Evolution of the fraction of each vorticity component with respect to total enstrophy $\int \omega_i(t)^2 dV / \int |\boldsymbol{\omega}(t)|^2 dV$ for the optimal perturbation from $t = 20$ to $t = 60$ with $k_x = k_{KH}$ and $k_z = 0.628$ (E-type). Continuous line corresponds to ω_y, dashed to ω_z and dash-dotted line to ω_x.

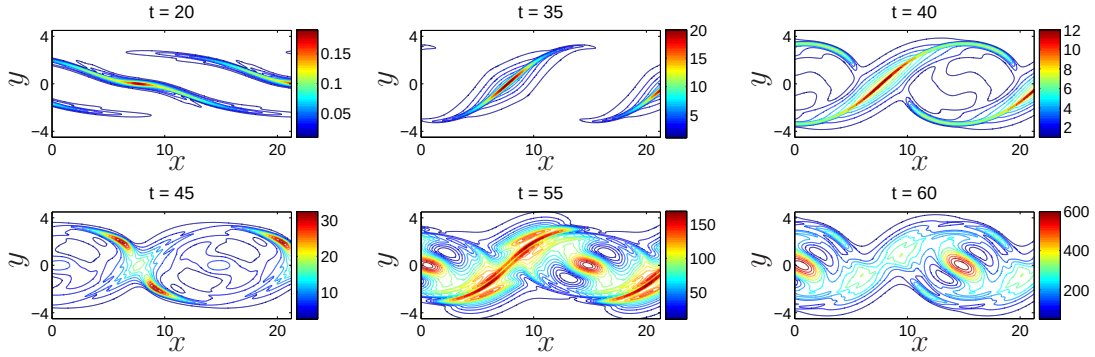

Figure 4.17: Scaled energy density of the optimal perturbation from $t = 20$ to $t = 60$ with $k_x = k_{KH}$ and $k_z = 0.628$ (E-type) at: a) $t = 20$; a) $t = 35$; a) $t = 40$; a) $t = 45$; a) $t = 55$; a) $t = 60$. At $t = T_0 = 20$, the integral over the domain of the energy density is set to one.

in the core.) This is consistent with our previous description that a key aspect of the development of an E-type perturbation is initially-braid-centred perturbations which couple with the billow core and hence trigger an elliptical/translative perturbation there. We believe it is still appropriate to identify this perturbation as of E-type due to the characteristic vorticity distribution shown in 4.16 (analogous to figure 4.9a), even though its fraction of energy within the core contour ellipse is just below our (frankly arbitrary) criterion, as shown in figure 4.14. It is clear that once again this relatively low wavenumber perturbation is strongly dominated by spanwise perturbation vorticity ω_z, indicative of the primary billow core perturbation characteristic of the elliptical instability or equivalently E-type perturbation behaviour.

4.5.2 H-type response

On the other hand, removing the early quasi-parallel flow evolution from the optimization interval does not have such a strong effect on the evolution of H-type perturbations, as is apparent from comparison of figures 4.18, 4.20 and 4.19 to their equivalents (for flows with $T_0 = 0$ i.e. figures 4.7(b), 4.11 and 4.9b). Considering the instantaneous growth rate first, as before the strain field makes a very strong contribution to the growth of the perturbation after an initial, brief extraction of energy from the mean shear via the Orr/lift-up mechanism. However, as time evolves, the perturbation remains strongly localized in the braid in the vicinity of the hyperbolic fixed point (unlike the E-type perturbation discussed above) and clearly has H-type character. This character is further confirmed by the vorticity compartmentalization

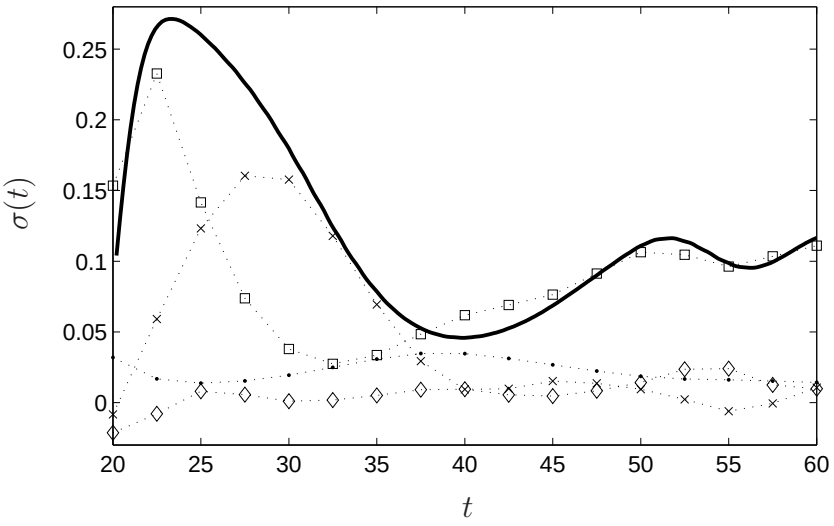

Figure 4.18: Instantaneous growth rate $\sigma(t)$ (thick continuous line) for the optimal perturbation from $t = 20$ to $t = 60$ and $k_z = 3.142$ of the H-type mode. Also shown are the dissipation ($\bullet$) and the growth rate contributions from the mean shear ($\square$), the shear 2D ($\lozenge$) and the strain 2D ($\times$).

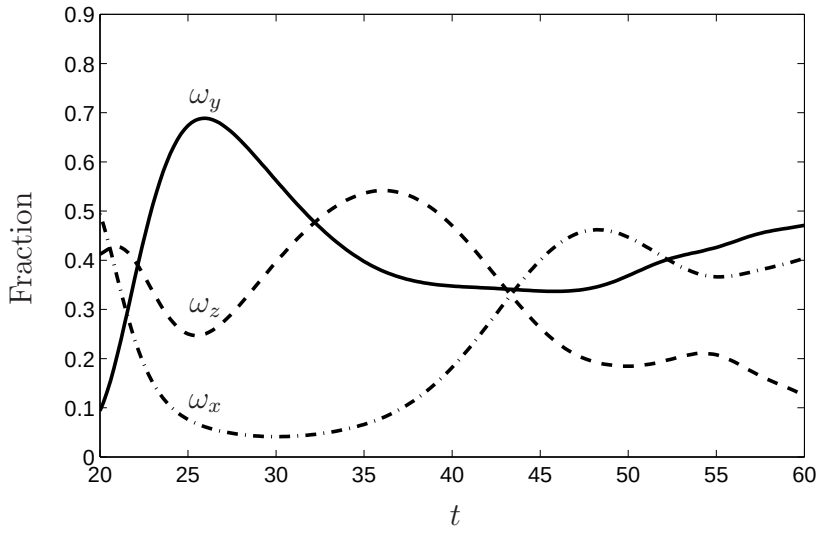

Figure 4.19: Evolution of the fraction of each vorticity component with respect to total enstrophy $\int \omega_i(t)^2 dV / \int |\boldsymbol{\omega}(t)|^2 dV$ for the optimal perturbation from $t = 20$ to $t = 60$ with $k_x = k_{KH}$ and $k_z = 3.142$ (H-type). Continuous line corresponds to ω_y, dashed to ω_z and dash-dotted line to ω_x.

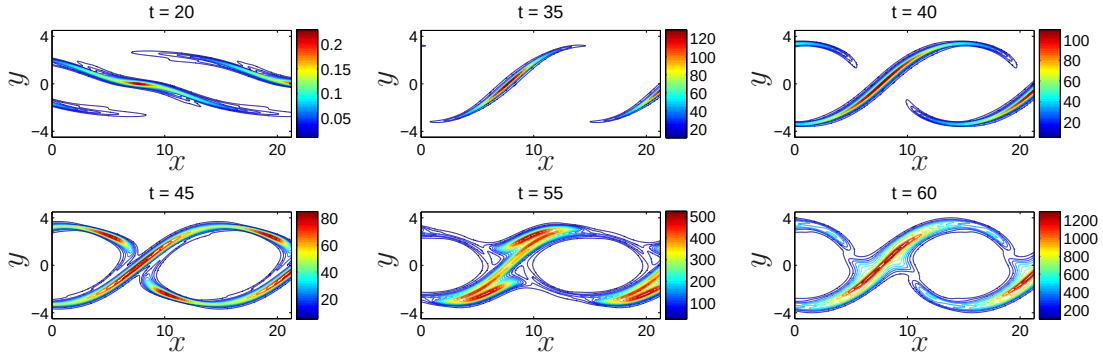

Figure 4.20: Scaled energy density of the optimal perturbation from $t = 20$ to $t = 60$ with $k_x = k_{KH}$ with $k_x = k_{KH}$ and $k_z = 3.142$ (H-type) at: a) $t = 20$; b) $t = 35$; c) $t = 40$; d) $t = 45$; e) $t = 55$; f) $t = 60$. At $t = T_0 = 20$, the integral over the domain of the energy density is set to one.

shown in figure 4.19, where the flow is initially dominated once again by vertical (cross-stream) vorticity ω_y which is then stretched and tilted by the braid-centred strain field. Therefore, removing the initial period from the optimization interval appears to have little qualitative effect on the H-type perturbations, and using non-modal stability theory, we appear to be able to identify optimal braid-centred perturbations which are very reminiscent in structure to the previously considered hyperbolic instability.

4.5.3 Anti-lift-up

Furthermore, by considering optimal perturbation growth on the flow from the time $T_0 = 20$, the central role of the hyperbolic region in the braid, even for development of ultimately core-centred E-type perturbations can be identified. In figure 4.21, we plot the velocity vectors in a streamwise plane for the initial time (i.e. at $T_0 = 20$) for both the optimal E-type perturbation (figure 4.21a) and the optimal H-type perturbation (figure 4.21b). In both cases, this initial perturbation is concentrated on the contracting manifold of the hyperbolic point in the braid between neighbouring billow cores and predominantly streamwise in the sense that it is locally aligned with the base flow velocity. For both perturbation types, this streamwise perturbation generates streamwise vortices on the instantaneously stretching manifold of the hyperbolic point, leading to a growth mechanism similar to the "anti-lift-up" mechanism recently discussed in Ortiz & Chomaz [83].

This mechanism is associated with a particular combination of convective non-normality (due to the transport of the perturbation by the base flow from one region

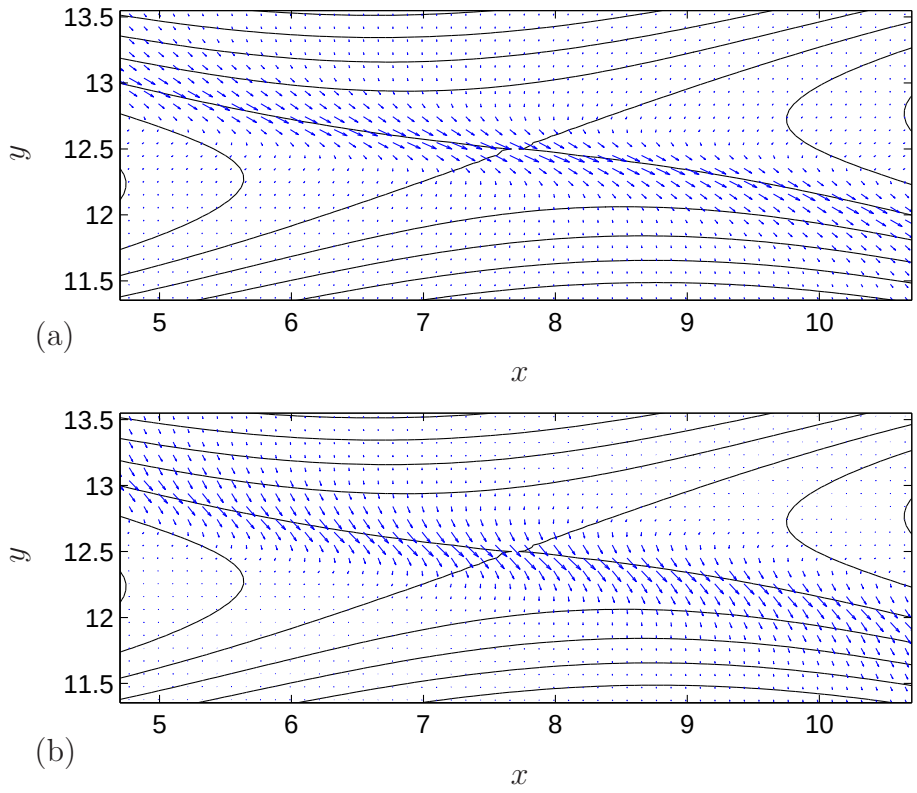

Figure 4.21: Velocity vectors in an $(x, y)-$plane for the initial condition of the optimal perturbations with $k_z = 0.628$ (E-type) in (a) and $k_z = 3.142$ (H-type) in (b). The black lines in (a) and (b) show instantaneous streamlines of the basic flow at the corresponding time $t = 20$.

to another) and tilting of the base flow vorticity by the perturbation. The difference here is that the cross-stream perturbation velocity is of the same order as the streamwise perturbation velocity, which possibly may be due to the facts that the base flow in the present case has somewhat different structure (with a strong vorticity sheet in the braid region) and is also evolving in time. In the E-type evolution (but not in the H-type evolution characterised by a significantly smaller spanwise wavelength), the spanwise wavelength of the E-type perturbation is sufficiently large for these streamwise vortices, created via the anti-lift-up mechanism, to induce a nontrivial displacement of the primary (evolving) billow core and excite an"elliptical" type of response of the core which eventually grows.

4.6 Conclusions

In this paper, we have investigated numerically the transient linear growth of three-dimensional perturbations in an homogeneous time-evolving shear layer, which are optimal in terms of their kinetic energy gain over a finite, predetermined time interval. We use the classic direct-adjoint looping method combined with power iteration to identify the optimal perturbations. We model the shear layer with an initial parallel velocity distribution $\mathbf{U}(y) = U_0 \tanh(y/d)\mathbf{e}_x$ with Reynolds number $Re = U_0 d/\nu = 1000$, where ν is the kinematic viscosity of the fluid. To understand whether the primary KH instability is essential to the transient perturbation growth, we have considered three different situations in detail. By use of a fictitious body force to counteract the effect of viscosity on the base flow shear layer, we are able to consider the transient finite Re perturbation growth in isolation of the primary KH billow growing. We then consider the transient growth, right from the start ($T_0 = 0$) of the roll-up of the primary billow, which initially involves a relatively short period when the time-evolving base flow is actually quite close to the (strictly) parallel frozen base flow. Finally, we consider an optimization from $T_0 = 20$ (the primary billow saturates at $t_{sat} = 35$) which essentially means that the base flow is strongly non-parallel throughout the optimization interval.

For short enough times, the most amplified perturbations on the frozen tanh profile are inherently three-dimensional, and are most appropriately described as hybrid or mixed perturbations which grow through a subtle combination of the lift-up and Orr mechanisms ('OL-type'), while for longer times, the optimal perturbations are two-dimensional, and are very similar to the KH normal mode, with a slight enhancement of gain due to extraction through the Orr mechanism (which we thus refer to as a K-type perturbation). However, for the two illustrative cases where we consider the time-evolving KH flow, we find that the structure of the predicted linear optimal perturbations depends crucially on the length and starting value of the optimizing time interval, as well as the particular spanwise wavenumber selected. If the time-evolving problem has an optimization interval which involves a base flow close in some sense to the initial parallel hyperbolic tangent shear flow for some non-trivial period, we find that hybrid OL-type perturbations continue to dominate over sufficiently short time intervals.

For longer time intervals however, which involve substantial evolution of the non-parallel primary KH billow into isolated elliptical vortices, we find two broad classes of inherently three-dimensional linear optimal perturbations, associated with different spanwise wavenumber. These two classes have clear points of similarity at low wavenumbers with the well-known core-centred elliptical instability as initially described by Waleffe [101], and at higher wavenumbers with the braid-centred hyperbolic instability, and so we refer to them as E-type and H-type perturbations respectively, as they have signatures associated with spanwise and vertical perturbation

vorticity respectively. We find that the H-type perturbation (at high wavenumber of the same order as that observed numerically by Caulfield & Peltier [29]) is relatively inefficient in extracting gain via the Orr and lift-up mechanisms.

However, the smaller wavenumber core-centred E-type perturbations are very efficient initially at extracting energy from the base flow by the Orr and lift-up mechanisms. Indeed, the flow evolution of such core-centred modes seems to pass through two stages. Initially OL-type behaviour occurs. Since in the time-evolving flow there is some structural differentiation between the braid and the core, this early-time OL-type behaviour is actually most strong in the braid. A spanwise-periodic structure develops there which then strongly perturbs the billow core, causing it to 'ring' and thus triggers vigorous E-type behaviour. When the start time of the optimization interval does not allow the OL-type hybrid perturbations much opportunity to grow, the dominant gain of the E-type perturbations is suppressed relative to the braid-centred H-type perturbations, essentially because the OL-type perturbation cannot grow so vigorously to trigger the core-centred E-type behaviour.

Nevertheless, we have demonstrated that non-modal stability analysis naturally recovers E-type and H-type perturbations in a time-evolving shear layer flow with qualitatively different growth mechanisms and spatial localizations. This implies that both types of secondary 'instabilities' can develop essentially independently. Since the relative significance of the H-type perturbations appears to increase as the start time T_0 of the optimization interval increases from zero, our results may be interpreted to suggest that the observed dominance of relatively high-wavenumber braid-centred rib vortices is associated with the secondary perturbations only starting to develop some time after the initial KH quasi-2D instability starts to grow.

However, the relevance of these linear calculations to such nonlinear flow evolution (and transition mechanisms) is of course not yet established. In particular, the observed dominance of such rib vortices may well be due to such structures being more well-suited to finite amplitude nonlinear energy extraction from the base flow, for example by nonlinear vortex stretching by the strain flow in the vicinity of the hyperbolic point in the braid. Further work is required involving careful direct nonlinear simulation to determine whether these non-modal stability calculations have identified realistic and relevant routes to transition. A particularly interesting question which could be investigated is whether OL-type perturbations, at sufficiently high amplitude could completely preclude the 'roll-up' of K-type KH billows, and thus, in some sense lead to 'bypass transition'. Alternatively, it would be very interesting to follow into the nonlinear regime the competition between E-type and H-type perturbations, or indeed their interaction with quasi-2D subharmonic merging instabilities, which we have deliberately suppressed in this paper by our choice of domain size.

Acknowledgements

Preliminary calculations on this problem were conducted by S. Iams for her M.Phil. at the BP Institute, University of Cambridge. The adjoint equations and the optimization algorithm were implemented on the version of the DNS code developed by Axel Deloncle. The Krylov method routine was adapted on a pre-existing version by Sabine Ortiz.

Chapter 5

Perturbation dynamics in stratified flows: The Craya-Herring frame

We introduce here the effect of density stratification, which is relevant to geophysical flows. By density stratification we refer to fluids with vertically dependent density and subject to a gravitational force. This situation leads to stratified flows, substantially different from unstratified flows in which the density is constant. When density decreases with height, the stratification is stable and gravity supplies a restoring force against vertical movements. We will consider only stable stratification.

A very important aspect of stratified fluids is the existence of waves. These are called internal gravity waves and their dynamics is of great interest [for reviews, see for example 96, 61]. Specially important are the interactions between waves and mean flows [21], which include mutual effects and mechanisms for wave generation and dissipation. Many theoretical studies of internal wave dynamics on mean flows use ray tracing equations relying on a slowly varying wavetrain assumption. This assumption allows for a separation of scales between short wavelengths and long scales for the envelope and mean flow variation length. Different aspects such as wave refraction, dispersion, critical and reflection levels can be consistently described with this description[96, 21, and references therein]. In a different approach, Andrews & McIntyre [3] developed the so-called generalized Lagrangian-mean theory. This is a hybrid theory that gives an Eulerian description of the flow fields, flow fields which are split in a Lagrangian-mean, obtained by averaging over particle positions, and a Lagrangian disturbance with zero average [21, 23]; among other results, this theory has allowed interesting formal results providing finite amplitude conservation laws for wave and vortex interactions [24, 22].

Assessing wave dynamics in a given flow requires the identification of the waves in that flow. When the slowly varying wavetrain assumption is made, waves are

well determined by construction. Similarly, in the generalized Lagrangian-mean theory, an identification between waves and the Lagrangian disturbance fields is often built-in. Identifying waves in a general case can be a difficult task and there is no generally valid way to do it; in some circumstances, one may even argue about whether the distinction makes any sense at all. This is arguably the case for (some) turbulent flows, for which the understanding of the role of waves is of great interest [72, 26, 87, 89]. In turbulence, the large complexity of the possible flow fields requires very general identification criteria; the large complexity is normally dealt with by focusing more on the statistics of flow realizations than on the full details. Leaving aside a quest for a definition of waves that remains valid in any possible context, the wave identification problem can be replaced, for completely general cases, by a well posed and physically motivated mathematical criteria. This can be done with the so-called Craya-Herring, or poloidal-toroidal decomposition to be detailed below; this decomposition is indeed used in studies of stratified turbulence [89, and references therein]. For the linear dynamics without basic flow, the Craya-Herring decomposition provides a separation of the velocity field in two parts, one of them corresponding exactly to the velocity field of internal waves. In other cases, the ability of such a decomposition for isolating what one can consider as "wave" can be only checked *a-posteriori*. In this chapter we use the Craya-Herring decomposition from a linear stability perspective. Assuming the price of an *a-priori* distinction, which is unavoidably uncertain, the Craya-Herring decomposition will allow us to deal with wave and vortex dynamics in very general terms.

We will consider the Craya-Herring decomposition of perturbations of an arbitrary horizontal two dimensional basic flow. To the best of my knowledge, the resulting equations are obtained here for the first time. We will make some comments on the structure of the resulting equations and their consequences for the energy of the perturbations. The application of the results will take place in the next chapter.

5.1 Governing equations

As is common in the literature, we will use the Boussinesq approximation [98]. The Boussinesq approximation involves considering density perturbations of a background density profile. The strength of the stratification depends on the gravity force and the gradient of the background density profile. With these two quantities one can define the Brunt-Väisälä frequency

$$N = \sqrt{-\frac{g}{\rho_0}\frac{\mathrm{d}\rho_b}{\mathrm{d}z}}, \tag{5.1}$$

where g is the acceleration of gravity, z is the vertical coordinate increasing upwards, $\rho_b(z)$ is the background density profile and ρ_0 is a reference value of the background density profile. We will consider constant Brunt-Väisälä frequency.

In the momentum equation under the Boussinesq approximation, leading to (5.2a,b) below, the presence of the density perturbations ρ is kept only when multiplied by gravity; that is the term that drives motion. The incompressibility condition remains and the density perturbation is advected by the flow and diffuses with a molecular diffusivity D. Thus, the linear dynamics of velocity $\mathbf{u} = (u_x, u_y, u_z)^T$ with vertical vorticity ω_z, viscosity ν and pressure p, perturbation of a horizontal basic flow $\mathbf{U} = U_x(x, y)\mathbf{e}_x + U_y(x, y)\mathbf{e}_y$with vorticity $\mathbf{\Omega} = \Omega\mathbf{e}_z = \nabla \times \mathbf{U}$, can be written as

$$\frac{\partial}{\partial t}\mathbf{u}_h = \mathbf{U} \times \omega_z\mathbf{e}_z + \mathbf{u}_h \times \mathbf{\Omega} - \nabla_h(p + \mathbf{u}_h{\cdot}\mathbf{U}) + \nu\nabla^2\mathbf{u}_h, \tag{5.2a}$$

$$\frac{\partial}{\partial t}u_z = -\left(\mathbf{U} \cdot \nabla\right) u_z - \frac{\partial p}{\partial z} - N^2\rho + \nu\nabla^2 u_z, \tag{5.2b}$$

$$\frac{\partial}{\partial t}\rho = -\mathbf{U} \cdot \nabla\rho + u_z + D\nabla^2\rho, \tag{5.2c}$$

$$\nabla \cdot \mathbf{u} = 0. \tag{5.2d}$$

In (5.2) and throughout this chapter, the sub-index h will refer to the horizontal components of an otherwise three dimensional entity, for example $\mathbf{u}_h = (u_x, u_y)^T$.

In the horizontal momentum equation (5.2a), the term $\mathbf{U} \times \omega_z\mathbf{e}_z$ represents the change in velocity induced by advection of ω_z by the base flow, and $\mathbf{u}_h \times \mathbf{\Omega}$ is the change in horizontal velocity induced by advection of Ω by the horizontal velocity of the perturbation. The quantity $\mathbf{u}_h{\cdot}\mathbf{U}$ inside the horizontal gradient in (5.2a) is the linearized version of $0.5\,(\mathbf{U} + \mathbf{u})^2$, sometimes called the dynamic pressure. In the density equation (5.2c), the term $-\mathbf{U} \cdot \nabla\rho$ describes advection of ρ by the base flow, and u_z mass transport from the background density profile. The term $N^2\rho$ in the vertical momentum equation (5.2b) accounts for the effect of gravity.

5.2 Craya-Herring frame

The three dimensional Fourier transform of each component of the velocity (or any scalar function) is defined as

$$\hat{a}(\mathbf{k}) = \int_{-\infty}^{\infty} e^{i\mathbf{k}\cdot\mathbf{x}} a(\mathbf{x})\, \mathrm{d}^3x. \tag{5.3}$$

The incompressibility condition (5.2d) in Fourier space reads

$$\mathbf{k} \cdot \hat{\mathbf{u}} = 0, \tag{5.4}$$

where $\hat{\mathbf{u}} = (\hat{u}_x, \hat{u}_y, \hat{u}_z)^T$ is the Fourier transform of the perturbation velocity $\mathbf{u}$. Constraint (5.4) means that $\hat{\mathbf{u}}(\mathbf{k})$ lies, for each $\mathbf{k}$, in a plane orthogonal to the wavenumber vector $\mathbf{k} = (k_x, k_y, k_z)^T$. Thus, constraint (5.4) can be satisfied by expressing the velocity vector $\hat{\mathbf{u}}$ in terms of two $\mathbf{k}$ dependent basis vectors which span the plane orthogonal to $\mathbf{k}$. With that in mind, one can define the basis of the so-called Craya-Herring (named after Craya [35] and Herring [63], see also [54, 89]), or poloidal-toroidal frame as

$$\mathbf{e}_1 = \frac{\mathbf{k} \times \mathbf{e}_z}{\|\mathbf{k} \times \mathbf{e}_z\|} = \frac{1}{k_h} \begin{pmatrix} k_y \\ -k_x \\ 0 \end{pmatrix}, \tag{5.5a}$$

$$\mathbf{e}_2 = \frac{\mathbf{k} \times (\mathbf{k} \times \mathbf{e}_z)}{\|\mathbf{k} \times (\mathbf{k} \times \mathbf{e}_z)\|} = \frac{1}{k k_h} \begin{pmatrix} k_z k_x \\ k_z k_y \\ -k_h^2 \end{pmatrix}, \tag{5.5b}$$

$$\mathbf{e}_3 = \frac{\mathbf{k}}{k} = \frac{1}{k} \begin{pmatrix} k_x \\ k_y \\ k_z \end{pmatrix}, \tag{5.5c}$$

where we have also introduced the total and horizontal wavenumber amplitudes respectively as $k \equiv \|\mathbf{k}\|$ and $k_h = \sqrt{k_x^2 + k_y^2}$. We assume here that $k, k_h \neq 0$. Written in terms of the orthonormal basis (5.5), the Fourier transform of the velocity vector reads

$$\hat{\mathbf{u}} = \phi_1 \mathbf{e}_1 + \phi_2 \mathbf{e}_2 \tag{5.6}$$

where

$$\phi_1 = \hat{\mathbf{u}} \cdot \mathbf{e}_1 = \frac{i}{k_h} \hat{\omega}_z, \tag{5.7a}$$

$$\phi_2 = \hat{\mathbf{u}} \cdot \mathbf{e}_2 = -\frac{k}{k_h} \hat{u}_z, \tag{5.7b}$$

and we have recovered the Fourier transformed vertical vorticity $\hat{\omega}_z = i k_x \hat{u}_y - i k_y \hat{u}_x$. Note that, as $\mathbf{e}_1$ is orthogonal to $\mathbf{e}_z$, the vertical velocity has no contribution on ϕ_1; this leads to an exact decoupling between ϕ_1 and internal gravity waves in the linear regime when there is no basic flow [87]. The other component $\phi_2 \mathbf{e}_2$ has a vertical projection and is dynamically coupled to buoyancy. We will thus identify $\phi_2 \mathbf{e}_2$ with gravity waves and we will refer to it as the gravity wave part of the velocity field. Conversely, $\phi_1 \mathbf{e}_1$ will be referred to as the vortical part. It must be kept in mind, however, that no such separation is rigorously possible in a general case. In particular, $\phi_2 \mathbf{e}_2$ can not satisfy a dispersion relation if no explicit time dependence is assumed. Despite these limitations, this is an objective wave-vortex distinction with a clear physical basis. A more precise, generally valid way to refer to the

components of the Craya-Herring decomposition is to call ϕ_1 and ϕ_2 respectively as the toroidal and poloidal components [89].

With the components of $\hat{\mathbf{u}}$ in the Craya-Herring basis, the horizontal velocity $\hat{\mathbf{u}}_h$ is split into 2 parts

$$\hat{\mathbf{u}}_h(\phi_1, \phi_2) = \hat{\mathbf{u}}_h^v(\phi_1) + \hat{\mathbf{u}}_h^w(\phi_2), \tag{5.8}$$

where $\hat{\mathbf{u}}_h^v$ is associated to the vertical vorticity and $\hat{\mathbf{u}}_h^w$ is horizontal velocity required to satisfy the incompressibility condition in the presence of vertical variability of vertical velocity (we assume $\hat{u}_z = 0$ for $k_z = 0$). Explicitly, decomposition (5.8) is

$$u_x = u_x^v + u_x^w = \frac{k_y}{k_h}\phi_1 + \frac{k_z k_x}{k k_h}\phi_2, \tag{5.9a}$$

$$u_y = u_y^v + u_y^w = -\frac{k_x}{k_h}\phi_1 + \frac{k_z k_y}{k k_h}\phi_2. \tag{5.9b}$$

From (5.9), we eliminate the $\hat{(\cdot)}$s to simplify notation. Using the definition of the gradients in fourier space as $\nabla \equiv i\mathbf{k}$ and $\partial_j \equiv ik_j$, the four relations implied by (5.9) can be summarized as

$$\mathbf{u}_h^v = \frac{1}{k_h}\mathbf{k} \times \phi_1 \mathbf{e}_z = \frac{1}{k_h^2}\nabla_h \times \omega_z \mathbf{e}_z, \tag{5.10a}$$

$$\mathbf{u}_h^w = \frac{k_z}{k k_h}\mathbf{k}_h \phi_2 = \frac{1}{k_h^2}\nabla_h \partial_z u_z. \tag{5.10b}$$

In this way, $\mathbf{u}_h^w$ is the gravity wave part of the horizontal velocity. The remaining horizontal velocity $\mathbf{u}_h^v$ corresponds to the vortical part (assuming $k_h \neq 0$).

From (5.10) it is clear that, in the horizontal plane, $\mathbf{u}_h^v$ is divergence free and $\mathbf{u}_h^w$ is irrotational. This fact suggests that through the $\mathbf{u}_h$ decomposition (5.8-5.10), ϕ_1 and ϕ_2 are related to the streamfunction and the velocity potential, well known of 2D flow. It is easy to verify that ϕ_1 is related to a two dimensional stream function ψ as

$$\psi = -\frac{i}{k_h}\phi_1, \tag{5.11a}$$

such that

$$(u_x^v, u_y^v) = (\partial_y \psi, -\partial_x \psi), \tag{5.11b}$$

and

$$k_h^2 \psi = \omega_z = -\Delta_h \psi. \tag{5.11c}$$

Similarly, the relation between ϕ_2 and the velocity potential Φ is

$$\Phi = \frac{i k k_h}{k_z}\phi_2, \tag{5.12a}$$

where

$$\mathbf{u}_h^w = \nabla_h \Phi, \tag{5.12b}$$

and

$$\Delta_h \Phi = \nabla_h \cdot \mathbf{u}_h^w. \tag{5.12c}$$

Naturally, the potential has the horizontal divergence as source.

Finally, defining $\phi_3 = N\rho$ we can arrange the whole dynamics in a single three dimensional vector field by defining

$$\mathbf{\Xi} \equiv \phi_1 \mathbf{e}_1 + \phi_2 \mathbf{e}_2 + \phi_3 \mathbf{e}_3 = \mathbf{u} + N\rho \mathbf{e}_3. \tag{5.13}$$

With this definition the spectral density of perturbation energy $\epsilon(\mathbf{k})$ is directly expressed as

$$2\epsilon(\mathbf{k}) = \phi_1^* \phi_1 + \phi_2^* \phi_2 + \phi_3^* \phi_3, \tag{5.14}$$

and the energy norm of the perturbation is defined as

$$E = \|\mathbf{\Xi}\| = \int \epsilon(\mathbf{k}) \, \mathrm{d}k_x \mathrm{d}k_y \mathrm{d}k_z \tag{5.15}$$

The simple form of (5.14) and (5.15) imply that the non-normality in the energy norm of the operator governing the time evolution of $\mathbf{\Xi}$, should appear explicitly on its matrix representation.

5.3 Perturbation dynamics in the Craya-Herring frame

The divergenceless part of the momentum equations (5.2a,b) reads in Fourier space

$$\frac{\partial \mathbf{u}}{\partial t} = \begin{pmatrix} U_y * \omega_z + \Omega * u_y \\ -U_x * \omega_z - \Omega * u_x \\ -i(U_x * k'_x u_z + U_y * k'_y u_z) \end{pmatrix} - \begin{pmatrix} ik_x \\ ik_y \\ 0 \end{pmatrix} \mathbf{U} \bullet \mathbf{u}_h - N^2 \rho \mathbf{e}_z - \nu k^2 \mathbf{u}, \tag{5.16}$$

where the vertical wavenumber enters through the argument of $\mathbf{u}$ and ρ, and in $k^2 = k_x^2 + k_y^2 + k_z^2$. The convolution operation $*$ between two fields $a(\mathbf{k})$ and $b(\mathbf{k})$ is defined as

$$(a * b)(\mathbf{k}) = \int a(\mathbf{k} - \mathbf{k}') b(\mathbf{k}') \, \mathrm{d}^2 k'_h = \int a(\mathbf{k}') b(\mathbf{k} - \mathbf{k}') \, \mathrm{d}^2 k'_h, \tag{5.17}$$

where $\mathrm{d}^2 k'_h = \mathrm{d}k'_x \mathrm{d}k'_y$. Here the integrals are two dimensional because convolutions involve the base flow assumed to have 2D dependence only. We have similarly defined the bullet sign $\bullet$ as

$$\mathbf{a} \bullet \mathbf{b} = \int \mathbf{a}(\mathbf{k} - \mathbf{k}') \cdot \mathbf{b}(\mathbf{k}') \, \mathrm{d}^2 k'_h = a_i * b_i, \tag{5.18}$$

sum over repeated indices being implied unless stated otherwise. The $\bullet$ operation is thus the expression in Fourier space of the inner product between vector fields in physical space. Primed variables as in (5.16) will be mute variables involved in the convolution, that is $U_x * k'_x u_z \equiv [U_x * \{k'_x u_z(\mathbf{k}')\}](\mathbf{k}) = U_x * u_z k'_x$, which is different from $k'_x U_x * u_z = (k'_x U_x) * u_z$; with this convention, k'_x behaves like a constant constrained to remain on one side of the convolution. We will reserve unprimed $\mathbf{k}$ and its components as the expression main tag, for example $k_x U_x * k'_h \phi_1 = k_x (U_x * k'_h \phi_1) \neq (k''_x U_x) * k'_h \phi_1$. As suggested by this very last expression, double and single prime will be used in the presence of two mute variables (each concerning a different side of the convolution).

The linearized Navier-Stokes equations under the Boussinesq approximation for ϕ_1 and ϕ_2, can be obtained by taking the inner products of equation (5.16) with $\mathbf{e}_1$ and $\mathbf{e}_2$, respectively; this is performed in detail in appendix A, in which there is also some extra discussion. The equation for ϕ_3 is obtained directly from (5.2c) by replacing ρ and u_z in terms of ϕ_3 and ϕ_2. Assuming for simplicity that the diffusivity D of the scalar ρ is equal to the viscosity ν (this is straightforwardly reverted by replacing ν by D in the diffusive term of the ϕ_3 equation), the resulting equations for $\boldsymbol{\Xi} = (\phi_1, \phi_2, \phi_3)^T$ are

$$\frac{\partial}{\partial t}\boldsymbol{\Xi} = \mathcal{L}\boldsymbol{\Xi} - \nu k^2 \boldsymbol{\Xi}. \tag{5.19a}$$

with (see appendix A for derivation)

$$\mathcal{L} = \begin{pmatrix} A_{k_h} + B_{k_h} & k_z C^{\Omega}_{1|k} & 0 \\ k_z \left(W_X - C^{\Omega}_{k|1} \right) & A_{k/k_h} + k_z^2 B_{k k_h} & \frac{k_h}{k} N \\ 0 & -\frac{k_h}{k} N & A_1 \end{pmatrix}, \tag{5.19b}$$

where the operators $A_{a(\mathbf{k})}$, $B_{b(\mathbf{k})}$ and $C^{\Omega}_{a(\mathbf{k})|b(\mathbf{k})}$ are defined according to their action on ϕ as

$$A_{a(\mathbf{k})}\phi = -\frac{i}{a(\mathbf{k})} \mathbf{U} \bullet \mathbf{k}'_h a(\mathbf{k}') \phi, \tag{5.20a}$$

$$B_{b(\mathbf{k})}\phi = \frac{i}{b(\mathbf{k})} k''^2_h \mathbf{U} \bullet \mathbf{k}'_h \frac{\phi}{b(\mathbf{k}')}, \tag{5.20b}$$

$$C^{\Omega}_{a(\mathbf{k})|b(\mathbf{k})}\phi = \frac{1}{a(\mathbf{k})} \frac{\mathbf{k}_h}{k_h} \cdot \left(\Omega * \frac{\mathbf{k}'_h}{k'_h} \frac{\phi}{b(\mathbf{k}')} \right), \tag{5.20c}$$

and (see also appendix B)

$$W_X \phi_1 = -\frac{1}{k k_h} \left[\Omega * k'_h + i \mathbf{U} \bullet (k_h^2 - k'^2_h) \left(\mathbf{k}' \times \frac{\mathbf{e}_z}{k'_h} \right) \right] \phi_1 \tag{5.21}$$

The role of the viscous terms in (5.19a) is well known, it represents diffusion and we will make no further consideration in what follows. Also known are the terms $\pm N k_h/k$ in (5.19b) which account for internal gravity waves.

The action of the operator $A_{a(\mathbf{k})}$ on ϕ, defined in (5.20a), implies advection of the quantity $a(\mathbf{k})\phi$ by the base flow; it will thus be called the advection operator. The action of the operator $B_{b(\mathbf{k})}$ on ϕ, defined in (5.20b), represents the self-induced reaction of ϕ to the base flow momentum transport it produces; it can be referred to as the base flow transport operator. The action of the operator $C^{\Omega}_{a(\mathbf{k})|b(\mathbf{k})}$ and its distribution within $\mathcal{L}$ represent, as we shall see, an effective Coriolis force induced on the perturbation by the advection of Ω by the perturbation; the $C^{\Omega}_{a(\mathbf{k})|b(\mathbf{k})}$ operator defined in (5.20c) will be called then the Coriolis operator. Finally, the operator W_X applies only on the vortical part ϕ_1 and excites the wave part ϕ_2; we will call W_X the wave exciting operator. We note in advance that the relevance of this operator is not limited to the excitation of waves by the vortical part; it plays an important role when the wave part ϕ_2 excites the vortical part ϕ_1.

In the remaining of this chapter and the next, some aspects of the structure of $\mathcal{L}$ and the role of the different terms should become clear. The wave exciting operator $W_X\phi_1$ (5.21) is expressed in a simpler form in terms of $\mathbf{u}^v_h$ (5.10a) as

$$W_X\phi_1 = -\frac{i}{kk_h}\left(\Omega * \omega_z + \mathbf{U}\bullet\nabla^2\mathbf{u}^v_h - \nabla^2(\mathbf{U}\bullet\mathbf{u}^v_h)\right). \tag{5.22}$$

To complete, we may add the effect of the Coriolis operator to provide similar expressions for the full effect of the vortex part ϕ_1 on the wave part ϕ_2, that is

$$\begin{aligned} k_z(W_X - C^{\Omega}_{k|1})\phi_1 = &-\frac{ik_z}{kk_h}\left[\Omega * \omega_z + \mathbf{U}\bullet\nabla^2\mathbf{u}^v_h - \nabla^2(\mathbf{U}\bullet\mathbf{u}^v_h)\right] \\ &-\frac{ik_z}{kk_h}\left[\Omega * \omega_z + \mathbf{u}^v_h\bullet\nabla^2\mathbf{U}\right] \end{aligned} \tag{5.23}$$

The terms of the Coriolis operator $k_z C^{\Omega}_{k|1}\phi_1$ can be read on the second line of (5.23). The $k_z(W_X - C^{\Omega}_{k|1})\phi_1$ terms have their origin on pressure, as detailed in the appendix B.

5.3.1 Rotating case and the Coriolis operator in $\mathcal{L}$

We can gain some insight on the structure of $\mathcal{L}$ by considering the rotating case. If the frame of reference rotates with angular velocity $f\mathbf{e}_z/2$ and the pressure is assumed to balance the centrifugal force, the modification of the Navier-Stokes equations (5.2) reduces to replacing Ω by $\Omega + f$ in (5.2a). It follows directly that the corresponding change in the expression for $\mathcal{L}$ reduces to replacing $C^{\Omega}_{a|b}$ by $C^{\Omega+f}_{a|b}$ in

(5.19b), while leaving the rest unchanged[1]. That is, if $\mathcal{L}_f$ is the equivalent of $\mathcal{L}$ in the rotating case, we have

$$\mathcal{L}_f = \begin{pmatrix} A_{k_h} + B_{k_h} & \frac{k_z}{k_h}\mathbf{k}_h \cdot \left([\Omega + f] * \frac{\mathbf{k}'_h}{k' k'_h} \right) & 0 \\ -\frac{k_z}{k k_h}\mathbf{k}_h \cdot \left([\Omega + f] * \frac{\mathbf{k}'_h}{k'_h} \right) + k_z W_X & A_{\frac{k}{k_h}} + k_z^2 B_{k k_h} & \frac{N k_h}{k} \\ 0 & -\frac{N k_h}{k} & A_1 \end{pmatrix}, \quad (5.24)$$

where $A_{a(\mathbf{k})}, B_{b(\mathbf{k})}$ and W_X are as given by (5.20a), (5.20b) and (5.21), respectively. This hints at interpreting those non diagonal terms as a non-uniform background rotation. This is a partial analogy because non-uniform background rotation would produce some extra modifications in $\mathcal{L}$.

The assimilation of those non diagonal terms to background rotation suggests that they are not an important source of non-normality. This can be made explicit by considering the case without base flow, $\mathbf{U} = 0$. If we consider

$$\phi_1 = \eta_1, \ \phi_2 = -\eta_2 \ \text{ and } \ \phi_3 = i\eta_3, \quad (5.25)$$

we obtain

$$\frac{\partial}{\partial t}\begin{pmatrix} \eta_1 \\ \eta_2 \\ \eta_3 \end{pmatrix} = i \begin{pmatrix} 0 & i\frac{k_z}{k} f & 0 \\ -i\frac{k_z}{k} f & 0 & -\frac{k_h}{k} N \\ 0 & -\frac{k_h}{k} N & 0 \end{pmatrix} \begin{pmatrix} \eta_1 \\ \eta_2 \\ \eta_3 \end{pmatrix}, \quad (5.26)$$

which is in explicitly Hermitian form, as it was discussed by Bartello [12]. In (5.26), the f-terms in the upper left half are responsible for inertial waves.

5.4 Energy evolution equation

From the expression for the energy density (5.14) follows that

$$\frac{\partial \epsilon}{\partial t} = \frac{1}{2}\boldsymbol{\Xi}^* \cdot \frac{\partial \boldsymbol{\Xi}}{\partial t} + c.c. \quad (5.27)$$

Using equation (5.19) for $\partial\boldsymbol{\Xi}/\partial t$ and integrating on the horizontal plane we have for the energy norm (5.15)

$$\frac{\partial E}{\partial t} = \int \mathrm{Re}[\overbrace{\phi_1^* A_{k_h}\phi_1 + \phi_2^* A_{k/k_h}\phi_2 + \phi_3^* A_1 \phi_3}^{\text{Advection terms}} + \overbrace{\phi_1^* B_{k_h}\phi_1 + k_z^2 \phi_2^* B_{k k_h}\phi_2}^{\text{Base flow transport}} + \underbrace{k_z(\phi_1^* C_{1|k}\phi_2 - \phi_2^* C_{k|1}\phi_1)}_{\substack{\text{Coriolis terms} \\ \text{(inertial waves)}}} + \underbrace{k_z \phi_2^* W_X \phi_1}_{\substack{\text{Non-normal} \\ \text{wave-vortex}}} + \underbrace{F_h^{-1}\frac{k_h}{k}(\phi_2^*\phi_3 - \phi_3^*\phi_2)}_{\text{Gravity waves}}] \, \mathrm{d}^2 k_h. \quad (5.28)$$

[1]That can be checked in the derivation of appendix A, in particular, in how including the f term modifies (A.1), (A.7) and (A.21).

The first line of (5.28) shows the energy contribution from the diagonal terms. Of those, the density advection term $A_1\phi_3$ does not contribute to energy changes. In the second line, the gravity waves terms produce no net contribution to perturbation energy; each of those terms accounts for energy transfers between kinetic and potential energy.

Let's consider the energy contributed through the Coriolis terms. The contribution to the total energy in the vortical part ϕ_1 is given by

$$\int \phi_1^* C^{\Omega}_{1|k}\phi_2 \,\mathrm{d}^2k_h = \int \phi_1(\mathbf{k})^*\Omega(\mathbf{k}_h-\mathbf{k}'_h)\phi_2(\mathbf{k}')\frac{\mathbf{k}_h\cdot\mathbf{k}'_h}{k_h k'_h k'}\,\mathrm{d}^2k'_h\mathrm{d}^2k_h, \tag{5.29a}$$

$$= \int \phi_1(\mathbf{k})^*\Omega(\mathbf{k}'_h-\mathbf{k}_h)^*\phi_2(\mathbf{k}')\frac{\mathbf{k}_h\cdot\mathbf{k}'_h}{k_h k'_h k'}\,\mathrm{d}^2k'_h\mathrm{d}^2k_h, \tag{5.29b}$$

$$= \int [\phi_2(\mathbf{k}')^*\Omega(\mathbf{k}'_h-\mathbf{k}_h)\phi_1(\mathbf{k})]^*\,\frac{\mathbf{k}_h\cdot\mathbf{k}'_h}{k_h k'_h k'}\,\mathrm{d}^2k_h\mathrm{d}^2k'_h, \tag{5.29c}$$

$$= \left[\int \phi_2^* C^{\Omega}_{k|1}\phi_1 \,\mathrm{d}^2k'_h\right]^*. \tag{5.29d}$$

Here we used the definition of $C^{\Omega}_{a|b}\phi$ (5.20c) twice and the reality condition $\Omega(\mathbf{k}_h) = \Omega(-\mathbf{k}_h)^*$ for getting (5.29b). The resulting term (5.29d) is minus the complex conjugate of the energy evolution term $-\phi_2^* C_{k|1}\phi_1$ in (5.28), corresponding to the Coriolis term effect on ϕ_2. As the contribution to the energy evolution is given by the real part of (5.29), the Coriolis terms in (5.28) cancel each other. Therefore, Coriolis terms give no net contribution to perturbation energy. Coriolis terms account for energy exchanges between ϕ_1 and ϕ_2, same as inertial waves. This result strongly reinforces the assimilation of the $C^{\Omega}_{a|b}$ operators to Coriolis forces.

As a consequence of the conservative nature of the wave terms in the second line of (5.28), the wave exciting term W_X accounts for all growth in perturbation energy that involves the product of ϕ_1 and ϕ_2.

5.4.1 Parallel shear flow

Approaching our main subject, we consider here a base flow of the form $\mathbf{U}(y) = U(y)\mathbf{e}_x$. The total energy contribution of the base flow transport terms $B_{k_h}\phi_1$ and

$B_{kk_h}\phi_2$ in (5.28) can be deduced from

$$\int \phi^* B_{b(\mathbf{k})}\phi \,\mathrm{d}k_y = ik_x \int \frac{\phi(\mathbf{k})^* U''(\mathbf{k}_y - \mathbf{k}'_y)\phi(\mathbf{k}')}{b(\mathbf{k})b(\mathbf{k}')}\,\mathrm{d}k'_y\mathrm{d}k_y, \tag{5.30a}$$

$$= ik_x \int \frac{\phi(\mathbf{k})^* U''(\mathbf{k}'_y - \mathbf{k}_y)^* \phi(\mathbf{k}')}{b(\mathbf{k})b(\mathbf{k}')}\,\mathrm{d}k'_y\mathrm{d}k_y, \tag{5.30b}$$

$$= -\int \left[ik_x \frac{\phi(\mathbf{k}')^* U''(\mathbf{k}'_y - \mathbf{k}_y)\phi(\mathbf{k})}{b(\mathbf{k})b(\mathbf{k}')}\right]^* \mathrm{d}k'_y\mathrm{d}k_y, \tag{5.30c}$$

$$= -\left[\int \phi^* B_{b(\mathbf{k})}\phi \,\mathrm{d}k'_y\right]^*. \tag{5.30d}$$

Here we used the definition of $B_b\phi$ (5.20b) twice, $b(\mathbf{k}) = b(\mathbf{k})^*$ in (5.30c), and the reality condition $U''(\mathbf{k}_h) = U''(-\mathbf{k}_h)^*$ for getting (5.30b). Equation (5.30) implies that $\mathrm{Re}(\int \phi^* B_{b(\mathbf{k})}\phi \,\mathrm{d}k_y) = 0$, so the base flow transport terms do not contribute to total perturbation energy. Note that this proof is no longer valid if we consider an arbitrary 2D basic flow.

We end this section by noting a simple example of the wave exciting term W_X associated with an energy increase in the vortical part. It occurs for the lift up mechanism in the $k_x = 0$ case of parallel flow. In such case, the dynamics in the (y, z)-plane decouples completely from the base flow shear. We show in 6.4.1 that in this case the energy due to horizontal velocity in ϕ_1 is excited by waves. It can be verified that in that case, there is no effect of ϕ_1 on ϕ_2, so we have

$$(W_X - C_{k|1})\phi_1 = 0, \Rightarrow W_X\phi_1 = C_{k|1}\phi_1. \tag{5.31}$$

On the other hand, we showed in (5.29) that the Coriolis terms produce no net energy increase but energy transfers between ϕ_1 and ϕ_2. The energy increase on ϕ_1 induced by ϕ_2 is given by the Coriolis term $C^{\Omega}_{1|k}\phi_2$ and is equal to

$$\int \mathrm{Re}[\phi_1^* C^{\Omega}_{1|k}\phi_2]\,\mathrm{d}^2k_h = \int \mathrm{Re}[\phi_2^* C^{\Omega}_{k|1}\phi_1]\,\mathrm{d}^2k_h, \tag{5.32a}$$

$$= \int \mathrm{Re}[\phi_2^* W_X\phi_1]\,\mathrm{d}^2k_h, \tag{5.32b}$$

where we have used 5.31. The situation here is an increase of ϕ_1-energy which is equal to the energy contribution of the wave exciting term W_X, regardless of the fact that the W_X term affects the evolution of phi_2. What happens is that there are two equal terms in the energy equation 5.28, and the contribution from the Coriolis term $C^{\Omega}_{k|1}\phi_1$ acting on ϕ_2, cancels one of them.

5.5 Concluding remark

The distribution of the elements of $\mathcal{L}$ manifests different kinds and degrees of non-normality of $\mathcal{L}$. The internal wave terms $\pm Nk_h/k$ and the ABC operators $A_{a(\mathbf{k})}$, $B_{b(\mathbf{k})}$ and $C^{\Omega}_{a(\mathbf{k})|b(\mathbf{k})}$, form a nearly antisymmetric matrix. Without W_X, the operator $\mathcal{L}$ can still be non-normal because of the spatial dependence of $\mathbf{U}$; the Orr mechanism, for example, would still be present in that case. Still, the wave exciting terms in W_X plays a substantially different role in $\mathcal{L}$; those are the terms involving wave vortex interactions and allowing for energy extraction from the base flow. In line with our previous discussion on 2.2, the wave exciting term $W_X\phi_1$ reflects what we could describe as a structural non-normality. These results will be applied to the results of next chapter concerning internal gravity wave emission from a horizontal shear layer.

Chapter 6

Non-normal effects on the horizontal shear layer with vertical stratification

Cristóbal Arratia, Sabine Ortiz, Jean-Marc Chomaz
Article in preparation

6.1 Introduction

Geophysical flows, due to their complexity, present a major challenge for their understanding and the prediction of their characteristics. Relevant aspects of their rich dynamics include vertical scale selection [15, 13] and internal wave generation [76, 99]. These aspects are very important for climate models and global budget estimates because of their influence on momentum fluxes and mixing. The size and complexity of real flows call for the detailed study of simpler, idealised flows which can reveal and allow the understanding of relevant dynamical processes.

Mixing or shear layers connecting two homogeneous streams of different but parallel velocities, are both of interest on their own and as an idealised model; they have thus been extensively studied [84]. Most studies on homogeneous (constant density) mixing layers have focused on their transition to turbulence and the presence of turbulent coherent structures. The origin of these two aspects of shear layers can be related to the linear dynamics of the (mean) velocity profile, in particular, to the Kelvin-Helmholtz instability related to the inflection point of the shear layer [42, 79]. In agreement with the Squire theorem [42] valid for the eigenmodes of plane parallel two dimensional basic flows, the Kelvin-Helmholtz (KH) unstable mode with the fastest growth is two dimensional (2D), i.e., independent of the spanwise direction. This instability leads to the Kelvin-Helmholtz billows, well documented coherent

structures in turbulent mixing layers (Brown & Roshko [20]) and the first stage of the transition to turbulence from an initially laminar mixing layer [84].

The effect of density stratification relevant to geophysical flows has also been extensively studied. Most of these studies consider mixing layers with stable density stratification in the plane of the shear [see 84, for a review]. In that case, buoyancy has a stabilizing effect. As established by the Richardson number criteria [42], if the gradient Richardson number, which locally measures the ratio of stratification strength and shear, is everywhere larger than 0.25, the shear layer is no longer unstable. Much less attention has been devoted to the dynamics of horizontal shear layers with vertical stratification. As discussed by Basak and Sarkar (2006) [13], there is considerable observational evidence and various geophysical situations, like flows around topography or edges of ocean currents, that motivate the study of stratified, horizontally sheared layers.

The DNS study of Basak & Sarkar [13, hereafter BS06] described the organization of the vorticity, density and dissipation fields resulting from the evolution of a horizontal shear layer. In the strongly stratified case of BS06, they observed that vertical vorticity concentrates on vertically dislocated KH billows. The dislocation spacing observed is such that the characteristic height of the rollers is of the order of the buoyancy length. Dissipation was observed to be strong in localized regions at the dislocation sites. Horizontal vorticity structured on thin layers, also at the dislocation sites. While maintaining their vertical size, the KH rollers kept increasing their horizontal extent by successive mergings, leading to the so-called pancake vortices. This result shows the appearance of three-dimensional (3D) structure.

While vertical stratification does not affect the 2D unstable modes of a horizontal shear layer, the buoyancy effect is less evident for general 3D perturbations. Deloncle, Chomaz & Billant [39] showed, in the inviscid case, that the growth rate σ_{KH} of the KH unstable mode is largest for 2D perturbations; that fact was not obvious because the Squire's theorem does not apply when buoyancy is in the spanwise direction of the 2D basic flow.

Deloncle *et al.* [39] also showed that, for strong stratification, the range of KH unstable vertical wavenumbers increases proportional to the Brunt-Väisälä frequency N. More precisely, they showed that for strong stratification the dependence of σ_{KH} on the horizontal Froude number F_h (the ratio of N^{-1} to the advective time scale) and vertical wavenumber k_z is given by the product $F_h k_z$, i.e.,

$$\sigma_{KH}(k_z, F_h) = \tilde{\sigma}_{KH}(F_h k_z). \tag{6.1}$$

Equation (6.1) is a manifestation of the more general self similarity of strongly stratified inviscid flow described by Billant & Chomaz [17]. Remarkably, the limiting relation (6.1) is quickly attained when $F_h < 1$ [39]. Because it is possible to have k_z of order 1 while $F_h k_z \ll 1$ (and thus growth rate close to the maximum at $k_z = 0$),

this finding implies a loss of selectivity for 2D modes in the strongly stratified case ($F_h \ll 1$). Deloncle *et al.* [39] argued that this loss of selectivity could explain the layering observed in BS06. That argument shows that there is no strong selectivity for 2D perturbations, and is thus consistent with the appearance of KH rollers with strong vertical variability. However, the precise mechanism for explaining the lengthscales and appearance of the vertical layering observed in BS06 [and in the subsequent work by Arobone & Sarkar 5] is still unclear. The structures observed in BS06 are excited from initial random fluctuations superposed on the shear layer, the evolution is thus determined by the response of the flow to such fluctuations.

Yet understanding the development of the linear perturbations on shear flows solely in terms of their unstable eigenmodes is incomplete. This fact has been increasingly acknowledged since the recognition that, regardless of the Squire's theorem and the absence of unstable modes, linearized dynamics of 3D perturbations on plane Couette and Poiseuille flow allows for very large energy amplification [25]. This increase in perturbation energy is possible for finite times when the linear operator is *non-normal* under the energy norm, implying that the eigenvectors are not orthogonal in the related inner product. Such is the general case in hydrodynamic stabilty; the eigenmodes are *not* normal-modes in the geometrical sense[1]. The need for characterizing the linear dynamics of non-normal systems has led to major developments on linear stability theory [see 90, for a review]. One way of objectively characterizing the linear dynamics is to compute the *optimal perturbation* for a prescribed time T, that is, the perturbation that leads to the largest possible amplification of perturbation energy during the $[0, T]$ time interval. An advantage of the optimal perturbations approach is that it usually yields robust features which do not necessarily depend on the details, that is the case on unstratified shear flow [49]. Other dynamical effects can be at play in the presence of stratification.

An aspect of geophysical flows that has drawn considerable attention concerns spontaneous generation of internal/inertia-gravity waves (IGW/RIGW according to the presence of rotation) [76]. This refers to wave emission from flows that evolve in perfect geostrophic balance or, in the non-rotating case, in the complete absence of vertical motions and density disturbances. This phenomenon has been demonstrated through DNS of balanced (rotating) flows by several authors [see for example 76, and references therein]. Important results concerning spontaneous emission of RIGW have been obtained on horizontal shear flow, in particular in the case of unbounded constant shear ([77, 99, 66, 81]); that idealized case allows for asymptotic analytic expressions for the amplitude of the generated waves [99, 81]. Bakas & Farrell [9, 10] studied the non rotating case; after describing mechanisms of IGW energy growth and decay [9], they also found spontaneous wave generation

[1]The adjective 'normal' in 'normal-mode' is in the sense of 'usual' or 'common', not in the sense of 'perpendicular' as when talking about the 'normal to a plane' [27].

and gave analytic expressions for unbounded constant shear [10].

Perturbations to unbounded constant shear allow solutions in terms of spatial Fourier modes with time dependent cross-stream wavenumber and amplitude. The time dependent wavenumber varies linearly in time. In each of the rotating and non-rotating case, gravity waves can be described by a single inhomogeneous ODE with time dependent coefficients. The inhomogeneous or forcing term of the ODE comes from the conserved potential vorticity and the homogeneous solutions describe wave propagation. When waves are absent, they are rapidly generated around the time when the cross-stream wavenumber crosses zero. A similar phenomena was previously described in [30] in the context of acoustic emission by sheared vortices in 2D flow. Chagelishvili *et al.*[30] explain the emission of acoustic waves in terms of a discontinuity in the particular solution which imposes the instantaneous appearance of the homogenous solution to smooth the full solution. In the involved analysis of Vanneste & Yavneh [99], the emitted RIGW appear as a Stokes phenomenon when time crosses a stokes line crossing the real axis when the time dependent wavenumber is zero. Bakas & Farrell [10] confirmed the Stokes phenomenon scenario for the IGW emission in unbounded flow. They also computed the eigenmodes in a bounded domain and linked the amplitude of the emitted IGW to the degree of non-normality between vortical and IGW eigenmodes in the energy inner product. A link between non-normality and wave emergence was also established in [53] for the acoustic case.

Following BS06 and Deloncle *et al.* (2007), we use the tanh profile and do not consider Coriolis effects. The organization of the article is as follows. Section 6.2 presents the base flow and describes the computation of the optimal perturbations. Section 6.3 describes the classical transient growth mechanisms of parallel shear flow without stratification in the present context of an inviscid shear layer. In section 6.4 we consider the effect of density stratification, show the approach to the strongly stratified similarity of [17] and describe the main differences with the unstratified case. We then describe the stratified version of the lift up mechanism (sub-section 6.4.1) and quantify the wave/vortex component of the optimal perturbations with the Craya-Herring decomposition (sub-section 6.4.2). This decomposition helps to characterize the strong production and emission of internal waves by the optimal perturbations, which is described and analysed in detail in section 6.5, showing how the Craya-Herring decomposition allows to clarify wave-vortex interactions and the role of non normality in the perturbative, linearized regime. In section 6.6 we discuss the relevance of the results, summarize the different types of optimal responses according to the perturbation wavenumbers, and comment about the possible relevance of the stratified lift-up mechanism. We conclude in section 6.7 by briefly recalling the main results.

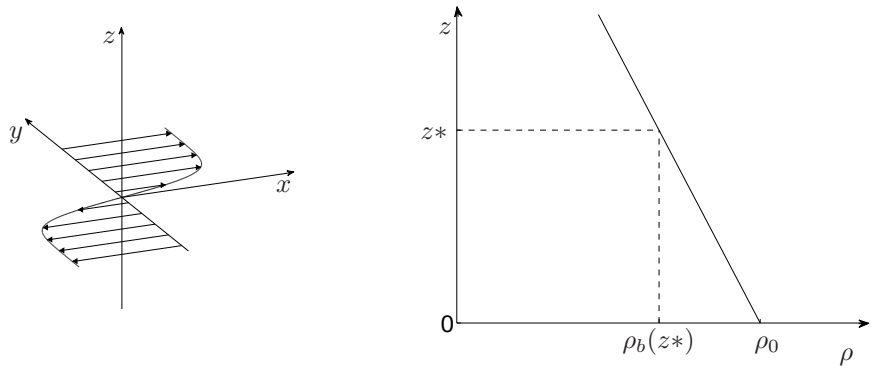

Figure 6.1: Diagrams of the basic flow velocity (left) and density (right).

6.2 Problem formulation

6.2.1 Base state and governing equations

We use the incompressible Euler equations under the Boussinesq approximation in cartesian coordinates $\mathbf{x} = (x, y, z)$ with gravity $\mathbf{g} = -g\mathbf{e}_z$. For the basic flow velocity field we consider a parallel shear flow of the form $\mathbf{U} = U(y)\mathbf{e}_x$ with $U = \tanh(y)$ (see figure 6.2.1). The model fluid presents a stable linear density profile $\rho_b(z) = \rho_0(1 - N^2 z/g)$, where $N = \sqrt{-g/\rho_0 d\rho_b/dz}$ is the Brunt-Väisälä frequency. Provided a pressure p_b in hydrostatic equilibrium with ρ_b, the velocity $\mathbf{U}$, density ρ_b and pressure p_b form an exact solution of the governing equations. The evolution of infinitesimal velocity $\mathbf{u}_p = (u_p, v_p, w_p)$, density ρ_p and pressure p_p disturbances of this basic flow is given by

$$\partial_t \mathbf{u}_p + U\partial_x \mathbf{u}_p + U' v_p \mathbf{e}_x = -\nabla p_p - \rho_p \mathbf{e}_z / F_h^2, \tag{6.2a}$$

$$\nabla \cdot \mathbf{u}_p = 0, \tag{6.2b}$$

$$\partial_t \rho_p + U\partial_x \rho_s + w_p = 0, \tag{6.2c}$$

where the sub-index p indicates that these are perturbation functions in physical coordinates and the superscript $'$ denotes partial derivative with respect to y. We define the horizontal Froude number as $F_h \equiv U_B/(LN)$, in which U_B and L are the unit velocity and length scales defined by the base flow velocity $\mathbf{U}$. The density field ρ_s is nondimensionalized in units of $L\rho_0 N^2/g$. As it stands on (6.2), L is the only externally imposed length scale of the problem. $F_h = N^{-1}$ is the only nondimensional parameter. It is given by the ratio between the inverse of the Brunt-Väisälä frequency N and the advective time scale $L/U_B = 1$.

As the coefficients of system (6.2) have no dependence on the x and z coordinates,

we can write the fields in spatial plane wave form as

$$[\mathbf{u}_p, \rho_p, p_p](x, y, z, t) = [\mathbf{u}, \rho, p](y, t)e^{i(k_x x + k_z z)} + c.c., \tag{6.3}$$

and consider the evolution of the disturbance fields independently for every pair of streamwise and vertical wavenumbers (k_x, k_z). Replacing (6.3) into (6.2) one obtains

$$\begin{aligned} D_t u &= -ik_x p - U'v, && \text{(6.4a)} \\ D_t v &= -p', && \text{(6.4b)} \\ D_t w &= -ik_z p - N^2\rho, && \text{(6.4c)} \\ D_t \rho &= w, && \text{(6.4d)} \\ ik_x u + v' + ik_z w &= 0, && \text{(6.4e)} \end{aligned}$$

where the time derivative following the basic flow is now $D_t = \partial_t + ik_x U$. The boundary conditions in the y direction are that $\mathbf{u}$, ρ and p' should vanish as $y \to \pm\infty$.

6.2.2 Computation of the optimal perturbations

We define the optimal gain as

$$G_{max}(k_x, k_z, T) = \max_{[\mathbf{u},\rho](y,0)} \{G(k_x, k_z, T)\}, \tag{6.5a}$$

where

$$G(k_x, k_z, t) = \frac{E(k_x, k_z, t)}{E(k_x, k_z, 0)}, \tag{6.5b}$$

and

$$E = \frac{\mathbf{u}^2}{2} + \frac{N^2\rho^2}{2}, \tag{6.6}$$

is the energy of the perturbation for (k_x, k_z) wavenumbers. For (k_x, k_z) wavenumbers $G_{max}(T)$ is the maximum attainable increase in energy up to the optimization time T. We characterize the transient growth by the optimal mean growth rate of the perturbation

$$\sigma_m(k_x, k_z, T) = \frac{1}{2T} \ln G(k_x, k_z, T), \tag{6.7}$$

which allows straightforward comparison with σ_{KH}.

The optimal perturbations are computed by the iterative procedure described by [32], whereby the succesive numerical integration of the direct and the time reversed adjoint equations is performed until convergence is achieved. The adjoint equations and optimization algorithm have been adapted on a pseudo-spectral DNS code with an Adams-Bashforth time scheme. The DNS code was originally developed by [100], [37] and [38].

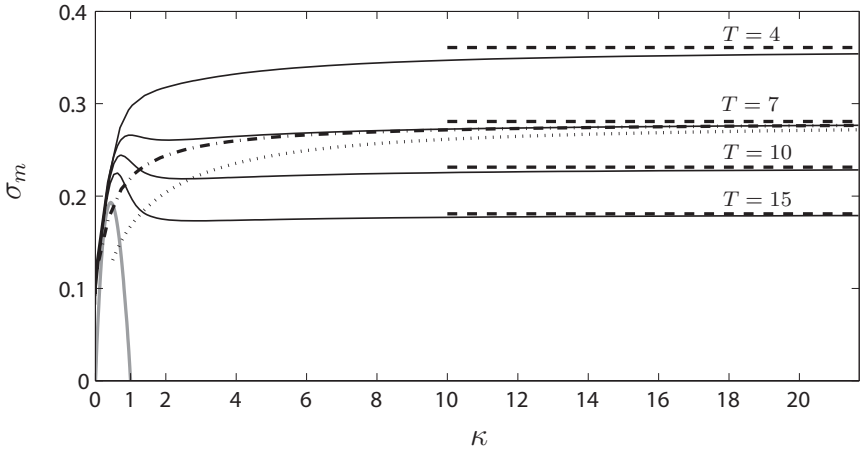

Figure 6.2: Optimal perturbations as a function of $\kappa = \sqrt{k_x^2 + k_z^2}$ and different T. Continuous black lines show σ_m versus k_x for different $T = 4, 7, 10, 15$, dashed lines correspond to σ_m^c for the constant shear case and the gray line to the modal growth rate of the KH instability. The dash-dotted line shows the corresponding mean growth rate ($T = 7$) for the lift-up mechanism, i.e., σ_m as a function of wavenumber k_z for the $k_x = 0$ case. The dotted line shows σ_m as a function of $k_v = k_z \min\{1, F_h\}$ for the stratified case with $F_h = 0.1$ and $k_x = 0$ (section 6.4.1).

6.3 Unstratified case ($F_h = \infty$)

6.3.1 2D case: shear instability and the Orr mechanism

The gray line on figure 6.2 shows $\sigma_{KH}\big|_{k_z=0}$, the growth rate of the KH instability for the 2D case, as computed by Michalke (1964) [79]. Those unstable KH modes exist for k_x in $]0, 1[$ and the maximum growth rate is $\sigma_{KH}^{max} = 0.1897$ [39]. In the KH unstable region, σ_{KH} also corresponds to the optimal mean growth rate σ_m in the limit $T \to \infty$, recovering the result from modal stability. The black continuous lines of figure 6.2 show σ_m as a function of k_x for $T = 4, 7, 10$ and 15. For $T = 15$, the curve of σ_m presents a notorious peak on the left part, in the KH unstable region. For smaller T, the peak becomes less conspicuous and drifts slightly to larger values of k_x. For $T = 10$, the peak is still the maximum of $\sigma_m\big|_{k_z=0}$ whereas it is only a local maximum for $T = 7$. For $T = 4$ the peak is no longer present. For $T = 7$ and 4, the maximum σ_m occurs in the large k_x limit. Large σ_m in the large k_x limit is a clear feature also for $T = 10$ and 15.

Figure 6.3 shows the evolution of the vorticity ω_z of the optimal perturbation for $k_x = 3.77$ and optimization time $T = 7$. Shown are the optimal initial perturbation (at time $t = 0$), the optimal response (at $t = T = 7$) and the optimal perturbation at

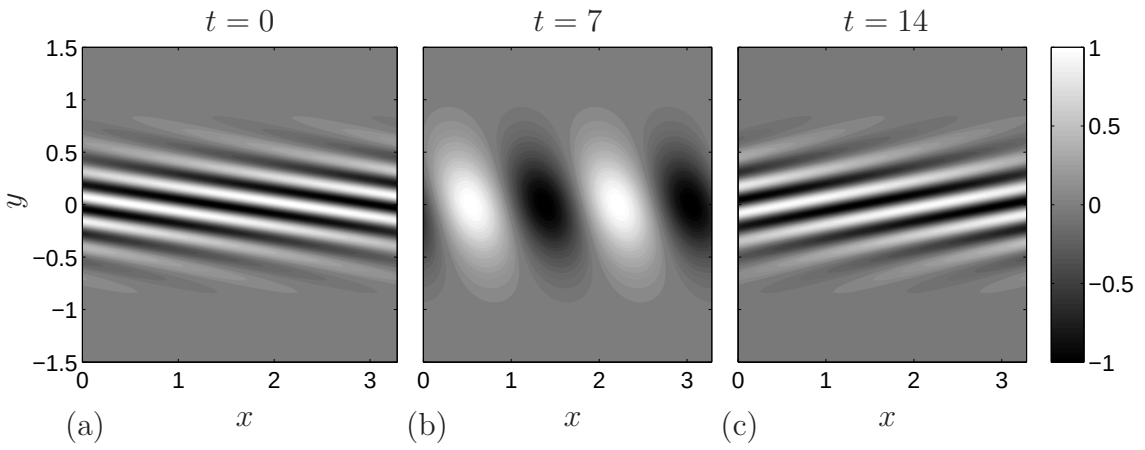

Figure 6.3: Optimal perturbations for the 2D case ($k_z = 0$). (a) ω_z distribution of the optimal perturbation for $k_x = 3.77$ and $T = 7$ at the initial time $t = 0$(a), the optimization time $t = T = 7$(b) and the later time $t = 14$(c). The horizontal axes show 2 wavelengths.

the later time $t = 14$. The contours of the optimal perturbation are initially oriented against the base flow shear (figure 6.3a). As time evolves to $t = 7$ (figure 6.3b), the corresponding ω_z is sheared to an almost cross-stream orientation, leading at this time to the maximum of energy amplification. As the optimal perturbation evolves in time until $t = 14$ (figure 6.3c), ω_z is sheared further and the perturbation energy decreases back to a lower value. The energy amplification results from the kinematic deformation of ω_z by the base flow. This kinematic deformation reduces the length of the ω_z contours while leaving unchanged the integral of the ω_z enclosed by the contours. Stokes theorem implies that the velocity magnitude along the (reduced in length) contours must increase to keep the circulation along the contours equal to the (constant) integral of ω_z. This mechanism of transient growth is the so called Orr mechanism [82, 45]. It produces a large increase in cross-stream velocity v. When time evolves further and ω_z is sheared as in figure 6.3(c), the kinematic process just described is reversed and the energy goes to zero as $t \to \infty$.

Farrell and Ioannou [48] give a closed expression of the optimal gain for 2D perturbations of unbounded constant shear base flow, when only the Orr mechanism operates. In that case there are closed analytic solutions in terms of plane waves with time dependent wavenumber, yielding that the optimal mean growth rate σ_m^c is

$$\sigma_m^c = \frac{1}{2T} \ln \left[1 + \frac{U_c'^2 T^2}{2} + U_c' T \sqrt{\left(\frac{U_c' T}{2} \right)^2 + 1} \right], \tag{6.8}$$

where U_c' is the constant shear rate. The dashed horizontal lines of figure 6.2 cor-

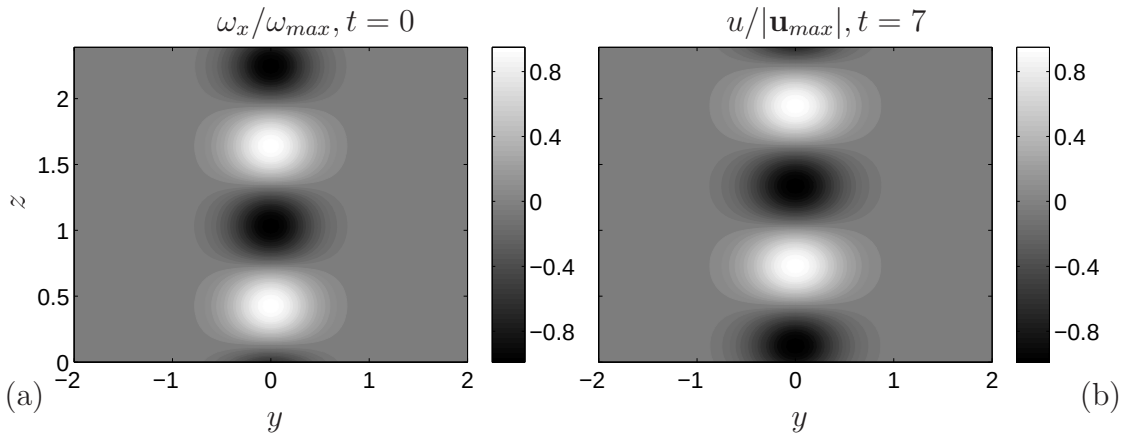

Figure 6.4: Optimal perturbations for $(k_x, k_z) = (0, 5.174)$ and $T = 7$. (a) ω_x of the optimal perturbation at $t = 0$. (b) u of the optimal perturbation at $t = T = 7$. The vorticity ω and velocity u fields are respectively normalized so that the maximum value of enstrophy $(\omega_x^2 + \omega_y^2 + \omega_z^2)$ and twice the energy is 1.

respond to $\sigma_m^c(T)$ with $U_c' = 1$, the maximum of U'. The figure 6.2 shows that σ_m approaches σ_m^c as k_x increases. This is because the Orr mechanism is responsible for the large differences between σ_m and σ_{KH} for $k_z = 0$, most notably for short T and large k_x (figure 6.2). Accordingly, the optimal perturbations become increasingly localized at $y = 0$, around the maximum of U' (not shown).

6.3.2 Lift-Up mechanism ($k_x = 0$)

Figure 6.4 shows the streamwise vorticity ω_x of the optimal initial perturbation (figure 6.4a) and the streamwise velocity u (figure 6.4b) of the optimal response, leading to the optimal gain at $T = 7$ for $k_z = 5.174$ and $k_x = 0$. The ω_x and u fields in figure 6.4 are respectively normalized by the maximum total enstrophy at $t = 0$ and twice the maximum total energy at $t = T = 7$. Both fields are localized around $y = 0$, in the region with strong shear. The colorbar on figure 6.4(a) reflects the fact that at the initial time, 97.6% of the total enstrophy is given by ω_x. As time evolves, ω_x remains constant and induces a constant cross-stream velocity v. That v excites u through transport of base flow momentum, generating streamwise streaks. The colorbar on figure 6.4(b) reflects the fact that, after the perturbation evolves to $t = 7$, most of the perturbation velocity corresponds to u. As time evolves further, the forcing of u by v remains constant, implying that the energy of the perturbation grows unbounded as $t \to \infty$. This mechanism of perturbation energy growth is known as lift-up mechanism [44, 70].

The dash-dotted line of figure (6.2) shows $\sigma_m(k_z)$ for $T = 7$ and $k_x = 0$. For

large wavenumbers this $\sigma_m(k_z)$ curve becomes very close to the corresponding $\sigma_m(k_x)$ curve of the Orr mechanism case, both curves approaching σ_m^c as $\kappa = \sqrt{k_x^2 + k_z^2} \to \infty$. This coincidence can be traced to the fact, noted by Farrell and Ioannou [48, they refer to the lift-up mechanism as the 'tilting mechanism'], that in the constant shear case the optimal gain is the same for the lift-up ($k_x = 0$) and for the Orr ($k_z = 0$) mechanisms. That is, the optimal mean growth rate for unbounded constant shear base flow, σ_m^c, is given by (6.8) in the $k_x = 0$ case too. Also for the lift-up mechanism, increasing κ allows for the optimal perturbations to become increasingly localized at $y = 0$, around the maximum of U' (see chapter 3).

Equation (6.8), being valid in the $\kappa \to \infty$ limit for the Orr and lift-up mechanisms, implies that with both mechanisms the energy gain can be arbitrarily large provided a sufficiently large T. However, one should keep in mind the important differences between the Orr and Lift-up mechanisms. On one side, the perturbation energy vanishes as $t \to \pm\infty$ and reaches a maximum value at a finite t for the Orr mechanism. On the other, the perturbation energy diverges as $t \to \pm\infty$ and reaches minimum value at a finite t for the lift-up mechanism.

6.3.3 General perturbations $k_x, k_z \neq 0$

Figure 6.5 shows gray levels of σ_m in the (k_x, k_z)-plane at optimization times $T = 7$ and $T = 15$. The colorbars indicate that σ_m decreases as T increases. The curve of neutral stability of the KH modes is indicated on each plot by a dash-dot line (white in 6.5a and black in 6.5b), limiting the region of $\kappa < 1$ where exponentially unstable modes exist. For $T = 15$, the largest σ_m occurs for $k_z = 0$, in the KH unstable region. The most amplified optimal response corresponds (almost exactly...) to an unstable KH mode when $T \gtrsim 15$ and approaches the most unstable mode as $T \to \infty$. For $T = 7$, the largest σ_m is at the boundary of the (k_x, k_z) region computed, far from the unstable domain. At this short optimization time, the maximum σ_m occurs in the large κ limit with $k_x, k_z \neq 0$; i.e., for three dimensional perturbations in the form of oblique short waves varying in the (x, z) plane. Large σ_m in the large κ limit with $k_x, k_z \neq 0$ is a clear feature also for $T = 15$.

The dashed lines on figure 6.5 roughly indicate r_{max}, the ratio k_z/k_x for which σ_m in the limit $\kappa \to \infty$ is maximum. Figure 6.5 indicates that r_{max} is larger for $T = 15$ than for $T = 7$. In the limit of large κ, σ_m increases monotonically when the ratio $r = k_z/k_x$ increases from 0 to r_{max}, and then decreases back as $r \to \infty$. When $r = 0$, the Orr mechanism is responsible for the energy amplification of the optimal perturbations. When r is finite, the perturbations are 3D and σ_m is larger. The larger gain for oblique wave perturbations is sometimes ascribed to a combination of the Orr and lift-up mechanisms. Farrell and Ioannou [48] describe this combination as a synergy between the two mechanisms whereby the increased v produced by the Orr mechanism excites u through the lift-up mechanism.

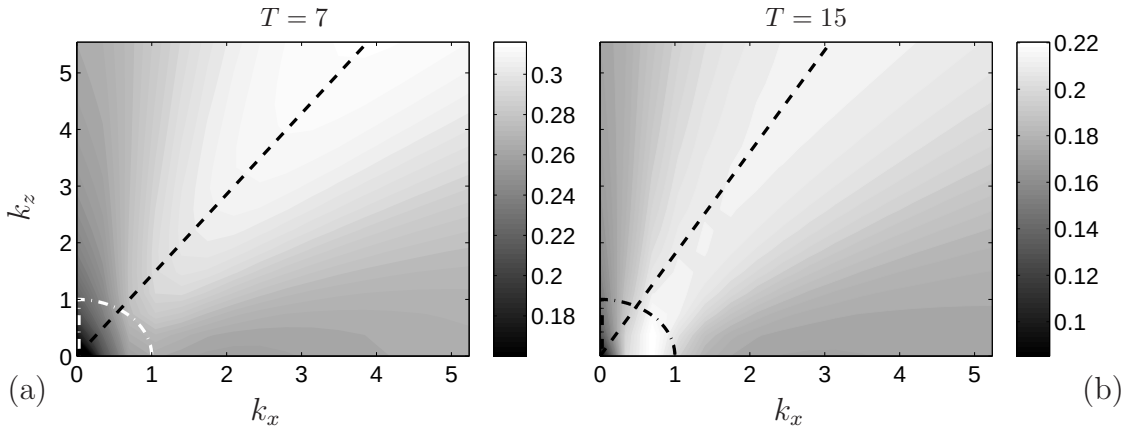

Figure 6.5: Mean growth rate of the optimal perturbations $\sigma_m(k_x, k_z, T)$ for $T = 7$(a) $T = 15$(b). The dash-dot line on each curve (white in 6.5a and black in 6.5b for better contrast) indicates the neutral curve of the KH instability. The dashed black lines, indicating schematically the ratio $r = k_z/k_x$ of the maximum σ_m in the $\kappa \to \infty$ limit, are drawn at $r = 10/7$ for $T = 7$ (a) and at $r = 9/5$ for $T = 15$ (b). The maximum of σ_m is at the largest computed $k_z = 5.544$, at $k_x = 3.84$ and given by $\max(\sigma_m) = 0.3166$ in (a), and at $k_x = 3.142$ and given by $\max(\sigma_m) = 0.2135$ in (b).

The dependence of σ_m on r for large κ is similar to the one shown in [49] for the constant shear base flow, similar T and large Reynolds number. Farrell and Ioannou[49] also studied the optimal perturbations for bounded Couette and Poiseuille flow for the same T. They showed that the r-dependence is a robust feature of the optimal perturbations to parallel shear flow for short enough wavelengths compared to the base flow lengthscale. Viscous damping increases as r decreases and implies the selection of a finite κ for the most amplified optimal perturbation.

6.4 Effect of stratification

Figure 6.6(a) shows the optimal mean growth rate σ_m as a function of k_z for different Froude numbers F_h, for an optimization time $T = 7$ and $k_x = 1.047$. The curve for $F_h = \infty$ corresponds to a vertical cut passing through $k_x = 1.047$, which is the maximum of $\sigma_m(k_x, k_z)\big|_{k_z=0}$ computed on figure 6.5(a). For $F_h \geq 0.5$, σ_m decreases for all computed $k_z > 0$ as F_h decreases. σ_m reaches a minimum around $F_h = 0.5$ and then increases for lower F_h, as shown by the curve of σ_m for $F_h = 0.1$.

Figure 6.6(b) shows the same σ_m as figure 6.6(a) but plotted in terms of the rescaled vertical wavenumber $k_v := k_z \min\{1, F_h\}$. In addition to the σ_m curves of figure 6.6(a), figure 6.6(b) also shows σ_m for $F_h = 0.2$ and $F_h = 0.05$. Figure 6.6(b)

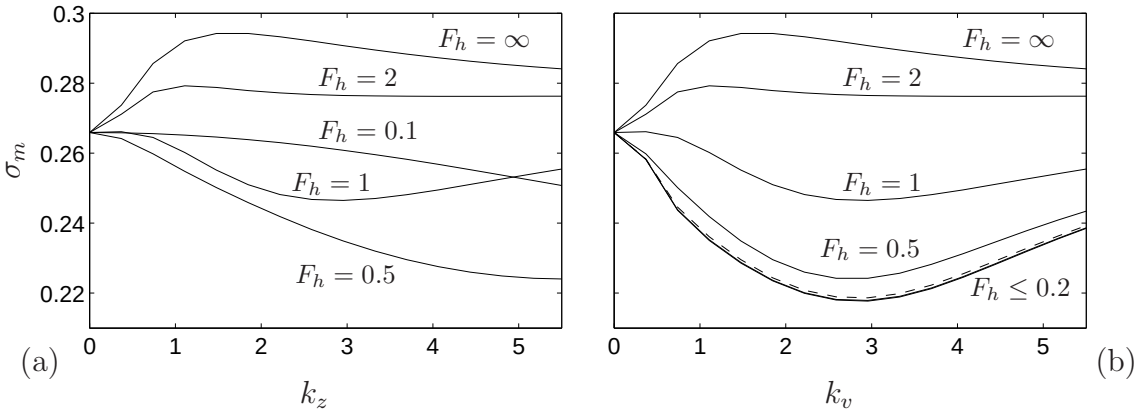

Figure 6.6: Mean growth rate of the optimal perturbations σ_m for $T = 7$ and $k_x = 1.047$. The corresponding F_h for each curve are as indicated on the figures, except for $F_h \leq 2$ detailed below. Figure (a) shows σ_m as a function of k_z and figure (b) as a function of $k_v = k_z \min\{1, F_h\}$. The dashed line in (b) corresponds to $F_h = 0.2$, which is very close to the almost undistinguishable curves for $F_h = 0.1, 0.05$.

shows that σ_m decreases monotonically with F_h for fixed k_v. In the small F_h limit, σ_m reaches a self-similar form such that

$$\sigma_m(k_z, F_h) = \tilde{\sigma}_m(F_h k_z) \tag{6.9}$$

Equation (6.9) is of the same form as (6.1) found by [39] and consistent with the more general self-similarity of strongly stratified inviscid flows [17].

Figure 6.7 shows graylevels of $\sigma_m(k_x, k_v)$ for $F_h = 1, 0.5, 0.1$ and 0.05, for the same optimization time ($T = 7$) as figures 6.6 and 6.5(a). The values in the colorbars indicate that the maximum of the computed $\sigma_m(k_x, k_v)$ decreases with F_h until $F_h \approx 0.1$, when it reaches the self similar form (6.9). The $\times$ sign in 6.7(a) indicates the 2D local maximum of σ_m, which for $F_h \geq 1$ is a saddle point in the (k_x, k_v)-plane because there $\partial^2 \sigma_m / \partial k_v^2 > 0$. The $\bullet$ sign in 6.7(b-d) indicates the same 2D local maximum of σ_m, which for the computed $F_h < 1$ is a local maximum also in the (k_x, k_v)-plane. The dashed black lines on figures 6.7(a,c,d) roughly indicate r_{max}, the ratio r for which σ_m in the limit $\kappa \to \infty$ is maximum. Note that in the stratified case we define $r = k_v/k_x$ and $\kappa = \sqrt{k_x^2 + k_v^2}$. When F_h decreases, r_{max} decreases until it reaches its self similar limit satisfying (6.9). The dashed white lines on figures 6.7(c,d) indicate r_{min}, roughly the ratio r at which the optimal perturbations are less amplified. The dashed lines on figure 6.7(b) are the same as those of figures 6.7(c,d).

The dependence of σ_m on r for large κ is notably different in the strongly stratified limit (figure 6.7c,d) from the unstratified case (figure 6.5a). In 6.7(c,d), when

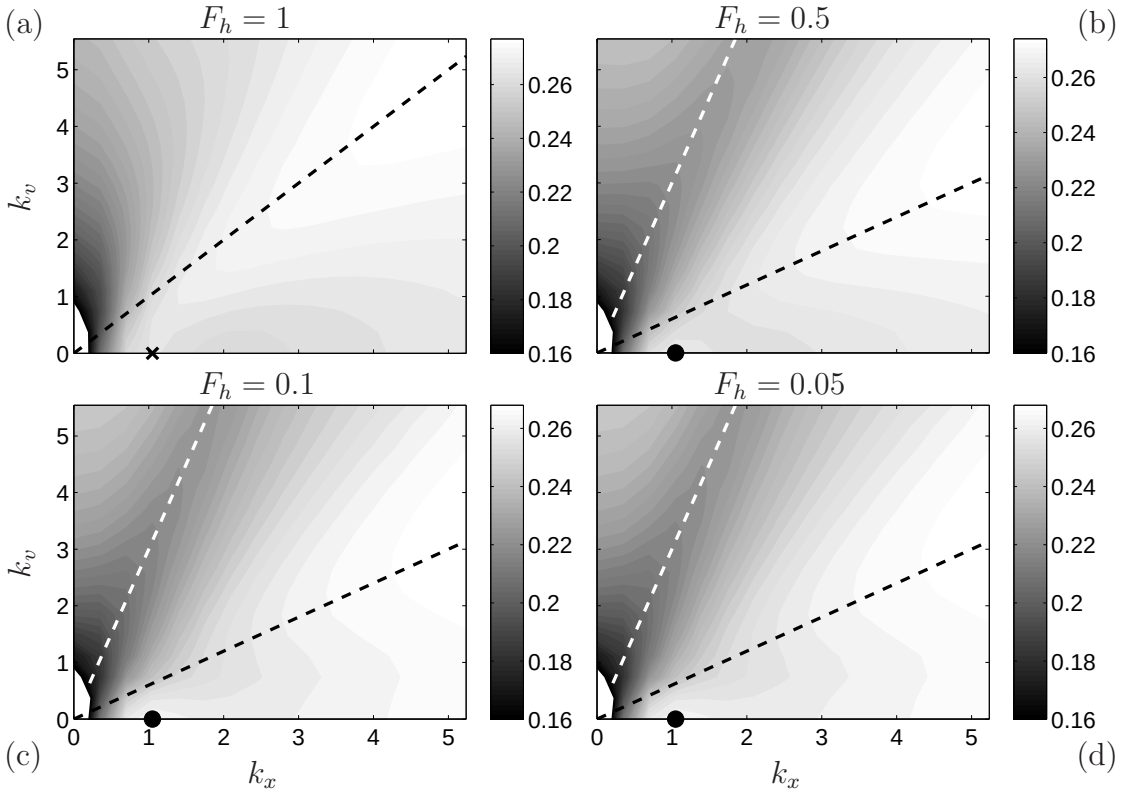

Figure 6.7: σ_m at $T = 7$ for different F_h, as indicated on each plot. The dashed black lines, indicating schematically r_{max}, are drawn at $r = 1$ for (a) and at $r = 3/5$ for (b-d). The dashed white lines, indicating schematically r_{min}, are drawn at $r = 3$. The maximum of σ_m is at the largest computed $k_x = 5.236$, at $k_v = 5.174$ and given by $\max(\sigma_m) = 0.2796$ in (a), at $k_v = 3.696$ and given by $\max(\sigma_m) = 0.2758$ in (b), at $k_v = 3.326$ and given by $\max(\sigma_m) = 0.2703$ in (c), and at $k_v = 3.326$ and given by $\max(\sigma_m) = 0.2701$ in (d).

r increases from 0, σ_m first decreases before increasing until around r_{max}, then decreases again until around r_{min}, and finally increases again as $r \to \infty$, when $k_x \to 0$. This is different for $F_h = 0.5$, in which case σ_m increases monotonically with r when r goes from 0 to around r_{max}. The corresponding qualitative description of σ_m for $F_h = 1$ is the same as in the unstratified case. For different optimization times in the strongly stratified limit (data not shown), r_{min} and r_{max} increase as T increases [8].

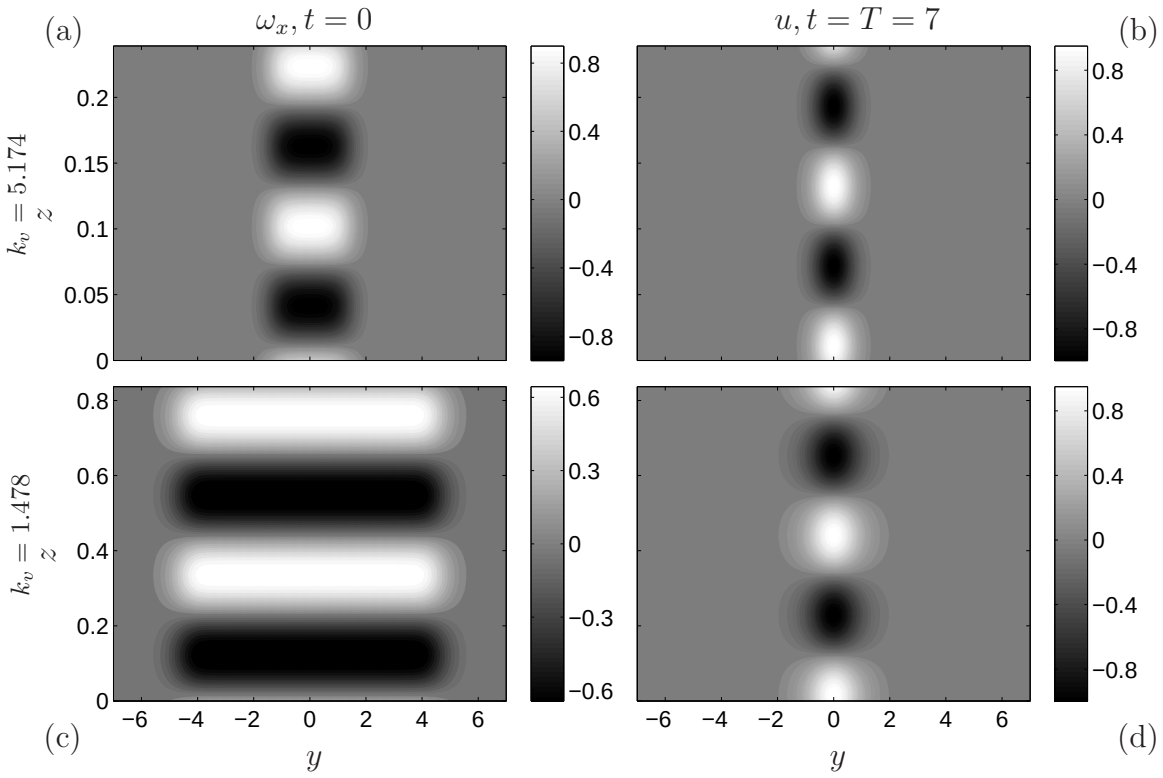

Figure 6.8: Optimal perturbations for $T = 7$ and $k_x = 0$. (a,c) ω_x of the optimal perturbation at $t = 0$. (b,d) u of the optimal perturbation at $t = T = 7$. (a,b) correspond to $k_v = 5.174$ and (c,d) to $k_v = 1.478$. The vorticity (velocity) fields are normalized so that the maximum density of enstrophy (two times energy: $\mathbf{u}^2 + N\rho^2$) is 1.

6.4.1 Stratified lift-up ($k_x = 0$)

As in the unstratified case, ω_x is unaffected by the base flow shear for $k_x = 0$. Figure 6.8 shows the streamwise vorticity ω_x of the initial optimal perturbations (fig. 6.8a,c) and the streamwise velocity u of the optimal responses (fig. 6.8b,d) for $F_h = 0.1$, $T = 7$ and two different k_v. Perturbation ω_x and u in 6.8 are normalized as those in figure 6.4 for the unstratified case. The colorbars in figure 6.8 are similar to those of figure 6.4 except for 6.8(c), reflecting that ω_x in 6.8(c) is less dominant in the optimal initial condition, although it still contains 88.15% of the total enstrophy the difference corresponding mainly to ω_y with a 11.79%; respectively, those percentages correspond to 95.14% and 4.86% in 6.8(a). For large k_v (fig. 6.8a,b), ω_x and u are less localized around $y = 0$ than in the unstratified case for the same k_v (note the different y axes in 6.8 and 6.4). For small k_v (fig. 6.8c,d), ω_x and u are less

localized around $y = 0$ than their large k_v counterparts, specially ω_x that becomes considerably extended. The vertical axes indicate that in both cases the ω_x contours have a large horizontal-to-vertical aspect ratio (figure 6.8a,c).

Figure 6.9 shows spatio-temporal diagrams of u, v and $F_h^{-1}\rho$ for 3 different optimal perturbations. The optimization time $T = 7$ is indicated on each plot by a horizontal line at $t = 7$. The left column 6.9(a,d,g) shows the streamwise velocity u, which increases largely in magnitude between $t = 0$ and $t = 7$. The middle 6.9(b,e,h) and right 6.9(c,f,i) columns respectively show v and $F_h^{-1}\rho$, each composed of two travelling structures that superpose during the optimization interval. The density perturbations corresponding to the right and left travelling structures have opposite signs and tend to cancel each other when superposing. The superposition involving v is constructive and centered at $y = 0$, around the maximum shear. As time evolves from $t = 0$ to $T = 7$, the large cross-stream velocity v excites u through transport of base flow momentum, generating streamwise streaks as in the unstratified case. Different from the unstratified case, v and w are not constant in time but —in this linear regime— correspond to a superposition of internal gravity waves that evolves accordingly.

The generation of streamwise velocity by the superposition of streamwise independent waves on horizontal shear has been discussed by Bakas and Farrell [9]. Here, it should be noted that the more relevant superposition for the amplification of perturbation energy is not the superposition of the right and left (v, ρ) travelling structures, but the superposition of plane waves that constitutes each of the travelling structures. Each of the travelling structures has a particle displacement field associated to it. It is the cross-stream component of this displacement field that produces the transport of streamwise momentum from the base flow. A horizontal redistribution of fluid particles remains after the travelling structures have passed so the streamwise streaks also remain. Each of the travelling structures produces a similar energy growth at its passage through the shear layer. The symmetry between the two travelling structures is a property of the optimal perturbation, but the underlying mechanism does not depend on such a precise superposition.

Figure 6.9(d-f) (middle row) shows the optimal perturbation in the strong stratification limit for $k_v \sim \mathcal{O}(1)$. The right and left travelling (v, ρ) structures are starting to cross the shear layer at $t = 0$; their cross-stream size is large enough so that they continue to cross the shear layer until about $t = T$. The passage of the travelling structures through the shear layer during the optimization interval, determines the cross-stream size of the structures through their propagation velocity. For larger k_v, figure 6.9(b,c) shows (v, ρ) travelling structures that cross the shear layer between $t = 0$ and $t = T$ as well. The propagation velocity of the (v, ρ) structures is lower, allowing for a more localized optimal perturbation; each of the travelling structures is comparable in size to the shear layer.

For $k_x = 0$, the propagation of internal gravity waves is subject to the usual

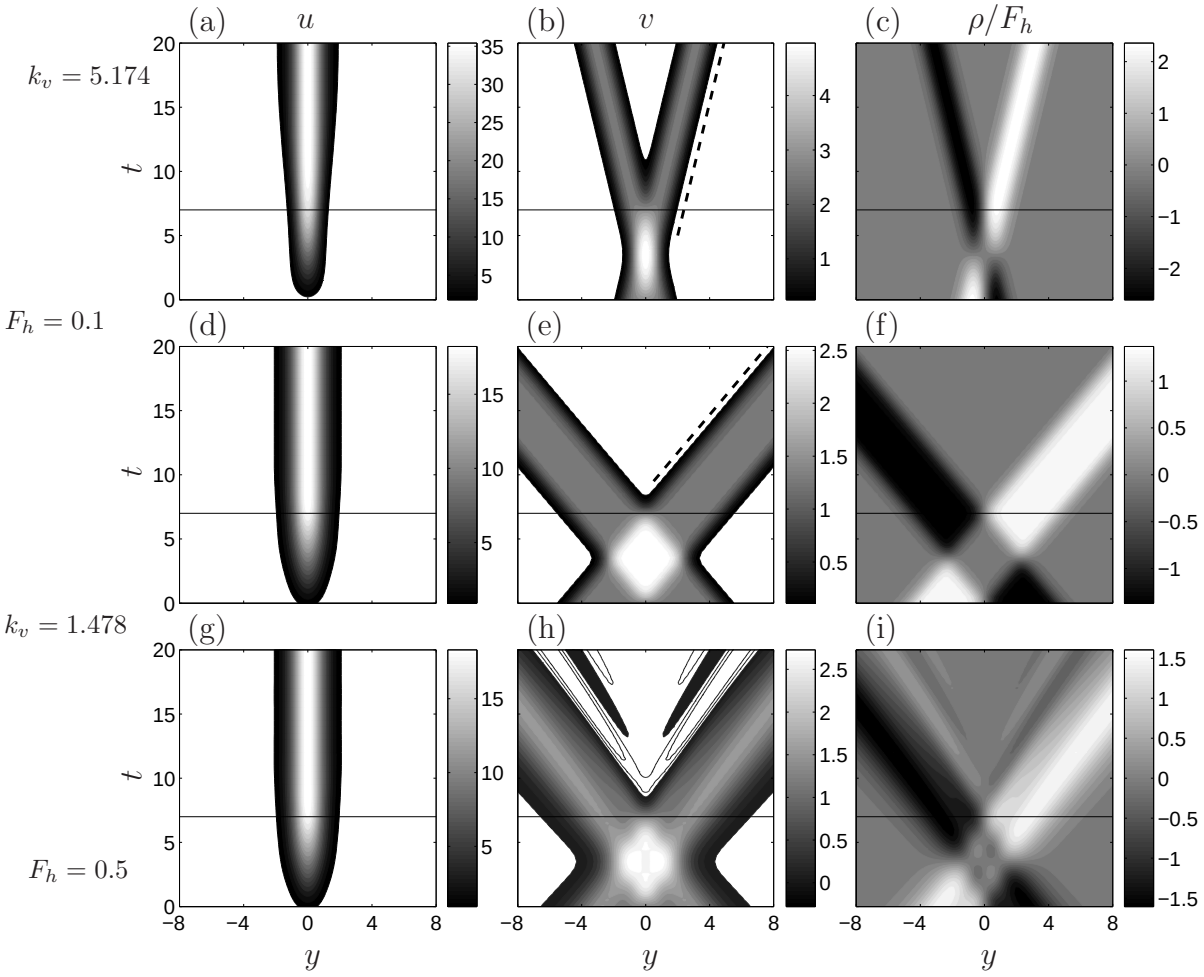

Figure 6.9: Spatio-temporal diagram of the optimal perturbations for $k_x = 0$, $T = 7$ (indicated by a horizontal line on each plot), $F_h = 0.1$ and $k_v = 5.174$ (a-c), $F_h = 0.1$ and $k_v = 1.478$ (d-f), and $F_h = 0.5$ and $k_v = 1.478$ (g-i). The left (a,d,g) middle (b,e,h) and right (c,f,i) columns respectively show cuts of u, v and $F_h^{-1}\rho$ at their maximum amplitude. The complex phase of v lags by $\pi/2$ that of ρ and has a difference of π with that of u. Negative contours of v in (h) are indicated by black lines at the levels -0.05 and -0.15. Dashed lines in (b) and (e) indicate k_v^{-1}, corresponding to the cross-stream wave velocity in the $F_h \to 0$ limit (see text). The axes are all as in the lower left plot.

dispersion relation

$$\omega = \pm \frac{F_h^{-1} k_y}{\sqrt{k_y^2 + k_z^2}}. \tag{6.10}$$

where k_y is the cross-stream wavenumber of the perturbation. For waves with large horizontal-to-vertical aspect ratio $k_y/k_z \ll 1$, the dispersion relation (6.10) can be expanded as

$$\omega = \pm \frac{1}{F_h} \frac{k_y}{k_z} \mp \frac{1}{2F_h} \left(\frac{k_y}{k_z} \right)^3 + \mathcal{O}\left([k_y/k_z]^5 \right). \tag{6.11}$$

Equation (6.11) implies that dispersive effects appear at third order in k_y/k_z. The Billant & Chomaz similarity implies that the vertical wavenumber k_z scales as F_h^{-1} so that expansion (6.11) becomes increasingly accurate as stratification gets stronger. Indeed, for $F_h \leq 1$ we have

$$\omega \approx \pm \frac{k_y}{k_v} \left(1 - F_h^2 \frac{k_y^2}{2k_v^2} \right), \tag{6.12}$$

which is now written in terms of the rescaled vertical wavenumber k_v. Equation (6.12) indicates that internal gravity waves become non-dispersive in the strong stratification limit $F_h \to 0$. The non-dispersive nature of the internal waves in the strongly stratified limit can be seen in figure 6.9 for $F_h = 0.1$; it allows the (v, ρ) structures to travel without noticeable dispersion (figures 6.9b,c for $k_v = 1.478$ and 6.9(e,f) for $k_v = 5.174$). In the strongly stratified limit, the phase and group velocities in the cross stream direction coincide and are given by $\omega/k_y = k_v^{-1}$, which corresponds to the slope of the dashed lines of figures 6.9(b,e). For $F_h = 0.5$, dispersive effects become noticeable as shown in figure 6.9(g-i).

The dependence of σ_m on k_v for $T = 7$ is shown by the dotted line of figure 6.2. Although the curve shown corresponds to $F_h = 0.1$, it should be remarked that $\sigma_m(k_v)$ converges rapidly to its $F_h \to 0$ limit. Indeed, $\sigma_m(k_v)$ does not change more than a 0.5% for all the computed optimal perturbations with $F_h \leq 1$. The rapid convergence of $\sigma_m(k_v)$ contrasts with the much slower convergence to non-dispersive dynamics, which is clear from the differences between $F_h = 0.1$ and $F_h = 0.5$ in figure 6.9. The difference of σ_m between the strongly stratified and unstratified cases is large for $k_v \sim \mathcal{O}(1)$ but decreases as k_v increases. Bakas & Farrell [9] found that, in the infinite constant shear case, the optimal mean growth rate approaches asymptotically a constant value $\sigma_m^\infty(T)$ in the $k_z/k_y \to \infty$ limit, where

$$\sigma_m^\infty = \frac{1}{2T} \ln(1 + U_c'^2 T^2). \tag{6.13}$$

Expression (6.13) sets an upper bound in energy growth for the $k_x = 0$ perturbations in the stratified case. This bound is slightly lower than its unstratified counterpart

given by σ_m^c in (6.8). More relevant than the similarity between σ_m^∞ and σ_m^c is the difference that, in the stratified case, perturbation energy does not keep increasing as $t \to \infty$.

The main effect of stratification for the generation of streamwise independent streaks is that the forcing by v is no longer constant in time. In this stratified lift-up, the optimal forcing is produced by an internal wave structure that can excite v only during a transient. This gives one example in which internal waves are important for the transient dynamics of a horizontal shear layer. It is instructive to inquire deeper into the possible relevance of internal waves.

6.4.2 Craya-Herring decomposition

Following [54], we define the Craya-Herring basis $(\mathbf{e}_1, \mathbf{e}_2, \mathbf{e}_3)$ as $\mathbf{e}_1 = \mathbf{k} \times \mathbf{e}_z / |\mathbf{k} \times \mathbf{e}_z|$, $\mathbf{e}_2 = \mathbf{k} \times (\mathbf{k} \times \mathbf{e}_z) / |\mathbf{k} \times (\mathbf{k} \times \mathbf{e}_z)|$ and $\mathbf{e}_3 = \mathbf{k}/k$, where $\mathbf{k} = (k_x, k_y, k_z)^T$ is the wave vector and $k = |\mathbf{k}|$ is its magnitude. In this orthonormal basis, the 3D-Fourier transform of the velocity field becomes $\hat{\mathbf{u}} = \phi_1 \mathbf{e}_1 + \phi_2 \mathbf{e}_2$ because $\hat{\mathbf{u}} \cdot \mathbf{e}_3 = 0$ due to the incompressibility condition. When $\sqrt{k_x^2 + k_y^2} \neq 0$, the energy density in spectral space $\epsilon(\mathbf{k})$ is given by

$$2\epsilon(\mathbf{k}) = |\phi_1|^2 + |\phi_2|^2 + |\phi_3|^2, \tag{6.14}$$

with

$$\phi_1 = \frac{i}{k_h} \hat{\omega}_z, \tag{6.15a}$$

$$\phi_2 = -\frac{k}{k_h} \hat{w}, \tag{6.15b}$$

$$\phi_3 = N \hat{\rho}, \tag{6.15c}$$

where $k_h = \sqrt{k_x^2 + k_y^2}$, and $\hat{\omega}_z$, $\hat{w}$ and $\hat{\rho}$ are the Fourier transformed vertical vorticity, vertical velocity and density. The total perturbation energy for wavenumbers (k_x, k_z) can be expressed as $E(k_x, k_y) = \int \epsilon(k_x, k_y, k_z)\, \mathrm{d}k_y$.

The $\phi_1 \mathbf{e}_1$ part of the velocity field is purely horizontal so it does not directly affect the disturbance density field. For the linear dynamics in the absence of a basic flow, decomposition (6.15) provides a separation of the fields in which the $\phi_1 \mathbf{e}_1$ part of the velocity field decouples from the internal wave dynamics given by ϕ_2 and ϕ_3. Despite the fact that the wave and vortical parts of the velocity field cannot be unambiguously split in a general case, this decomposition provides an objective, physically motivated way of quantifying the wave content of the perturbative field. We will thus refer to the different components as the wave and vortex parts of the flow fields.

Figure 6.10 shows the fraction of the total energy contained in the vortex part ϕ_1 of the velocity field, for the optimal perturbations with $T = 7$ and $F_h = 1$ and 0.1.

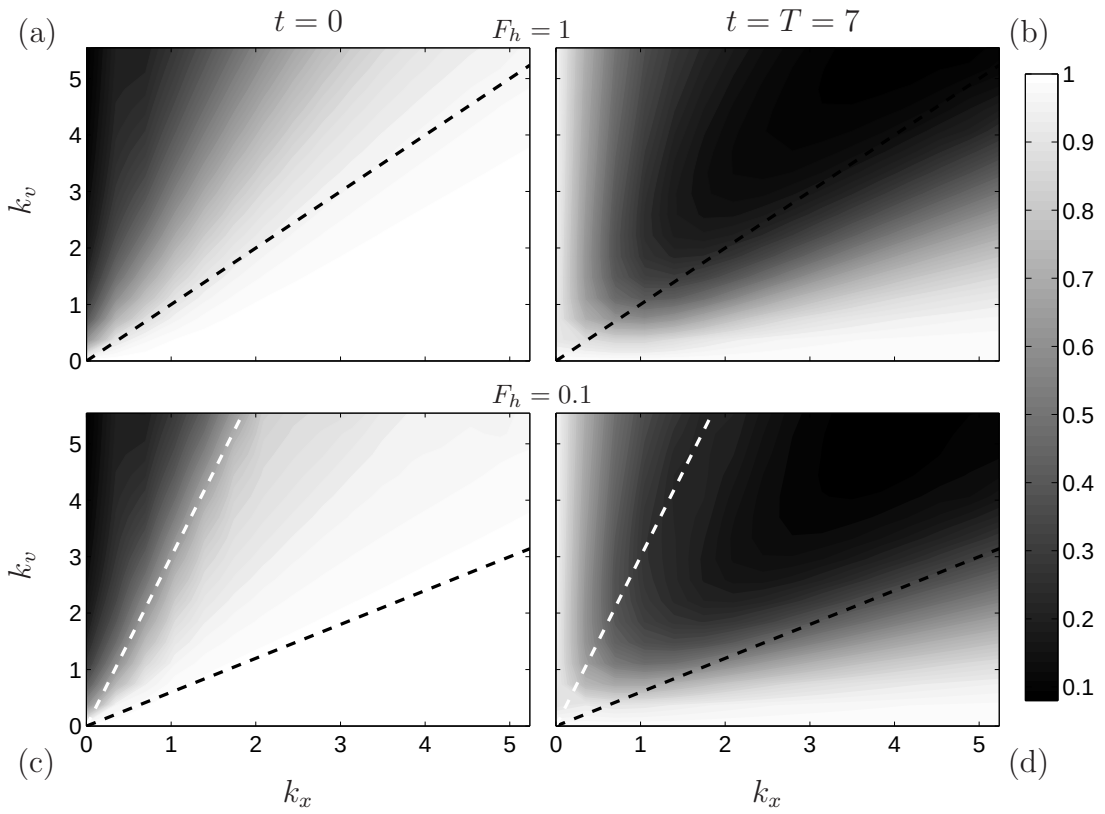

Figure 6.10: Energy fraction in the vortical part $\frac{\int |\phi_1|^2 \, \mathrm{d}k_y}{E}$ for the optimal perturbations at $t = 0$ (left column a,c) and optimal response at $t = 7$ (right column b,d). Froude numbers are $F_h = 1$ for the top row (a,b) and $F_h = 0.1$ for the bottom one (c,d), as indicated on the figure. Here, for $k_x = 0$, the energy of the horizontal mean flow (which corresponds to $\sqrt{k_x^2 + k_y^2} = 0$) has been added to the energy of ϕ_1. The dashed lines correspond to those of figure 6.7.

Figure 6.10 shows the energy fractions of the optimal initial condition ($t = 0$) and the optimal response ($t = T = 7$). Also shown are the corresponding dashed lines of figure 6.7 indicating the ratios r_{max} and r_{min}. Dark shades indicate that most of the perturbation energy corresponds to gravity waves. In the left column (fig. 6.10a,c) we observe that the wave content of the optimal initial condition depends mainly on r. The energy of the optimal initial condition is completely given by the vortex part for $r = 0$, the energy of the wave part becoming increasingly important as r increases. The dashed white line of r_{min} in 6.10(c) coincides roughly with the region where the energy of the optimal initial condition changes from being mostly vortex to mostly wave. The energy of the optimal response (b,d) is mostly given by the vortex part for $k_x \sim 0$ and for $k_v \sim 0$, while for most of the domain where

$k_x, k_v \gtrsim 1$, the energy of the optimal response is mainly in the wave part.

6.5 Wave emission

For $k_x, k_v \gtrsim 1$, there is strong generation of internal waves. A very important aspect concerns whether the generated wave energy remains in the wave part after T. Figure 6.11 shows spatio-temporal diagrams of the vertical vorticity ω_z (a,c), vertical velocity w (b,d), and the vortex and wave energy density (respectively in figures 6.11e and 6.11f), for the optimal perturbation with $F_h = 0.1$, $T = 7$ and $(k_x, k_v) = (4.887, 2.957)$. This (k_x, k_v) is in the region of wave generation and large energy growth (close to the dashed black line in 6.7 and 6.10). From $t = 0$ to 7, the energy of the perturbation shown in 6.11 grows by a factor of 43.57, more than any unstable mode during that time. Initially, most of the energy growth occurs on the vortical part (fig. 6.11e). Wave energy starts being noticeable around $t = 5$ and then increases quickly when part of the vortex energy is transferred into the wave part of the flow. The generated wave is then radiated away after the optimization time.

Figure 6.12 shows $G(t)$ of the optimal perturbations for $F_h = 0.1$, same (k_x, k_v) as in figure 6.11 and several optimization times. In all cases $G(t)$ increases initially between zero and $t \gtrsim T$, and then stabilizes at a nearly constant level (T is indicated by the $\bullet$'s) corresponding to the inviscid propagation of the waves outside the shear region. The dashed line shows the gain of the most unstable eigenmode. The thick black line approximating G_{max} for $(k_x, k_v) = (4.887, 2.957)$ indicates that, for these (k_x, k_v), σ_m is larger than σ_{KH} up to $T \approx 13.5$. Figure 6.12 reflects that the mechanisms of wave generation and radiation shown in figure 6.11 remains for different T. It should be mentioned that r_{max} increases with T and that the qualitative behaviour described in figure 6.11 is the same for different optimization times[8]. Another check of the robustness of the wave emission mechanism described here has been performed by setting $\phi_2 = \phi_3 = 0$ in the optimal initial condition. The resulting evolution of the perturbation was very little affected, which supports that this process can be considered as an example of spontaneous generation of internal waves.

6.5.1 Role of non-normality on wave-vortex interactions

The perturbation evolution equations (6.4) can be written in the Craya-Herring basis as

$$\frac{\partial}{\partial t}\begin{pmatrix}\phi_1\\ \phi_2\\ \phi_3\end{pmatrix} = \begin{pmatrix} A_{k_h} + B_{k_h} & k_z C_{1|k} & 0 \\ k_z\left(W_X - C_{k|1}\right) & A_{k/k_h} + k_z^2 B_{kk_h} & \frac{k_h}{k} F_h^{-1} \\ 0 & -\frac{k_h}{k} F_h^{-1} & A_1 \end{pmatrix}\begin{pmatrix}\phi_1\\ \phi_2\\ \phi_3\end{pmatrix}, \quad (6.16a)$$

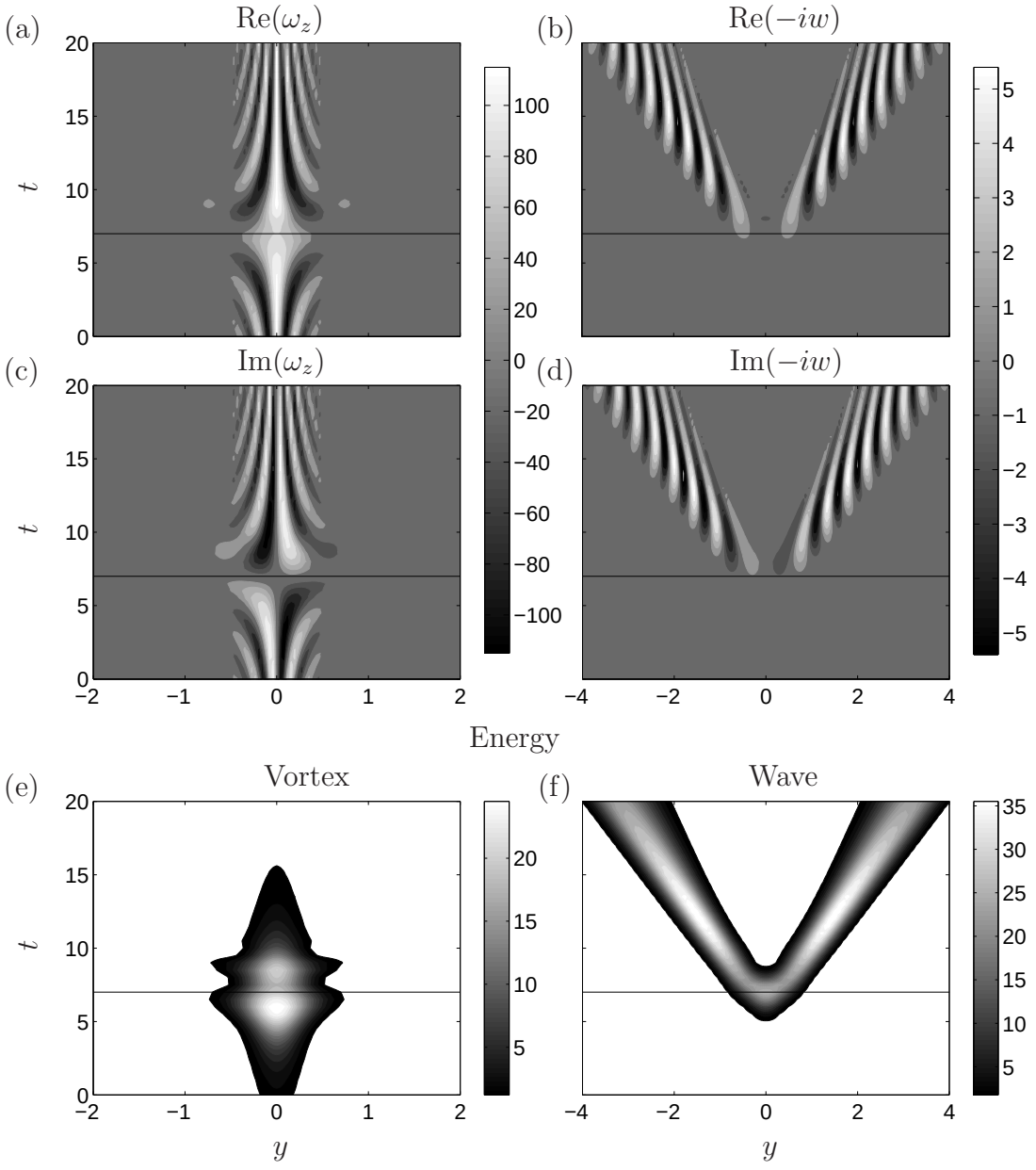

Figure 6.11: Spatio-temporal diagrams of the optimal perturbation for $T = 7$ (horizontal line), $(k_x, k_v) = (4.887, 2.957)$ and $F_h = 0.1$. At $y = 0$, the complex phase of $\hat{\omega}_z$ leads that of $\hat{w}$ by $\pi/2$; it has been set so that $\hat{\omega}_z$ is purely real at $(y, t) = (0, 0)$. The initial energy amplitude is normalized to one.

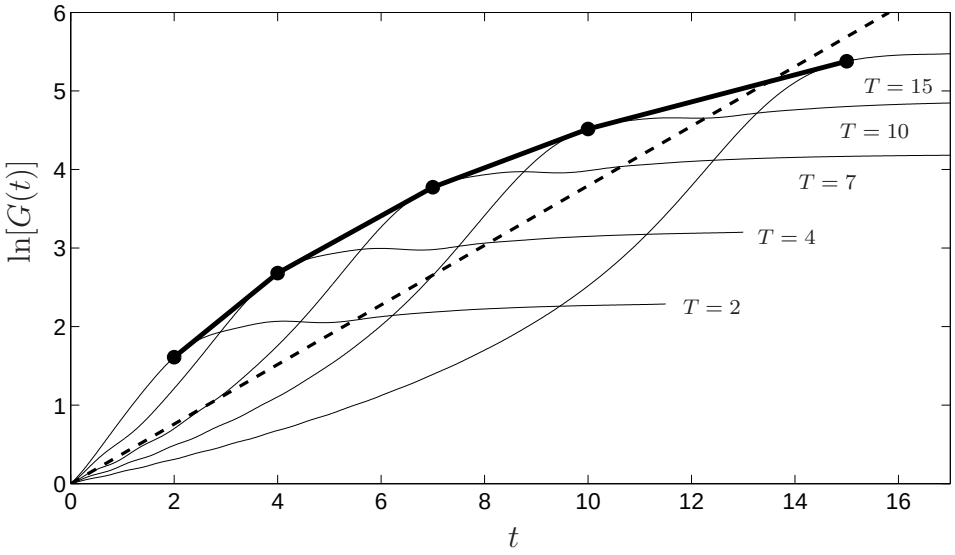

Figure 6.12: Evolution of the energy gain $G(t)$ (thin lines) of the optimal perturbations for $(k_x, k_v) = (4.887, 2.957)$ and $T = 2, 4, 7, 10$ and 15. The optimal gain $G_{max}(T)$ corresponding to each curve is indicated by a $\bullet$ sign. The $\bullet$ signs are connected by a thick black line that approximates the envelope of $G(t)$ for $(k_x, k_v) = (4.887, 2.957)$. The dashed line indicates the gain of the most unstable eigenmode.

where the convolution operators $A_{a(\mathbf{k})}$, $B_{b(\mathbf{k})}$, $C_{a(\mathbf{k})|b(\mathbf{k})}$ and W_X are defined according to their action as

$$A_{a(\cdot)}\phi = -\frac{ik_x}{a(k_x,k_y,k_z)} \int \hat{U}(k_y - l_y) a(k_x, l, k_z) \hat{\phi}(l)\, \mathrm{d}l, \tag{6.16b}$$

$$B_{b(\cdot)}\phi = \frac{ik_x}{b(k_x,k_y,k_z)} \int \hat{U}''(k_y - l) \frac{\hat{\phi}(l)}{b(k_x,l,k_z)}\, \mathrm{d}l, \tag{6.16c}$$

$$C_{a(\cdot)|b(\cdot)}\phi = -\frac{1}{a(k_x,k_y,k_z)} \int \hat{U}'(k_y - l) \frac{k_x^2 + k_y l}{k_h\sqrt{k_x^2 + l^2}} \frac{\phi(l)}{b(k_x,l,k_z)}\, \mathrm{d}l, \tag{6.16d}$$

and

$$W_X\phi_1 = \frac{1}{kk_h} \int \left(\hat{U}'(k_y - l)\sqrt{k_x^2 + l^2} - i\hat{U}(k_y - l) \frac{l(k_y^2 - l^2)}{\sqrt{k_x^2 + l^2}} \right) \phi_1(l)\, \mathrm{d}l. \tag{6.16e}$$

The equations for ϕ_1 and ϕ_2 in (6.16) can be obtained by taking the dot product between the Fourier transform of the momentum equations (6.2a) and the Craya-Herring base vectors $\mathbf{e}_1$ and $\mathbf{e}_2$. The equation for ϕ_3 can be obtained directly from the Fourier transform of the density equation 6.2c.

The off-diagonal terms proportional to N are responsible for the internal gravity waves. The action of the operator $A_{a(\mathbf{k})}$ on ϕ implies advection of the quantity $a(\mathbf{k})\phi$ by the base flow. The action of the operator $B_{b(\mathbf{k})}$ on ϕ represents the reaction on ϕ due to the transport of base flow by ϕ. The presence of the operator $C_{a|b}$ on (6.16a) has its origin on the transport of base flow vorticity; it represents an effective Coriolis force on the perturbation. The operator W_X acts on the vortical part ϕ_1 and affects the wave part ϕ_2, breaking the nearly anti-symmetric structure of the evolution matrix in (6.16a). The non-normality of the evolution operator that involves effects between the wave and vortex parts is represented here by the $k_z W_X \phi_1$ term.

The equation for ϕ_1 corresponds to the ω_z equation. The term $A_{k_h}\phi_1$ represents advection of $k_h\phi_1$ and accounts for the advection of vertical vorticity ω_z by the base flow note 6.15a. The term $B_{k_h}\phi_1$ is the reaction of the base flow on ϕ_1, it represents the transport of base flow vorticity by the ϕ_1 perturbation. The term $k_z C_{1|k}\phi_2$ is the effect of ϕ_2 on ϕ_1, it represents the three dimensional effect of stretching of base flow vorticity by vertical velocity w.

The equation for ϕ_2 corresponds to the vertical velocity equation with the pressure solved in terms of (ϕ_1, ϕ_2, ϕ_3). The term $A_{k/k_h}\phi_2$ represents advection of $k\phi_2/k_h$ by the base flow. Using the dispersion relation $\omega = F_h^{-1}k_h/k$, the advected quantity becomes $F_h\phi_2/\omega$, which evokes a connection with wave action[21]. The term $k_z^2 B_{kk_h}\phi_2$ is the reaction of the base flow on ϕ_2 and $k_z(W_X - C_{k|1})\phi_1$ represents effects on ϕ_2 that originate on pressure fluctuations driven by ϕ_1. The term $\frac{k_h}{k}F_h^{-1}\phi_3$ is the effect of gravity on ϕ_2.The equation for ϕ_3 contains advection of densitty by the base flow $A_1\phi_3$ and the effect of the vertical velocity $-\frac{k_h}{k}F_h^{-1}\phi_2$.

The energy evolution of the perturbations is given by

$$\frac{\partial E}{\partial t} = \int \mathrm{Re}[\overbrace{\phi_1^* A_{k_h}\phi_1 + \phi_2^* A_{k/k_h}\phi_2 + \phi_3^* A_1\phi_3}^{\text{Advection terms}} + \overbrace{\phi_1^* B_{k_h}\phi_1 + k_z^2\phi_2^* B_{kk_h}\phi_2}^{\text{Base flow transport}} + \underbrace{k_z(\phi_1^* C_{1|k}\phi_2 - \phi_2^* C_{k|1}\phi_1)}_{\substack{\text{Coriolis-like terms}\\ \text{(inertial waves)}}} + \underbrace{k_z\phi_2^* W_X\phi_1}_{\substack{\text{Non-normal}\\ \text{wave-vortex}}} + \underbrace{F_h^{-1}\frac{k_h}{k}(\phi_2^*\phi_3 - \phi_3^*\phi_2)}_{\text{Gravity waves}}]\,\mathrm{d}k_y. \tag{6.17}$$

The origin of each of the terms is stated in (6.17). Several terms in (6.17) give no net contribution to perturbation energy. Such is the case for the two base flow transport terms, each of which gives a zero contribution in this case of parallel shear flow. The same is obviously the case for the sum of the gravity wave terms, which account for kinetic/potential energy transfers and give no net contribution. Remarkably, that is also the case for the Coriolis-like terms, which account for $\phi_1 \leftrightarrow \phi_2$ transfers and give no net energy contribution. All change in perturbation energy associated directly to both ϕ_1 and ϕ_2 is given by the non-normal wave-vortex term. The other changes in perturbation energy are given by the advection terms $\phi_1^* A_{k_h}\phi_1$ and $\phi_2^* A_{k/k_h}\phi_2$.

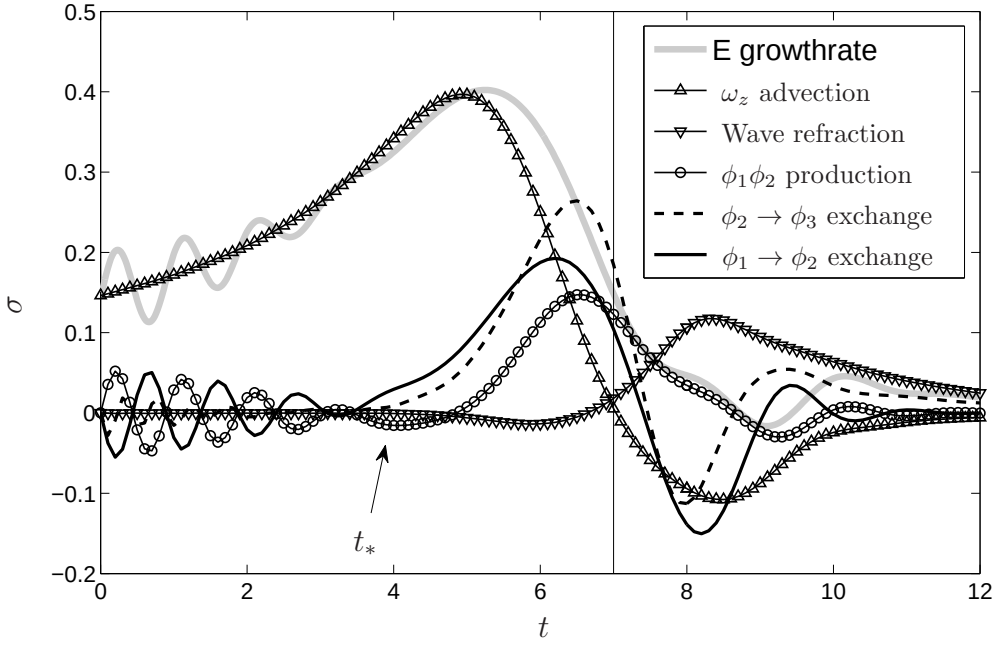

Figure 6.13: Decomposition of the instantaneous growth rate σ into the contribution from the different effects. The meaning of each curve is indicated in the legend. The $\phi_3 \to \phi_2$ and $\phi_2 \to \phi_1$ exchanges are omitted; they are, respectively, exactly opposite to the $\phi_2 \to \phi_3$ and $\phi_1 \to \phi_2$ exchanges.

While the term $\phi_1^* A_{k_h} \phi_1$ accounts for the KH instability and the Orr mechanism, the term $\phi_2^* A_{k/k_h} \phi_2$ accounts for wave refraction.

Figure 6.13 shows the contribution to the instantaneous growth rate σ (shown by the thick gray line) of each of the relevant terms in (6.17). The W_X and the two advection terms, which are those that contribute to total perturbation energy, are shown with $\circ$ (wave-vortex term W_X), $\triangle$ ($k_h\phi_1$ advection) and $\triangledown$ ($k\phi_2/k_h$ advection) symbols. The lines without symbols indicate energy transfers between components. The continuous line indicates the energy going into ϕ_2 from ϕ_1 and the dashed line the energy going into ϕ_3 from ϕ_2; the lines corresponding to the inverse of those transfers are not shown. At the beginning and up to $t \sim 5$, σ is mostly given by the $\phi_1^* A_{k_h} \phi_1$ term, except for oscillations taking place up to $t \sim 3$. The oscillations of σ correspond to the contribution of the non-normal $k_z \phi_2^* W_X \phi_1$ term acting on the equation for ϕ_2. However, from $t = 0$ to $t_* \sim 4$, the W_X term and the $\phi_1 \to \phi_2$ exchange term nearly cancel each other, implying that the variations in the amplitude of ϕ_2 are not an important contribution to σ. The oscillations in σ are indeed due to fluctuations in the amplitude of ϕ_1. The oscillations in ϕ_1 are

given by the $k_z\phi_1^* C_{1|k}\phi_2$ term ($\phi_2 \to \phi_1$), whose contribution to σ is almost equal to that of $k_z\phi_2^* W_X\phi_1$ (energy growth in ϕ_2) for $t \in [0, t_*]$; the energy contribution of those two terms is approximately equal to minus the contribution of the $\phi_2^* C_{k|1}\phi_1$ term ($\phi_1 \to \phi_2$), implying the cancellation of the energy variations in ϕ_2. For $t \gtrsim t_*$, the W_X and $\phi_1 \to \phi_2$ contributions stop canceling each other and it is at that point that the amplitude of wave energy starts increasing. Also at $t \sim t_*$, kinetic energy starts being transferred into potential energy, as indicated by the dashed line. For $t_* \lesssim t \lesssim T$, the $\phi_1 \to \phi_2$ transfer term ($\phi_2^* C_{k|1}\phi_1$) is large implying a large transfer of energy going from the vortical part to the wave part, and the $\phi_1\phi_2$ production term ($k_z\phi_2^* W_X\phi_1$) is also large implying perturbation energy growth in the wave part. After the optimization time, the wave refraction term $\phi_2 A_{k/k_h}\phi_2$ induces more energy growth, compensating the energy decay induced by the ω_z advection term.

This description of the evolution of perturbation energy exemplifies the role of the non-normal $W_X\phi_1$ term on the wave-vortex interactions. On one side, the $W_X\phi_1$ term can account for the energy increase produced by the effect of waves on the vortical part; this is what happens in figure 6.13 for $0 < t \lesssim t_*$ and for stratified lift up (6.4.1). On the other side, the $W_X\phi_1$ term can account for perturbation energy increase associated to wave generation by vortical motion. Which of the roles is played depends on the Coriolis-like terms, which can be seen as transfer terms directing the energy to either ϕ_1 or ϕ_2.

6.6 Discussion

Figure 6.7 and 6.5 indicate that the transient growth for 3D perturbations decreases when stratification increases. Different is the case for the KH instability in which stratification, acting in a direction perpendicular to the plane of the base flow, is actually destabilizing [39] and the 2D modes, wherein the most unstable one, are unaffected. These two effects produce that the 2D maximum of σ_m at $k_x \approx 1$ goes from a saddle to a maximum in the (k_x, k_v)-plane (from $\times$ to $\bullet$ in 6.7). This decrease in transient growth with stratification can explain the appearance of KH billows in the strongly stratified case of BS06. In BS06, a shear layer was simulated with strong noise in the velocity fields as initial condition. Because of the magnitude of the initial noise, fast transition occurred and no KH billows were observed in their unstratified control case. Using the same initial condition with different stratification levels, they found increasing coherence of the late flow fields as stratification was increased, wherein the mentioned KH billows.

Figures 6.7 and 6.10 help in distinguishing three main regions on the (k_x, k_v) plane. First, for $k_v \sim 0$, the dynamics is dominated by the vertical vorticity (figure 6.10) and σ_m decreases with k_v in the strongly stratified limit (figure 6.7c,d). Second, for $k_x, k_v \gtrsim 1$, the optimal perturbations result in the generation of wave energy from

the vortical part (figure 6.10); these perturbations are strongly amplified around $r \sim r_{max}$ (figure 6.7). Third, for $k_x \sim 0$, the optimal transient growth consists of waves generating large horizontal velocity (figure 6.10 and section 6.4.1).

In the region in which $k_v \sim 0$, the dynamics is essentially 2D. The Orr mechanism dominates the inviscid transient growth for short time and for large k_x, while the KH instability becomes increasingly important as T increases (figure 6.2).

For $k_x, k_v \gtrsim 1$, there is strong generation of internal waves. This strong wave generation is consistent with that discussed by [10] for the constant shear case, and analogous to that described by [99] and [66] in a rotating frame. Here we have shown that this wave generation is an efficient mechanism for the amplification of perturbation energy, the most efficient indeed for short times $T \sim 7$ and comparable to the KH instability for intermediate times. The waves are emitted away from the shear layer. By performing a detailed analysis of the governing equations in the Craya-Herring frame, we have shown that there are two simultaneous effects involved in the generation and emission of internal waves. On one side, there is energy transfer from the vortical part to the wave part in a way analogous to inertial waves, here induced by the base flow vorticity. Simultaneously, there is energy extraction from the basic flow to the wave part; this is different from wave refraction because this transfer is mediated by the vortical part.

In the region around $k_x = 0$ there can be a large growth rate of perturbation energy, growth rate that is not sustained in time. As described in section 6.4.1, this growth of perturbation energy is related to the cross-stream transport of fluid parcels, as is the case for the usual lift up mechanism. This mechanism is more efficient and can persist for longer times when the vertical wavelength of the perturbations is short. A finite wavenumber of maximum amplification would be found in the presence of viscosity. This stratified lift up mechanism produces horizontal flow with vertical shear; vertically sheared horizontal flow is ubiquituous in stratified flows. In this case we have also shown that for waves with large horizontal-to-vertical aspect ratio, the Billant & Chomaz self-similarity of strongly stratified flows [17] corresponds to non-dispersive waves.

6.6.1 Possible relevance of the stratified lift-up

A different cross-stream transport involving KH billows, has been described by Arobone & Sarkar [5] in relation to the layered structure observed in BS06 and [5]. According to their description, "*The segments of the vortices that have been displaced in the transverse direction then are advected downstream by the mean flow shearing apart the vortices until pancake vortices form*"[5]. The pancake vortices they describe have a vertical size such that the vertical Froude number based on their size is order one, corresponding here to $F_h k_z \sim \mathcal{O}(1)$, similar to the zig-zag instability an to the neutral stability curve of the KH instability. They add that

the deformation of the billows is likely driven by a process similar to the zig-zag instability or to the growth of a 3D KH modes followed by the kinematic decorrelation of Lilly [72]. Another driving mechanism could be at the development of the pairing instability between succesive billows. These three mechanisms are present for vertical length scales such that $F_h k_z \sim \mathcal{O}(1)$, which is consistent with the vertical length of the KH billows.

In BS06 and [5], a shorter, viscous length scale is associated to the dislocations between KH billows. Considering that the layering is driven by one of the mechanism described in the previous paragraph, the vertical length of the dislocations can be interpreted in terms of momentum diffusion between layers displacing horizontally relative to each other. The stratified lift up mechanism described in 6.4.1 provides a different mechanism, relevant for perturbation amplification at smaller vertical scales. Early developing KH billows showing displacement with fine vertical structure and large streamwise correlation (involving succesive billows), could plausibly have an origin on the stratified lift up just described. The existence of horizontal shear layers with such a structure, however, can not be determined from BS06 or [5]. Moreover, assessing the pertinence of this lift up mechanism would require a study of its role within the nonlinear development of the instability. There is at this point no clear indication that this stratified lift up mechanism plays a role in the early development of those dislocations.

Finally, it should be remarked again that this stratified lift up mechanism does not rely on an exact symmetry of the internal waves crossing the shear layer. Indeed, any structure inducing a horizontal displacement would lead to a streamwise streak like perturbation. That is the case for a wavepacket with a size comparable to its main wavelength. In particular, soliton-like travelling structures should produce perturbations in a lift up like manner when crossing shear layers in a perpendicular way.

6.7 Summary and main conclusion

We computed the optimal perturbations for short time in a horizontal shear layer with and without density stratification. We described the effect of stratification on the amplification of the optimal perturbations and performed a Craya-Herring decomposition that allowed us to classify different types of perturbations according to the wave content of the initial and final optimal perturbations.

We have shown that the wave generating mechanism of vertically stratified horizontal shear flow [10] has a strong potential for emission of internal gravity waves. In the Craya-Herring frame, we have given a precise quantitative description of the wave-vortex interactions and the role of non normality in the linear perturbative regime.

Chapter 7

Conclusions and perspectives

Various aspects of the stability of shear flow have been studied, and several new results have been obtained.

In chapter 6, we have computed the optimal perturbations of a horizontal shear layer with vertical stratification. Three main dynamical regimes are identified: quasi two-dimensional horizontal flow, streamwise streak generation by streamwise independent internal waves crossing the shear layer (the 'stratified lift-up' in section 6.4.1), and internal wave generation and emission. The first regime is less interesting in this context, so only the latter two were described in detail. In the stratified lift-up case, it was also noted that the limit approached by the strongly stratified self-similarity of Billant & Chomaz [17] corresponds to non dispersive waves. The internal wave generation and emission was characterized with a Craya-Herring decomposition. We provided a detailed description of the wave emission process in terms of the energy production and exchanges between different components. This description was possible thanks to the original account of the perturbative dynamics of stratified flows that was developed in chapter 5.

Several open questions remain on this topic. In particular, whether the generated waves can be actually emitted or not should depend on non linear effects such as the time development of the base flow. A study like that of chapter 4 could give some indications, altough the Reynolds number required to observe substantial wave generation might be large (short wave perturbations are damped in our viscous results in [7]). One can expect that the shortest waves remain 'captured' in the (base) flow [see 24, for wave capture] because their intrinsic propagation velocity is low. That would yield a finite wavelength for the emitted waves, short enough so that the wave generation process is efficient but long enough so that the generated waves can escape.

Other very important question concerns the decomposition developed in chapter 5. We provide some expressions that could serve as a diagnostic of gravity wave

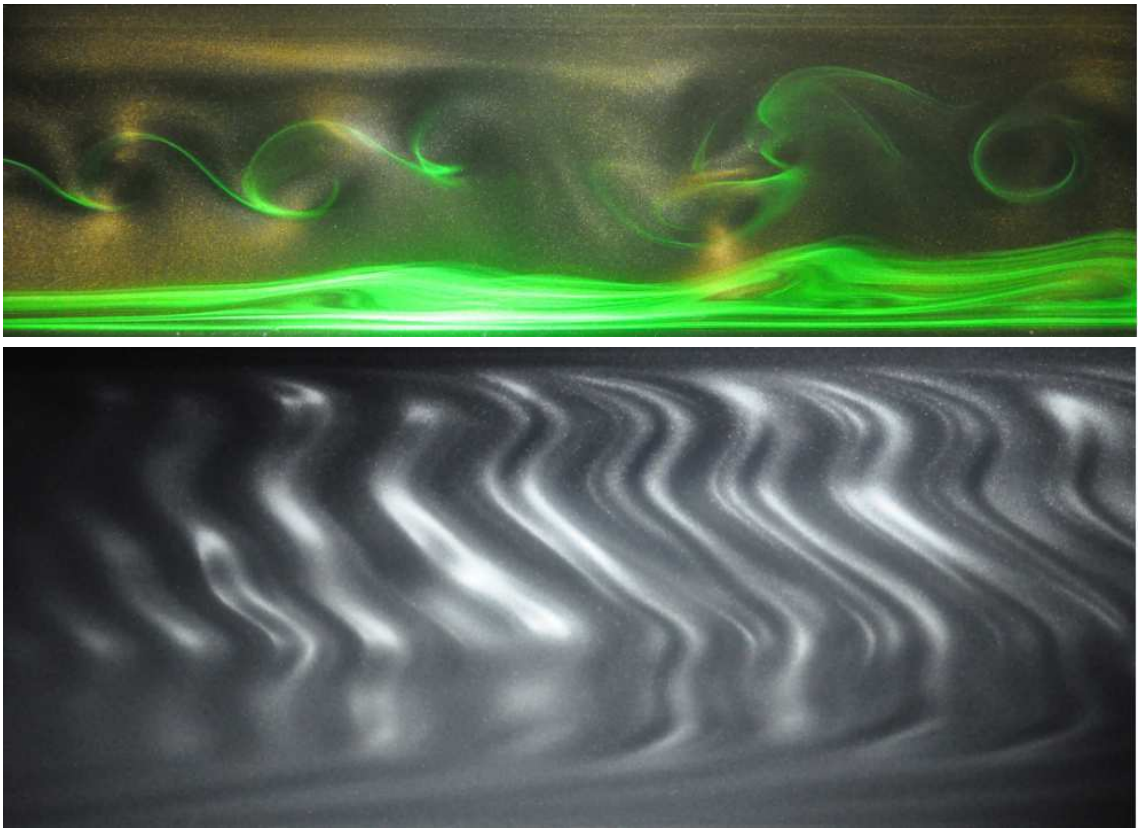

Figure 7.1: Top (top) and side (bottom) view of the vertically stratified horizontal shear layer produced at DAMTP.

emission. However, a key limitation for its broader applicability concerns the assumption of vertical homogeneity of the base flow. It would thus be important to derive the analogous decomposition for a more general base flow, still with two components but with arbitrary vertical dependence. I think that the addition of that vertical dependence should not add too many complications for the derivation. To have been able to include the effects of a rotating frame in this decomposition is also important for its applicability. In a rotating case, however, the identification of the toroidal (ϕ_1) and poloidal (ϕ_2) components respectively to potential vorticity and waves is lost [87]. However, the role of the non normal term for the energetics remains valid in the rotating case, and the full decomposition could also be applied on time dependent base flows.

Another aspect on stratified flows concerns experiments. During my PhD, I had the opportunity to spend 7 weeks at the Department of Applied Mathematics and Theoretical Physics (DAMTP) in Cambridge. That visit was possible thanks to a David Crighton Fellowship, to which I applied with the support of Prof. Colm

Caulfield and J.M. Chomaz. The main goal of the visit was to study the horizontal shear layer with vertical stratification experimentally. The project was then performed in collaboration with the Director of the Batchelor's Laboratory, Prof. S. Dalziel. The idea was to observe the vertical structure that such a flow develops. We made use of the stratified water channel (Kovasznay type [80]) existing at DAMTP. The tank consists on a closed channel driven by two stacks of horizontal disks, whose rotation drives the flow horizontally by viscous drag. By placing a vertical splitter plate, we were able to produce and characterize a horizontal shear layer. Several experimental techniques were achieved: dye and pearlescence visualization, synthetic schlieren and particle image velocimetry. In the top image of figure 7.1, the KH billows resulting from the shear layer can be observed thanks to pearlescence and fluorescein. A merging of 2 billows can be observed after the 3rd billow from the left. An important difficulty, however, came from the fact that the horizontal velocity attained in the flow was not uniform in the vertical, thus producing vertical shearing of the KH billows, as can be seen on the bottom picture. This non-uniformity is most likely due to the excitation of low internal wave modes when the system is accelerated. Accelerating without generating those waves is then analogous to pushing a bucket of water without perturbing the surface; it can hardly be avoided. That problem made it substantially difficult to assess the intrinsic vertical lengthscales that appear naturally from a vertically homogeneous flow. Still, quantitative data was carefully obtained and further post-processing could allow some conclusions. One direction could be to look for correlations between vertical variations and the flow velocity. Another could be the comparison to DNS.

In chapter 4 we have computed the optimal perturbations on a time developing mixing layer. Thus, we have been able to eliminate a strong assumption of previous studies concerning the secondary instabilities of shear layers, the freezing in time of the base flow. This has allowed us to establish a connection between the usual transient growth of parallel shear flow and the secondary instabilities of the Kelvin-Helmholtz billows. When we consider optimal perturbations starting early with respect to the evolution of the base flow ($T_0 = 0$), they have time to growth considerably when the flow is still nearly parallel. The resulting most amplified optimal perturbations (occurring $k_z \lesssim 1$ for $T_0 = 0$) localize first around the hyperbolic stagnation point as the billow forms, and then strongly excites the elliptical instability centred at the billow core. The resulting perturbation resembles a displacement of the billows. The situation changes if we consider optimal perturbations starting later with respect to the evolution of the base flow ($T_0 = 20$). In that case the hyperbolic point is present from the early stages of the optimization interval, allowing the optimal perturbation to efficiently exploit the transient growth mechanism of the hyperbolic point [28]. Thus, in this case the most amplified optimal perturbations grow around the 'braid', and roll up around the billow core as commonly observed

in simulations and experiments.

Some extensions of this work concern nonlinear DNS, either with random initial conditions and specially with optimal initial conditions. That should allow to see whether the found mechanisms are still relevant in more realistic situation. That would require careful attention on the amplitude of the initial conditions. Some preliminary simulations with stochastic initial conditions have been performed, the result seem consistent with the linear predictions. A possibility that seems interesting for future research is to assess the receptivity of the 2D flow to stochastic forcing at different times. That might yield an idea of the moments during the evolution that are more prone to trigger transition. The effect of the Reynolds number is likely to be very relevant in that case, eventually giving a clue on the mixing transition [40].

In chapter 3 we have found a new equation that determines the optimal and sub-optimal perturbations for inviscid streamwise-independent perturbations in arbitrary plane shear flow. Those are the type of perturbations that grow due to the lift-up mechanism. The new equation constitutes an eigenvalue problem, the optimal and sub-optimal perturbations appear as eigenfunctions and their associated eigenvalues determine the gain of the perturbations. We have used this equation to give analytic solutions for the optimal perturbations of plane Couette and Poiseuille flow. We have also provided asymptotic approximations for large spanwise wavenumber k_z for two general types of shear profile: maximum shear within the domain and maximum shear at a wall. Those asymptotic expressions provided good approximations for the optimal gain for $k_z \gtrsim 10$ and scaling laws for the shape of the optimal perturbations.

One possible extension of the work of chapter 3 is the consideration of viscous effects. This, however, breaks the time reflexional symmetry of the problem, so obtaining comparable analytical results seems unlikely. A more viable alternative is to heuristically add dissipation to the inviscid results, conserving the structure provided by the set of eigenfunctions (note that the forcing on u by these v-eigenfunctions satisfy orthogonality relations).

A procedure similar to that of chapter 3 should be applicable in the case of the anti lift-up mechanism [4], which takes place for axisymmetric perturbations around vortices. Finally, considering the condition for optimal initial time (3.16) can yield to some interesting insight on the evolution of oblique waves described in section 2.5.3. Despite their apparent simplicity, understanding the dynamics of these oblique waves is non trivial.

Another interesting aspect is to understand what is possible to obtain from the characterization of non-normal effects sketched in section 2.3. Some preliminary tests on the simplest models confirm that the 'conserved quantity' is actually con-

served, although no quantitative statement concerning the meaning of (2.32) can be made for the moment.

I could think (naively for sure!) that its possible to establish some connection with detail balance [102], the quantum origins of the classical [104], the origins of time asymmetry [2] or the dynamical description of living systems [55, 69]...

Appendix A

Derivation of the Craya-Herring equations and some extra discussion

To obtain the dynamical equations in the Craya-Herring frame, we project the governing equations (5.16) on the base $\mathbf{e}_i$. Note that adding the pressure term in (5.16) would not contribute when taking the inner product with either $\mathbf{e}_1$ or $\mathbf{e}_2$. However, because of the different expression used for the horizontal and vertical momentum equations (resp. 5.2a and 5.2b), the second term in (5.16) coming from $-\nabla(\mathbf{U}\cdot\mathbf{u})$ has to be included. That term would not contribute if the expression analogous to (5.2a) was used for the vertical momentum equation too. The horizontal vorticity of the perturbation would appear explicitly instead, leading of course to the same result.

In the following, I detail the analytical procedure used to compute (5.19b) while giving physical interpretations of the different terms and equations. For convenience, the components of the basic flow U_x and U_y will be sometimes called U and V, respectively.

A.1 Vortical part

Computing (5.16)$\cdot\mathbf{e}_1$, omitting the viscous term and multiplying by k_h gives

$$\begin{aligned} k_h\frac{\partial\phi_1}{\partial t} &= k_yV*\omega_z + k_xU*\omega_z + k_y\Omega*u_y + k_x\Omega*u_x \\ &= -i[k_yV+k_xU]*k'_h\phi_1 + k_y\Omega*(u_y^v+u_y^w) + k_x\Omega*(u_x^v+u_x^w). \end{aligned} \tag{A.1}$$

Here we have used (5.7a) and the components of $\mathbf{u}_h = (u_x^v+u_x^w, u_y^v+u_y^w)^T$ are given by (5.9). Note that the ks in the squared braces are not primed and thus do

not inmediately represent derivatives of $\mathbf{U}$; because of the convolution those terms represent derivatives of products. We can expand those derivatives by performing some simple manipulations. For example, on the first term we have

$$\begin{aligned} -ik_yV * k'_h\phi_1 = & -i\int k_yV(\mathbf{k}_h-\mathbf{k}'_h)\phi_1(\mathbf{k}'_h,k_z)k'_h\,\mathrm{d}k'_x\mathrm{d}k'_y \\ = & -i\int (k_y-k'_y+k'_y)V_-\phi'_1k'_h\,\mathrm{d}k'_x\mathrm{d}k'_y \\ = & -\int ik'_h\{(k_y-k'_y)V_-\phi'_1+V_-\phi'_1k'_y\}\,\mathrm{d}k'_x\mathrm{d}k'_y \\ = & -\int k'_h\{\partial_yV_-\phi'_1+V_-\partial_y\phi'_1\}\,\mathrm{d}k'_x\mathrm{d}k'_y \\ = & -\partial_yV * k'_h\phi_1 - V * k'_h\partial_y\phi_1, \end{aligned} \tag{A.2}$$

where in the integrals we denote $b' = b(\mathbf{k}')$ and $a_- = a(\mathbf{k}-\mathbf{k}')$ for any a and b. Doing the same on the second term, we obtain for the squared parenthesis in (A.1)

$$\begin{aligned} i[k_yV + k_xU] * k'_h\phi_1 &= (\partial_yV * \phi_1 + V * \partial_y\phi_1)k'_h \\ &\quad + (\partial_xU * \phi_1 + U * \partial_x\phi_1)k'_h \\ &= (U * \partial_x\phi_1 + V * \partial_y\phi_1 + \nabla\cdot\mathbf{U} * \phi_1)k'_h \\ &= U * k'_h\partial_x\phi_1 + V * k'_h\partial_y\phi_1 \\ &= \mathbf{U}\bullet k'_h\nabla\phi_1. \end{aligned} \tag{A.3}$$

The term $\mathbf{U}\bullet k'_h\nabla\phi_1$ shows that expression (A.3) is the advection of $k_h\phi_1$ by the basic flow $\mathbf{U}$. These operations can and will be performed more compactly. Doing similar manipulations on the other terms we can get

$$k_h\frac{\partial\phi_1}{\partial t} = -\mathbf{U}\bullet k'_h\nabla\phi_1 - i(\mathbf{u}^v_h\bullet\nabla\Omega + \mathbf{u}^w_h\bullet\nabla\Omega) - k_z\Omega * u_z. \tag{A.4}$$

We keep $\mathbf{u}^w_h$ and $\mathbf{u}^v_h$ rather than ϕ_1 and ϕ_2 for interpretation purposes. Indeed, the role of each term in (A.4) is clear, including the term of advection by the base flow already mentioned. The terms $\mathbf{u}^v_h\bullet\nabla\Omega + \mathbf{u}^w_h\bullet\nabla\Omega$ correspond to base flow vorticity Ω as a source/sink of vorticity through advection by the perturbation, or transport of Ω by the perturbation. In this term there is no distinction whether $\mathbf{u}_h$ comes from the vortical part ϕ_1 or the wave part ϕ_2, thus revealing an effect of waves on vortical structures. The last term in (A.4) corresponds to stretching of basic vorticity by the spanwise perturbation velocity, thus inducing alternate thickening and thinning of vortex tubes in the spanwise direction. This is an effect of waves into the vortical part which is presesnt even when Ω is uniform. Replacing $k_h\phi_1 = i\omega_z$ into (A.4) one recovers the classical vorticity equation in the z direction.

In terms of ϕ_1 and ϕ_2 one obtains

$$\frac{\partial \phi_1}{\partial t} = L_{11}\phi_1 + L_{12}\phi_2, \tag{A.5a}$$

where

$$L_{11}\phi_1 = -\frac{1}{k_h} i\mathbf{U} \bullet \mathbf{k}'_h k'_h \phi_1 - i\nabla\Omega \bullet (\mathbf{k}'_h \times \mathbf{e}_z) \frac{\phi_1}{k_h k'_h}, \tag{A.5b}$$

$$= -\frac{i}{k_h}\left[\mathbf{U} \bullet \mathbf{k}'_h k'_h - k''^2_h \mathbf{U} \bullet \frac{\mathbf{k}'_h}{k'_h}\right]\phi_1, \tag{A.5c}$$

and

$$L_{12}\phi_2 = -i\frac{k_z}{k_h}\nabla\Omega \bullet \frac{\mathbf{k}'_h}{k' k'_h}\phi_2 + \frac{k_z}{k_h}\Omega * \frac{k'_h}{k'}\phi_2,$$

$$= \frac{k_z}{k_h}\Omega\left[\mathbf{k}''_h \bullet \mathbf{k}'_h + 1 * k'^2_h\right]\frac{\phi_2}{k' k'_h}. \tag{A.5d}$$

We will detail how to obtain (A.5c) later in A.1.2. Now we note that (A.5d) simplifies to

$$L_{12}\phi_2 = \frac{k_z}{k_h}\mathbf{k}_h \cdot \left(\Omega * \frac{\mathbf{k}'_h}{k' k'_h}\phi_2\right), \tag{A.5e}$$

using the fact that for any a and b

$$\begin{aligned} a(\mathbf{k}''_h \bullet \mathbf{k}'_h + 1 * k'^2_h)b &= \int a_- \left[(\mathbf{k}_h - \mathbf{k}'_h)\cdot \mathbf{k}'_h + k'^2_h\right] b' \,\mathrm{d}k'_x \mathrm{d}k'_y \\ &= \int a_- \left[\mathbf{k}_h \cdot \mathbf{k}'_h - \mathbf{k}'_h \cdot \mathbf{k}'_h + k'^2_h\right] b' \,\mathrm{d}k'_x \mathrm{d}k'_y \\ &= \int a_- \left[\mathbf{k}_h \cdot \mathbf{k}'_h\right] b' \,\mathrm{d}k'_x \mathrm{d}k'_y \\ &= a * (\mathbf{k}_h \cdot \mathbf{k}'_h b) = \mathbf{k}_h \cdot (a * \mathbf{k}'_h b). \end{aligned} \tag{A.6a}$$

Note that convolution manipulations such as (A.6a) (or similarly (A.2) and (A.3)) can be performed more compactly by replacing $\mathbf{k}''$ by $\mathbf{k} - \mathbf{k}'$ and passing $\mathbf{k}'$ to the other side of the convolution. At the same time, the vectorial part of the operation must be computed in the normal way on one side. For example (A.6a) becomes

$$\begin{aligned} a(\mathbf{k}''_h \bullet \mathbf{k}'_h + 1 * k'^2_h)b &= a\left[(\mathbf{k}_h - \mathbf{k}'_h) \bullet \mathbf{k}'_h + 1 * k'^2_h\right] b, \\ &= a\left[\mathbf{k}_h \bullet \mathbf{k}'_h - 1 * (\mathbf{k}'_h \cdot \mathbf{k}'_h) + 1 * k'^2_h\right] b, \\ &= a * (\mathbf{k}_h \cdot \mathbf{k}'_h b) = \mathbf{k}_h \cdot (a * \mathbf{k}'_h b). \end{aligned} \tag{A.6b}$$

The extension to cross products of this way of computing is straigth-forward. We will see that in this way we can apply to convolutions some geometric results of vector products.

A.1.1 Effect of waves on the vortical part

Lets focus for the moment on the wave-vortex interaction term L_{12}. In (A.5e) we observe that the two effects of waves on the vortical motion described in equation (A.4) can be expressed in a single term. Using (5.10b), this contribution can be also written as

$$L_{12}\phi_2 = -\frac{i}{k_h}\nabla_h \cdot (\Omega * \mathbf{u}_h^w)\,, \tag{A.7a}$$

or, replacing ϕ_1 from (5.7a) and restricting to the wave part contributions, the evolution of ω_z reduces to

$$\frac{\partial \omega_z}{\partial t} = -\nabla_h \cdot (\Omega * \mathbf{u}_h^w) + \phi_1\text{-terms}. \tag{A.7b}$$

Equation (A.7) shows that the net effect of waves into the vortical part, when integrated on a horizontal surface, reduces to a contribution on the boundary. This contribution is the flux of base flow vorticity by horizontal wave velocity.

We end by noting that result (A.7) can be directly seen from the equation (A.1). The round-trip we have taken passing through the vorticity equation (A.4) has given us the opportunity to present the calculation procedure provide equivalent expressions and give some physical interpretations.

A.1.2 Perturbative, two dimensional vortex dynamics

Some physical remarks and definitions can be made while proceeding to the derivation of (A.5c). First, from (A.5a) and (A.5b) we can write

$$k_h \frac{\partial \phi_1}{\partial t} + \mathbf{U} \bullet \nabla'_h k'_h \phi_1 = -i\nabla\Omega \bullet (\mathbf{k}'_h \times \mathbf{e}_z)\,\frac{\phi_1}{k'_h} + \phi_2\text{-terms}, \tag{A.8a}$$

or, in terms of ω_z from (5.7a),

$$\frac{\partial \omega_z}{\partial t} + \mathbf{U} \bullet \nabla_h \omega_z = -\nabla\Omega \bullet (\mathbf{k}'_h \times \mathbf{e}_z)\,\frac{\phi_1}{k'_h} + \phi_2\text{-terms'}. \tag{A.8b}$$

The source term $-\nabla\Omega \bullet (\mathbf{k}'_h \times \mathbf{e}_z)\,\phi_1/k'_h$ represents the instantaneous rate of change of ω_z of a fluid particle advected by the base flow. It can be rewritten as

$$\begin{aligned} -\nabla\Omega \bullet (\mathbf{k}'_h \times \mathbf{e}_z)\,\frac{\phi_1}{k'_h} &= i\Omega(k''_x * k'_y - k''_y * k'_x)\frac{\phi_1}{k'_h}, \\ &= i\mathbf{k}''_h\Omega \otimes \frac{\mathbf{k}'_h}{k'_h}\phi_1, \end{aligned} \tag{A.9}$$

where we have introduced the symbol $\otimes$ analogous to $\bullet$ but for the cross-product; in the plane this is $\mathbf{a} \otimes \mathbf{b} = \epsilon^{ij} a_i * b_j$ where ϵ^{ij} is the 2D Levi-Civita tensor. This

definition helps revealing some amusing aspects of (A.9) which are not evident as it stands. I shall next refer to those and other aspects while illustrating a little more the calculational procedure; to procede more directly to (A.5c) the reader may skip until (A.13). From (A.9) we can procede as before in (A.6b) with the $\bullet$ operation replaced by $\otimes$, that is

$$\begin{aligned} i\mathbf{k}''_h\Omega \otimes \frac{\mathbf{k}'_h}{k'_h}\phi_1 &= i\left[\mathbf{k}_h\Omega \otimes \mathbf{k}'_h - \Omega * (\mathbf{k}'_h \times \mathbf{k}'_h)\right]\frac{\phi_1}{k'_h} \\ &= i\mathbf{k}_h \times \left(\Omega * \frac{\mathbf{k}'_h\phi_1}{k'_h}\right) = \nabla \times (\Omega * \nabla\psi), \end{aligned} \tag{A.10}$$

where in (A.10) we replace by the streamfunction ψ from (5.11a). Applying Stokes theorem in physical space and neglecting ϕ_2-terms, the variation of the integrated ω_z on a horizontal surface S advected by $\mathbf{U}$, reduces to a line integral over the surface boundary ∂S. This integral must correspond to the flux of Ω advected by $\mathbf{u}^v_h$, which explicitly becomes

$$\int_{\partial S} \Omega\nabla\psi \cdot \mathrm{d}\mathbf{l}. \tag{A.11}$$

The integrated variation of advected ω_z given by (A.11) is of course zero if the boundary ∂S is a streamline, in which case $\nabla\psi \cdot \mathrm{d}\mathbf{l} = 0$. This just reflects the fact that the integrated ω_z can not change if there is no flux at any point in ∂S. A less obvious result can be obtained by exchanging the roles of Ω and ψ in (A.10), that is

$$\begin{aligned} i\mathbf{k}''_h\Omega \otimes \frac{\mathbf{k}'_h}{k'_h}\phi_1 &= i\mathbf{k}''_h\Omega \otimes \frac{\mathbf{k}_h}{k'_h}\phi_1 - \Omega(\mathbf{k}''_h \times \mathbf{k}''_h) * \phi_1 \\ &= i\mathbf{k}_h \times \left(\Omega\mathbf{k}''_h * \frac{\phi_1}{k'_h}\right) = \nabla \times (\psi * \nabla\Omega). \end{aligned} \tag{A.12}$$

We can apply the same argument as that leading from (A.10) to (A.11) but with the roles of Ω and ψ still exchanged. It results that the integrated variation of advected ω_z is zero if the boundary ∂S is an isovalue of Ω, in which case $\nabla\Omega \cdot \mathrm{d}\mathbf{l} = 0$. As should become clear soon, these remarks are valid in general for perturbative, two dimensional incompressible and inviscid flow.

To obtain (A.5c), we expand $\otimes$ and $\Omega = i\epsilon^{lm}k_l U_m$ succesively in (A.9) to get

$$i\mathbf{k}''_h\Omega \otimes \frac{\mathbf{k}'_h}{k'_h}\phi_1 = i\epsilon^{ij}k''_i\Omega * k'_j\frac{\phi_1}{k'_h}, \tag{A.13a}$$

$$= -\epsilon^{ij}k''_i\epsilon^{lm}k''_l U_m * k'_j\frac{\phi_1}{k'_h}, \tag{A.13b}$$

$$= -(\delta^{il}\delta^{jm} - \delta^{im}\delta^{jl})k''_i k''_l U_m * k'_j\frac{\phi_1}{k'_h}, \tag{A.13c}$$

$$= -k''^2 U_j * k'_j\frac{\phi_1}{k'_h}. \tag{A.13d}$$

From (A.13b) to (A.13c) we use the antisymmetry of ϵ^{ij}, and in (A.13c) the second term is zero for the null divergence of $\mathbf{U}$. Replacing the source term (A.13d) back into the right hand side of (A.8a) (and inserting the i factor not present in A.9), the final form of $L_{11}\phi_1$ as in (A.5c) follows directly.

Gathering all terms and using the velocity potential for the wave part, the evolution equation for ϕ_1 can be written as

$$\frac{\partial \Delta_h \psi}{\partial t} + \mathbf{U} \bullet \nabla_h \Delta_h \psi = \Delta_h \mathbf{U} \bullet \nabla \psi + \nabla_h \cdot \Delta_h (\Omega * \nabla_h \Phi) + \nu \Delta \Delta_h \psi. \tag{A.14}$$

Note that the only explicit dependence on k_z of (A.14) is on the viscous term $\nu\Delta\Delta_h\psi = \nu(k_h^2 + k_z^2)k_h^2$. If $\Phi = 0$, equation (A.14) corresponds to a reduction to two dimensional incompressible flow of the full 3D problem, reduction that results in an increased viscous dissipation (lower Reynolds number) for the 2D problem. This is what is done with the Squire transformation applicable for the eigenmodes of a parallel basic flow. It can indeed be verified that equation (A.14) leads to the Orr-Sommerfeld equation in that case (see [42] p.156). It could even seem that if $\Phi = 0$ for the initial condition, ψ would evolve according to equation (A.14) as if ψ really corresponded to 2D incompressible flow. This is not the case because, as can be seen from the full equation (5.19), ψ can excite the 2D divergent (wave) part so that for later times we will in general have $\Phi \neq 0$. In particular, the Squire theorem will apply for the eigenmodes of the full problem satisfying $\phi_2 = 0$. More generally, an extension to non-parallel basic flow of the Squire theorem can only apply for a reduced set of eigenmodes having ϕ_2 such that $\nabla_h \cdot (\Omega \nabla_h \Phi(\phi_2)) = 0$.

A.2 Wave part

The dynamical equation for the wave part ϕ_2 can be determined in an analogous way to that for ϕ_1. Taking the inner product (5.16) $\cdot\, \mathbf{e}_2$, multiplying by k/k_h and omitting viscous terms we have

$$\begin{aligned} \frac{k}{k_h}\frac{\partial \phi_2}{\partial t} = & -\mathbf{U} \bullet \nabla \phi_2 \frac{k_h'}{k'} + N\phi_3 - ik_z \mathbf{U} \bullet (\mathbf{u}_h^v + \mathbf{u}_h^w) \\ & + \frac{k_z}{k_h^2}\left(\mathbf{k}_h \times [\mathbf{U} * \omega_z] + \mathbf{k}_h \times \{\Omega * (\mathbf{u}_h^v + \mathbf{u}_h^w)\}\right). \end{aligned} \tag{A.15}$$

In a naive first look at (A.15), it could seem that the first term corresponds to advection, the second to buoyancy, and the rest to (the effective) pressure. However, the pre-factor of the time derivative term compared to the factor of $\widehat{\nabla\phi_2}$ in the convolution, indicate that the effect of the first term is not just advection. The familiar physical effects of advection, pressure and buoyancy enter (A.15) in a non trivial

way. For the interested reader, the role of the pressure and the connection between (A.15) and the vertical momentum equation (5.2b) is revealed in the Appendix B. We procede now as before, writing the equation for ϕ_2 as

$$\frac{\partial \phi_2}{\partial t} = L_{21}\phi_1 + L_{22}\phi_2 + L_{23}\phi_3. \tag{A.16}$$

A.2.1 Effects of the wave part on the wave part

Using (5.10b) on the last term of the first line of (A.15) yields for $L_{22}\phi_2$

$$\frac{k}{k_h} L_{22}\phi_2 = -i\mathbf{U}\bullet\mathbf{k}'_h \frac{k'_h}{k'}\phi_2 - ik_z\mathbf{U}\bullet\mathbf{k}'_h \frac{k_z}{k'k'_h}\phi_2 - i\frac{k_z}{k_h^2}\nabla_h\times\Omega\mathbf{u}_h^w, \tag{A.17a}$$

$$= -i\mathbf{U}\bullet\mathbf{k}'_h\left(\frac{k_h'^2+k_z^2}{k'k'_h}\right)\phi_2 - i\frac{k_z}{k_h^2}\nabla_h\Omega\otimes\mathbf{u}_h^w, \tag{A.17b}$$

$$= -i\mathbf{U}\bullet\mathbf{k}'_h\frac{k'}{k'_h}\phi_2 - i\frac{k_z}{k_h^2}(\Delta_h\mathbf{U})\bullet\mathbf{u}_h^w, \tag{A.17c}$$

where we have used that $\mathbf{u}_h^w$ is irrotational (from A.17a to A.17b) and $\mathbf{U}$ divergence free (from A.17b to A.17c, as in A.13). Writing from (A.17c) the evolution equation for ϕ_2 in terms of u_z while keeping only terms with ϕ_2 yields

$$\frac{k^2}{k_h^2}\frac{\partial u_z}{\partial t} + \mathbf{U}\bullet\nabla u_z\frac{k'^2}{k_h'^2} = \frac{k_z^2}{k_h^2}(\Delta_h\mathbf{U})\bullet\nabla_h\frac{u_z}{k_h'^2} + \phi_1,\phi_3\text{-terms}. \tag{A.18}$$

Equation (A.18) shows that k^2u_z/k_h^2 is advected by the base flow; the u_z term on the right hand side acts as a source of k^2u_z. The source of k^2u_z is given by k_z^2 times the inner product between $\Delta_h\mathbf{U}$ and the gradient of u_z/k_h^2.

A.2.2 Wave excitation by the vortex part

Keeping only the vortical terms in (A.15) gives

$$\frac{k}{k_h}L_{21}\phi_1 = -ik_z\mathbf{U}\bullet\mathbf{u}_h^v + \frac{k_z}{k_h^2}\left(\mathbf{k}_h\times[\mathbf{U}*\omega_z] + \mathbf{k}_h\times\{\Omega*\mathbf{u}_h^v\}\right). \tag{A.19}$$

We can write the contribution to waves from the vortical part as

$$k^2\frac{\partial u_z}{\partial t} = \partial_z[\underbrace{\Delta_h(\mathbf{U}\bullet\mathbf{u}_h^v)}_{\text{Dynamic pressure}} - \underbrace{\nabla_h\times(\omega_z*\mathbf{U})}_{\omega_z\text{ advection}} - \underbrace{\nabla_h\times(\Omega*\mathbf{u}_h^v)}_{\Omega\text{ advection}}] + \phi_2,\phi_3\text{-terms}, \tag{A.20}$$

which is in amenable form to be brought back to real space. In (A.20) we see that the contributions from the vortical to the wave part appear as a forcing term on k^2u_z;

this is the same quantity being forced by the wave part as shown by (A.18), which is different from the advected quantity $k^2 u_z/k_h$. Equation (A.20) also shows that the contributions to $k^2 u_z$ integrated on a horizontal surface reduce to the vertical derivative of three boundary terms. The first term corresponds to the flux of the pressure head gradient and the other two correspond to the line integral of the ω_z advected by $\mathbf{U}$ and the line integral of Ω advected by $\mathbf{u}_h^v$.

In the last term of (A.19), corresponding to the Ω advection term, we have

$$\mathbf{k}_h \times \{\Omega * \mathbf{u}_h^v\} = \Omega * \left\{ \mathbf{k}_h \times (\mathbf{k}'_h \times \mathbf{e}_z) \frac{\phi_1}{k'_h} \right\}, \tag{A.21a}$$

$$= -\Omega * \mathbf{k}_h \cdot \mathbf{k}'_h \frac{\phi_1}{k'_h}, \tag{A.21b}$$

$$= -\mathbf{k}_h \cdot \left(\Omega * \frac{\mathbf{k}'_h}{k'_h} \phi_1 \right), \tag{A.21c}$$

where we have first used (5.10a) and then simplified the double cross-product (as in A.13). The form of the term (A.21c) is similar to that of the wave term exciting the vortical part (A.5e); as shown by (5.24), the combination of these terms can be understood as an effective Coriolis force. Finally, the full wave forcing term $L_{21}\phi_1$ in terms of ϕ_1 is

$$L_{21}\phi_1 = \frac{k_z}{k k_h} \left[-\Omega * k'_h \phi_1 + (\partial_x V + \partial_y U) * \frac{(k_x'^2 - k_y'^2)}{k'_h} \phi_1 - 4 \partial_x U * \frac{k'_x k'_y}{k'_h} \phi_1 \right]. \tag{A.22}$$

Appendix B should be checked for local expressions equivalent to (A.19) and (A.20) which are in boundary term form.

Appendix B

Explicit role of pressure and the connection of the poloidal evolution with the vertical momentum equation

In equation (A.15) we have

$$\frac{k}{k_h}\frac{\partial \phi_2}{\partial t} = -\overbrace{\mathbf{U}\bullet\widehat{\nabla\phi_2}\frac{k_h'}{k'}}^{u_z \text{ advection}} + \overbrace{N\phi_3}^{\text{buoyancy}} + \frac{k_z}{k_h^2}(\underbrace{\mathbf{k}_h\times[\mathbf{U}*\omega_z]}_{\omega_z \text{ advection}} + \underbrace{\mathbf{k}_h\times\{\Omega*\mathbf{u}_h\}}_{\Omega \text{ advection}} - \underbrace{ik_h^2\mathbf{U}\bullet\mathbf{u}_h}_{\text{Dynamic pressure}}). \tag{B.1}$$

Note that, to obtain (B.1) we have already projected $\mathbf{u}(\mathbf{k})$ in a divergence free direction, so the pressure effect is already taken into account in an implicit way. As specified on the different terms in (B.1), we know where the different terms come from; that knowledge, together with the previous analysis in appendix A, allows some insight on the different physical effects entering (B.1). Our purpose now is to provide extra insight on the way in which different physical effects affect the evolution of ϕ_2. For that we will find the connection between (B.1) and the equation for u_z; that connection will require finding explicitly the role of the pressure p.

Denoting by Q the second line of (B.1) we have

$$i\frac{k_h^2}{k_z}Q = i\mathbf{k}_h\times[\mathbf{U}*\omega_z] + i\mathbf{k}_h\times\{\Omega*\mathbf{u}_h\} + k_h^2\mathbf{U}\bullet\mathbf{u}_h, \tag{B.2a}$$

$$= [\Omega*\omega_z + \nabla_h\omega_z\otimes\mathbf{U}] + \{\Omega*\omega_z + \nabla_h\Omega\otimes\mathbf{u}_h\} - \Delta_h(\mathbf{U}\bullet\mathbf{u}_h), \tag{B.2b}$$

$$= 2\Omega*\omega_z + \nabla_h\omega_z\otimes\mathbf{U} + \nabla_h\Omega\otimes\mathbf{u}_h - \Delta_h(\mathbf{U}\bullet\mathbf{u}_h), \tag{B.2c}$$

where in going from (B.2a) to (B.2b) we have proceeded as before in (A.2). (This can be followed by using the condensed notation introduced in (A.6b), for example in $\mathbf{k}_h \times [\mathbf{U} * \omega_z]$ replace $\mathbf{k}_h \to \mathbf{k}_h - \mathbf{k}'_h + \mathbf{k}'_h$, form Ω from $(\mathbf{k}_h - \mathbf{k}'_h) \times \mathbf{U}$, and then $\mathbf{k}'_h \times [\mathbf{U} * \omega_z] = \mathbf{k}'_h \times [\omega_z * \mathbf{U}] = \mathbf{k}'_h \omega_z \otimes \mathbf{U}$ for $\nabla_h \omega_z \otimes \mathbf{U}$.) Note that all the expression (B.2c) has a clear-cut form in physical space if the inverse Fourier transform is applied. We can thus manipulate the expression (B.2c) as if the convolutions where products and follow standard techniques of tensorial calculus. For example on the last term of (B.2c) we have

$$\Delta_h(\mathbf{U} \cdot \mathbf{u}_h) = (U_i u_i)_{,jj} = U_{i,jj} u_i + U_i u_{i,jj} + 2U_{i,j} u_{i,j}, \tag{B.3}$$

where i and j vary in $\{1, 2\}$ and indices after a comma denote partial derivatives. We may also note that for the third term in (B.2c) we have

$$\begin{aligned} \nabla_h \Omega \times \mathbf{u} &= \epsilon^{ij} U_{j,il} \epsilon^{lm} u_m = (\delta^{il}\delta^{jm} - \delta^{im}\delta^{jl}) U_{j,il} u_m \\ &= U_{j,ii} u_j - U_{j,ij} u_i \\ &= \nabla^2 \mathbf{U} \cdot \mathbf{u}, \end{aligned} \tag{B.4}$$

where we use the antisymmetry of ϵ^{ij} and the incompressibility of $\mathbf{U}$, exactly as in (A.13). Lets call $Q_p(\mathbf{x})$ the inverse Fourier transform of $Q(\mathbf{k})$, and respectively Q_p^v and Q_p^w the vortical and wave contributions such that $Q_p = Q_p^v + Q_p^w$. Then, now in physical space, we have from (B.2c) the vortex part Q_p^v as

$$\Delta_h Q_p^v = \partial_z \left[2\Omega\omega_z + \mathbf{U} \cdot \nabla^2 \mathbf{u}_h^v + \mathbf{u}_h^v \cdot \nabla^2 \mathbf{U} - \nabla^2 (\mathbf{U} \cdot \mathbf{u}_h^v) \right], \tag{B.5a}$$

$$= \partial_z \left[2\Omega\omega_z - 2U_{i,j} u_{i,j}^v \right], \tag{B.5b}$$

$$= \partial_z \left[\Omega\omega_z - 2S_{ij}^B S_{ji}^v \right], \tag{B.5c}$$

where we have done as (B.4) for writing (B.5a) and then used (B.3) to reduce to (B.5b). Given that $\mathbf{u}_h^w$ is 2D irrotational, we have a different expression for the wave part Q_p^w which is

$$\Delta_h Q_p^w = \partial_z \left[\mathbf{u}_h^w \cdot \nabla_h^2 \mathbf{U} - \nabla_h^2 (\mathbf{U} \cdot \mathbf{u}_h^w) \right], \tag{B.6a}$$

$$= \partial_z \left[-U_i u_{i,jj}^w - 2U_{i,j} u_{i,j}^w \right], \tag{B.6b}$$

$$= \partial_z \left[-(\mathbf{U} \cdot \nabla_h)(\nabla_h \cdot \mathbf{u}_h^w) - 2S_{ij}^B S_{ji}^w \right]. \tag{B.6c}$$

In (B.5c) and (B.6c) we have that $S_{ij}^B = (U_{i,j} + U_{j,i})/2$ is the symmetric part of the $\nabla\mathbf{U}$ tensor and S_{ij}^v (S_{ij}^w) is the analogous for the vortical (wave) part of the horizontal perturbation. We have also used that $u_{i,j}^w = u_{j,i}^w$ to go from the $\mathbf{U} \cdot \nabla_h^2 \mathbf{u}_h^w$ term in (B.6b) to the advective like term $(\mathbf{U} \cdot \nabla_h)(\nabla_h \cdot \mathbf{u}_h^w)$ in (B.6c). Putting together $Q_p = Q_p^v + Q_p^w$ from (B.5c) and (B.6c), and using that $\nabla_\mathbf{h} \cdot \mathbf{u}_h^w = -\partial_z u_z$ we have

$$\Delta_h Q_p = (\mathbf{U} \cdot \nabla_h) \partial_z^2 u_z + \partial_z \left[\Omega\omega_z - 2S_{ij}^B S_{ji} \right] \tag{B.7}$$

where $S_{ji} = S^w_{ji} + S^v_{ji}$.

Now, to find the pressure, we take the divergence of the full Navier-Stokes equations which yields

$$-\Delta p - N^2 \partial_z \rho = (U_i u_{\mu,i})_{,\mu} + (u_i U_{j,i})_{,j}, \tag{B.8a}$$
$$= U_{i,\mu} u_{\mu,i} + U_i u_{\mu,i\mu} + u_{i,j} U_{j,i} + u_i U_{j,ij}, \tag{B.8b}$$
$$= 2U_{i,j} u_{j,i} = 2S^B_{ij} S_{ji} - \Omega \omega_z, \tag{B.8c}$$

where greek indices in (B.8a) and (B.8b) vary from 1 to 3 and the second derivative terms $U_i u_{\mu,i\mu}$ and $u_i U_{j,ij}$ in (B.8b) are zero for incompressibility. From (B.7) and (B.8) we have

$$\Delta_h Q_p = \partial_z \left[(\mathbf{U} \cdot \nabla_h) \partial_z u_z + \Delta p + N^2 \partial_z \rho \right], \tag{B.9a}$$

or back in Fourier space

$$Q = \frac{k_z^2}{k_h^2} \mathbf{U} \bullet \nabla_h u_z + \frac{i k_z k^2}{k_h^2} p + \frac{k_z^2}{k_h^2} N^2 \rho. \tag{B.9b}$$

We can now replace the expresion for Q from (B.9b) on the second line of the ϕ_2 equation (B.1) and, rewriting in terms of u_z and ρ we have

$$\begin{aligned} \frac{k^2}{k_h^2} \frac{\partial u_z}{\partial t} = & -\mathbf{U} \bullet \nabla_h u_z - N^2 \rho \\ & - \frac{k_z^2}{k_h^2} \mathbf{U} \bullet \nabla_h u_z - \frac{k_z^2}{k_h^2} N^2 \rho - \frac{i k_z k^2}{k_h^2} p, \end{aligned} \tag{B.10a}$$
$$= -\frac{k^2}{k_h^2} \mathbf{U} \bullet \nabla_h u_z - \frac{k^2}{k_h^2} N^2 \rho - \frac{i k_z k^2}{k_h^2} p, \tag{B.10b}$$
$$= \frac{k^2}{k_h^2} \left[-\mathbf{U} \bullet \nabla_h u_z - \partial_z p - N^2 \rho \right], \tag{B.10c}$$

which, as is clear from (B.10c), is the vertical momentum equation multiplied by k^2/k_h^2. Thus, as shown in the passage from (B.10a) to (B.10b), the Q terms in the second line of (B.10a) included, besides the pressure, the k_z^2 term of the advection and buoyancy terms Laplacian. Not surprisingly, all vortical terms exciting the wave part in (B.1) come directly from the pressure. Not so obvious was the way, explicited in (B.6) and (B.7), in which the $\partial_z^2 \mathbf{U} \cdot \nabla_h u_z$ term and the pressure p combine to form the pressure head $\nabla^2 (\mathbf{U} \cdot \mathbf{u}^w_h)$ and the term $\mathbf{u}^w_h \cdot \nabla^2_h \mathbf{U}$ in (B.6a). As seen on (A.17) and (A.18), the latter two terms are key to easily obtain the form of the advected quantity $k^2 u_z / k_h$ and the source term $\frac{k_z^2}{k_h^2} (\Delta_h \mathbf{U}) \bullet i \mathbf{k}'_h \frac{u_z}{k'^2_h}$.

Bibliography

[1] Abramowitz, M., and Stegun, I. *Handbook of Mathematical Functions*. Dover Publications, 1964.

[2] Aharonov, Y., Popescu, S., and Tollaksen, J. A time-symmetric formulation of quantum mechanics. 27–32.

[3] Andrews, D. G., and Mcintyre, M. E. An exact theory of nonlinear waves on a lagrangian-mean flow. *Journal of Fluid Mechanics 89*, 04 (1978), 609–646.

[4] Antkowiak, A., and Brancher, P. On vortex rings around vortices: an optimal mechanism. *Journal of Fluid Mechanics 578* (2007), 295–304.

[5] Arobone, E., and Sarkar, S. The statistical evolution of a stratified mixing layer with horizontal shear invoking feature extraction. *Physics of Fluids 22*, 11 (2010), 115108.

[6] Arratia, C., Iams, S., Chomaz, J.-M., and Caulfield, C.-C. Transient Growth on the Homogenous Mixing Layer. In *SEVENTH IUTAM SYMPOSIUM ON LAMINAR-TURBULENT TRANSITION* (2010), Schlatter, P and Henningson, DS, Ed., vol. 18 of *IUTAM Bookseries*, Int Union Theoret & Appl Mech; Vetenskapsradet; Linne FLOW Ctr; Dantec Dynam; Cambridge Univ Press; Springer, pp. 453–456. 7th IUTAM Symposium on Laminar-Turbulent Transition, Royal Inst Technol, Stockholm, SWEDEN, JUN 23-26, 2009. See supplementary material.

[7] Arratia, C., Ortiz, S., and Chomaz, J. M. Transient evolution and high stratification scaling in horizontal mixing layers. In *ADVANCES IN TURBULENCE XII - PROCEEDINGS OF THE 12TH EUROMECH EUROPEAN TURBULENCE CONFERENCE* (2009), Eckhardt, B, Ed., vol. 132 of *Springer Proceedings in Physics*, pp. 183–186. 12th EUROMECH European Turbulence Conference, Marburg, GERMANY, SEP 07-10, 2009. See supplementary material.

[8] Arratia, C., Ortiz, S., and Chomaz, J. M. Inviscid transient growth on horizontal shear layers with strong vertical stratification. 7th International Symposium on Stratified Flows, Rome, ITALY, AUG 22-26, 2011. See supplementary material.

[9] Bakas, N. A., and Farrell, B. F. Gravity waves in a horizontal shear flow. part i: Growth mechanisms in the absence of potential vorticity perturbations. *Journal of Physical Oceanography 39*, 3 (2009), 481–496.

[10] Bakas, N. A., and Farrell, B. F. Gravity waves in a horizontal shear flow. part ii: Interaction between gravity waves and potential vorticity perturbations. *Journal of Physical Oceanography 39*, 3 (2009), 497–511.

[11] Ballentine, L. E. *Quantum Mechanics*. Prentice Hall, 1998.

[12] Bartello, P. Geostrophic adjustment and inverse cascades in rotating stratified turbulence. *Journal of the Atmospheric Sciences 52*, 24 (1995), 4410–4428.

[13] Basak, S., and Sarkar, S. Dynamics of a stratified shear layer with horizontal shear. *Journal of Fluid Mechanics 568*, -1 (2006), 19–54.

[14] Bayly, B. J. Three-dimensional instability of elliptical flow. *Phys. Rev. Lett. 57* (Oct 1986), 2160–2163.

[15] Billant, P., and Chomaz, J.-M. Experimental evidence for a new instability of a vertical columnar vortex pair in a strongly stratified fluid. *Journal of Fluid Mechanics 418* (2000), 167–188.

[16] Billant, P., and Chomaz, J.-M. Three-dimensional stability of a vertical columnar vortex pair in a stratified fluid. *Journal of Fluid Mechanics 419* (2000), 65–91.

[17] Billant, P., and Chomaz, J.-M. Self-similarity of strongly stratified inviscid flows. *Physics of Fluids 13*, 6 (2001), 1645–1651.

[18] Bitbol, M. Ontology, matter and emergence. *Phenomenology and the Cognitive Sciences 6* (2007), 293–307. 10.1007/s11097-006-9041-z.

[19] Brancher, P., Chomaz, J. M., and Huerre, P. Direct numerical simulations of round jets: Vortex induction and side jets. *Physics of Fluids 6*, 5 (1994), 1768–1774.

[20] Brown, G. L., and Roshko, A. On density effects and large structure in turbulent mixing layers. *Journal of Fluid Mechanics 64*, 04 (1974), 775–816.

[21] Bühler, O. *Waves and Mean Flows*. Cambridge University Press, 2009.

[22] Bühler, O. Wave-vortex interactions in fluids and superfluids. *Annual Review of Fluid Mechanics 42*, 1 (2010), 205–228.

[23] Bühler, O., and McIntyre, M. E. On non-dissipative wave-mean interactions in the atmosphere or oceans. *Journal of Fluid Mechanics 354* (1998), 301–343.

[24] Bühler, O., and McIntyre, M. E. Wave capture and wave-vortex duality. *Journal of Fluid Mechanics 534* (2005), 67–95.

[25] Butler, K. M., and Farrell, B. F. Three-dimensional optimal perturbations in viscous shear flow. *Physics of Fluids A: Fluid Dynamics 4*, 8 (1992), 1637–1650.

[26] Cambon, C. Turbulence and vortex structures in rotating and stratified flows. *European Journal of Mechanics - B/Fluids 20*, 4 (2001), 489 – 510.

[27] Caulfield, C. P. *Personal communication*.

[28] Caulfield, C. P., and Kerswell, R. R. The nonlinear development of three-dimensional disturbances at hyperbolic stagnation points: A model of the braid region in mixing layers. 1032–1043.

[29] Caulfield, C. P., and Peltier, W. R. The anatomy of the mixing transition in homogeneous and stratified free shear layers. *Journal of Fluid Mechanics 413* (2000), 1–47.

[30] Chagelishvili, G. D., Tevzadze, A. G., Bodo, G., and Moiseev, S. S. Linear mechanism of wave emergence from vortices in smooth shear flows. *Phys. Rev. Lett. 79*, 17 (Oct 1997), 3178–3181.

[31] Chomaz, J.-M. Fully nonlinear dynamics of parallel wakes. *Journal of Fluid Mechanics 495* (2003), 57–75.

[32] Corbett, P., and Bottaro, A. Optimal linear growth in swept boundary layers. *Journal of Fluid Mechanics 435*, -1 (2001), 1–23.

[33] Corcos, G. M., and Lin, S. J. The mixing layer: deterministic models of a turbulent flow. part 2. the origin of the three-dimensional motion. *Journal of Fluid Mechanics 139* (1984), 67–95.

[34] Corcos, G. M., and Sherman, F. S. The mixing layer: deterministic models of a turbulent flow. part 1. introduction and the two-dimensional flow. *Journal of Fluid Mechanics 139* (1984), 29–65.

[35] Craya, A. *Contribution à l'analyse de la turbulence associée à des vitesses moyennes*. PhD thesis, Univ. Grenoble, France, 1958. Also in *Publ. Sci. Tech. 345*, Ministère de l'air (1958).

[36] Davies, E. B. *Linear Operators and their Spectra*. Cambridge University Press, 2007. *online version at* http://www.mth.kcl.ac.uk/staff/eb_davies/LOTS.html.

[37] Delbende, I., Chomaz, J.-M., and Huerre, P. Absolute/convective instabilities in the batchelor vortex: a numerical study of the linear impulse response. *Journal of Fluid Mechanics 355*, -1 (1998), 229–254.

[38] Deloncle, A., Billant, P., and Chomaz, J.-M. Nonlinear evolution of the zigzag instability in stratified fluids: a shortcut on the route to dissipation. *Journal of Fluid Mechanics 599*, -1 (2008), 229–239.

[39] Deloncle, A., Chomaz, J.-M., and Billant, P. Three-dimensional stability of a horizontally sheared flow in a stably stratified fluid. *Journal of Fluid Mechanics 570*, -1 (2007), 297–305.

[40] Dimotakis, P. E. Turbulent mixing. *Annual Review of Fluid Mechanics 37*, 1 (2005), 329–356.

[41] Donnadieu, C., Ortiz, S., Chomaz, J.-M., and Billant, P. Three-dimensional instabilities and transient growth of a counter-rotating vortex pair. *Physics of Fluids 21*, 9 (2009), 094102.

[42] Drazin, P. G., and Reid, W. H. *Hydrodynamic Stability*. Cambridge University Press, 2004.

[43] Driscoll, T. A., and Trefethen, L. N. Pseudospectra for the wave equation with an absorbing boundary. *Journal of Computational and Applied Mathematics 69*, 1 (1996), 125 – 142.

[44] Ellingsen, T., and Palm, E. Stability of linear flow. *Physics of Fluids 18*, 4 (1975), 487–488.

[45] Farrell, B. Developing disturbances in shear. *Journal of the Atmospheric Sciences 44*, 16 (1987), 2191–2199.

[46] Farrell, B., and Ioannou, P. Generalized stability theory .1. Autonomous operators. *JOURNAL OF THE ATMOSPHERIC SCIENCES 53*, 14 (JUL 15 1996), 2025–2040.

[47] Farrell, B., and Ioannou, P. Generalized stability theory .2. Nonautonomous operators. *JOURNAL OF THE ATMOSPHERIC SCIENCES 53*, 14 (JUL 15 1996), 2041–2053.

[48] Farrell, B. F., and Ioannou, P. J. Optimal excitation of three-dimensional perturbations in viscous constant shear flow. *Physics of Fluids A: Fluid Dynamics 5*, 6 (1993), 1390–1400.

[49] Farrell, B. F., and Ioannou, P. J. Perturbation growth in shear flow exhibits universality. *Physics of Fluids A: Fluid Dynamics 5*, 9 (1993), 2298–2300.

[50] Farrell, B. F., and Ioannou, P. J. Stochastic forcing of the linearized navier–stokes equations. *Physics of Fluids A: Fluid Dynamics 5*, 11 (1993), 2600–2609.

[51] Farrell, B. F., and Moore, A. M. An adjoint method for obtaining the most rapidly growing perturbation to oceanic flows. *Journal of Physical Oceanography 22*, 4 (1992), 338–349.

[52] Gallaire, F., and Chomaz, J.-M. Three-dimensional instability of isolated vortices. *Physics of Fluids 15*, 8 (2003), 2113–2126.

[53] George, J., and Sujith, R. I. Emergence of acoustic waves from vorticity fluctuations: Impact of non-normality. *Phys. Rev. E 80*, 4 (Oct 2009), 046321.

[54] Godeferd, F. S., and Cambon, C. Detailed investigation of energy transfers in homogeneous stratified turbulence*. *Physics of Fluids 6*, 6 (1994), 2084–2100.

[55] Goldenfeld, N., and Woese, C. Life is physics: Evolution as a collective phenomenon far from equilibrium. *Annual Review of Condensed Matter Physics 2*, 1 (2011), 375–399.

[56] Guégan, A., Huerre, P., and Schmid, P. J. Optimal disturbances in swept hiemenz flow. *Journal of Fluid Mechanics 578* (2007), 223–232.

[57] Gustavsson, L. H. Energy growth of three-dimensional disturbances in plane poiseuille flow. *Journal of Fluid Mechanics 224* (1991), 241–260.

[58] Hanifi, A., and Henningson, D. S. The compressible inviscid algebraic instability for streamwise independent disturbances. 1784–1786.

[59] Hazel, P. Numerical studies of the stability of inviscid stratified shear flows. *Journal of Fluid Mechanics 51*, 01 (1972), 39–61.

[60] Held, I. M. Pseudomomentum and the orthogonality of modes in shear flows. *Journal of the Atmospheric Sciences 42*, 21 (1985), 2280–2288.

[61] Helfrich, K. R., and Melville, W. K. Long nonlinear internal waves. *Annual Review of Fluid Mechanics 38*, 1 (2006), 395–425.

[62] Henningson, D. Comment on 'transition in shear flows. nonlinear normality versus non-normal linearity' [phys. fluids 7, 3060 (1995)]. 2257–2258.

[63] Herring, J. R. Approach of axisymmetric turbulence to isotropy. *Physics of Fluids 17*, 5 (1974), 859–872.

[64] Hill, D. C. Adjoint systems and their role in the receptivity problem for boundary layers. *Journal of Fluid Mechanics 292* (1995), 183–204.

[65] Hussain, A. K. M. F. Coherent structures and incoherent turbulence. In *Turbulence and Chaotic Phenomena in Fluids* (1984), T. Tatsumi, Ed., pp. 453–460.

[66] Kalashnik, M. V., Mamatsashvili, G. R., Chagelishvili, G., and Lominadze, J. G. Linear dynamics of non-symmetric perturbations in geostrophic horizontal shear flows. *Quarterly Journal of the Royal Meteorological Society 132*, 615 (2006), 505–518.

[67] Kerswell, R. R. Elliptical instability. *Annual Review of Fluid Mechanics 34*, 1 (2002), 83–113.

[68] Klaassen, G. P., and Peltier, W. R. The influence of stratification on secondary instability in free shear layers. *Journal of Fluid Mechanics 227* (1991), 71–106.

[69] Kupiec, J.-J., and Sonigo, P. Seuil, 2000.

[70] Landahl, M. T. A note on an algebraic instability of inviscid parallel shear flows. *Journal of Fluid Mechanics 98*, 02 (1980), 243–251.

[71] Landau, L. D., and Lifshitz, E. M. *Quantum Mechanics: Non-Relativistic Theory.* Pergamon Press, 1977.

[72] Lilly, D. K. Stratified turbulence and the mesoscale variability of the atmosphere. *Journal of the Atmospheric Sciences 40*, 3 (1983), 749–761.

[73] Luchini, P., and Bottaro, A. Grtler vortices: a backward-in-time approach to the receptivity problem. *Journal of Fluid Mechanics 363* (1998), 1–23.

[74] Malik, M., Alam, M., and Dey, J. Nonmodal energy growth and optimal perturbations in compressible plane couette flow. 034103.

[75] Mcintyre, M. E. On the "wave momentum" myth. *Journal of Fluid Mechanics 106* (1981), 331–347.

[76] McIntyre, M. E. Spontaneous imbalance and hybrid vortex-gravity structures. *Journal of the Atmospheric Sciences 66*, 5 (2009), 1315–1326.

[77] McWilliams, J. C., and Yavneh, I. Fluctuation growth and instability associated with a singularity of the balance equations. *Physics of Fluids 10*, 10 (1998), 2587–2596.

[78] Metcalfe, R. W., Orszag, S. A., Brachet, M. E., Menon, S., and Riley, J. J. Secondary instability of a temporally growing mixing layer. *Journal of Fluid Mechanics 184* (1987), 207–243.

[79] Michalke, A. On the inviscid instability of the hyperbolic tangent velocity profile. *Journal of Fluid Mechanics 19*, 04 (1964), 543–556.

[80] Odell, G. M., and Kovasznay, L. S. G. A new type of water channel with density stratification. *Journal of Fluid Mechanics 50*, 03 (1971), 535–543.

[81] Ólafsdóttir, E. I., Daalhuis, A. B. O., and Vanneste, J. Inertia-gravity-wave radiation by a sheared vortex. *Journal of Fluid Mechanics 596* (2008), 169–189.

[82] Orr, W. M. The stability or instability of the steady motions of a perfect liquid and of a viscous liquid. part i: A perfect liquid. *Proceedings of the Royal Irish Academy. Section A: Mathematical and Physical Sciences 27* (1907), pp. 9–68.

[83] Ortiz, S., and Chomaz, J.-M. Transient growth of secondary instabilities in parallel wakes: Anti lift-up mechanism and hyperbolic instability. *Physics of Fluids 23*, 11 (2011), 114106.

[84] Peltier, W. R., and Caulfield, C. P. Mixing efficiency in stratified shear flows. *Annual Review of Fluid Mechanics 35*, 1 (2003), 135–167.

[85] Pierrehumbert, R. T., and Widnall, S. E. The two- and three-dimensional instabilities of a spatially periodic shear layer. *Journal of Fluid Mechanics 114* (1982), 59–82.

[86] Reddy, S. C., and Henningson, D. S. Energy growth in viscous channel flows. *Journal of Fluid Mechanics 252* (1993), 209–238.

[87] Riley, J. J., and Lelong, M.-P. Fluid motions in the presence of strong stable stratification. *Annual Review of Fluid Mechanics 32*, 1 (2000), 613–657.

[88] Rogers, M. M., and Moser, R. D. The three-dimensional evolution of a plane mixing layer: the kelvin-helmholtz rollup. *Journal of Fluid Mechanics 243* (1992), 183–226.

[89] Sagaut, P., and Cambon, C. *Homogeneous Turbulence Dynamics*. Cambridge University Press, 2008.

[90] Schmid, P. J. Nonmodal stability theory. *Annual Review of Fluid Mechanics 39*, 1 (2007), 129–162.

[91] Schmid, P. J., and Henningson, D. S. *Stability and Transition in Shear Flows*. Springer, 2001.

[92] Shepherd, T. G. Time development of small disturbances to plane couette flow. *Journal of the Atmospheric Sciences 42*, 17 (1985), 1868–1872.

[93] Shepherd, T. G. Symmetries, conservation laws, and hamiltonian structure in geophysical fluid dynamics. vol. 32 of *Advances in Geophysics*. Elsevier, 1990, pp. 287 – 338.

[94] Soundar, J. J. J., Chomaz, J.-M., and Huerre, P. Transient growth in rayleigh-bnard-poiseuille/couette convection. *Physics of Fluids Submitted* (2011).

[95] Squire, H. B. On the stability for three-dimensional disturbances of viscous fluid flow between parallel walls. *Proceedings of the Royal Society of London. Series A 142*, 847 (1933), 621–628.

[96] Staquet, C., and Sommeria, J. Internal gravity waves: From instabilities to turbulence. *Annual Review of Fluid Mechanics 34*, 1 (2002), 559–593.

[97] Teschl, G. *Ordinary Differential Equations and Dynamical Systems*. Graduate Studies in Mathematics, Amer. Math. Soc., Providence, (to appear)., 2012. *online version at* http://www.mat.univie.ac.at/ gerald/ftp/book-ode/.

[98] Vallis, G. K. *Atmospheric and Oceanic Fluid Dynamics*. Cambridge University Press, Cambridge, U.K., 2006.

[99] Vanneste, J., and Yavneh, I. Exponentially small inertia-gravity waves and the breakdown of quasigeostrophic balance. *Journal of the Atmospheric Sciences 61*, 2 (2004), 211–223.

[100] Vincent, A., and Meneguzzi, M. The spatial structure and statistical properties of homogeneous turbulence. *Journal of Fluid Mechanics 225*, -1 (1991), 1–20.

[101] Waleffe, F. On the three-dimensional instability of strained vortices. *Physics of Fluids A: Fluid Dynamics 2*, 1 (1990), 76–80.

[102] Weiss, J. Coordinate invariance in stochastic dynamical systems. *TELLUS SERIES A-DYNAMIC METEOROLOGY AND OCEANOGRAPHY 55*, 3 (MAY 2003), 208–218.

[103] Winant, C. D., and Browand, F. K. Vortex pairing : the mechanism of turbulent mixing-layer growth at moderate reynolds number. *Journal of Fluid Mechanics 63*, 02 (1974), 237–255.

[104] Zurek, W. H. Decoherence, einselection, and the quantum origins of the classical. *Rev. Mod. Phys. 75* (May 2003), 715–775.

Supplementary material

Contribution to the proceedings of the following conferences:

- 7th IUTAM Symposium on Laminar-Turbulent Transition, Royal Inst Technol, Stockholm, SWEDEN, JUN 23-26, 2009.
  Article corresponding to reference [6].
- 12th EUROMECH European Turbulence Conference, Marburg, GERMANY, SEP 07-10, 2009.
  Article corresponding to reference [7].
- 7th International Symposium on Stratified Flows, Rome, ITALY, AUG 22-26, 2011.
  Article corresponding to reference [8].

Transient Growth on the Homogenous Mixing Layer

Cristobal Arratia, Sarah Iams, Jean-Marc Chomaz and Colm-Cille Caulfield

Abstract We compute the three-dimensional (3D) optimal perturbations of an homogeneous mixing layer. We consider as a base state both the hyperbolic tangent (*tanh*) velocity profile and the developing two-dimensional (2D) Kelvin-Helmholtz (KH) billow. For short enough times, the most amplified perturbations on the *tanh* profile are 3D and result from a combination between the lift-up and Orr mechanisms[1]. For developing KH billows, there are different mechanisms that prevail depending on the initial amplitude of the billow, the spanwise wavenumber and the time of the response observed. We determine when the largest transient growth at a particular time is associated with an optimal response reminiscent of the elliptic or hyperbolic instability.

1 Introduction

Homogeneous (constant density) mixing layers are ubiquitous sheared flows which are known to exhibit the KH instability. The KH instability may lead to the roll-up of spanwise vortices, the KH billows, which are the outcome of the non-linear saturation of the growing unstable KH mode. These essentially 2D KH billows can be subject to 3D instabilities and may exhibit transition to turbulence [2]. Much research has addressed the linear instability mechanisms for transition on the KH

Cristobal Arratia, Jean-Marc Chomaz
Laboratoire d'Hydrodynamique, Ecole Polytechnique-CNRS, e-mail: arratia@ladhyx.polytechnique.fr

Sarah Iams, Colm-Cille Caulfield
BP Institute, University of Cambridge, Madingley Road, Cambridge CB3 0EZ, UK
S. Iams now at the Center for Applied Mathematics, Cornell University
C. Caulfield also at Department of Applied Mathematics and Theoretical Physics, University of Cambridge, Centre for Mathematical Sciences, e-mail: cpc12@cam.ac.uk

billows [3] and several unstable eigenmodes have been found to be mainly localized in two different flow regions:

- the vortex core, where the elliptic instability occurs on the strained closed streamlines.
- the braid, where the hyperbolic instability occurs on the region separating consecutive billows. The hyperbolic flow stretches vorticity generating streamwise vortices.

However, because of the non stationarity of the KH billows, classic modal analysis relies on the separation of time scales implied by freezing the basic state. Moreover, because of the non-normality of the linearized Navier-Stokes equations, linear growth of 3D perturbations should be described by the non-modal stability theory.

We characterize the appearance of 3-dimensionality on the mixing layer by computing the optimal transient growth of perturbations $\mathbf{u}(\mathbf{x},t)$ during a finite time interval $[0,T]$ over a basic state $\mathbf{U}$. The optimal perturbations that attain the optimal transient growth are solutions of the maximization problem $G(T) = \max_{\mathbf{u}_0}\left(\|\mathbf{u}(T)\|^2/\|\mathbf{u}_0\|^2\right)$. To find the optimal perturbations we use a direct adjoint iterative technique [4] in which we solve the direct and adjoint Navier-Stokes equations with a pseudo-spectral code. The basic states considered and the results are discussed in the following.

2 Hyperbolic Tangent Velocity Profile

We consider $\mathbf{U}(y) = \tanh(y)\mathbf{e}_x$ as the base state. We can write the perturbation velocity as $\mathbf{u} = \mathbf{u}'(y,t)e^{i(k_x x + k_z z)}$ and we characterize the gain of the optimal perturbations by their mean growthrate $\sigma_m(k_x,k_z,T) = \log(G)/2T$.

As shown in figure 2(a) for $T = 7$, for short optimization times ($T < 14$) the most amplified optimal perturbations are 3D. They correspond to a combination of the Orr and the lift-up mechanisms as is common for the transient growth in shear flows

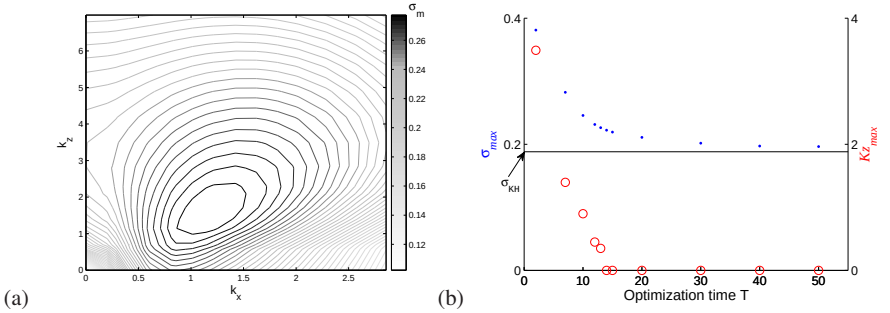

Fig. 1 (a) Mean growthrate σ_m of the optimal perturbations for $T = 7$. (b) σ_{max} (dots) and Kz_{max} (circles), i.e. maximum over (k_x,k_z) of $\sigma_m(T)$ and associated k_z.

[1]. As the optimization time increases, the most amplified optimal perturbations become 2D as the unstable KH modes start to dominate (see circles in fig. 2(b)). As T increases further, the optimal responses approaches the KH mode and the perturbations approach the corresponding adjoint mode. The dots in figure 2(b) show how the mean growthrate of the most amplified optimal perturbation approaches from above the largest growthrate of the KH instability σ_{KH}.

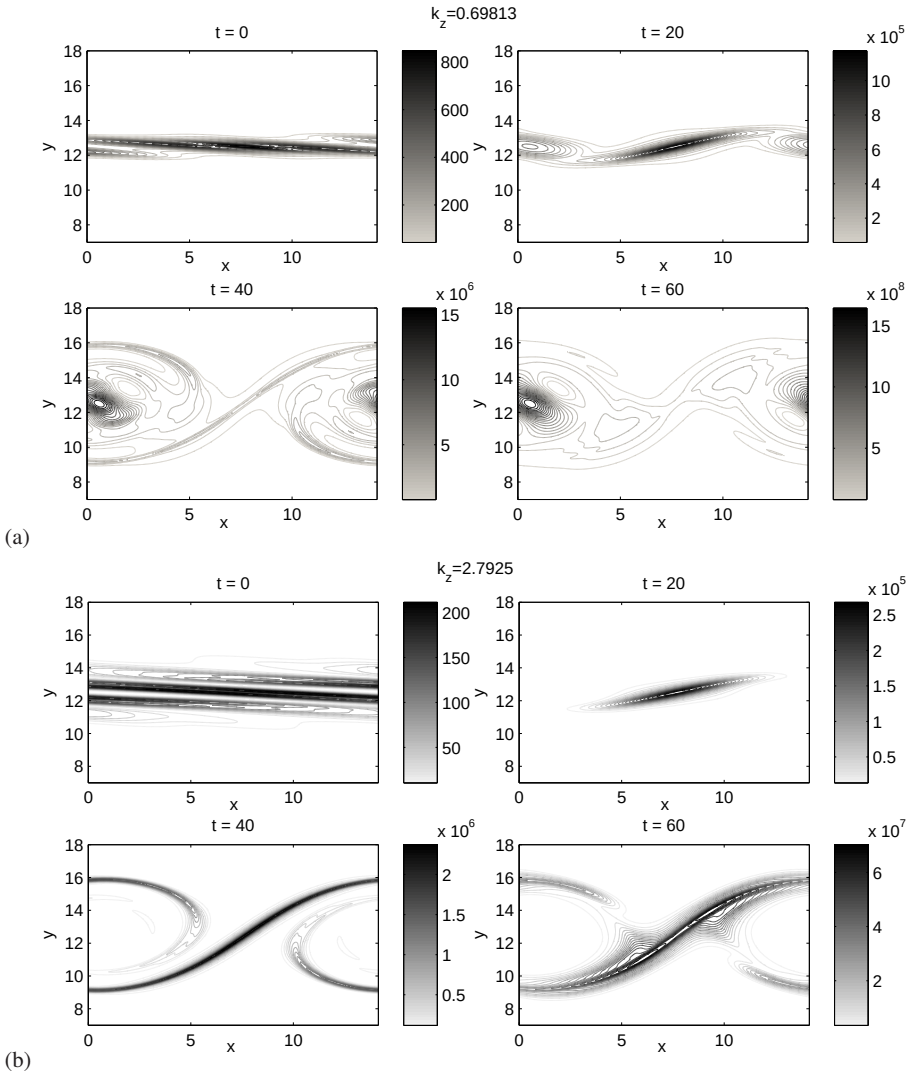

Fig. 2 Energy density snapshots for the two types of responses observed: (a) Elliptic response dominant for small k_z when $T_{sat} = 35$, (b) Hyperbolic response for large k_z and $T_{sat} = 35$. Snapshots times and corresponding wavenumber are indicated on each plot. Optimization time is $T = 60$.

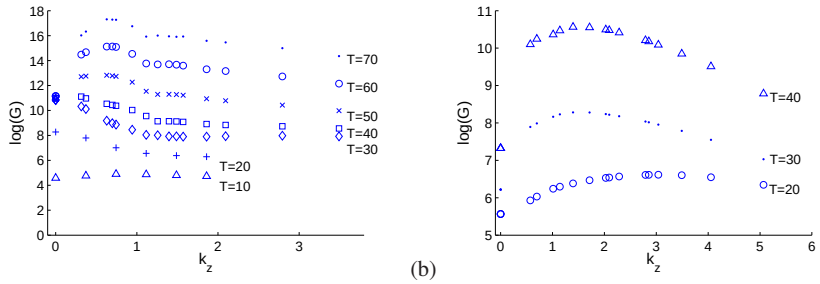

Fig. 3 $G(k_z,T)$) for $T_{sat} = 35$ (a) and $T_{sat} = 15$ (b). Symbols for each T are indicated on plots.

3 Developing KH billow

We consider the fully nonlinear development of the 2D KH instability as our time dependent basic state. As initial condition for the basic state we use the most unstable linear KH mode, the initial amplitude being characterized by the saturation time T_{sat}, time at which the amplitude of the 2D field superposed on the *tanh* profile reaches its maximum energy. The basic flow fixes the streamwise wavenumber at $k_x = 0.44$ (the most unstable KH mode) and supresses the subharmonic instability. The perturbative field now is $\mathbf{u} = \mathbf{u}'(x,y,t)e^{i(k_z z)}$ and the optimal gain becomes a function of 3 variables $G(k_z, T_{sat}, T)$. We calculated optimal perturbations for $T_{sat} = 35$ and $T_{sat} = 15$.

The optimal responses for $T_{sat} = 35$ and different k_z and T reveal both the elliptic and hyperbolic mechanisms. The largest gain for $T > 50$ occurs at $k_z \approx 0.7$ and is associated to an elliptic type of response as seen on fig. 2(a). Hyperbolic response dominates for larger k_z. For $T_{sat} = 15$, the optimal response is of hyperbolic type for all times and wavenumbers explored, except at large time ($T = 40$) for the 2 smallest k_z computed. The gain of the calculated optimal perturbations is shown in figure 3.

With these computations we have determined the mechanisms that have the greater potential for linear growth on mixing layers.

References

1. Farrell, B.F., Ioannou, P.J.: Perturbation growth in shear flow exhibits universality. Phys. Fluids A, **5**, 2298–2300 (1993)
2. Caulfield, C.P., Peltier, W.R.: The anatomy of the mixing transition in homogeneous and stratified free shear layers. J. Fluid. Mech. **413**, 1–47 (2000)
3. Fontane, J., Joly, L.: The stability of the variable-density Kelvin-Helmholtz billow. J. Fluid. Mech. **612**, 237–260 (2008)
4. Corbett, P., Bottaro, A.: Optimal linear growth in swept boundary layers. J. Fluid. Mech. **435**, 1–23 (2001)

Transient evolution and high stratification scaling in horizontal mixing layers

C. Arratia[a], S. Ortiz[a,b] and J. M. Chomaz[a]

[a] Laboratoire d'Hydrodynamique (LadHyX), École Polytechnique-CNRS, 91128 Palaiseau Cedex, France
[b] UME/DFA, ENSTA, chemin de la Hunière, 91761 Palaiseau Cedex, France
cristobal.arratia at ladhyx.polytechnique.fr

1 Introduccion

Mixing layers (sheared flows in homogeneous or stratified fluid) are present in many geophysical contexts and may lead to turbulence and mixing. In several cases, mixing layers are known to exhibit the Kelvin-Helmholtz instability leading to the roll-up of spanwise vortices, the Kelvin-Helmholtz (KH) billows. This is an essentially two-dimensional (2D) process. In fact, in the homogeneous cases the Squire's theorem implies that the most unstable mode is 2D. However, Squire's theorem applies only for the exponentially growing perturbations that control the large time dynamics and is not valid for the transient dynamics at short time. Indeed, Iams et al.[1] have shown that, in the non-stratified case, the most amplified optimal perturbations for short times are three-dimensional (3D) and result from a cooperation between the lift-up and Orr mechanisms[2]. This provides a finite time mechanism for spanwise scale selection, scale that may persist at later times if nonlinearities are strong enough.

In the present contribution, we extend the computation of 3D, finite time optimal perturbations to the case of an horizontal mixing layer with vertical linear stratification. As discussed by Deloncle *et al.*[4], the Squire's theorem does not apply to this horizontal shear layer when the fluid is stratified, but the inviscid stability analysis of [4] shows that the most unstable mode is still 2D. The nonlinear dynamics of such an horizontal shear vertically stratified has been numerically simulated by Basak & Sarkar[3]. They observed the development of a disordered 3D structure made of a pilling up of horizontal layers where the velocity is mainly horizontal and decorrelated from one layer to the next. The evolution equations, being homogeneous in z, impose no vertical scale in the flow evolution and the mechanism selecting this scale has yet to be understood. Extrapolating from the homogeneous case, transient growth is a possible linear mechanism that might explain the vertical scale selection.

In the present paper, optimal transient growth are therefore computed for an horizontal shear flow vertically stratified.

2 Formulation and Methods

Using cartesian coordinates $\mathbf{x} = (x, y, z)$ with z increasing upwards, and time coordinate t, we consider the evolution of the perturbative velocity $\mathbf{u}(\mathbf{x}, t)$ and density $\rho(\mathbf{x}, t)$ fields according to the linearized incompressible Navier-Stokes equations in the Boussinesq approximation. Our base state is $\mathbf{U_B} = U_0 \tanh(y/L)\hat{x}$ with a stable linear density stratification $\rho_B(z) = \rho_0(1 - N^2 z/g)$, where ρ_0 is a reference density, g is the acceleration of gravity and $N = \sqrt{-g/\rho_0 d\rho_B/dz}$ is the Brunt-Väisälä frequency. The adimensionalization is such that $L = U_0 = 1$, so that the value of the Brunt-Väisälä frequency N measures the buoyancy strength as the ratio between the advective and the buoyancy time scales: the stronger the stratification, the faster it affects the dynamics. The corresponding adimensional parameter is the horizontal Froude number $F_h \equiv U_0/LN = N^{-1}$, which goes to zero in the high stratification limit. The other adimensional parameters of the problem, coming from viscocity ν and molecular diffusivity D, correspond to the Reynolds $Re = U_0 L/\nu$ and the Schmidt $Sc = \nu/D$ numbers. Throughout the paper their values will be $Re = 1000$ and $Sc = 1$.

The homogeneity in x and z of the evolution equations allows us to rewrite the fields as $[\mathbf{u}, \rho](x, y, z, t) \longrightarrow [\mathbf{u}, \rho](y, t)e^{i(k_x x + k_z z)}$ and consider independently the linear evolution of the different streamwise-spanwise wavenumbers. Because of the latter, for each point in the (k_x,k_z)-plane we can define the optimal gain as

$$G(T) \equiv max_{[\mathbf{u},\rho](y,0)} \left(\frac{\int \mathbf{u}^2(T) + N^2\rho^2(T)dy}{\int \mathbf{u}^2(0) + N^2\rho^2(0)dy} \right), \tag{1}$$

i.e., the maximum attainable increase in energy up to time T. We span the (k_x,k_z)-plane for each time T at which we compute the optimal perturbation, that is, the initial condition $[\mathbf{u}, \rho](y, 0)$ that attains the optimal gain G. These optimal perturbations are computed by the iterative procedure proposed by Corbett & Bottaro[5], whereby the succesive numerical integration of the direct and the time reversed adjoint equations is performed until convergence is achieved. For the computations we use a pseudo-spectral method with an Adams-Bashfort time scheme.

In the following, we characterize our results by the optimal mean growthrate of the perturbation

$$\sigma_m(k_x, k_z, T) \equiv \frac{ln(G(k_x, k_z, T))}{2T} \tag{2}$$

which allows an easier comparison with the maximum growthrate of the most unstable KH mode, $\sigma_{KH} \approx 0.18$ as a reference.

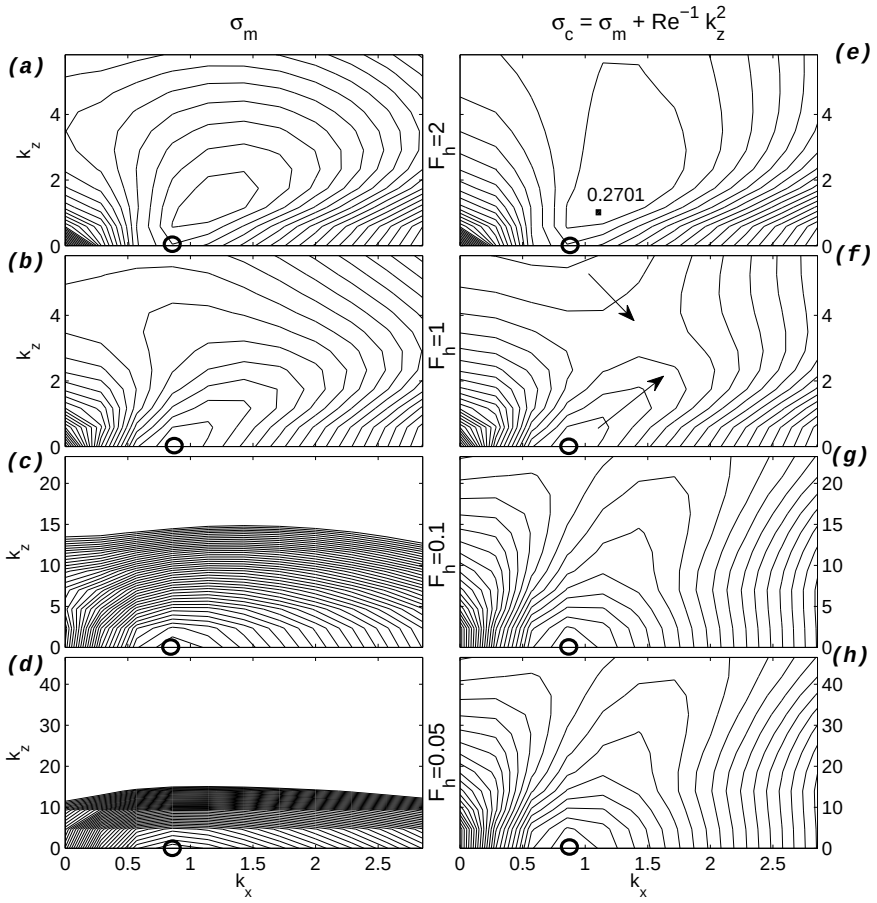

[b]

Fig. 1. Amplification of the optimal perturbations for T=7.
On the left column we show the positive isolines of the optimal mean growthrate (the right column shows the same values corrected to compensate the viscous dissipation of perturbations, see text) for 4 different F_h numbers as indicated on each row. The values of the isolines are defined equally in all figures, decreasing in steps of 0.006 from the overall maximum value $\simeq 0.2701$ (marked by the (■) in ***e***). The arrows in (***f***) represent the decreasing directions of the contours and the (○) on each plot represents the maximum gain for 2D perturbations, which has the same value of $\simeq 0.26$ in all figures. The horizontal (resp. vertical) axes are equal on each column (resp. row). Note the change in the vertical axis in the last 2 rows.

3 Results and Discussion

In the figure 1(***a-d***), we show contours of $\sigma_m(k_x, k_z) > 0$ for $T = 7$ and for different levels of stratification. For moderate stratifications ($F_h = 2$, figure 1(***a***)), the most amplified optimal perturbations are 3D. In this case there is essentially no difference with the homogeneous case of [1], the largest optimal gain being associated with the combination of the lift-up and Orr mechanisms. When stratification is increased (figures 1(***b,c,d***)), the optimal perturbations with the largest gain becomes 2D ($k_z = 0$).

In order to take into account the viscous diffusion, we plot the corrected optimal mean growthrate $\sigma_c(k_x, k_z) = \sigma_m(k_x, k_z) + Re^{-1}k_z^2$ (right column of fig. 1***e*** - ***h***), where only the diffusion in z is compensated since for small F_h, large k_z are destabilized. In the $F_h = 1$ case (fig. 1 (***f***)), we observe that the most amplified perturbation is 2D and due to the Orr mechanism alone, as confirmed by looking at the perturbation field data (not shown).

In the strongly stratified cases ($F_h = 0.1, 0.05$), we note that the dependence on the vertical wavenumber scales as F_h^{-1}, as it is evident from the almost perfect invariance with the Froude number of the contours when plotted in the scaled range of vertical wavenumbers. This scaling law corresponds to the inviscid self similarity proposed by Billant & Chomaz[6], which extends the analyses of Riley *et al.* [7] and Lilly [8]. Here we generalize this scaling for finite viscosity and capture the F_h dependence in the high stratification limit as

$$\sigma_m(k_x, k_z, T, F_h, Re) \approx \sigma_c(k_x, k_z F_h, T) - Re^{-1}k_z^2. \tag{3}$$

This shows that the inviscid scaling of the high stratification limit is indeed valid for the linear transient growth of perturbations, viscosity being easily accounted for by adding the corresponding damping term.

Despite transient growth does not select a particular vertical length-scale, the scaling found affects the receptivity by increasing the range of vertical scales sensitive to noise and decreasing the selectivity for 2D structures. Current research is on how this selectivity is affected by nonlinearities.

References

1. S. Iams, C. Arratia, C. Caulfield and J. M. Chomaz, In preparation (2009).
2. B. Farrel and P. J. Ioannou, Phys. Fluids A **5**, 2298 (1993).
3. S. Basak and S. Sarkar, J. Fluid. Mech. **568**, 19 (2006).
4. A. Deloncle, J. M. Chomaz and P. Billant, J. Fluid. Mech. **570**, 297 (2007).
5. P. Corbett and A. Bottaro J. Fluid. Mech. **435**, 1 (2001).
6. P. Billant and J. M. Chomaz, Phys. Fluids **13**, 1645 (2001).
7. J. J. Riley, R. W. Metcalfe and M. A. Weissman in *Nonlinear Properties of Internal Waves,* edited by B. J. West, AIP Conf. Proc. **76**, 79 (1981).
8. D. K. Lilly J. Atmos. Sci. **40**, 749 (1983).

Inviscid transient growth on horizontal shear layers with strong vertical stratification.

Cristóbal Arratia, Sabine Ortiz, Jean-Marc Chomaz

Laboratoire d'Hydrodynamique (LadHyX), École Polytechnique-CNRS.
cristobal.arratia@ladhyx.polytechnique.fr

Abstract

We report an investigation of the three-dimensional stability of an horizontal free shear layer in an inviscid fluid with strong, vertical and constant density stratification. We compute the optimal perturbations for different optimization times and wavenumbers. The results allow comparing the potential for perturbation energy amplification of the free shear layer instability and the different mechanisms of transient growth. We quantify the internal wave energy content of the perturbations and identify different types of optimal perturbations. Intense excitation of gravity waves due to transient growth of perturbations is found in a broad region of the wavevector plane. Those gravity waves are eventually emitted away from the shear layer.

1 Introduction

During the last years, there has been an increased interest in the effects of horizontal shear in geophysical flows. In that context, a horizontal mixing layer with vertical stratification is one idealized flow model presenting the effect of shear and also the free shear or Kelvin-Helmholtz (KH) instability. The two dimensional (2D) modes of the KH instability are not affected by stratification. The vertical structure developing in such a flow is however strongly affected by stratification, as shown by the direct numerical simulations (DNS) performed by Basak and Sarkar (2006). Basak and Sarkar (2006) show the appearance of a layered structure consisting of a stack of pancake vortices with a vertical correlation length of the order of the buoyancy length. Despite the non applicability of Squire's theorem to this flow, Deloncle et al. (2007) have shown that the most unstable mode is still 2D. This implies that modal stability analysis on the parallel shear layer does not select a specific vertical lengthscale. For strong stratification, however, the range of unstable vertical wavenumbers widens proportionally to the inverse of the Froude number, which means that stronger stratification destabilizes smaller vertical lengthscales. This is a consequence of the self similarity of strongly stratified inviscid flows found by Billant and Chomaz (2001).

Another important aspect of horizontal shear flows with vertical stratification concerns internal gravity wave generation and emission. The generation and emission of internal waves has been studied, among others, by Vanneste and Yavneh (2004) in the rotating case and by Bakas and Farrell (2009b) in the non-rotating case. Both studies focus on linearized dynamics of perturbations of plane constant shear flow, which allows finding analytic expressions for the generated wave amplitude in different asymptotic regimes. This simplified model has no unstable modes nor intrinsic horizontal lengthscale.

Here we consider linearized perturbations of a horizontal mixing layer with a tanh velocity profile and vertical stratification on a non-rotating frame. We study the sensitivity to initial conditions by computing the optimal perturbations, perturbations that maximize

the energy growth up to an optimization time T. We compute the optimal perturbations for a broad range of streamwise and spanwise wavenumbers and for different optimization times T. In this way we can determine, for different times, whether the KH instabilty or other transient growth mechanisms are more efficient in extracting energy from the basic flow. We then quantify the vortex and gravity wave energy content of the perturbations by means of a Craya-Herring, or poloidal-toroidal, decomposition (Godeferd and Cambon, 1994). This decomposition helps identifying different types of optimal perturbations according to their wave/vortex energy content. We show that some of the optimal perturbations involve the generation of waves that are eventually radiated away from the shear layer.

2 Formulation and Methods

We consider the evolution of the perturbative velocity $\mathbf{u}(\mathbf{x},t)$ and density $\rho(\mathbf{x},t)$ fields according to the linearized incompressible Euler equations in the Boussinesq approximation. Here $\mathbf{x}=(x,y,z)$ is the cartesian coordinate vector with z increasing upwards, and t is the time coordinate. Our base state is $\mathbf{U}=\tanh(y)\mathbf{e}_x$ with a stable linear density stratification $\rho_B(z)=\rho_0(1-N^2z/g)$, where ρ_0 is a reference density, g is the acceleration of gravity and $N=\sqrt{-g/\rho_0 d\rho_B/dz}$ is the Brunt-Väisälä frequency. With this variables, the horizontal Froude number corresponding to the ratio between the buoyancy and advective time scales is $F_h=N^{-1}$.

Linearity and homogeneity in x and z of the evolution equations allow us to rewrite the fields as $[\mathbf{u},\rho](x,y,z,t)\longrightarrow[\mathbf{u},\rho](y,t)e^{i(k_x x+k_z z)}$, and to consider independently the evolution of the different streamwise-spanwise wavenumbers. Because of the latter, for each point in the (k_x,k_z)-plane we can define the optimal gain as

$$G(T)=\max_{[\mathbf{u},\rho](y,0)}\left(\frac{E(T)}{E(0)}\right), \tag{1}$$

where the total energy E is given up to a constant by

$$E=\int\left(\mathbf{u}^2+N^2\rho^2\right)\,\mathrm{d}y. \tag{2}$$

Thus, $G(T)$ is the maximum attainable increase in energy up to the optimization time T. We span the (k_x,k_z)-plane for each time T at which we compute the optimal perturbation. We characterize the transient growth by the optimal mean growthrate of the perturbation

$$\sigma_m(k_x,k_z,T)=\frac{1}{2T}\int_0^T\frac{\partial}{\partial t}\log\left[E(k_x,k_z,t)\right]\mathrm{d}t, \tag{3}$$

where $E(k_x,k_z,t)$ is the energy of the optimal perturbation. Using definition (3) we can directly compare the amplification of the optimal perturbations with the growthrate of the most unstable KH mode, $\sigma_{KH}=0.1897$ (Deloncle et al., 2007).

The optimal perturbations are computed by the iterative procedure described by Corbett and Bottaro (2001), whereby the succesive numerical integration of the direct and the time reversed adjoint equations is performed until convergence is achieved. The adjoint equations and optimization algorithm have been adapted on a pseudo-spectral DNS code

with an Adams-Bashforth time scheme. The DNS code was originally developed by Vincent and Meneguzzi (1991), Delbende et al. (1998) and Deloncle et al. (2008).

Throughout this paper we will use $F_h = 0.1$, which is small enough so that the strongly stratified similarity described by Billant and Chomaz (2001) holds to a very good approximation (Arratia et al., 2011), as is also the case for the eigenmodes (Deloncle et al., 2007) and the viscous transient growth after correcting by the viscous damping factor $e^{\nu k_z^2 T}$ (here ν is the viscosity, Arratia et al., 2009). In this context, the main consequence of this scaling law is that, for $F_h \lesssim 0.1$, we can plot the results as a function of $k_z F_h$ to capture the dependence on both k_z and F_h. The results are not significantly different for $F_h < 1$ (Arratia et al., 2011).

3 Results

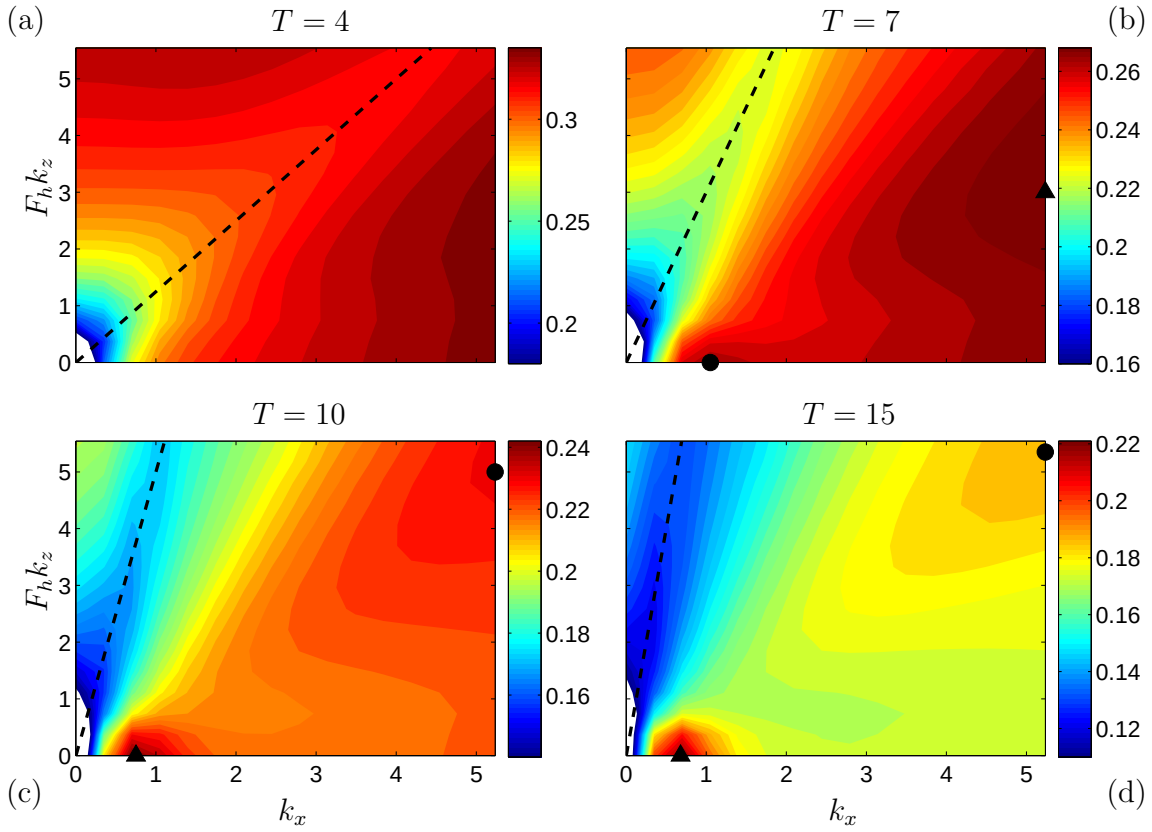

Figure 1: Optimal mean growthrate $\sigma_m(k_x, F_h k_z)$ for optimization times $T = 4$ (a), $T = 7$ (b), $T = 10$ (c), and $T = 15$ (d). The colorbar is indicated next to each figure. The horizontal and vertical axis are the same on all figures, as shown in the lower left figure (c). The values of the ratio $F_h k_z / k_x$ indicated by the dashed lines are $r_{min} = 5/4, 3, 5$ and 8 for $T = 4, 7, 10$ and 15, respectively. In (b), (c) and (d), the ▲ indicates the maximum of the computed σ_m (at the boundary in (c) and the • indicates a secondary local maximum (at the boundary in (c) and (d).

Figure 1 shows $\sigma_m(k_x, F_h k_z)$ for $T = 4, 7, 10$ and 15. The colorbars indicate that σ_m decreases as T increases. The dashed line on each of the figures indicates roughly the ratio $r = F_h k_z / k_x$ at which the optimal perturbations are less amplified. The value of r corresponding to the dashed lines, say r_{min}, increases as T increases. For $T = 4$, σ_m increases as $k = \sqrt{k_x^2 + (F_h k_z)^2}$ increases and shows no clear maximum. For $T = 7, 10$

and 15, the global maximum of the computed σ_m is indicated by a ▲ and a second, local maximum of the computed σ_m is marked by a •; these are located at large k and around the KH unstable region with $k_z = 0$. For $T = 7$, the maximum occurs for large k at the ▲ around $r = 3/5$, and the maximum close to the KH unstable region is only a local maximum. For $T = 10$ and 15, the global maximum is 2D and located in the KH unstable region, while the secondary maximum appears at large k, at the boundary of the domain.

3.1 Craya-Herring decomposition

Following Godeferd and Cambon (1994), we define the Craya-Herring basis $(\mathbf{e}_1, \mathbf{e}_2, \mathbf{e}_3)$ as $\mathbf{e}_1 = \mathbf{k}\times\mathbf{e}_z/|\mathbf{k}\times\mathbf{e}_z|$, $\mathbf{e}_2 = \mathbf{k}\times(\mathbf{k}\times\mathbf{e}_z)/|\mathbf{k}\times(\mathbf{k}\times\mathbf{e}_z)|$ and $\mathbf{e}_3 = \mathbf{k}/|\mathbf{k}|$, where $\mathbf{k} = (k_x, k_y, k_z)^T$ is the wave vector. In this orthonormal basis, the Fourier transform of the velocity field becomes $\hat{\mathbf{u}} = \hat{\phi}_1\mathbf{e}_1 + \hat{\phi}_2\mathbf{e}_2$ because $\hat{\mathbf{u}}\cdot\mathbf{e}_3 = 0$ due to the incompressibility condition. When $\sqrt{k_x^2 + k_y^2} \neq 0$, the energy density in spectral space $\epsilon(\mathbf{k})$ is given by

$$\epsilon(\mathbf{k}) = |\hat{\phi}_1|^2 + |\hat{\phi}_2|^2 + |\hat{\phi}_3|^2, \tag{4}$$

with

$$\hat{\phi}_1 = \frac{i}{\sqrt{k_x^2 + k_y^2}}\hat{\omega}_z, \tag{5a}$$

$$\hat{\phi}_2 = -\sqrt{\frac{k_x^2 + k_y^2 + k_z^2}{k_x^2 + k_y^2}}\hat{u}_z, \tag{5b}$$

$$\hat{\phi}_3 = N\hat{\rho}, \tag{5c}$$

where $\hat{\omega}_z$ is the Fourier transformed vertical vorticity. The total energy may be expressed as $E = \int \epsilon \, \mathrm{d}k_x\mathrm{d}k_y\mathrm{d}k_z$.

The $\hat{\phi}_1\mathbf{e}_1$ part of the velocity field is purely horizontal so it does not directly affect the disturbance density field. For the linear dynamics in the absence of a basic flow, decomposition (5) provides a separation of the fields in which the $\hat{\phi}_1\mathbf{e}_1$ part of the velocity field decouples from the internal wave dynamics given by $\hat{\phi}_2$ and $\hat{\phi}_3$. Despite the fact that the wave and vortical parts of the velocity field can not be unambiguously split in a general case, this decomposition provides an objective, physically motivated way of quantifying the wave content of the perturbative field. We will thus refer to the different components as the wave and vortex parts of the flow fields.

Figure 2 shows the fraction of the total energy contained in the vortex part $\hat{\phi}_1$ of the velocity field, for each of the optimal perturbations of figure 1. Figure 2 shows the energy fractions of the optimal initial condition ($t = 0$) and the optimal response ($t = T$). Also shown are the dashed lines of figure 1 indicating r_{min}, the value of $r = F_h k_z/k_x$ where the optimal perturbations have lower growth. Blue contours indicate that most of the perturbation energy corresponds to gravity waves. In the left column we observe that the wave content of the optimal initial condition depends mainly on r. The energy of the optimal initial condition is given by the vortex part for $r = 0$ and the energy of the wave part becomes increasingly important as r increases. It can be seen that the dashed lines at r_{min} coincide, roughly but consistently for all T, with the region where the energy of the optimal initial condition changes from being mostly vortex to mostly wave. The energy of the optimal response, on the other hand, is mostly given by the vortex part for

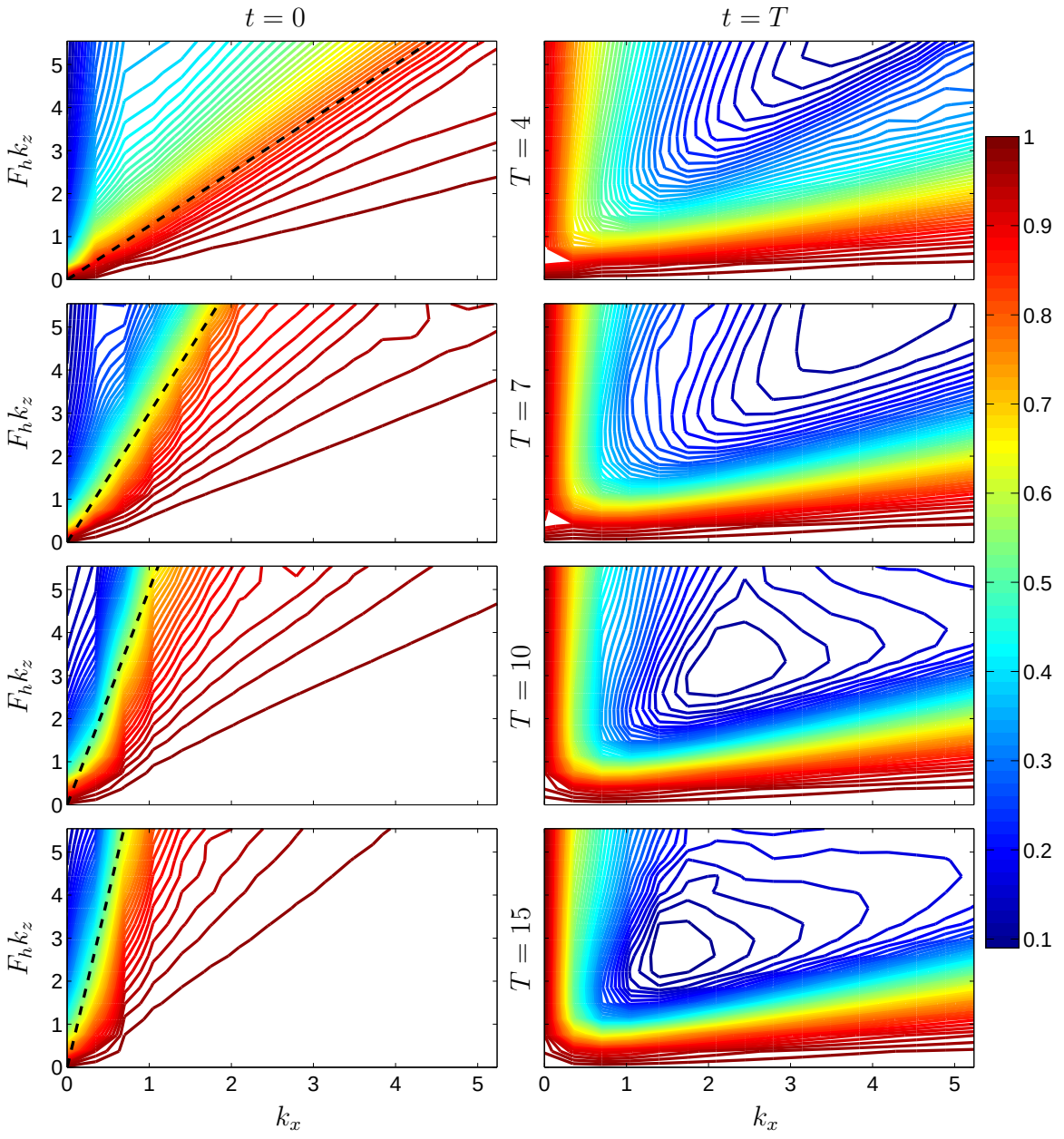

Figure 2: Energy fraction in the vortical part $\frac{\int |\hat{\phi_1}|^2 \, \mathrm{d}k_y}{E}$ for the optimal perturbations at $t = 0$ (left column) and optimal response at $t = T$ (right column). The optimization time for each row, starting from above, are $T = 4$, $T = 7$, $T = 10$ and $T = 15$, as indicated on the figure. Here, for $k_x = 0$, the energy of the horizontal mean flow (which corresponds to $\sqrt{k_x^2 + k_y^2} = 0$) has been added to the energy of $\hat{\phi}_1$.

$k_x \sim 0$ and for $F_h k_z \sim 0$, while for most of the domain where $k_x, F_h k_z \gtrsim 1$, the energy of the optimal response is mainly in the wave part.

4 Discussion

Figures 1 and 2 help in distiguishing three main regions on the $(k_x, F_h k_z)$ plane. First, for $F_h k_z \sim 0$, the dynamics is dominated by the vertical vorticity (figure 2) and is essentially

2D. In this region, the Orr mechanism dominates the inviscid transient growth for short time (figure 1a) and for large k_x, while the KH instability becomes increasingly important as T increases (figures 1b-d). Second, for $k_x \sim 0$, the optimal transient growth consists of waves generating large horizontal velocity (figure 2), giving large transient growth for short times (figures 1a,b). The mechanism involved here is the transient generation of streamwise streaks during the passage of waves through shear (Bakas and Farrell, 2009a; Arratia et al., 2011). This transient growth mechanism is similar to the lift-up mechanism, it produces streamwise velocity as a result of cross-stream transport. This mechanism is perhaps related to the cross-stream transport of KH billows that is linked to the layered structure reported by Basak and Sarkar (2006) (Arobone and Sarkar, 2010). Third, for $k_x, F_h k_z \gtrsim 1$ and $r \lesssim r_{min}$, the optimal perturbations result mainly in the generation of wave energy from the vortical part (figure 2). This is an efficient mechanism of perturbation energy growth, the most efficient indeed for intermediate times ($T = 7$ in figure 1b). In the absence of viscosity, this mechanism does not seem to reach a maximum of σ_m for finite (k_x, k_z).

An important aspect concerns whether the generated wave energy remains in the wave part after T. Figure 3 shows spatio-temporal diagrams of the vortex and wave energy density for an optimal perturbation at $T = 7$, for (k_x, k_z) in the region of wave generation and largest energy growth (close to the ▲ in figure 1b). From $t = 0$ to 7, the perturbation energy grows by a factor of 43.6, more than any unstable mode during that time. Initially, most of the energy growth occurs on the vortical part. Wave energy starts being noticeable around $t = 5$ and then increases quickly when the vortex energy is transferred into the wave part of the flow. The generated wave is then radiated away after the optimization time. This qualitative behaviour is the same for different optimization times.

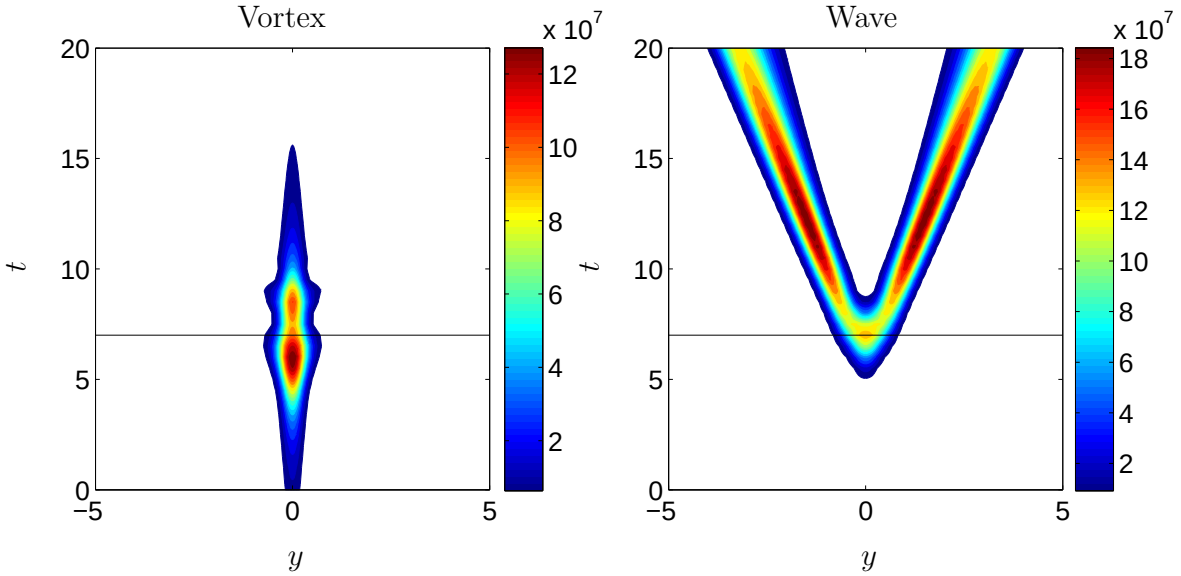

Figure 3: Spatio-temporal diagram of the optimal perturbation for $T = 7$ (horizontal line), $(k_x, F_h k_z) = (4.89, 2.96)$. Colorbar shows the energy density of the vortex (left) and internal gravity wave (right) components of the flow. The vortex energy density is obtained by taking the inverse Fourier transform in the y direction of $|\hat{\phi}_1|^2$ evaluated at the corresponding (k_x, k_z). The same is done with $|\hat{\phi}_2|^2 + |\hat{\phi}_3|^2$ for the energy of the wave part.

5 Conclusion

We have computed the optimal perturbations on a horizontal mixing layer with strong vertical stratification. For short optimization times (up to T between 7 and 10), the most amplified perturbations occur for large wavenumbers, away from the KH unstable region that dominates for large T. We have done a Craya-Herring decomposition to quantify the wave and vortex energy content of the optimal perturbations. Using this decomposition we can distinguish 3 main different types of optimal perturbations: quasi 2D for $F_h k_z \sim 0$, streamwise streaks generated by waves for $k_x \sim 0$, and waves generated by vortical motion for $k_x, F_h k_z \gtrsim 1$ and $r \lesssim r_{min}$.

An important result is the fact that, for moderate times ($T \sim 7$), the most amplified optimal perturbations produce waves that are eventually radiated away from the shear layer. This wave generation and emission mechanism remains efficient in the large wavenumber region even for larger T, when the KH instability becomes the most efficient mechanism.

References

Arobone, E. and Sarkar, S. (2010). The statistical evolution of a stratified mixing layer with horizontal shear invoking feature extraction. *Physics of Fluids*, 22(11):115108.

Arratia, C., Ortiz, S., and Chomaz, J. M. (2009). Transient evolution and high stratification scaling in horizontal mixing layers. In Eckhardt, B, editor, *ADVANCES IN TURBULENCE XII - PROCEEDINGS OF THE 12TH EUROMECH EUROPEAN TURBULENCE CONFERENCE*, volume 132 of *Springer Proceedings in Physics*, pages 183–186, HEIDELBERGER PLATZ 3, D-14197 BERLIN, GERMANY. SPRINGER-VERLAG BERLIN. 12th EUROMECH European Turbulence Conference, Marburg, GERMANY, SEP 07-10, 2009.

Arratia, C., Ortiz, S., and Chomaz, J. M. (2011). In preparation.

Bakas, N. A. and Farrell, B. F. (2009a). Gravity waves in a horizontal shear flow. part i: Growth mechanisms in the absence of potential vorticity perturbations. *Journal of Physical Oceanography*, 39(3):481–496.

Bakas, N. A. and Farrell, B. F. (2009b). Gravity waves in a horizontal shear flow. part ii: Interaction between gravity waves and potential vorticity perturbations. *Journal of Physical Oceanography*, 39(3):497–511.

Basak, S. and Sarkar, S. (2006). Dynamics of a stratified shear layer with horizontal shear. *Journal of Fluid Mechanics*, 568(-1):19–54.

Billant, P. and Chomaz, J.-M. (2001). Self-similarity of strongly stratified inviscid flows. *Physics of Fluids*, 13(6):1645–1651.

Corbett, P. and Bottaro, A. (2001). Optimal linear growth in swept boundary layers. *Journal of Fluid Mechanics*, 435(-1):1–23.

Delbende, I., Chomaz, J.-M., and Huerre, P. (1998). Absolute/convective instabilities in the batchelor vortex: a numerical study of the linear impulse response. *Journal of Fluid Mechanics*, 355(-1):229–254.

Deloncle, A., Billant, P., and Chomaz, J.-M. (2008). Nonlinear evolution of the zigzag instability in stratified fluids: a shortcut on the route to dissipation. *Journal of Fluid Mechanics*, 599(-1):229–239.

Deloncle, A., Chomaz, J.-M., and Billant, P. (2007). Three-dimensional stability of a horizontally sheared flow in a stably stratified fluid. *Journal of Fluid Mechanics*, 570(-1):297–305.

Godeferd, F. S. and Cambon, C. (1994). Detailed investigation of energy transfers in homogeneous stratified turbulence*. *Physics of Fluids*, 6(6):2084–2100.

Vanneste, J. and Yavneh, I. (2004). Exponentially small inertia-gravity waves and the breakdown of quasigeostrophic balance. *Journal of the Atmospheric Sciences*, 61(2):211–223.

Vincent, A. and Meneguzzi, M. (1991). The spatial structure and statistical properties of homogeneous turbulence. *Journal of Fluid Mechanics*, 225(-1):1–20.